2015

The design and development of novel metal oxide nanocomposites for sunlight driven water cleaning

Kanlaya Pingmuang
University of Wollongong

UNIVERSITY OF WOLLONGONG

Department of Chemistry

The Design and Development of Novel Metal Oxide Nanocomposites for Sunlight Driven Water Cleaning

Kanlaya Pingmuang

This thesis is presented as part of the requirement for the Award of the Degree of Doctoral of Philosophy of the University of Wollongong

August 2015

ABSTRACT

Photocatalytic degradation of environmental pollutants using a visible light-driven photocatalysts has attracted much attention in order to effectively utilize the majority of the solar energy. Bismuth vanadate ($BiVO_4$) has been one of the semiconducting materials used as visible light driven photocatalysts due to its physical and chemical properties and remarkable photocatalytic performance. However, the individual $BiVO_4$ exhibits low efficiency in photodegradation of organic pollutants. The recombination of photogenerated electron and hole pairs and redox potentials of the generated electron are considered as the factors that affect to its photocatalytic efficiency. In this regard, the primary aims of this work are to synthesis $BiVO_4$ by a simple, cost effective and environmentally friendly method and to improve its photocatalytic efficiency by coupling with selected metal oxides, providing appropriate different band edge positions. To achieve these goals, $BiVO_4$ nanoparticles were prepared by a single-step microwave at the low temperature of 90°C (< 300 W) for a short holding time of 1 h. The photocatalytic activity of the $BiVO_4$ was studied through monitoring degradation of Rhodamine B (RhB) and Methylene blue (MB) as model dyes under a simulated solar irradiation. The influence of parameters including film thickness, initial dyes concentration, solar light intensity and reactor volume on the photocatalytic activities of the $BiVO_4$ were investigated. The $BiVO_4$ was modified by coupling with CeO_2, TiO_2 and WO_3 in order to enhance transport of charge carriers that can improve photocatalytic degradation of dyes. Additionally, possible mechanisms of the three composites in photocatalytic degradation of dyes were also investigated by monochromatic light experiments and reactive species quenching study.

.

ACKNOWLEDGEMENTS

I would like to express my sincere gratitude to many people responsible for helping me throughout this thesis and greatly increased the quality of my education. First of all, I would like to express my deepest appreciation to A/P Jun Chen and Andrew Nattestad for their supervision, valuable suggestions and all support, they have given me throughout my student life in Australia. I also would like to thank A/P Sukon Phanichphant, my supervisor at Chiang Mai University for her support and visits to the University of Wollongong. I have been so fortunate to have their as my supervisors and without them I could not have achieved as much. My thanks go to Prof. Gordon Wallace for Joint Ph.D. program between Chiang Mai University and University of Wollongong.

Furthermore, I would like to gratefully acknowledge the financial support from Thailand Graduate Institute of Science and Technology and the Graduate School, Chiang Mai University for providing all the financial supports. I also would like to thank The Australian National Fabrication Facility (ANFF), ARC Centre of Excellence for Electromaterials Science (ACES), The Electron Microscopy Centre (EMC) at University of Wollongong (Australia), and Faculty of Sciences Chiang Mai University for the facility support. Besides, I would also like to thank all members of the Intelligent Polymer Research Institute (IPRI), University of Wollongong, Australia for their help and warm friendship.

Last but not least, I would like to express my deepest gratitude to my family, my most beloved mom, Baokeaw, dad, Sangwan, and my brother, Paisan, without their continued support and encouragements I would not have completed this work. Mom and dad are wonderful parents and I will forever be grateful for everything they have done for me throughout my life.

Kanlaya Pingmuang

TABLE OF CONTENTS

LIST OF FIGURES

LIST OF TABLES

CHAPTER 1

INTRODUCTION

As reported by the United Nations, the world's population is currently increasing and expected to rise to 36.4 billion people by the year 2300.[1] That means more of the basic needs, food, water, shelter and energy, will be required with as well as growing pollution concerns. One of the major pollutions in our world is water contamination with toxic chemicals and pathogens, which are released from both industries and households.[2] Therefore, recycling of wastewater, removal or degradation of hazardous materials and contaminants, is a significant global challenge. In this regard, several methods have been reported to achieve this goal. The advanced oxidation process (biological, chemical or physical), is based on the production of highly reactive species to oxidize organic pollutants in wastewater to ultimate products, has been considered as an attractive treatment method, especially the photochemical oxidation process called "heterogeneous photocatalysis".[3] Castellote and Bengtsson have given the definition of photocatalysis process is "the acceleration of a photoreaction by the presence of a catalyst".[4]

Heterogeneous photocatalysis for water purification has attracted much attention since Honda and Fujishima reported using Titanium dioxide (TiO_2) electrode material for water splitting in 1972,[5] however, the application of TiO_2 is limited to absorption in the UV light range, which corresponds to only 4% of solar energy due to TiO_2 anatase wide band gap energy of 3.2 eV, as shown in Figure 1.1.[6] Therefore, extensive research has been undertaken to find a "green" energy source (solar light) to solve environmental concerns that devoted the development of visible light driven photocatalyst in order to effectively utilize the majority of the solar energy.[6] As one of the earliest studied Bismuth vanadate ($BiVO_4$) be widely used in environmental

purification, hydrogen production, carbon dioxide reduction, since $BiVO_4$ has been demonstrated to be an active visible light responsive photocatalyst owing to its narrow band gap energy of 2.4 eV.[7] Moreover, this material is stable in water. Its application as photocatalyst for environmental treatment has been extensively investigated.[8-10] However, difficult separation of photogenerated electron-hole pair in $BiVO_4$ photocatalyst is one of the main reasons accounting for its poor photocatalytic efficiency, which the charge separation lifetime normally is about 40 ns.[11] In order to improve the photocatalytic efficiency of $BiVO_4$, modification of $BiVO_4$ by coupling with other metal oxide semiconductor with appropriate different band edge potentials has been investigated.

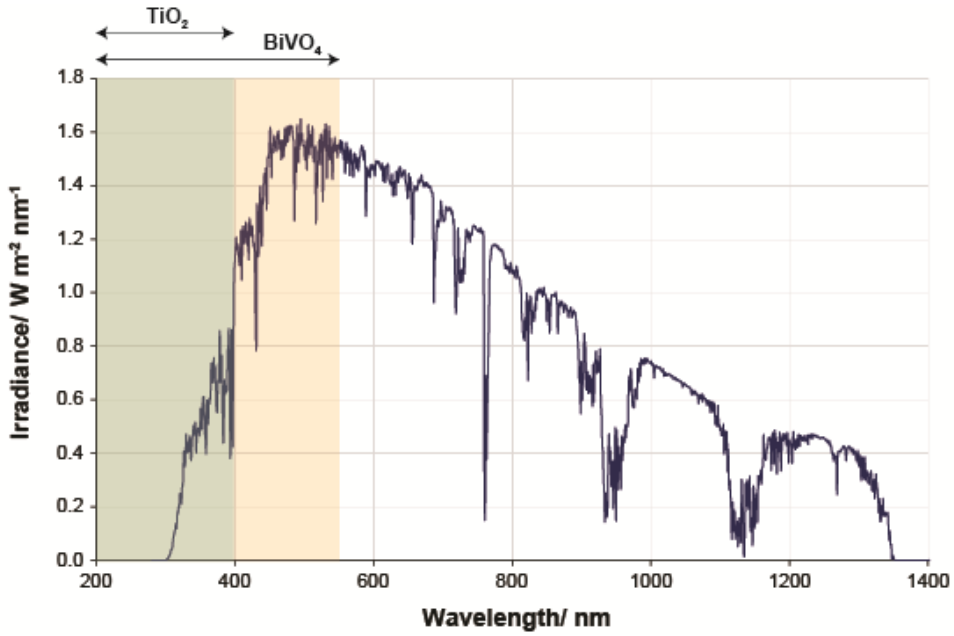

Figure 1.1 Spectrum of solar radiation AM1.5 source NREL defined in ASTMG173.

The aim of this research project is more fully realise the potential of $BiVO_4$ as a low band gap photocatalyst capable of photoactivation a visible light region for water purification applications through approaches including modification this photocatalyst to enhance its photocatalytic activity by reducing charge separation in the photocatalyst.

It is hypothesised that by coupling $BiVO_4$ with other semiconductor provided different band edge potentials, it is possible to increase charge separation of the oxidation and reduction sites, and reduce the recombination of photogenerated electrons and holes. The increase of charge separation of the reaction sites may significantly increase the efficiency of the photocatalysis process. Thus, the specific objectives of this research are:

1. To investigate and optimise the parameters of photocatalytic degradation of organic xanthene and azo dyes and overcome the limitations presented by conventional systems either based on loose powder or dense films.

   In order to realise a viable system for wastewater purification, more practical heterogeneous photocatalysis, including the immobilisation of photocatalysts, on a substrate are required. Thus, in this research a doctor blading technique was chosen to immobilise photocatalyst films on a glass substrate, for degradation of Rhodamine B and Methylene blue dyes. Furthermore, photocatalytic degradation parameters including thickness of catalyst film, dye concentration, solar light intensity and reactor values were also investigated and optimised in this research.

2. To investigate novel synthetic method as a microwave heating process to overcome limitation of hydrothermal and precipitation methods.

   $BiVO_4$ nanoparticles were synthesised by the solution phase synthetic method with microwave process as a simple, fast synthesis procedures and industrially viable low temperature synthesis method. Furthermore, the physical characteristics and photocatalytic activity of the microwave synthesised $BiVO_4$ were also compared to $BiVO_4$ synthesised by the precipitation and hydrothermal methods.

3. To improve the photocatalytic degradation for organic xanthene and azo dyes by means of $BiVO_4$ coupling with metal oxide.

   Mixed oxide systems of $BiVO_4/CeO_2$, $BiVO_4/TiO_2$ and $BiVO_4/WO_3$ with different conduction band and valence band edges were synthesised by wet chemical processes including the precipitation and sol-gel methods. Their mechanisms for photocatalytic degradation of and Rhodamine B and Methylene blue dyes were also compared and discussed in this work with intention to increase the charge separation lifetime and hence photocatalyst reactivity and stability.

References

1. U. Nations, *World Population in 2300*, New York, 2004.
2. D. S. Bhatkhande, V. G. Pangarkar and A. A. C. M. Beenackers, *J. Chem. Technol. Biotechnol.,* 2002, **77**, 102–116.
3. N. Muhd Julkapli, S. Bagheri and S. Bee Abd Hamid, *Scientific World J.*, 2014, **2014**, 25.
4. M. Castellote and N. Bengtsson, in *Applications of Titanium Dioxide Photocatalysis to Construction Materials*, eds. Y. Ohama and D. Van Gemert, Springer Netherlands, 2011, vol. 5, ch. 2, pp. 5–10.
5. A. Fujishima and K. Honda, *Nature*, 1972, **238**, 37–38.
6. Y. Zhou, F. Krumeich, A. Heel and G. R. Patzke, *Dalton Trans.*, 2010, **39**, 6043–6048.
7. A. Walsh, Y. Yan, M. N. Huda, M. M. Al Jassim and S. H. Wei, *Chem. Mater.*, 2009, **21**, 547–551.
8. A. Kudo, K. Omori and H. Kato, *J. Am. Chem. Soc.*, 1999, **121**, 11459–11467.
9. Y. Park, K. J. McDonald and K.-S. Choi, *Chem. Soc. Rev.*, 2013, **42**, 2321–2337.
10. C. Martinez Suarez, S. Hernández and N. Russo, *Appl. Catal., A*, 2014, .
11. F. F. Abdi, T. J. Savenije, M. M. May, B. Dam and R. van de Krol, *J. Phys. Chem. Lett.*, 2013, **4**, 2752–2757.

CHAPTER 2

LITERATURE REVIEW

2.1 Organic dye pollutants

Synthetic textile dyes are one of the largest groups of the toxic organic compounds represented in wastewater. The totally global production of the synthetic dyes, especially from textile industries, is more than 700,000 tons per years[1, 2] of this around one thousand tons of wastewater treatments containing synthetic textile dyes are classified into azo compounds and their derivatives, annually released into natural streams.[1, 2] These dyes can cause considerable environmental pollution and are serious health-risk factors. The photochemical treatment method is the promising technique to solve the above problems using the heterogeneous photocatalysts, including TiO_2, ZnO, CeO_2 and WO_3, to produce highly reactive species such as $^{\bullet}OH$ to oxidize dye pollutants in wastewater.[3, 4] Based on water soluble dyes in the literature concerning photocatalysis, organic dyes can be classified into cationic, anionic and non-ionic dyes.[5] Cationic and anionic dyes are typically highly water soluble with bright colours in water. Cationic dyes is are referred to basic dyes due to the presence of positive ion in its molecule structure, while anionic dyes with negative charge on it show acidic properties.[5, 6] Cationic and anionic azo dyes are used to colour wool, silk, nylon, fibre and polyester materials especially in textile industries.[6] These dyes are toxic, which can cause allergic dermatitis, skin irritation and even cancer.[7, 8]

As such researches typically use cationic azo dyes including Rhodamine B (RhB) and Methylene Blue (MB) dyes for degradation studies. Since, both dyes carry a positive charge it is assumed that under neutral conditions will be adsorbed onto photocatalysts with negatively charged surfaces such as $BiVO_4$, and these dyes are

the most used model pollutants.[9-12] Regarding to MB was heavily used in early studies, it has been pointed out that this dye auto-degrades readily and may not be representative of all the types of molecules for which photocatalysis is industrially relevant. Therefore, RhB is observed to be a more appropriate dye which is chosen as a model dye for photocatalysis study comparing to the MB dye.[13]

2.1.1 Mechanism for degradation of Rhodamine B (RhB)

Rhodamine B (RhB) is as a xanthene dye widely used in textile and food industries as a colorant. It is well-known as a fluorescent dye in aqueous environments, which can be easily detected down to very low concentration using photoluminescence measurements.[14] RhB is like many xanthene dyes harmful to human and animals if swallowed and causes eyes and skin irritation,[9, 14] also has chemical similarity to a range of dyes used (which can also cause human). Hence, it was chosen as a model dye of organic pollutants in wastewater to investigate the photocatalytic properties of the synthesised photocatalysts in this work.

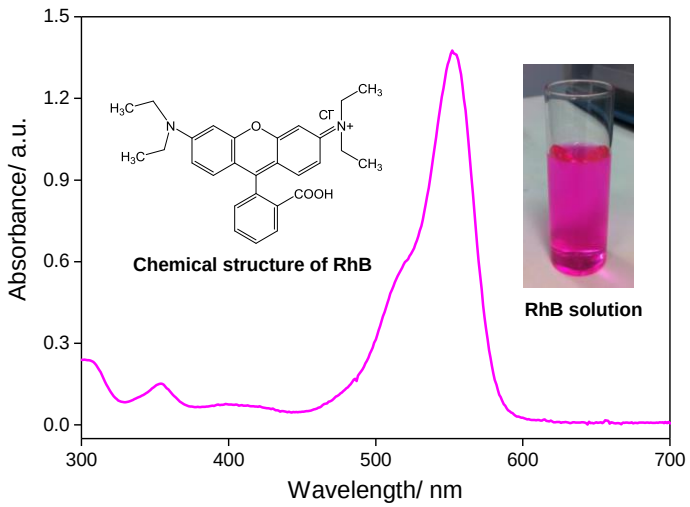

Figure 2.1 UV-visible absorbance spectrum of a 25 μM RhB in aqueous solution with path length = 1 cm (inset right) and chemical structure of RhB (inset left).[9]

The chemical structure and physical properties of RhB dye has presented inset in Figure 2.1 and Table 2.1, respectively. RhB is a high solubility in water, with a red appearance and maximum absorption (λ_{max}) value at 553 nm (Figure 2.1).[14]

Table 2.1 The physical and chemical properties of Rhodamine B (RhB).[9, 14]

IUPAC name	N-[9-(ortho-carboxyphenyl)-6-(diethylamino)-3Hxanthen-3-ylidene] diethyl ammonium chloride
Molecular formula	$C_{28}H_{31}ClN_2O_3$
Molecular weight	479.02 g/mol
Melting point	210 to 211°C
Solubility in water	15 g/L
Absorption maximum	553 nm
Molecular diameter	1.6 nm
pH	5.3 (5 g/L in water)

Two pathways of RhB dominate the photodegradation reaction process: (1) directly by cleavage of dye chromophore structure and (2) by *N*-deethylatin then cleavage of the remnant chromophore.[10, 15] Following the first pathway the main absorption peak position remains constant at 553 nm (RhB) while the peak intensity decreases. For the second pathway, the characteristic absorption gradually shifts to shorter wavelengths due to the hypochromic effect of *N*-ethyl group removal.

As shown in Table 2.2., five *N*-deethylatedintermediates of RhB, namely, *N,N*-diehyl-*N'*-ethylrhodamine (DER), *N,N*-diethylrhodamine (DR), *N*-ethyl-*N'*-ethylrhodamine (EER), *N*-ethylrhodamine (ER), and Rhodamine 110 (R), were obtained during photocatalytic process and provided a different position of main adsorption spectrum.[10, 16] Figure 2.2 shows two possible pathways for light induced photocatalytic degradation of RhB.[10, 15] Firstly, cationic RhB molecules (diethylamine group) would

adsorb on the surface of catalyst particle. Then, the *N*-deethylation process of RhB produces the *N*- deethylated intermediates during the photocatalytic reaction. Simultaneously, photogenerated active species such as ·OH and/or photogenerated holes directly attract the central carbon group of RhB molecules to cleave the chromophore structure of RhB. Furthermore, the reactive species also reacted with *N*-de-ethylated intermediates in the system, even during *N*-de-ethylation of RhB.

Table 2.2 Structure and UV-vis absorption characteristics of RhB decomposition intermediates form reported by Wang *et al.*.[17]

Species/intermediates	**Structure**	**λ_{max} (nm)**
Rhodamine B (RhB)	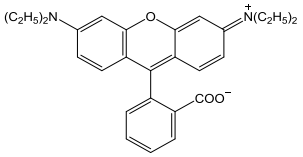	553
N,N-diethyl-*N'*-ethylrhodamine (DER)	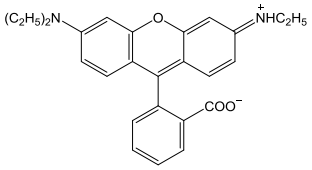	541
N,N-diethylrhodamine (DR)	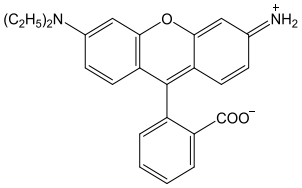	527
N-ethyl-*N'*-ethylrhodamine (EER)	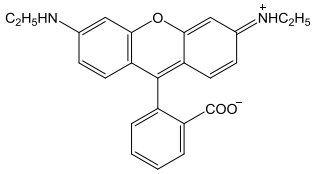	531
N-ethylrhodamine (ER)	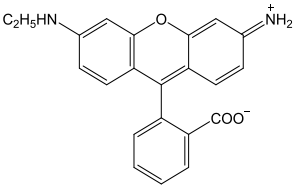	514
Rhodamine 110 (R)	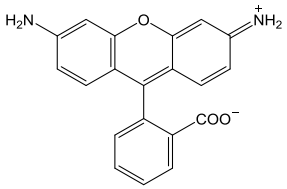	502

Primary oxidation products including adipic acid, phthalic acid, isophthalic acid, and terephthalic acid are generated from the intermediates. Then these oxidation products were further degraded into smaller compounds such as ethane-1,2-diol, butane-1,3-diol, propane-1,2,3-triol, and so forth, during the decolourisation process. Finally, the above small molecules were mineralised to form CO_2, H_2O, NO_3^- and NH_4^+.

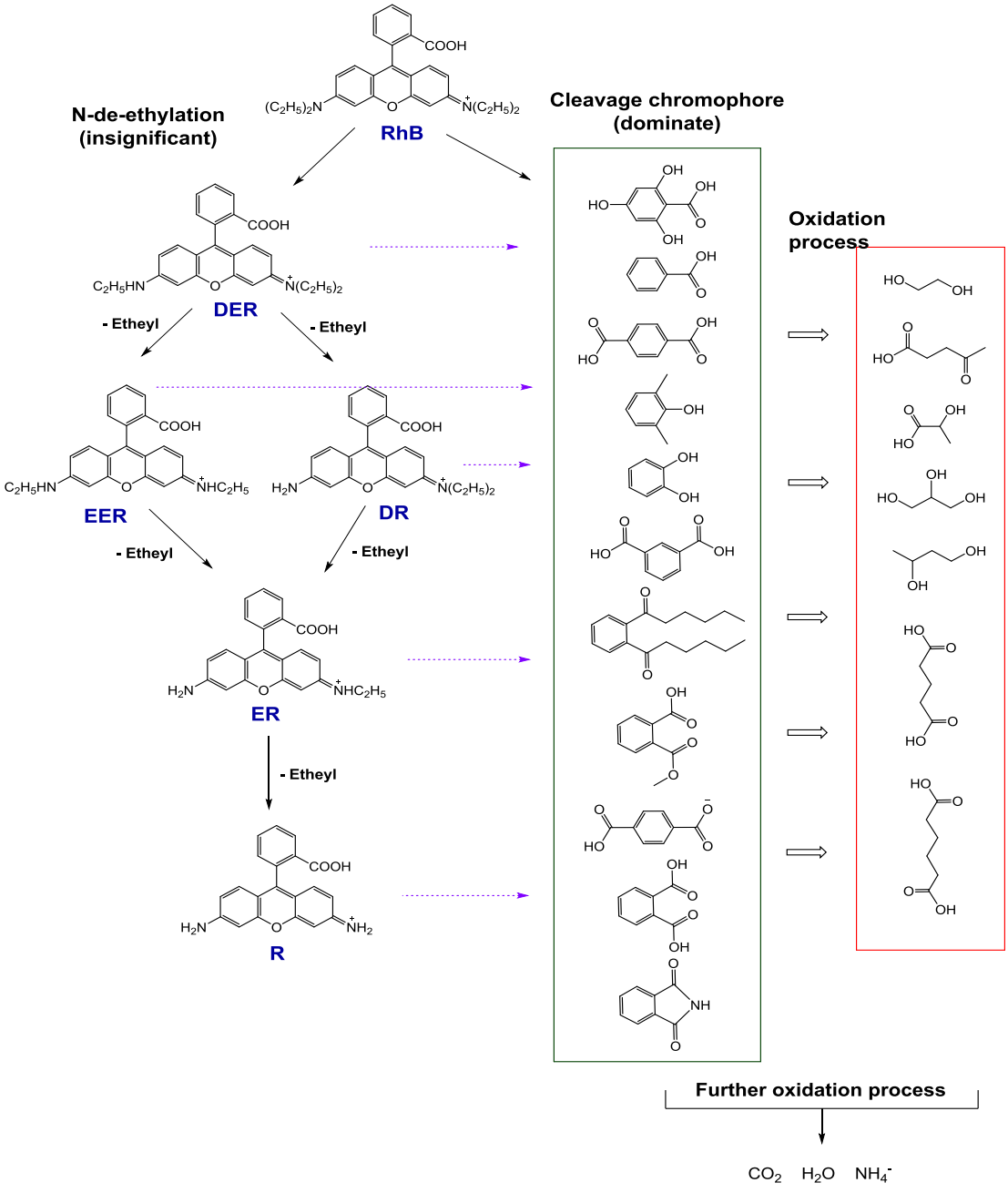

Figure 2.2 Intermediates of photocatalytic degradation pathway of RhB detected by mass spectrometry analysis from the reported by Luan *et al.*.[10, 15]

2.1.2 Mechanism for degradation of methylene blue (MB)

Methylene blue (MB) or methylthionine chloride is common azo dye used for photocatalytic studies due to its stability, solubility in water and being non-biodegradable.[18] Thus in many studies, MB was chosen as the model dye for studying the photocatalytic properties of the synthesised semiconductors. Moreover, it is a common pollutant in sewage industry, and azo dye in textile industry.

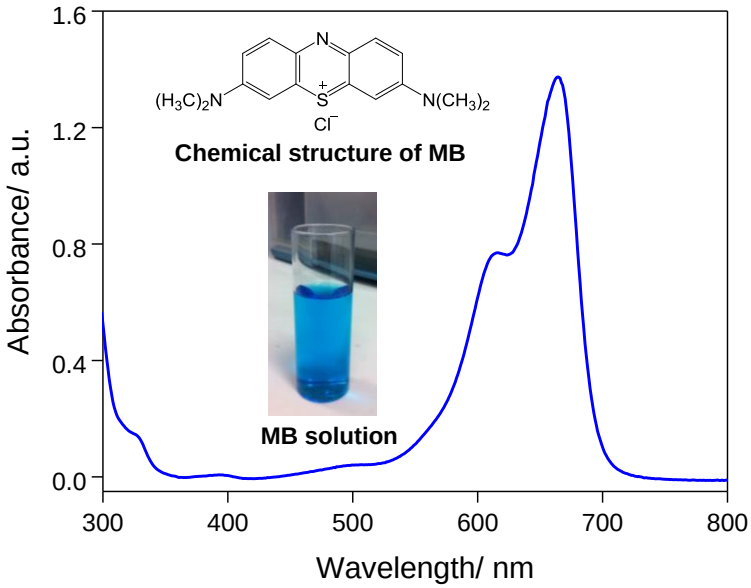

Figure 2.3 UV-visible absorbance spectrum of a 45μM of MB in aqueous solution with path length = 1 cm (inset bottom) and chemical structure of MB (inset top).[18]

MB is a heterocyclic aromatic chemical compound as presented inset Figure 2.3 and the physical and chemical properties of MB is presented in Table 2.3. MB is a brightly coloured blue cationic dye, with maximum absorption value at 664 nm (Figure 2.3). Mills *et al.* reported that there are two reduced forms of MB including; a *leuco*-methylene blue (LMB) is stable in aqueous solution, and a *semi*-reduced radical ($MB^{\bullet-}$), which is pale yellow in colour (λ_{max} = 420 nm) and readily disproportionate (k = 3×10^9 $Lmol^{-1}s^{-1}$) to form MB and LMB (Equation (2.1)).[19]

$$2MB^{\bullet -} \longrightarrow MB + LMB \quad (2.1)$$

Table 2.3 The physical and chemical properties of Methylene blue (MB).[18]

IUPAC name	3,7-bis(dimethylamino) phenothiazin-5-ium chloride
Molecular formula	$C_{16}H_{18}N_3SCl$
Molecular weight	319.85 g/mol
Melting point	180°C
Solubility in water	110 mM
Absorption maximum	664 nm
Molecular diameter	0.80 nm
pH	5 (45 µM in water)

The oxidized form of MB, ($MB^{\bullet +}$, λ_{max} = 520 nm), appears to be quite stable and easily reduced back to MB in acidic solutions, but irreversibly decomposes in slightly basic condition (pH = 9.1). Furthermore, MB easily forms dimers in aqueous solution as shown in Equation (2.2).

$$2MB \overset{K_D}{\longleftrightarrow} (MB)_2 \quad (2.2)$$

Where K_D is the equilibrium constant associated with the dimerization process (3970 $L.mol^{-1}$). The most structures of the MB type compounds highlighted above are illustrated in Table 2.4 with the associated redox potential data at pH 0 reported by Linsebigler *et al.*.[19]

Table 2.4 Structure and UV-vis absorption characteristics of methylene blue and its common reduced and oxidized form reported by Linsebigler *et al.*.[19]

Species/Structure	Abbreviation	λ_{max} (nm)	E^0 *vs*. NHE (V)	Other properties
Methylene blue 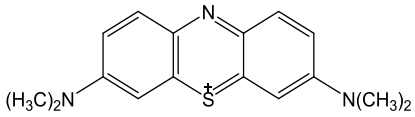	MB	660, 614, 292		K_D = 3970 L mol^{-1}
Semi-reduced methylene blue 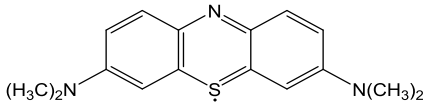	$MB^{\bullet-}$	420	($MB/MB^{\bullet-}$) = -0.23	Readily disproportion to form MB and LMB
Leuco-methylene blue 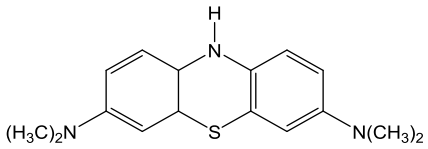	LMB	256	(MB/LMB) = 0.011 (pH 7) and 0.532 (pH 0)	
Oxidised methylene blue 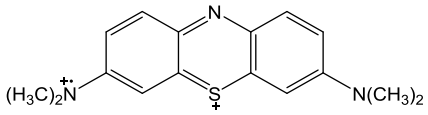	$MB^{\bullet+}$	520	($MB^{\bullet+}$/MB) = 1.08	Stable in acid (pH 1) and unstable base (pH 9)

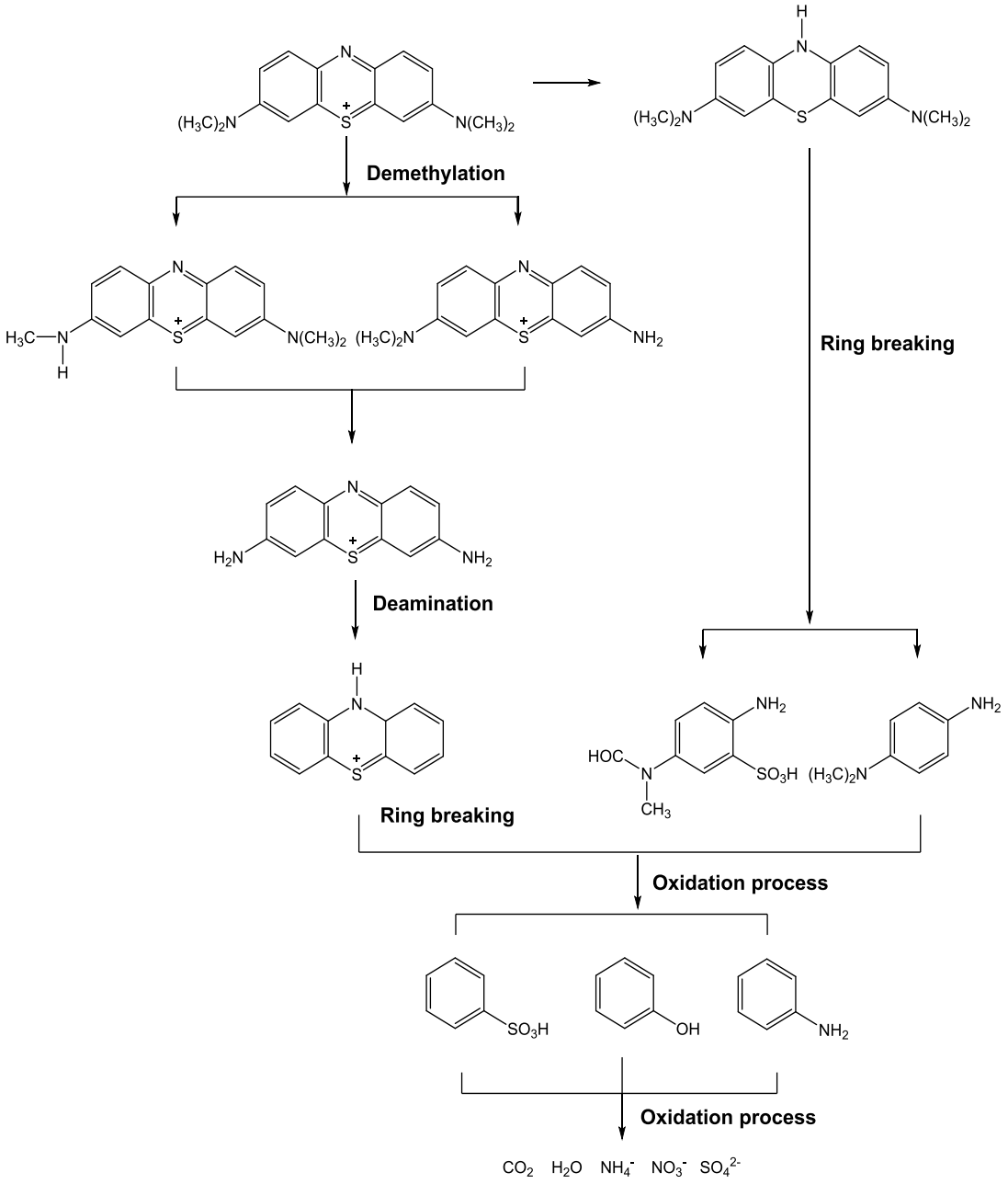

Figure 2.4 Possible photocatalytic degradation pathway of MB reported by Herrmann *et al.*.[20]

Many researchers have focused on the mechanisms and intermediates for photocatalysis of MB by using various metal oxide semiconductors as photocatalyts.[11, 12, 17, 21] It has been observed that the heterogeneous photocatalysis not only decolourised MB, but also completely mineralisation it to CO_2, NO_x, SO_x and

H_2O. The possibly intimidates of MB during photocatalytic degradation process are shown in Figure 2.4, which were analysed by using mass spectrometry.[17, 22] In Figure 2.4, Herrmann *et al.*[20] show MB degradation processes by four steps: (1) demethylation and/or deamination; (2) breaking of the MB central aromatic ring at the bonds of C–S^+═C; (3) conversion of the above intermediates from the step to smaller organic species such as R–NH_3^+, aldehydic/carboxylate species, aniline, and phenol; and finally (4) further minimisation to ultimate products such as CO_2, NH_4^+, NO_3^- and SO_4^{2-}.[17, 20, 22]

2.2 Principles of semiconductor photocatalysis

The principle mechanisms of heterogeneous photocatalysis for degradation of dye pollutants in wastewater over a semiconductor (SC) as photocatalyst, such as TiO_2, ZnO, CeO_2, WO_3, $BiVO_4$, etc., are presented in Figure 2.5. There are two main mechanisms including direct and indirect semiconductor photocatalysis for given photocatalytic reaction of dye degradation.[3, 19, 23, 24]

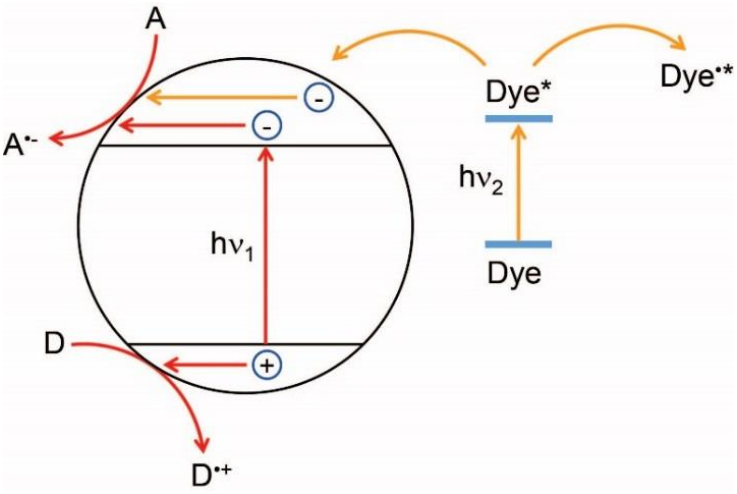

Figure 2.5 Schematic representation of direct (via $h\nu_1$) and indirect (via $h\nu_2$) semiconductor photocatalysis.[24]

In the direct photocatalysis mechanism, the SC is exposed to light with energy equal to or higher than its band gap energy, electrons are promoted from the valence band (VB) to conduction band (CB) of the SC. As a result of this, an electron (e^-) and hole (h^+) pair is produced (Equation (2.3)) at the CB and VB, respectively.

$$SC + hv \longrightarrow SC(e^-) + SC(h^+) \quad (2.3)$$

Both e^- and h^+ can migrate to the SC surface, where they can participate in redox reactions with other adsorbed species on the surface of SC. In most cases, the e^- can reduce acceptor molecules such as oxygen (O_2), reaction process, while the h^+ can oxidise donor molecules such as water (H_2O), oxidation process.[24]

For the reduction process, the e^- at the CB of SC surface can reduce oxygen molecule to superoxide anion radical ($O_2^{\bullet-}$) as presented in Equation (2.4). This $O_2^{\bullet-}$, in the presence of dye scavengers (Dye), may form dye peroxide radical (Dye−$OO^{\bullet}$), (Equation (2.5)) or hydrogen peroxide (H_2O_2), (Equation (2.6)). H_2O_2 can also be decomposed by the e^- at the CB to $^{\bullet}OH$ as shown in Equation 2.7.

$$SC(e^-) + O_2 \longrightarrow O_2^{\bullet-} \quad (2.4)$$

$$O_2^{\bullet-} + Dye \longrightarrow Dye–OO^{\bullet} \quad (2.5)$$

$$O_2^{\bullet-} + HO_2^{\bullet} + H^+ \longrightarrow H_2O_2 + O_2 \quad (2.6)$$

$$H_2O_2 + e^- \longrightarrow 2OH^{\bullet} \quad (2.7)$$

For the oxidation process, the high oxidative potential of the h^+ in the SC allows the direct oxidation of organic dyes, to produce a reactive intermediate (Equation (2.8)). However, this depends entirely upon the SC having CB and VB at a sufficiently position (Standard hydrogen electrode, NHE) value. Highly reactive $^{\bullet}OH$ can also be

generate either by the decomposition of water (Equation (2.9)) or by the reaction of the h^+ with OH^- (Equation (2.10)). The $^{\bullet}OH$ is an extremely strong, non-selective oxidant which leads to decomposition of organic pollutants in wastewater.[19]

$$h^+ + \text{Dye} \longrightarrow \text{Dye}^{\bullet+} \longrightarrow \text{Oxidation of dye} \quad (2.8)$$

$$h^+ + H_2O \longrightarrow H^+ + OH^{\bullet} \quad (2.9)$$

$$h^+ + OH^- \longrightarrow OH^{\bullet} \quad (2.10)$$

The main species for decomposing organic dye are these $OH^{\bullet}$, which are generated from both of oxidation and reduction processes (Equation (2.11)).[19]

$$OH^{\bullet} + \text{Dye} \longrightarrow \text{Degradation of dye} \quad (2.11)$$

The indirect photocatalysis mechanism, the organic dye absorbs light, photo-excitation of dye occurs from the ground state (Dye) to an excited state (Dye*) as shown in Equation (2.12).[2, 19, 24, 25] This exited dye may inject an electron into the CB of SC, where it is converted into a semi-oxidized radial cation ($Dye^{\bullet+}$) as shown in Equation (2.12).[2, 25] This pathway can occur only when the excited state reduction potential of dye is equal to or more negative than the CB of SC (Equation (2.13)).[2, 4] The resulting separation of both photogenerated e^- and h^+ of SC shows down recombination. Moreover, basic process of the dye sensitising can also inject h^+ into the VB of SC if the VB energy is negative enough.

$$\text{Dye} + hv \longrightarrow \text{Dye}^* \quad (2.12)$$

$$\text{Dye}^* + SC \longrightarrow SC(e^-) + \text{Dye}^{\bullet+} \quad (2.13)$$

In this process, adsorbed dye is excited by light irradiation, and e^- from the excited dye may be injected to the CB of the catalyst, where it is scavenged by O_2 molecule

to produce $O_2^{\bullet-}$, and then the $OH^{\bullet}$ radicals are generated as previously described in Equations (2.6) and (2.7).[2]

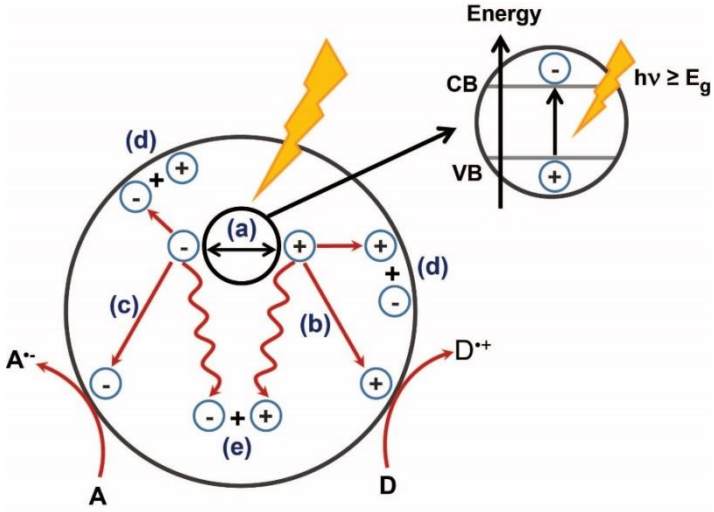

Figure 2.6 Schematic illustration of (a) electron-hole pair formation; (b) donor oxidation by a hole; (c) acceptor reduction by an electron; (d) and (e) electron-hole recombination on the surface or in the bulk. Adapted from Cargnello *et al.*.[26]

Figure 2.6 shows possible pathways of the photogenerated e^- and h^+ in a SC photocatalyst: (1) changes reached to the surface of the SC, (a) the e^- can reduce an adsorbed acceptor and (b) h^+ can oxidise an adsorbed donor. Otherwise, (2) the e^- and h^+ recombine on the surface or in the bulk, releasing energy as heat or photon emission, with no net chemical change to the system (the reserve of Equation (2.14)).[24]

$$SC(e^-) + SC(h^+) \longrightarrow N + E \qquad (2.14)$$

where N is the neutral centre and E the energy released in the heat form ($h\nu' < h\nu$).

2.3 Bismuth vanadate ($BiVO_4$)

Over the past decade, a variety semiconductors have been reported as visible-light-induced photocatalysts (e.g., Fe_2O_3, CdS, $BiVO_4$, etc.), with improved the solar conversion efficiencies.[27] Since the report of $BiVO_4$ as a photocatalyst for water splitting by Kudo *et al.* in 1999,[28] $BiVO_4$ has become popular as a highly responsive visible-light driven, photocatalyst for water oxidation.[28-30] As such $BiVO_4$ can be also used in water purification application for degradation of organic pollutants due to its suitable physicochemical properties, low cost, non-toxicity and high chemical stability.[30-32] $BiVO_4$, it has also been used as a gas sensing semiconductor, a non-toxic alternate to Pb compounds in yellow pigment paints and a cathode electrode material in lithium rechargeable batteries.[33, 34]

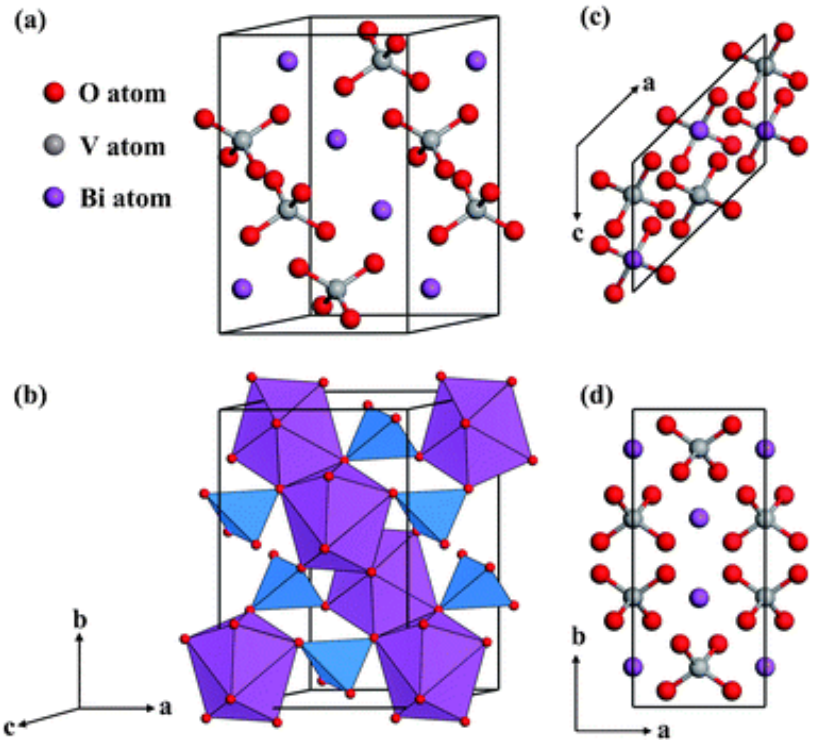

Figure 2.7 (a) Crystal structure representation of monoclinic $BiVO_4$, (b) vanadium tetrahedron (VO_4) in blue and bismuth dodecahedron in purple (BiO_8), (c) the corresponding top view, and (d) side view of the structure, taken from Zhao *et al.*.[35]

The photocatalytic properties of $BiVO_4$ are strongly dependent on its morphology and crystalline form. Generally, synthetic $BiVO_4$ was found to exist in two crystalline phases including monoclinic and tetragonal types. Between the two polymorphs, the monoclinic structure is reported to possess the highest photocatalytic activity in part due to its direct band gap energy of 2.4 eV.[36]

Figure 2.7 presents the monoclinic $BiVO_4$ structure consisting of corner-sharing bismuth dodecahedra (BiO_8) and vanadium tetrahedra (VO_4) reported by Walsh *et al.* and Zhao *et al.*, the physical and electronic properties of $BiVO_4$ are also reported in Table 2.5.[37, 38] Therefore, many synthesis methods have been focused on the selective preparation of the monoclinic $BiVO_4$ photocatalyst.

Table 2.5 The physical and electronic properties of monoclinic $BiVO_4$.[38, 39]

Unit cell mass	395.92 g mol^{-1}
Density	6.1 g cm^{-3}
Appearance	Bright yellow powder
Melting point	1000°C
Refractive index	2.45
Space group	*C*2/*c*
Point group	C^6_{2h}
Unite cell	(a = 7.224Å, b = 11.522 Å, c = 5.108Å, $\alpha = \beta = 90°$, and $\gamma = 135.003°$
Bond length	Bi–O (2.416 Å x 2, 2.418 Å x 2, 2.446 Å x 2, 2.449 Å x 2) V–O (1.730 Å x 2, 1.731Å x 2)
Phase transition	Tetragonal to monoclinic phase (350–500°C)
Band gap energy	Direct band gap of ~ 2.4–2.5 eV

2.4 Modification of photocatalysts: Enhancement of photocatalytic activity

The electronic band structure of a semiconductor plays an important role in its photocatalytic properties, and controls the light absorption, charge separation, migration and the recombination of e^- and h^+. A simplified electronic structure of n-type semiconductor is shown in Figure 2.8. The work function (φ_{SC}) is defined as the energy difference between the vacuum level (E_{vac}) and the Fermi level (E_F). The E_{vac} is defined as the energy of an electron at rest (and hence with free electron).[40, 41]

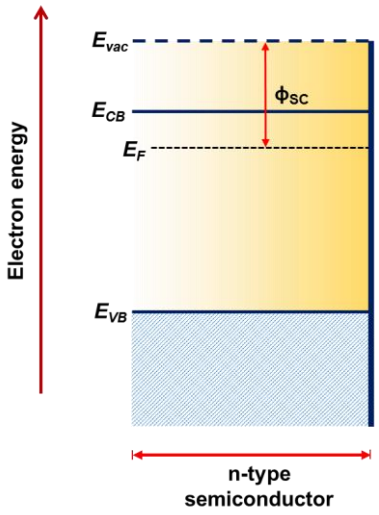

Figure 2.8 Energy level diagram of a n-type semiconductor adapted from Guijarro *et al.*.[115]

In order to improve the photocatalytic activity of $BiVO_4$, the recombination rate between e^- and h^+ pair need to be reduced due to its high recombination rate of the photoproduced e^- and h^+ pairs, with excitation half-light of about 40 ns reported by Abdi *et al.*.[42] Several methods have been undertaken to fabricate an electronic barrier in the photocatalyst. In general, there are three approaches; metal doping, metal deposition and coupling with other metal oxide, which increase the lifetime of the photogenerated e^- and h^+.[43-46] These all serve to prevent the recombination of e^- and h^+, and thus the e^- and h^+ have more opportunities to participate in reduction and oxidation reactions for the degradation of the organic pollutants on their surface.

2.4.1 Doping with transition metal ions

The performance of photocatalysts can be changed by doping the transition metal ions into the semiconductor photocatalysts. The dynamics of e^- and h^+ recombination and interfacial charge transfer will be affected.[88, 93]

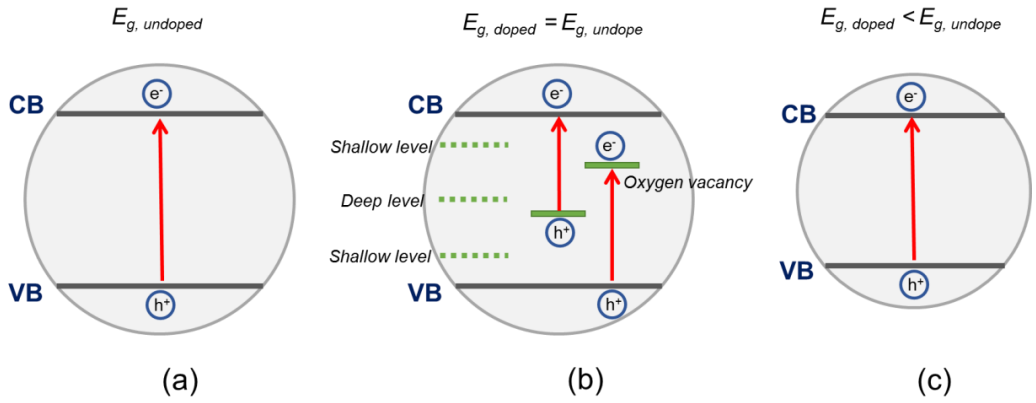

Figure 2.9 Scheme for electronic band structures (a) an unloaded semiconductor, (b) doping-induced shallow-level and deep-level trap states and (c) doping-induced band gap narrowing adapted from Jiangtian *et al.*.[27]

Once incorporated into the interior of semiconductors, the transition metals may occupy either lattice substitutional or interstitial sites, resulting in the formation of additional energy levels within the band gap (Figure 2.9(b)). [27, 47] Thus, the imperfections in the semiconductor lattice generate trap sites for the e^- or h^+, leading to a decrease in the levels of e^- and h^+ recombination. However, if an electron is trapped in a deep trapping site, it will have a longer lifetime, but it will also have a lower redox potential. This might result in a decrease in the photoreactivity. In another case, doping into a semiconductor can lead to narrowing of the band gap (Figure 2.9(c)), which bring the benefit of increasing the light absorption in the visible light region.[122] However, the effect of doping on semiconductors is governed by several factors including the type and concentration of dopant, preparation method, the structure, and physical and chemical properties of the semiconductor photocatalyst.

2.4.2 Metal deposition

The ability of a metal that is deposited on semiconductor surface to mediate the photogenerated electrons away from the semiconductor may give rise to a Schottky junction, which is created at the semiconductor interface, just outside the crystal surface and not interacting with the crystal as show in Figure 2.10.[48]

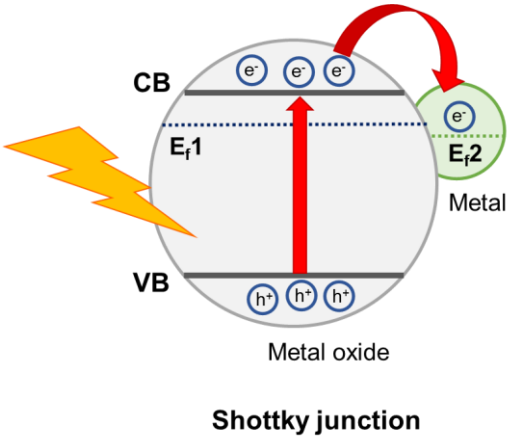

Figure 2.10 Schematic illustration of photogenerated charges transfer for metal deposition on metal oxide.[48]

Recently, Ag, Au, Pt and Pd have been employed with $BiVO_4$, produced through impregnation, deposition-precipitation or hydrothermal methods.[49-51] Generally, the Fermi energy of noble metals is lower than the conduction band edge of $BiVO_4$, thus photopromoted e^- can be captured by the noble metals, and this facilitates e^- and h^+ separation and enhances photocatalytic performance of this metal loading $BiVO_4$.

2.4.3 Coupling of other semiconductors

The coupling of two metal oxide semiconductors is also used to prolong the separation of e^- and h^+ pairs. The potential barrier formed at the interface depends on the work functions of the two materials. When both semiconductors are brought into intimate contact, their CB and VB edges with different energy levels are formed. The transfer of e^- and h^+ could be rationalised as show in Figure 2.11.

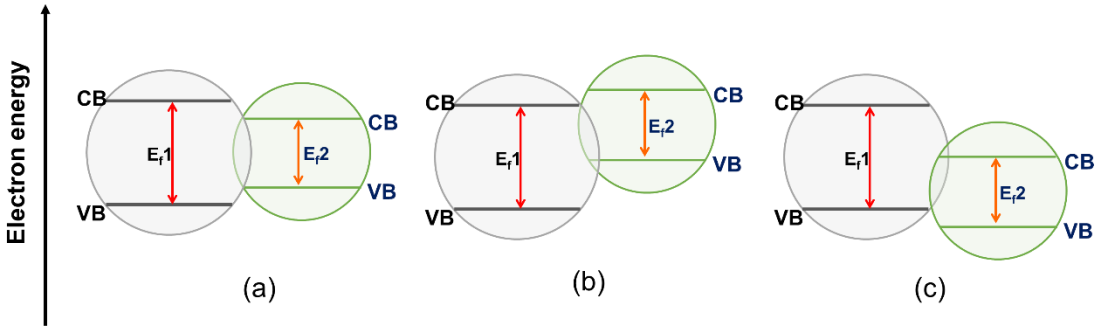

Figure 2.11 Schematic diagram illustrations of (a) VB and CB of a small band gap semiconductor located in between, (b) more negative, and (c) more positive than of a large band gap semiconductor

An energy barrier for two coupling materials, the e^- transfer from a region of higher band edge positions of semiconductor to another one with lower band edge positions, whereas the h^+ transfer from lower band edge positions to the one with higher band edge positions.[43, 44] This provides an approach to achieve a more efficient charge separation, an increased lifetime of the charge carriers and an enhanced interfacial charge transfer to adsorbed substrates.[52]

As presented in Table 2.6, a number of publications in coupling $BiVO_4$ with other metal oxides for water purification applications have been increasing. The band positions of several semiconductors in contact with aqueous electrolyte at pH 0 are shown in Figure 2.12.

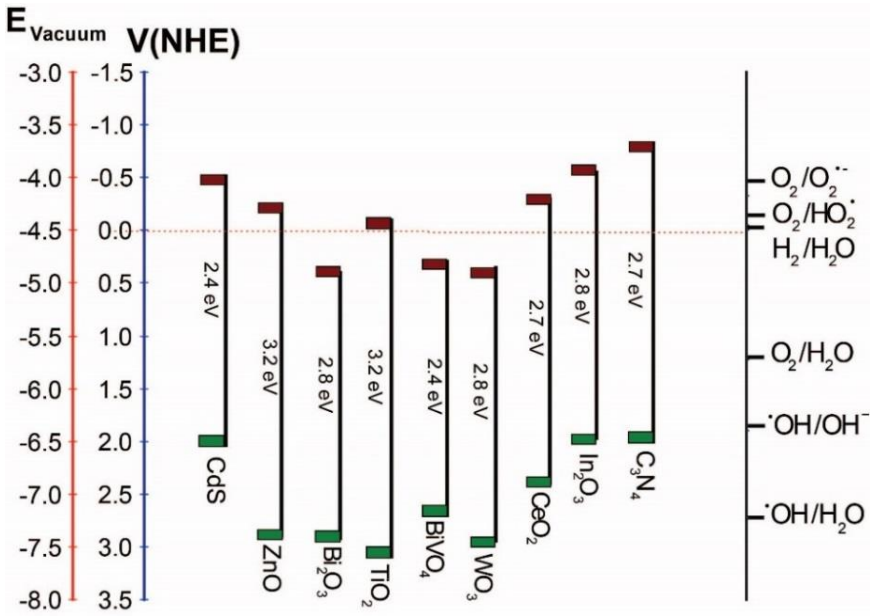

Figure 2.12 Band gap and redox potential for different semiconductors at pH 0.[27, 47, 52-54]

The coupling metal oxide in $BiVO_4$ to improve charge separation, accomplishes vector displacement of charges on two semiconductors and retards e^- and h^+ recombination, thereby giving e^- and h^+ have more opportunities to participate in reduction and oxidation reactions for the degradation of the organic dye on their surface.[45, 46] As in Figure 2.12, the CB and VB of $BiVO_4$ are located in between CB and VB of TiO_2, more positive than of CeO_2, and more negative than of WO_3. Hence, the photocatalytic activity and mechanisms for degradation dyes of these coupling semiconductors might be different, which were also studied in this search.

Table 2.6 Modification of $BiVO_4$ photcatalysts by coupling with other metal oxide and their photocatalytic properties.

Catalyst	$BiVO_4$ synthesis	Composite synthesis	Physical characterisation	Photocatalytic performance	Ref.
$Co_3O_4/BiVO_4$	• Hydrothermal method • $Bi(NO_3)_3 \cdot 5H_2O$ and NH_4VO_3 in HNO_3 • pH 9 (NH_4OH) • 200°C for 48 h	• Impregnation method • $Co(NO_3)_2$ with $BiVO_4$ powder in DI water • Calcination: 300–500°C for 2 h	• Monoclinic $BiVO_4$ • Spherical particles of Co_3O_4 (20–50 nm) deposited on surface of $BiVO_4$ (an irregular shape, 1–2 μm)	• Phenol: 18 mg L^{-1} • Catalyst loading: 3 g L^{-1} • 1000 W Xe lamp (λ>400 nm) • 6% in 3 h ($BiVO_4$) • 30% in 3 h (5 wt.%$Co_3O_4/BiVO_4$)	55
$BiVO_4/Bi_2O_3$	• Hydrothermal method • $Bi(NO_3)_3 \cdot 5H_2O$ in water • NH_4VO_3 in water • Methyl pyrrolidon as surfactant • Stirring at RT for 4 h	• Calcination: 600°C for 6 h	• Tetragonal $BiVO_4$ • Monoclinic Bi_2O_3 • Spherical particles (200–500 nm)	• RhB: 10 mg L^{-1} • Catalyst loading: 1.2 g L^{-1} • 500 W Philps lamp (λ>380 nm) • 12% in 2 h ($BiVO_4$) • 6% in 2 h (Bi_2O_3) • 99% in 2 h (25 wt.% $BiVO_4/Bi_2O_3$)	56
$BiVO_4/Bi_2O_2CO_3$	• One step hydrothermal method • Bi_2O_3 and NH_4VO_3 in HNO_3 • Urea • 180°C for 24 h	• N/A	• Monoclinic $BiVO_4$ • Tetragonal $Bi_2O_2CO_3$ • $Bi_2O_2CO_3$ nanosheet with $BiVO_4$ nanoparticle	• RhB: 20 mg L^{-1} • Catalyst loading: 5 g L^{-1} • 350 W Xenon lamp (λ>420 nm) • 54% in 1 h ($BiVO_4$) • 47% in 1 h ($Bi_2O_2CO_3$) • 97% in 1 h ($BiVO_4/Bi_2O_2CO_3$)	57

Catalyst	$BiVO_4$ synthesis	Composite synthesis	Physical characterisation	Photocatalytic performance	Ref.
$V_2O_5/BiVO_4$	• Precipitation method • $Bi(NO_3)_3 \cdot 5H_2O$ and NH_4VO_3 in water • Colloidal carbon spheres (CCSs) as template • Heated at 90°C for 20 h	• Calcination: 450°C for 2 h	• Monoclinic $BiVO_4$ • Orthorhombic V_2O_5 • Tightly bound between $BiVO_4$ and $V2O_5$ nanoparticles	• MB: 10 mg L^{-1} • Catalyst loading: 1 g L^{-1} • 500 W Xe lamp (λ>400 nm) • 73% in 1 h ($BiVO_4$) • 5.3% in 1 h (V_2O_5) • 92% in 3 h (5.3 wt.% $V_2O_5/BiVO_4$)	58
$BiVO_4/TiO_2$	• Hydrothermal method • $Bi(NO_3)_3 \cdot 5H_2O$ in HNO_3 • NH_4VO_3 in NaOH • pH 11–12 (NH_4OH) • 180°C for 6 h	• Precipitation method • $Ti(OC_3H_7)_4$ in HNO_3 • $BiVO_4$ powder • String at 40°C for 12 h • Calcination: 500°C for 3 h	• Monoclinic $BiVO_4$ • Anatase, rutile and brookite TiO_2 • Small spherical TiO_2 deposited on surface of large irregular $BiVO_4$	• Benzene gas • Catalyst loading: 1.35 g • 500 W Xe arc lamp (450<λ<500 nm) • 25% in 8 h ($BiVO_4$) • 22% in 8 h (TiO_2) • 92% in 8 h (0.5 wt.% $BiVO_4/TiO_2$)	59
$BiVO_4/CeO_2$	• Precipitation method • $Ce(NO_3)_3 \cdot 6H_2O$ in ethylene glycol • Added NH_4OH • Heated at 50°C for 24 h • Calcination: 500°C for 2 h	• Hydrothermal method • $Bi(NO_3)_3 \cdot 5H_2O$ and NH_4VO_3 in HNO_3 • pH 7 (NH_4OH) • CeO_2 powder • 120°C for 6 h	• Monoclinic $BiVO_4$ • Cubic CeO_2 • Spherical CeO_2 (5–10 nm) deposited on surface of rod-like $BiVO_4$ (100 nm)	• MB and MO: 20 mg L^{-1} • Catalyst loading: 1 g L^{-1} • 50 W Halogen lamp (λ>400 nm, 185 mW cm^{-1}) • 60% (MB) in 30 min for $BiVO_4$ • 20% (MB) in 30 min for CeO_2 • 80% (MB) and 62% (MO) in 30 min for $0.6BiVO_4/0.4CeO_2$	60

Catalyst	$BiVO_4$ synthesis	Composite synthesis	Physical characterisation	Photocatalytic performance	Ref.
$Bi_2S_3/BiVO_4$	• Hydrothermal method • $Bi(NO_3)_3{\cdot}5H_2O$ in ethylene glycol and water • NH_4VO_3 in AOT • 160°C for 18 h	• Hydrothermal method • $BiVO_4$ powder and thioacetamide in water • 120°C for 8 h	• Monoclinic $BiVO_4$ • Orthorhombic Bi_2S_3 • Olive shape (1 μm) • XPS and TEM identified composite	• RhB: 10 mg L^{-1} • Catalyst loading: 1 g L^{-1} • 500 W Xe lamp (λ>400 nm) • 62% in 8 h ($BiVO_4$) • 8% in 8 h (Bi_2S_3) • 100% in 8 h ($Bi_2S_3/BiVO_4$)	61
$TiO_2/BiVO_4$	• One step hydrothermal method • $Bi(NO_3)_3{\cdot}5H_2O$ in HNO_3 • NH_4VO_3 in NaOH • $(NH_4)_2TiF_6$ • 200 °C for 1 h	• N/A	• Monoclinic $BiVO_4$ • Anatase TiO_2 • Spherical $BiVO_4$ (3 μm) with subnanoparticle (200–300 nm) • Slab TiO_2 (0.5–1 μm)	• RhB: 20 mg L^{-1} • Catalyst loading: 2 g L^{-1} • 300 W Mercury lamp • 80% in 6.5 h ($BiVO_4$) • 94% in 6.5 h (20 wt.% $TiO_2/BiVO_4$)	62
$WO_3/BiVO_4$	• Metal organic decomposition method • $Bi(NO_3)_3{\cdot}5H_2O$ in acetic acid • $C_{10}H_{14}O_5V$ in acetylacetone • Spin coater on FTO substrate (40 × 20 mm) • Dried at 150°C for 5 min	• Spin coater (the second layer) • H_2WO_4 in NH_4OH, PEG and ethanol • Calcination: 550°C for 1 h	• Monoclinic $BiVO_4$ • Monoclinic WO_3 • Spherical shape (100–300 nm) with 1 μm film thickness	• Electrophotocatalysis • MB: 5 mg L^{-1} in 0.1 Na_2SO_4 • Applied 0.2 V vs. Ag/AgCl • 500 W Xenon lamp (λ>420 nm) • 80% in 2 h ($WO_3/BiVO_4$)	63

Catalyst	$BiVO_4$ synthesis	Composite synthesis	Physical characterisation	Photocatalytic performance	Ref.
$Bi_2O_3/BiVO_4$	• One step solvothermal method • $Bi(NO_3)_3 \cdot 5H_2O$ in ethylene glycol • NH_4VO_3 in L-lysine template and water • 160°C for 24 h	• Calcination: 450 °C for 3 h	• Monoclinic $BiVO_4$ • Tetragonal Bi_2O_3 • Peanut-like shape (2.5 μm nm length and 1–1.5 μm width)	• MB: 20 μM • Catalyst loading: 0.5 g L^{-1} • 350 W Xe lamp (25 cm) • 95% in 1.5 h ($BiVO_4$) • 30% in 1.5 h (Bi_2O_3) • 100% in 1 h ($Bi_2O_3/BiVO_4$)	64
$Ag_3PO_4/BiVO_4$	• Hydrothermal method • $Bi(NO_3)_3 \cdot 5H_2O$ and NH_4VO_3 in HNO_3 • pH 7 (NH_4OH) • SDS as surfactant • 180°C for 24 h	• Deposition method • $Na_2HPO_4 \cdot 12H_2O$ and $AgNO_3$ in water • Stirring with $BiVO_4$ powder for 7 h in a dark condition	• Monoclinic $BiVO_4$ • Cubic Ag_3PO_4 • Small particles of Ag_3PO_4 (~5 nm) dispersed on the $BiVO_4$ (040) facets (a truncated bipyramid shape, 500 nm)	• MB: 10 mg L^{-1} • Catalyst loading: 0.5 g L^{-1} • 300 W Xe arc lamp (λ≥420 nm, 10 cm) • 75% in 30 min ($BiVO_4$) • 100% in 10 min ($Ag_3PO_4/BiVO_4$)	65
$BiVO_4/CuCr_2O_4$	• Precipitation method • $Bi(NO_3)_3 \cdot 5H_2O$ and NH_4VO_3 in PEG-4000 and water • Stirring at 20°C for 3 h • Calcined at 400°C for 10 h	• Sol-gel method • $Cu(NO_3)_2 \cdot 2H_2O$ and $Cr(NO_3)_3 \cdot 9H_2O$ in water • Calcined at 800°C for 1.5 h • Impregnation method • $BiVO_4$ and $CuCr_2O_4$ powder in ethanol • Kept at 90°C for 10 h	• Monoclinic $BiVO_4$ • Tetragonal $CuCr_2O_4$ • Spherical shape of $CuCr_2O_4$ (65 nm) dispersed on large $BiVO_4$	• MB: 1 g L^{-1} • Catalyst loading: 0.25 g L^{-1} • 65 W Philips lamp (25 cm) • 100% in 3 h (1:0.25$BiVO_4/CuCr_2O_4$)	66

Catalyst	$BiVO_4$ synthesis	Composite synthesis	Physical characterisation	Photocatalytic performance	Ref.
$BiOBr/BiVO_4$	• Hydrothermal method • $Bi(NO_3)_3 \cdot 5H_2O$ and NH_4VO_3 in mixed solvent of diethylene glycol and water • 140°C for 12 h	• Precipitation-deposition method • $BiVO_4$ and TTAB in water mixed with $Bi(NO_3)_3 \cdot 5H_2O$ in HNO_3 • Stirring overnight at RT	• Monoclinic $BiVO_4$ • Tetragonal BiOBr • Flake-like $BiVO_4$ nanostructure with aggregated BiOBr microsphere	• MB: 10 mg L^{-1} • Catalyst loading: 1 g L^{-1} • 500 W Xe arc lamp ($\lambda \geq 420$ nm, 10 cm) • 10% in 1 h ($BiVO_4$) • 74% in 15 min ($BiOBr/BiVO_4$)	.[67]
$BiVO_4/ZnO$	• Reflux process • $Bi(NO_3)_3 \cdot 5H_2O$ in HNO_3 • NH_4VO_3 in water • pH 7 ($NaHCO_3$) • 95°C for 8 h	• Hydrothermal method • $Zn(NO_3)_2 \cdot 6H_2O$ in oxalic acid and water • 120°C for 6 h	• Monoclinic $BiVO_4$ • Wurtzite ZnO • ZnO nanobundles and $BiVO_4$ nanosheets	• Acid Violet 7 (AV 7), Evens Blue (EB) and Reactive Red 120 (RR 120): 0.5 mM • Catalyst loading: 4 g L^{-1} • Natural sun light • 99.2–99.7% in 75 min ($BiVO_4/ZnO$)	[68]
$BiOCl/BiVO_4$	• Hydrothermal method • $Bi(NO_3)_3 \cdot 5H_2O$ in HNO_3 • NH_4VO_3 in NaOH • pH 11–12 (NaOH) • 180°C for 6 h	• Hydrothermal method • $BiVO_4$ powder in HCl • 180°C for 10 h	• Monoclinic $BiVO_4$ • Tetragonal BiOCl • Sheets (1–3 μm width and 0.1–0.3 μm thickness)	• MO: 26.3 μM • Catalyst loading: 1 g L^{-1} • 500 W Xenon lamp ($\lambda > 400$ nm) • 22% in 11 h ($BiVO_4$) • 16% in 11 h (BiOCl) • 90% in 11 h for (0.75 wt.% $BiOCl/BiVO_4$)	[69]

Catalyst	$BiVO_4$ synthesis	Composite synthesis	Physical characterisation	Photocatalytic performance	Ref.
$rGO/BiVO_4$	• Hydrothermal method • $Bi(NO_3)_3 \cdot 5H_2O$ in HNO_3 • NH_4VO_3 in NH_4OH • SDS as surfactant • pH 7 (NH_4OH) • 180°C for 24 h	• Evaporation-induced self-assembly process • GO and $BiVO_4$ powder in ethanol and water • at 80°C for 24 h • Irradiated by visible light for 3 h	• Monoclinic $BiVO_4$ • Peak at 12° rGO (XRD) • $BiVO_4$ polyhedral (1 μm) deposited on rGO sheets (2 nm thickness)	• MB: 10 mg L^{-1} • Catalyst loading: 1 g L^{-1} • 300 W Xenon lamp ($\lambda \geq 420$ nm) • 70% in 2 h ($BiVO_4$) • 100% in 2 h for (2.5 wt.% $rGO/BiVO_4$)	70
$BiVO_4/AgVO_3$	• Hydrothermal method • NH_4VO_3 and $AgNO_3$ in water • pH 8 (NH_4OH) • 180°C for 12 h	• Hydrothermal method • Ag_3VO_3 powder and $Bi(NO_3)_3 \cdot 5H_2O$ in water • 160°C for 12 h	• Monoclinic $BiVO_4$ • Monoclinic $AgVO_3$ • Board-like $BiVO_4$ (1–2 μm) • $AgVO_3$ nanowire (175 nm)	• RhB: 10 mg L^{-1} • Catalyst loading: 1 g L^{-1} • 300 W Xe lamp (λ>420 nm) • 21% in 4 h ($BiVO_4$) • 4% in 4 h ($AgVO_3$) • 68% in 4 h for (15 wt.% $BiVO_4/AgVO_3$)	71
$ZnFe_2O_4/BiVO_4$	• Precipitation method • $ZnCl_2$ and $FeCl_3$ in water • $Bi(NO_3)_3 \cdot 5H_2O$ and NH_4VO_3 in HNO_3 • pH 9 (NaOH)	• Calcination: 500°C for 5 h	• Monoclinic $BiVO_4$ • Cubic $ZnFe_2O_4$ • Grain-like $ZnFe_2O_4$ (5 nm) dispersed on surface of block-like $BiVO_4$ (200 nm)	• MB: 10 mg L^{-1} • Catalyst loading: 1 g L^{-1} • 500 W Halogen lamp (λ>420 nm, 106.8 mW cm^{-2}) • 70% in 5 h ($BiVO_4$) • 59% in 5 h ($ZnFe_2O_4$) • 99% in 5 h ($ZnFe_2O_4/BiVO_4$)	72

Catalyst	$BiVO_4$ synthesis	Composite synthesis	Physical characterisation	Photocatalytic performance	Ref.
$C_3N_4/BiVO_4$	• Thermal condensation of melamine • Calcined at 520°C for 4 h	• Hydrothermal method • C_3N_4 and NH_4VO_3 in water • $Bi(NO_3)_3 \cdot 5H_2O$ in glacial acetic acid • pH 8 (NaOH) • 180°C for 24 h	• Monoclinic $BiVO_4$ • Graphite-like C_3N_4 (XRD) • Irregularly shaped $BiVO_4$ dispersed on C_3N_4	• MB: 10 mg L^{-1} • Catalyst loading: 1 g L^{-1} • 300 W Xenon lamp (λ>420 nm) • 60% in 1.5 h ($BiVO_4$) • 50% in 1.5 h (C_3N_4) • 78% in 1.5 h ($0.7:0.3 C_3N_4/BiVO_4$)	73
$BiPO_4/BiVO_4$	• One step hydrothermal method • $Bi(NO_3)_3 \cdot 5H_2O$ and NH_4VO_3 in HNO_3 • $NaH_2PO_4 \cdot 2H_2O$ in water • pH 0.5 (NH_4OH) • 180°C for 10 h	• N/A	• Monoclinic $BiVO_4$ • Monoclinic $BiPO_4$ • Small irregular $BiPO_4$ particles dispersed on surface of large $BiVO_4$ particles	• MB: 10 mg L^{-1} • Catalyst loading: 0.5 g L^{-1} • 500 W Xe lamp (λ>400 nm) • 72% in 1.5 h ($BiVO_4$) • 1% in 1.5 h ($BiPO_4$) • 92% in 5 h (10 wt.% $BiPO_4/BiVO_4$)	
$Cu_2O/BiVO_4$	• Hydrothermal method • $Bi(NO_3)_3 \cdot 5H_2O$ in HNO_3 • NH_4VO_3 in NaOH • EDTA as surfactant • pH 7 (NaOH) • 180°C for 24 h	• Hydrothermal method • $Cu(CH_3OO)_2 \cdot H_2O$ in ethanol or diethylene glycol • $BiVO_4$ powder • EDTA as surfactant • 180°C for 2 h	• Monoclinic $BiVO_4$ • Spherical Cu_2O (5–15 nm) dispersed on surface of plate-like $BiVO_4$ (500–800 nm)	• RhB: 10 mg L^{-1} • Catalyst loading: 2 g L^{-1} • 5300 W Xe lamp (λ>420 nm) • 50% in 2.5 h ($BiVO_4$) • 99% in 2.5 h ($1:2 Cu_2O/BiVO_4$)	74

Catalyst	$BiVO_4$ synthesis	Composite synthesis	Physical characterisation	Photocatalytic performance	Ref.
$BiVO_4/Bi_2WO_6$	• Precipitation method • $Bi(NO_3)_3 \cdot 5H_2O$ in HNO_3 • NH_4VO_3 in NaOH • EDTA as surfactant • pH 7 (NaOH) • Calcined at 500°C for 3 h	• Hydrothermal method • $Bi(NO_3)_3 \cdot 5H_2O$ and Na_2WO_4 in HNO_3 • pH 7 (NaOH) • 180°C for 10 h	• Monoclinic $BiVO_4$ • Orthorhombic Bi_2WO_6 • Plate like Bi_2WO_6 dispersed on surface of irregular blocky $BiVO_4$ (0.2–1.8 μm)	• MB: 10 mg L^{-1} • Catalyst loading: 1 g L^{-1} • 500 W iodine-wolfram lamp (λ>400 nm) • 42% in 1.5 h ($BiVO_4$) • 36% in 1.5 h (Bi_2WO_6) • 92% in 5 h ($0.3BiVO_4/0.7Bi_2WO_6$)	75
$BiVO_4/Bi_2O_3$	• One step hydrothermal method • $Bi(NO_3)_3 \cdot 5H_2O$ in water • NH_4VO_3 in water • 150°C for 12 h	• N/A	• Monoclinic $BiVO_4$ • Tetragonal Bi_2O_3 • Belt like $BiVO_4$ (500 nm) covered by spherical Bi_2O_3 (50 nm)	• RhB: 1 mM • Catalyst loading: 1 g L^{-1} • 350 W Xenon lamp (λ>400 nm) • 48% in 3 h ($BiVO_4$) • 36% in 3 h (Bi_2O_3) • 90% in 3 h (1.3 wt.% $BiVO_4/Bi_2O_3$)	76
$BiIO_4/BiVO_4$	• One step hydrothermal method • $Bi(NO_3)_3 \cdot 5H_2O$ in water • I_2O_5 and NH_4VO_3 in water • 180°C for 24 h	• N/A	• Monoclinic $BiVO_4$ • Orthorhombic $BiIO_4$ • Rod like $BiIO_4$ (200–500 nm) dispersed on surface of dendritic $BiVO_4$ (0.5–1.5 μm)	• RhB: 10 μM • Catalyst loading: 1 g L^{-1} • 500 W Xenon lamp • 14% in 5 h ($BiVO_4$) • 3% in 5 h ($BiIO_4$) • 40% in 5 h (15 wt.% $BiIO_4/BiVO_4$)	77

2.5 Properties of selected other metal oxides used for photocatalysis

2.5.1 Titanium dioxide (TiO_2)

Titanium dioxide (TiO_2) is a one of most popular photocatalysts in water purification and water splitting, since Honda-Fujishima's initial report in 1972.[78] TiO_2 has three main polymorphic structures including anatase, rutile and brookite, which can all be described in terms of (TiO_6^{2-}) octahedral as shown in Figure 2.13.[79] The three crystal structure differ by the distortion of each octahedral and by the assembly patterns of the octahedral chains.[19, 80] Generally, TiO_2 is an n-type semiconductor, the band gap energies is 3.2 eV for anatase and brookite, and 3.0 eV for rutile.[81]

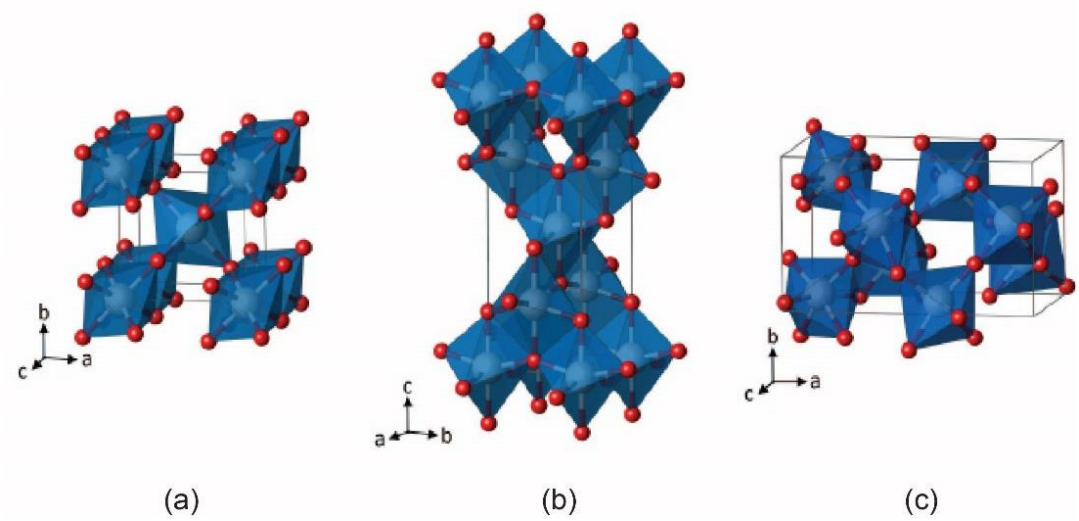

Figure 2.13 Polymorphic structures of TiO_2 (a) rutile, (b) anatase and (c) brookite, taken from Landmann *et al.*.[79]

Many different preparation methods of TiO_2 have previously been reported including solution precipitation,[82] hydrothermal method,[83, 84] flame spray pyrolysis,[82, 85] chemical solvent decomposition (CSD),[86] chemical vapor decomposition (CVD)[87] and sol-gel processes.[88-90] Furthermore, the TiO_2 photocatalyt has been studied for air treatment, water spitting and water purification due to its photo-stability, non-toxicity, redox efficiency and availability.

There are various reports available on photocatalytic dye degradation of TiO_2 nanoparticles. Most of them has been carried out with anatase phase TiO_2 due to its high photocatalytic efficiency and adsorption affinity for organic dye pollutants.

Yang *et al.* synthesised anatase TiO_2 microspheres by a facile microwave-assisted hydrothermal method at 180°C for 30 min.[83] Photocatalytic decontamination of Cr(VI) and methyl orange (MO) of the TiO_2 microspheres were enhanced comparing to of Degussa P25. Liu *et al.* prepared porous TiO_2 hollow aggregates with large surface area by a hydrothermal method at 160°C for 6 h without using any templates.[84] The porous TiO_2 showed better photocatalytic activity than a commercial TiO_2 (Degussa P25) in degradation of RhB.

Chin *et al.* prepared TiO_2 nanoparticles with high purity of anatase phase using a chemical vapor condensation method and also examined effects of this synthesis conditions.[86] A decrease in TTIP vapor concentration and residence time in a furnace resulted in an increase in surface area of the TiO_2 and poor crystallinity. Photocatalytic activity of the prepared TiO_2 nanoparticle was higher than of P25 in degradation of MB due to its content of hydroxyl groups on the surface.

Beyers *et al.* reported that mesoporous TiO_2 with anatase phase was synthesised by sol-gel process using titanium(IV) tetraisopropoxide (TTIP) as precursor and cetrimonium bromide (CTAB) as surfactant.[89] The mesoporous TiO_2 showed significantly increased photocatalytic activity in the degradation of Rhodamine 6G with changing the synthesis condition from basic to acid. Lu *et al.* synthesised crystalline TiO_2 nanoparticles at room temperature, titanium(IV) ethoxide and spherical polyelectrolyte brush particles as a precursor and template, respectively leading to the formation of well-dispersed TiO_2 nanoparticles.[90] The TiO_2 nanoparticles exhibited high photocatalytic activity for degradation of RhB dye under UV irradiation.

Hu *et al.* reported that uniform TiO_2/SiO_2 composite microspheres were synthesised by a self-assembly process using octadecyltrimethoxysilane (C18TMS) and tetrabutyl titanate at low temperature (60°C).[91] The C18TMS and reaction temperature played important roles in the formation of the synthesised composite microspheres. The composite microspheres exhibited single anatase phase and good photocatalytic activity on degradation of RhB.

Zhang *et al.* designed and prepared 3D TiO_2 sheeted networks by a self-supported construction using tetrabutyl titanate as precursor.[92] The 3D TiO_2 sheets had a single phase of anatase with porous structure leading to its high photocatalytic activity for degradation of RhB.

2.5.2 Cerium dioxide (CeO_2)

Cerium dioxide (CeO_2) is also an n-type semiconductor of an energy gap of about 2.8–3.2 eV, depending on the method for preparation, that originates from the O2p/Ce4f transition. CeO_2 has strong redox capabilities, which makes it suitable in photocatalysts and hydrogen evolution under UV light irradiation.[93] It has been extensively studied and employed in various applications due to its properties.[93] The capability of cerium atoms to switch between the Ce^{3+} and Ce^{4+} ionic state, in the oxidized and reduced condition, enables it to be used widely in various catalytic and functional systems such as electrolytes in solid oxide fuel cells,[94] gas sensors,[95] oxygen storage materials[96] and organic compound decomposition catalysts.[60, 97]

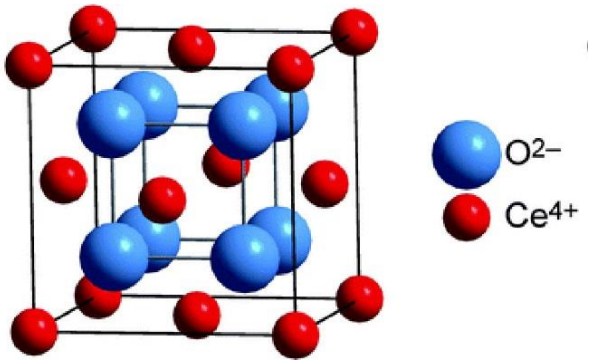

Figure 2.14 Crystal structure representation of cubic CeO_2 taken from Souza *et al.*.[98]

The CeO_2 semiconductors with cubic fluorite-type structure (Figure 2.14) have been synthesised by means of a variety of methods, including the homogenous precipitation,[99, 100] hydrothermal processes,[93] gas condensation,[101] spray pyrolysis,[102] sol-gel methods,[103] and sonochemical synthesis.[104]

The application of CeO_2 in photocatalytic degradation of organic dyes have been studied and reported in a few review papers. Balavi *et al.* reported that CeO_2 nanoparticles were synthesised by a simple microemulsion and sol-gel methods.[103] The microemulsion method could produce a smaller TiO_2 nanoparticles with high surface, so that provided a better photocatalytic degradation of Reactive Orange 16 in comparison with the sol-gel method.

Nanjundaiah *et al.* synthesised CeO_2 nanoparticles by solution combustion method using ammonium cerium(IV) nitrate as an oxidizer and EDTA as fuel at 450°C.[105] The CeO_2 nanoparticles exhibited good photocatalytic degradation of trypan blue dye and antibacterial activity against *P. aeruginosa*.

Channei *et al.* reported Fe-doped CeO_2 nanoparticles were prepared by a two-step combination of precipitation and impregnation methods and the prepared nanoparticles were fabricated in film form by a doctor blade technique.[100] 1.50 mol%

Fe-doped CeO_2 film enhanced photocatalytic degradation of MO compared with bare CeO_2 films, since the presence of Fe^{3+}, confirmed by an x-ray photoelectron spectroscopy and photoluminescence spectroscopy, act as electron acceptor and/or hole donor, resulting longer charge carrier separation.

2.5.3 Tungsten trioxide (WO_3)

Tungsten trioxide (WO_3) is also a n-type semiconductor with band gap energy of about 2.5–3.0 eV, depending on its stoichiometry, defects, and crystalline structures.[106, 107] WO_3 has different crystalline structures (tetragonal, orthorhombic, and monoclinic phases) with the most common being monoclinic (Figure 2.15) with an indirect band gap.[107]

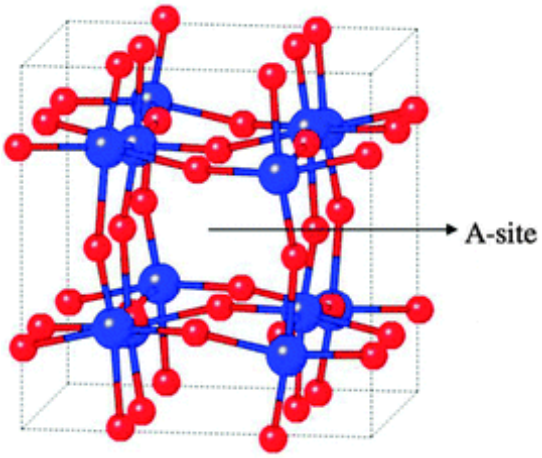

Figure 2.15 Crystal structure of a monoclinic WO_3 taken from Bignozzi *et al.*.[108]

The monoclinic WO_3 nanoparticles have once again been synthesised by various techniques such as flame pyrolysis,[109] thermal decomposition,[110] and wet chemical process such as sol-gel,[111] precipitation,[112, 113] and solvothermal/hydrothermal processes.[114-117] The WO_3 has been employed in various applications such as solar cells,[118] electrochromic devices,[119] gas sensors[120] and photocatalysts.[113, 115-117]

Liu *et al.* synthesised a monoclinic WO_3 by a precipitation method then modified with an ionic liquid [Bmim]I (1-butyl-3-methylimidazoliumiodide) through a impregnation method.[113] The [Bmim]I-modified WO_3 enhanced photocatalytic activity in degradation of RhB compared to bare WO_3 sample due to improvement of recombination of photoexcited electron-hole pairs in the [Bmim]I-modified WO_3.

Xu *et al.* reported that 3D flower-like and wheel-like WO_3 microstructures based on the spontaneous aggregation of WO_3 nanorods were fabricated via hydrothermal method at 180°C for 24 h.[115] Sodium tungstate (VI) dihydrate and hydrochloric acid were used as starting precursor and pH adjustor, respectively, which the morphologies of products could be controlled by adjusting pH of precursor solution. The 3D-WO_3 microstructures exhibited a high photocatalytic activity in degradation of RhB due to its providing high charge separation efficiency and long photocarrier lifetime.

Guo *et al.* prepared $WO_3 \cdot H_2O$ nanosheets and microspheres by hydrothermal method at 100°C for 10 h with different amounts of citric acid.[116] The $WO_3 \cdot H_2O$ microspheres showed higher photocatalytic degradation of RhB than the nanosheets that attributed to its higher surface area. Xiang *et al.* reported a modification of WO_3 nanorods with decorating Au nanoparticles were prepared by a combination of ion exchange and hydrothermal method at 180°C for 24 h.[117] the modified Au nanoparticles onto the surfaces of WO_3 nanorods enhanced highly response and selectivity for H_2 sensors and high photocatalytic activity for degradation of RhB than pure WO_3.

2.6 Synthetic methods for production of $BiVO_4$

Various synthetic methods such as solid state reactions,[121-123] precipitation reactions,[16, 36, 124-126] sol-gel processes,[28, 127, 128] hydrothermal methods[12, 129-131] and microwave assisted treatments[132-135] have previously been employed to synthesise $BiVO_4$ and are summarised in Table 2.7.

2.6.1 Precipitation method

One of the best-known methods to synthesise nanoparticles of $BiVO_4$ powder is the precipitation method, which involves dissolving salt precursors such as nitrates and carbonates taking a stoichiometric mixture of soluble salts of metal and precipitating them as hydroxides, citrates, oxalate or formats. After that, the mixture is separated, dried and heated to give final products.[136]

In this system, $Bi(NO_3)_3.5H_2O$ and NH_4VO_3 in aqueous solution were used as starting precursors as presented in Equation (2.15) and Equation (2.16), respectively.

$$Bi(NO_3)_3 \longrightarrow Bi^{3+} + 3NO_3^- \quad (2.15)$$

$$NH_4VO_3 \longrightarrow NH_4^+ + VO_3^- \quad (2.16)$$

In basic conditions:

$$Bi^{3+} + 3OH^- \longrightarrow Bi(OH)_3 \quad (2.17)$$

$$VO_3^- + 3OH^- \longrightarrow VO_3(OH)^{2-} \longrightarrow VO_4^{3-} + H^+ \quad (2.18)$$

$$Bi(OH)_3 + VO_4^{3-} + H^+ \longrightarrow BiVO_4 + H_2O + 2OH^- \quad (2.19)$$

When adding a basic solution such as sodium hydroxide (NaOH) or ammonium hydroxide (NH_4OH) to the mixture of bismuth nitrate ($Bi(NO_3)_3$) and ammonium metavanadate (NH_4VO_3) aqueous solution, precipitates are usually formed as metal

hydroxides as shown in Equation (2.17) for $Bi(OH)_3$. Under basic conditions, vanadium tetrahedral ions (VO_4^{3-}) are formed as presented in Equation (2.18). The resulting nitrate salts including $NaNO_3$ or NH_4NO_3, are then washed away and the hydroxide (OH^-) is burned off by a calcination step to obtain the $BiVO_4$ powder, as shown in Equation (2.19). However, one of the major disadvantages of the precipitation method is the difficulty to control the particle size and chemical homogeneity in preparation of tertiary metal oxide such as $BiVO_4$. Additionally, the precipitation processes need high-temperature treatment, such as a calcination step after the precipitation reaction.

2.6.2 Hydrothermal method

Hydrothermal synthesis is a single-step method to synthesis metal oxide nanomaterials without the need for post-preparation processing that involves crystal growth of materials under high boiling point aqueous solution (< 100°C) and high vapour pressure (< 1 bar). Since the critical point of water is at 374°C and 221 bar, this method is usually carried out below the critical points.[137] The hydrothermal method has an important advantage of using water as a solvent, which is the environmental benefit and cheaper than other solvents.[24]

Hydrothermal synthesis typically will produce a homogeneous, highly crystalline, powders, this method however requires a Teflon-lined stainless-steel autoclave. This is a batch process that poses issues for scale up especially with regard to pressure vessel design. The number of publications on $BiVO_4$ powders prepared by hydrothermal methods have been increasing rapidly since the first report by Lui *et al.* in 2003.[129] Table 2.7 presents a summary of techniques use to synthesis $BiVO_4$ nanoparticles as photocatalyst note on performance.

2.6.3 Microwave method

Microwave processing has been employed in synthesis of both organic and inorganic materials, since this method can provide a rapid and homogenous heating of the reaction to the desired temperature leading to time and energy savings.[26, 79, 138] This preparation technique in a synthesis of inorganic nanoparticles combine a solution phase method with microwave heating process that microwave irradiation is applied to chemical reactions.

There are two main mechanisms of the microwave heating, called dipolar polarisation and ionic conduction.[26, 138] Generally, polar molecules and conducting ions in system can absorb microwaves resulting rotation of the polar molecules, such as water or other solvent dipoles, and replacement of charged ions in the conducting ions, such as precursor molecules or other solute, respectively.[26] This allows to provide a highly supersaturated solutions due to rapid decomposition of the precursors, in which nucleation and growth will occur, and then produce the desired products.[139] However, the number and size of nuclei formation depend on the degree of supersaturation, which can be controlled by certain parameters such as precursor and solvent types, frequency and temperature.[138, 139]

Recently, microwave-assisted hydrothermal and microwave synthesis of $BiVO_4$ photocatalysts have become increasingly popular due to advantages such as shorter reaction times, lower temperature and pressure, requirement the direct transfer of energy instead of heat. These factors allow for the production of smaller particle sizes and high purity materials.

Table 2.7 Synthetic methods for preparation of $BiVO_4$ and their photocatalytic properties.

Synthesis type	Precursors	Synthesis conditions	Crystallinity/morphology	Photocatalytic performance	Ref.
Solid state reaction	• Bi_2O_2 powder • V_2O_5 powder	• Use a boll mill with acetone medium • Heat: 500–620°C • 4–54 h • Pressure: 40 MPa • Calcination: 300°C	• Mixture of Monoclinic and tetragonal phases • Monoclinic phase after calcination • Irregular particle (300 nm)	• N/A	140
	• $Bi(NO_3)_3{\cdot}5H_2O$ powder • NH_4VO_3 powder	• Ground in agate mortar at RT • Heat: 120°C • 24 h • Calcination: 700 C for 8 h	• Mixture of Monoclinic and tetragonal phases • Compact particles (10 μm)	• RhB: 10 μM • Catalyst loading: 1 g L^{-1} • 500 W Xe lamp (λ>400 nm) • 16% in 180 min	125, 141
Sol-gel process	• $BiCl_2$ in ethanol • $VO(OC_2H_5)_3$ in 2-propanol	• Refluxing for 5 h at 82°C	• Monoclinic phase	• N/A	127
	• $BiCl_2$ in ethanol • $VO(OC_3H_7)_3$ in 2-propanol	• Add 20% benzene • Stirring at RT • Calcination 200–500°C for 4 h	• Amorphous (200°C) • Monoclinic phase (> 300°C) • Spherical shape (200–400 nm)	• O_2 evaluation • $FeCl_3$ solution (4 mM, 200 mL) • Catalyst loading 0.4 g L^{-1} • 0.1 M NaOH • 1.0 V *vs.* Ag/AgCl. • 300 W Xe lamp (λ>420 nm)	128

Synthesis type	Precursors	Synthesis conditions	Crystallinity/morphology	Photocatalytic performance	Ref.
Precipitation process	• $Bi(NO_3)_3{\cdot}5H_2O$ in HNO_3 • NH_4VO_3 in NH_4OH	• pH 9 (NH_4OH) • at 60°C • Calcination at 350–400°C for 2h in air	• Tetragonal phase (no calcination) • Monoclinic phase (calcination)	• N/A	36
	• $[Bi_6O_4(OH)_4](OH)(NO_3)_5{\cdot}0.5H_2O$, $Bi(NO_3)_3{\cdot}5H_2O$ or $BiONO_3{\cdot}H_2O$ in HNO_3 • NH_4VO_3 in HNO_3	• pH 1–2 (NaOH) • at 0–100°C	• Monoclinic phase • Tetragonal phase • Mixture of monoclinic and tetragonal phases • Spherical particles (1–4 μm)	• N/A	124
	• $Bi(NO_3)_3{\cdot}5H_2O$ in HNO_3 • NH_4VO_3 in HNO_3	• pH 9 (NH_4OH) • RT • Calcination: 200–600°C for 61 h	• Amorphous (200°C) • Monoclinic phase (300–600°C) • Spherical shape (50–200 nm, increasing with calcined temp) • BET: 4.2–31 $m^2\ g^{-1}$(increasing with calcined temp)	• MB: 40 μM • Catalyst loading: 4 g L^{-1} • 200W Xenon arc lamp • 97.6 % in 4 h (the sample calcined at 300°C)	126
	• $Bi(NO_3)_3{\cdot}5H_2O$ in HNO_3 • NH_4VO_3 in NH_4OH	• pH 9 (NH_4OH) • at 70°C • Calcination: 200°C for 61 h	• Monoclinic phase • Spherical shape (250–300 nm) • BET: 1.5 $m^2\ g^{-1}$	• RhB: 5 mg L^{-1} • Catalyst loading: 1 g L^{-1} • Xe lamp (λ < 390 nm) • 99 % in 360 min (pH 10)	16
	• $Bi(NO_3)_3{\cdot}5H_2O$ and NH_4VO_3 in DI water • Cetrimonium bromide (CTAB) as surfactant	• Oil bath at 80°C for 12 h • Dried at 80°C for 12 h	• Monoclinic phase • Spherical shape (400–700 nm) • BET: 1.75 $m^2\ g^{-1}$	• RhB: 10 μM • Catalyst loading: 1 g L^{-1} • 500 W Xenon lamp (420 nm filter cut off) • 100% in 20 min	142

Synthesis type	Precursors	Synthesis conditions	Crystallinity/morphology	Photocatalytic performance	Ref.
Precipitation process (continued)	• $Bi(NO_3)_3 \cdot 5H_2O$ and NH_4VO_3 in mixture (H_2SO_4 + HNO_3 + H_2O_2) • Ethylenediaminetetraacetic acid (EDTA) as surfactant	• pH 9–10 (NH_4OH) • RT • Calcination: 450°C for 4 h	• Monoclinic phase • Moss-like shape • BET: 115 $m^2 g^{-1}$	• MB or phenol or 2,4,6-trichlorophenol: 30 mg L^{-1} • Catalyst loading: ~0.33 g L^{-1} • 100 W tungsten lamp (30 cm) • 95% in 5 h for MB • 100% in 6 h for phenol and 2,4,6-trochlorophenol	143
Hydrothermal method	• $Bi(NO_3)_3 \cdot 5H_2O$ in aqueous solution • $NaVO_3$ or V_2O_5 in NaOH	• pH 7 • 100–200°C • 12 h	• Monoclinic phase ($NaVO_3$ source, temp > 120°C and V_2O_5 source, temp ≥ 160°C) • Mixture of monoclinic and tetragonal phases ($NaVO_3$ source, temp < 120°C) • Rod-like shape, 200 nm (V_2O_5 source) • Plate-like in shape, 2 μm ($NaVO_3$ source)	• N/A	129
	• $Bi(NO_3)_3 \cdot 5H_2O$ in HNO_3 • NH_4VO_3 in aqueous solution	• 170°C • 120–130 h	• Monoclinic phase • Polyhedral shape (5 μm)	• N/A	125
	• $Bi(NO_3)_3 \cdot 5H_2O$ in HNO_3 • NH_4VO_3 in NaOH	• 180°C • 10–20 h	• Monoclinic phase • Spherical shape (44–53 nm)	• N/A	33

Synthesis type	Precursors	Synthesis conditions	Crystallinity/morphology	Photocatalytic performance	Ref.
Hydrothermal method (continued)	• $Bi(NO_3)_3 \cdot 5H_2O$ in HNO_3 solution • NH_4VO_3 in NaOH solution	• pH 4–9 (NaOH) • 120°C • 12 h	• Monoclinic phase (Bi:V mole ratio as 1:1): nanosheet (pH 4), dendritic (pH 6) and flower-like shapes (pH 9) • Tetragonal phase (Bi:V mole ratio as 4:3): solid ball (pH4, 6 and 9) • BET: 3.2 $m^2 g^{-1}$	• RhB and MB: 25 mg L^{-1} • Catalyst loading: 2.5 g L^{-1} • 400 W Xe lamp (λ>420 nm) • 77.8% in 6 h for RhB (monoclinic, flower-like) • 90% in 30 min for MB (tetragonal, ball-like)	144
	• $Bi(NO_3)_3 \cdot 5H_2O$ (in glacial acetic acid) • NH_4VO_3 (in NH_4OH)	• 180°C • 12 h	• Monoclinic phase • Peanut-like shape (1.5x3 µm) • BET: 4.1 $m^2 g^{-1}$	• RhB: 10 mg L^{-1} • Catalyst loading: 1 g L^{-1} • 500 W Xe lamp (5 cm) • 62.5% in 3 h	145
	• $Bi(NO_3)_3 \cdot 5H_2O$ in HNO_3 • NH_4VO_3 in NaOH	• pH 1.7–11.5 (NaOH and HNO_3) • 180°C • 6 h	• Monoclinic phase with a crystal-like shape: pH 11.5 (1.86 $m^2 g^{-1}$) and 8.8 (2.33 $m^2 g^{-1}$) • Tetragonal phase, a spherical shape: pH 1.7 (4.21 $m^2 g^{-1}$) • Mixture of both phases with a layered flower-like shape: pH 3.2–6.8 (4.08-4.98–2.33 $m^2 g^{-1}$)	• MO: 10 mg L^{-1} • Catalyst loading: 2 g L^{-1} • 500 W xenon lamp (420 nm filter cut off) and distance 10 cm • 98.5% in 1 h of the sample at pH 6.9	146
	• $Bi(NO_3)_3 \cdot 5H_2O$ (in HNO_3) • NH_4VO_3 (in NaOH)	• pH 5 (NaOH) • 180°C (300 W) • 3 h	• Monoclinic phase • Microspheres (2−5 mm) composing of small nanosheets • BET: 60.8 $m^2 g^{-1}$	• MB: 8 mg L^{-1} • Catalyst loading: 5 g L^{-1} • 300 W Xe arc lamp (λ>420 nm) • 91% in 3.5 h	147

Synthesis type	Precursors	Synthesis conditions	Crystallinity/morphology	Photocatalytic performance	Ref.
Hydrothermal method (continued)	• $Bi(NO_3)_3 \cdot 5H_2O$ (in glacial acetic acid) and NH_4VO_3 (in water)	• pH 5 and 9 (triethylamine, TEA) • 100°C • 2–20 h	• Monoclinic phase • Peanut-like shape, 3–4 μm (pH 5) • Needle-like shape, ~0.5 μm (pH 9) • BET: 3.5–6.5 $m^2\ g^{-1}$	• MB: 10 mg L^{-1} • Catalyst loading: 1 g L^{-1} • a PMA 2200 UVA photometer (35 W m^{-1}) • 60% in 2 h (k_{app} =0.12 ms^{-1})	131
	• $Bi(NO_3)_3 \cdot 5H_2O$ and V_2O_5 in water • K_2SO_4	• 200°C • 24 h	• Monoclinic phase • Sheet-like shape (10–40 mm thickness) • BET: 15.6 $m^2\ g^{-1}$	• MB: 10 mg L^{-1} • Catalyst loading: 4 g L^{-1} • LED Hg lamp (λ>450 nm) • 100% in 45 min (k_{app}: 0.002 s^{-1})	148
	• $Bi(NO_3)_3 \cdot 5H_2O$ in water • NH_4VO_3 in water	• pH 1– 9 (NaOH) • 180°C • 15 h	• Monoclinic phase • Fishbone like shape composed of nanorods (200–500 nm in length).	• MB: 5 μM • Catalyst loading 0.2 g L^{-1} • 500 W Xe lamp (λ>420 nm) • 100% in 3 h	149
	• $Bi(NO_3)_3 \cdot 5H_2O$ in HNO_3 • $K_6V_{10}O_{28}\ 9H_2O$ in NaOH	• pH 2–8 (NaOH) • 180°C • 24 h	• Monoclinic phase • Irregular shape (1–5μm): pH 6–8 • Spheres (5μm) composed of small spherical particles (100–300 nm): pH 2–4	• N/A	150
Hydrothermal method with surfactant	• $Bi(NO_3)_3 \cdot 5H_2O$ in HNO_3 • NH_4VO_3 in NaOH • Sodiumdodecyl benzene-sulfonate (SDBS)	• 200°C • 1.5 h	• Monoclinic phase • Spherical shape (500 mm)	• RhB: ~20 μM • Catalyst loading: 5 g L^{-1} • Natural sunlight • 72% in 3 h	130

Synthesis type	Precursors	Synthesis conditions	Crystallinity/morphology	Photocatalytic performance	Ref.
Hydrothermal method with surfactant (continued)	• $Bi(NO_3)_3 \cdot 5H_2O$ in HNO_3 • NH_4VO_3 in NaOH • SDBS	• pH 7 (NaOH) • 200°C • 1.5 h	• Monoclinic phase • Nanosheets with a thickness of 10−40 nm	• RhB: 20 μM • Catalyst loading: 5 g L^{-1} • Sun light (No mention) • ~70% in 3 h	130
	• $Bi(NO_3)_3 \cdot 5H_2O$ in HNO_3 • NH_4VO_3 in NaOH or NH_4OH • EDTA	• No adjust pH • 120°C • 6 h	• Monoclinic phase • A quasi-quadratic starlike shape (1−2 μm)	• MB: 15 mg L^{-1} • Catalyst loading: 0.25 g L^{-1} • 500 W Xe lamp (λ>420 nm) • 91% in 25 min	151
	• $Bi(NO_3)_3 \cdot 5H_2O$ and NH_4VO_3 in water • Triblock copolymer (P123)	• pH 3 (NH_4OH) at 80°C for 6 h • pH 6 ($NaHCO_3$) at 180°C for 6 h	• Monoclinic phase • pH 3: porous octapod-like shape and BET 11.8 m^2 g^{-1} • pH 6: porous spherical shape and BET 8.1 m^2 g^{-1}	• MB (10 μM) and catalyst loading of 0.1 g L^{-1} • Phenol (100 μM) with H_2O_2 and catalyst loading of 2 g L^{-1} • 300 W Xe lamp (λ>400 nm) • 100% in 2 h for MB (the sample synthesised at pH 6) • 91% in 4 h for phenol (the sample synthesised at pH 3)	152
	• $Bi(NO_3)_3 \cdot 5H_2O$ and NH_4VO_3 in water • EDTA	• 180°C • 3 h	• Mixture of tetragonal and monoclinic phases • Microsphere (1–4 μm) composing of rods (0.3–1 μm)	• N/A	153
	• $Bi(NO_3)_3 \cdot 5H_2O$ in HNO_3 • NH_4VO_3 in NaOH • P123	• pH 6 (NaOH) • 180°C • 6 h	• Monoclinic phase • Rod-like shape (~500 nm in diameter and ~2 μm in length) • BET: 3.2 m^2 g^{-1}	• MB: 10 μM • Catalyst loading 1 g L^{-1} • 300 W Xe lamp (λ>400 nm) • 90% in 2 h	12

Synthesis type	Precursors	Synthesis conditions	Crystallinity/morphology	Photocatalytic performance	Ref.
Hydrothermal method with surfactant (continued)	• $Bi(NO_3)_3 \cdot 5H_2O$ in HNO_3 • NH_4VO_3 in NaOH • Tween-80	• 120–180°C • 3 h	• Monoclinic phase with spherical shape (120–140°C) • Tetragonal phase with decahedral shape (160–180°C)	• MB: 5 mg L^{-1} (H_2O_2 assistance) • Catalyst loading 3.3 g L^{-1} • 500 W Xe lamp • 63.5% in67 h (Sample at 480°C)	154
	• $Bi(NO_3)_3 \cdot 5H_2O$ in HNO_3 • NH_4VO_3 in NaOH • Hexadecyl trimethyl ammoniumbromide (HTAB) or polyvinyl alcohol (PVA)	• 180°C • 6 h	• Monoclinic phase • Flower-like shape with 5–10 µm in size (HTAB) • Spherical shape with 150 nm in size (PVA)	• MO: 10 mg L^{-1} • Catalyst loading: 2 g L^{-1} • 500 W Xe lamp (10 cm) • 85% in 1.5 h (Flower-like sample)	155
	• $Bi(NO_3)_3 \cdot 5H_2O$ in HNO_3 • NH_4VO_3 in NaOH • Sodium acetate	• pH 1–10 (NaOH or HNO_3) • 180°C • 6 h	• Monoclinic phase (pH 1-9) • Peanut-like (pH 1), oval-like (pH 4), twin-quadrangle (pH 7), and four-pointed star shape (pH 9) • 2–4 µm in size	• MB: 10 mg L^{-1} • Catalyst loading: 1 g L^{-1} • A solar simulator AM 1.5G (1000 w m^{-2}) • 95.5% in 4 h	136
	• $Bi(NO_3)_3 \cdot 5H_2O$ in HNO_3 • NH_4VO_3 in HNO_3 • SDBS	• pH 1–10 (NH_4OH) • 180°C • 6 h	• Monoclinic phase • T shape (200 nm diameter with 1–2 µm length) • BET: 1.6 m^2 g^{-1}	• MB: 40 mg L^{-1} • Catalyst loading: 1 g L^{-1} • 500 W U-shaped xenon lamp • 47% in 1 h	156

Synthesis type	Precursors	Synthesis conditions	Crystallinity/morphology	Photocatalytic performance	Ref.
Hydrothermal method with surfactant (continued)	• $Bi(NO_3)_3 \cdot 5H_2O$ in HNO_3 • NH_4VO_3 in water • Ethylenediamine (EN)	• pH 0.45–7.04 (EN) • 160°C • 16 h	• Monoclinic phase with hexahedral shape (1–2 μm) :pH 0.45–0.72 • Mixture of monoclinic and tetragonal phases with shape (1–2 μm): pH 2.04–7.04 • BET: 0.029–1.4 $m^2 g^{-1}$	• RhB: 10 mg L^{-1} • Catalyst loading: 1 g L^{-1} • 300 W Xe arc lamp (>400 nm) • 87% in 2.5 h	157
Solvothermal method	• $Bi(NO_3)_3 \cdot 5H_2O$ and NH_4VO_3 in ethanol-water mixture	• pH 3.5–4 (HNO_3) • 160°C • 12 h	• Monoclinic phase • 2D disc-like structures (1 μm diameter with 20 nm thickness) • BET: 10.6 $m^2 g^{-1}$	• RhB: 10 μM • Catalyst loading: 1 g L^{-1} • 300 W tungsten halogen lamp (420 nm filter cut off) • 100% in 2.5 h	158
	• $Bi(NO_3)_3 \cdot 5H_2O$ in mixture of ethanol : acetic acid : water as 1:1:3 volume • NH_4VO_3 in HN_4OH	• pH 1.7–7.98 (HN_4OH or NaOH) • 80°C • 3 h	• Monoclinic phase with intensity decreased as increasing pH • Peanut (pH 4.9), dumbbells (pH 6.26), and flower and needle (pH 7.38–7.98)	• RhB: 5 mg L^{-1} • Catalyst loading: 0.4 g L^{-1} • Nature sun light • 98% in 10 h (Sample at pH 6.26)	159
	• $Bi(NO_3)_3 \cdot 5H_2O$ in ethylene glycol • NH_4VO_3 in water	• 180°C • 24 h	• Monoclinic phase • Rod with widths 60–90 nm and lengths 1 μm	• RhB: 10 μM • Catalyst loading: 2 g L^{-1} • 250 W high-pressure Hg lamp (380 nm cut-off filter) • 70% in 2.5 h	160

Synthesis type	Precursors	Synthesis conditions	Crystallinity/morphology	Photocatalytic performance	Ref.
Microwave assisted hydrothermal method	• $Bi(NO_3)_3 \cdot 5H_2O$ in water • NH_4VO_3 in water	• A MDS-8 closed vessel microwave chemistry workstation • 200°C • 40 min	• Monoclinic phase • Polyhedral shape (3.5–4 μm)	• RhB: 20 μM • Catalyst loading: 10 g L^{-1} • 350 W Xenon lamp • 48% in 4 h	161
	• $Bi(NO_3)_3 \cdot 5H_2O$ in water • NH_4VO_3 in water	• pH 0.59–12.93 (NaOH) • 200°C (Microwave irradiation) • 40 min	• Monoclinic phase: pH 0.59 (a polyhedral, 2−3 μm edge length, BET = 0.16 $m^2 g^{-1}$) and pH 4.26–9.76 (an oblate spheroid, 1 μm) • Tetragonal phase: pH 2.55 (a dense sphere, 2−3 μm) • Monoclinic and tetragonal phases: pH 0.70–3.65 (a dense sphere, 2−4 μm; and pH 10.44−12.93 (irregular rodlike, 100 nm, or fish-rib-like, 1 μm)	• RhB: 20 μM • Catalyst loading: 2 g L^{-1} • 350 W Xenon lamp • >97% in 2 h of the synthesised sample at pH 0.70	135
	• $Bi(NO_3)_3 \cdot 5H_2O$ in HNO_3 • NH_4VO_3 in NaOH	• 200°C (Microwave irradiation) • 60 min	• Monoclinic phase • Numerous with sub-particles of 200–300 nm) • BET: 0.61 $m^2 g^{-1}$	• RhB: 20 μM • Catalyst loading: 2 g L^{-1} • 350 W Xenon lamp • 65% in 5.5 h	62
Microwave process	• $Bi(NO_3)_3 \cdot 5H_2O$ in DI water • NH_4VO_3 in DI water	• pH 3 • 100°C (800 W microwave) • 5 h	• Monoclinic phase • Strawberry-like shape (200 nm) composing small particles (5 nm) • BET = 5.8 $m^2 g^{-1}$	• Ciprofloxacin (CIP): 20 μM • Catalyst loading: 1.5 g L^{-1} • 150 W Tungsten Halogen lamp (λ>420 nm) • >67.6% in 1 h	133

Synthesis type	Precursors	Synthesis conditions	Crystallinity/morphology	Photocatalytic performance	Ref.
Microwave process (continued)	• $Bi(NO_3)_3 \cdot 5H_2O$ in HNO_3 solution • $NaVO_3$ or V_2O_5 in NaOH solution • CTAB as surfactant	• pH 1 • 120 W microwave • 10–40 min	• Monoclinic phase with 1–2 μm in size of sheet-like shape (40 min) • Mixture of monoclinic and tetragonal phases (20–35 min, and 260–280 W for 10 min) • Tetragonal phase with 10–20 nm in size of polydisperse nanoparticle (10 min)	• RhB: 20 μM • Catalyst loading: 5 g L^{-1} • 300 W Xe lamp • 99% in 4 h (a monoclinic sample)	132
	• $Bi(NO_3)_3 \cdot 5H_2O$ in diethylene glycol (DEG) • NH_4VO_3 in DI water	• pH 2 • 110°C for 20 min • 2 s sonication (800 W) • 1 s microwave irradiation (500 W)	• Monoclinic phase • Spherical nanoparticles (150 nm)	• RhB: 10 μM • Catalyst loading: 0.5 g L^{-1} • 500 W Xenon lamp (400 nm cut-off filter) • >99% in 5 h	134
Reflux method	• $Bi(NO_3)_3 \cdot 5H_2O$ and NH_4VO_3 in HNO_3 solution	• pH 6–7 ($NaHCO_3$) • Heat at 80°C (in a reflux system) for 2–9 h	• Mixture of monoclinic and tetragonal phases (2 h) • Monoclinic phase (>6 h) • Microtubes with square cross-sections (2−5 μm)	• RhB: 10 μM • Catalyst loading: 1 g L^{-1} • 500 W Xe lamp (λ>400 nm) • 96% in 180 min	141
Sonochemical route	• $Bi(NO_3)_3 \cdot 5H_2O$ and NH_4VO_3 in water	• Ultrasound irradiation for 60 min • Dried at 80°C for 10 h	• Monoclinic phase • Irregular shape (300 mm) composing of small spherical particles (50nm) • BET: 4.16 m^2 g^{-1}	• MO: 40 mg L^{-1} • Catalyst loading: 1 g L^{-1} • 500 W Hg lamp (λ>400 nm) • 90% in 30 min	162

Table 2.8 Summary of advantages and disadvantages for synthetic methods of metal oxide semiconductors.[136, 137, 163]

Synthetic methods	Advantages	Disadvantages
Precipitation	○ Simple technique ○ Low cost production	○ Require high temperature treatment ○ Slow grow rate ○ Difficult to control particle size and morphology
Hydrothermal	○ One step reaction ○ Simple setup ○ Temperature below melting point of reactants ○ High product purity ○ Control the particle size	○ Require a Teflon line and stainless steel autoclave as reactor ○ Long time consuming ○ High pressure
Microwave	○ One step reaction ○ Simple method ○ Low cost production ○ Short reaction time ○ Reduce energy consumption ○ High product purity ○ Promising for large-scale production	○ Microwave radiation ○ Parameters to optimise

This review (Table 2.7) provides an introduction of three different synthetic methods including precipitation, hydrothermal and microwave methods to prepare $BiVO_4$ nanoparticles. The photocatalytic applications of $BiVO_4$ nanoparticles are also given, which presents variety results depending on their crystalline structures, morphologies, surface area and electronic properties. As the reviews in Table 2.7, it can be concluded that the monoclinic structure with high crystallinity, small particles with

large surface are and low band gap energy are important properties that influence of the photocatalytic activity of $BiVO_4$. As mentioned in this reviews, all of these preparation methods for synthesis $BiVO_4$ have advantages and disadvantages as summarised in Table 2.8. However, the microwave synthesis seem to be an effective method for the synthesis of $BiVO_4$ nanoparticles due to its simple and possible scale-up batch, low cost and “green chemistry” features with operating at low temperature, low pressure and short time.

2.7 Application of photocatalytic materials

Most of the photocatalytic studies in water purification used metal oxide photocatalysts in fine powder forms which have large surface areas leading to high photocatalytic activity. However, suspensions of the photocatalyst, especially nano-sized particles, have two majors operating issues with the regards to the practicality of using powder catalysts: (1) a centrifugation or filtration processes is required to separate catalysts from suspensions between purification batches, which significantly impedes the rate which treated water can be removed and (2) the catalyst particles can aggregate during the continual stirring process. Contradictory requirements are easily suspended during catalysts and easily removed to release treated water. Photocatalysts in film form are an attractive alternative for resolving these technical problems. Some researchers have reported the fabrication of the $BiVO_4$ films with various methods.

Chemical vapour deposition (CVD) is an applied material processing technology. This method can deposit an inorganic thin film through chemical reactions of gaseous species onto a substrate with a conformal and elaborate coverage.[24] Generally, CVD is performed in hot or cold wall reactors, with or without carrier gases, at above atmospheric pressures, and temperatures in the range of 200–1600°C.[164] A CVD method for fabrication of $BiVO_4$ was reported by Barreca *et al.* in 1999, where they

prepared the thin $BiVO_4$ films on aluminium oxide (Al_2O_3) substrate using oxygen atmosphere, and vanadyl (IV) acetyl acetonate and triphenyl bismuth as precursors.[107, 159, 164] In 2002, Neves *et al.* prepared pure monoclinic $BiVO_4$ on a glass substrate by a chemical bath deposition method (CBD) using a thermal treatment of aqueous solutions instead of the flame treatment, containing a bismuth (III) ethylene diamine tetra-acetate chelate and vanadium (V) species.[165] However, these fabrication methods have the drawback that they typically produce dense structures, which provides low surface area leading to low photocatalytic activity.

Ultrasonic spray pyrolysis (USP) is one of deposition methods which based on a decomposition of the liquid precursor solution by ultrasonic vibrations and using a carrier gas stream to transport the precursor towards the substrate.[166] The synthesis of $BiVO_4$ films by USP was reported by Li *et al.* in 2010.[164, 167] The $BiVO_4$ thin films were deposited onto indium tin oxide (ITO) glass using a mixture of starting precursors. $Bi(NO_3)_3$ and NH_4VO_3 were dissolved in 0.01 M HNO_3, and NH_4OH aqueous solutions, respectively, before both solutions were mixed together, and EDTA added. The films were investigated by electrochemical and photo-electrochemical measurements with respect to splitting water using solar energy.

Dip and spin coating processes are widely used to fabricate thin films on a variety of substrate materials. Thin film deposition by dip coating involve the substrate being fully immersed in the solution or suspension, while spin coating process involves the application of a precursor solution on one side of a rapidly rotating substrate.[168] These techniques may be used with a huge variety of precursor preparations. Recently, spin coating techniques have further been used to fabricate the $BiVO_4$ thin films, as shown in the following reports.

Luo *et al.* synthesised monoclinic scheelite $BiVO_4$ thin films by a chemical solution approach (polymer-assisted deposition) in which the precursor solutions were

composed of $Bi(NO_3)_3$ and $NaVO_3$ in aqueous solutions with ethylene-diaminetetraacetic acid (EDTA) and polyethyleneimine (PEI), respectively.[164] The mixture of both was spin-coated on Fluorine-doped tin oxide (FTO) glass at 2000 rpm for 30 s. Then the films were annealed at 500°C for 1 h. It was found that the as-prepared films were yellowish and partial transparent, and had a monoclinic structure with particle sizes in the range of 50–80 nm. Chatchai *et al.* reported the water oxidation of coupled WO_3/$BiVO_4$ thin film, which was deposited on FTO substrate by spin coating (1000 rpm, 40 s) from precursor solutions. Here a single coating of WO_3 layer was first applying on a ITO substrate and subsequently multiple coating of $BiVO_4$ was applied before being dried at 150°C for 5 min.[169] The results showed that the composite films enhanced the photocurrent efficiencies 10 times under solar light irradiation compared to pure WO_3.

Saito *et al.* also synthesised $BiVO_4$/WO_3 photoelectrodes by spin coating for water splitting applications.[170] The $BiVO_4$/WO_3 films with several different thicknesses of $BiVO_4$, were coated each precursor solutions, peroxotungstic acid (H_2WO_4) as precursor of WO_3, and bismuth oxide (Bi_2O_3) and vanadium oxide (V_2O_5) as precursor of $BiVO_4$, on FTO with a spin coater (1000 rpm, 30 s) and then calcination at 500°C for 30 min. Jiang *et al.* prepared ITO/$BiVO_4$/CdS and ITO/CdS/$BiVO_4$ multilayer electrodes using spin coating and ultrasonic spray pyrolysis methods on ITO glass for hydrogen production from water under visible light illumination.[171] For the ITO/CdS/$BiVO_4$ film electrode, the CdS precursor solution was transferred to the heated ITO (400°C) under flowing nitrogen gas. After that a $BiVO_4$ layer was deposited by spin coating several times. This film was then annealed at 500°C for 2 h. The ITO/$BiVO_4$/CdS electrode had the order first and second steps exchanged. The results showed that the ITO/CdS/$BiVO_4$ electrode gave a high photocurrent density and incident photon to current efficiency (IPCE).

In 2010, Xie *et al.* reported monoclinic $BiVO_4$ films composed of nanoparticles with 100 nm in size by a citrate-precursor chemical route.[172] $Bi(NO_3)_3$ and NH_4VO_3 were dissolved in a dilute HNO_3 and deionised water respectively. Citric acid was added into the Bi^{3+} stock solution and adjusted to pH 7 by addition of NH_4OH. Then the above solution was mixed with the V^{5+} stock solution under stirring at 363 K for 6 h. The resulted gel was dip-coated with rate of 5 cm/min on glass substrate, and the coated film was then dried at 150°C for 2 h. Furthermore, the $BiVO_4$ film exhibited high photocatalytic degradation of Acid Orange 7 (78.9% in 3 h) under visible-light irradiation.

In 2011, Zhou *et al.* reported a monoclinic $BiVO_4$ thin film, fabricated on ITO glass, for decomposition of 2,4-dichlorophenol and Bisphenol A under visible light irradiation.[173] Firstly, the mixed precursor solution was prepared using bismuth(III) oxide (Bi_2O_3), NH_4VO_3 and diethylene triamine pentaacetic acid (DTPA), dissolved in deionised water and adjusted pH as 10 by ammonia. These were dried at 80°C for 48 h, before being combined with deionised water and polyethylene glycol 400 (PEG 400). ITO glass was dipped into the precursor solution withdraw at 1 mm/s, dried at 80°C and then the coated glass was annealed at 400–600°C in air.

In 2012, Jia *et al.* fabricated $BiVO_4$ thin film electrodes on FTO glass for water splitting by dip coating of an aqueous HNO_3 solution of $Bi(NO_3)_3$ and NH_4VO_3, and calcining at 573–723K for 2 h.[174] The as-prepared $BiVO_4$ films had a monoclinic structure, and the surface of $BiVO_4$ film was uniformly 300–400 nm in thickness. In 2012, Silva *et al.* fabricated $BiVO_4$ through solution combustion synthesis (SCS) combined with the dip coating process.[175] The SCS is a method for synthesis of nanomaterials, based on the combination of an aqueous solution of metal nitrate and a fuel, gas phase combustion.[176] The preparation of the precursor gel, $Bi(NO_3)_3$ and NH_4VO_3 was dissolved with citric acid in aqueous solution, then NH_4OH was added until a pH of 7

was reached. This was followed by adding urea into the above mixture. The mixture was kept at 80°C for 20 h. For the thin film deposition, the above prepared gel was coated on FTO substrate with dipping rate of 10 cm min^{-1}, after that the coated films were annealed at 500°C by 1 h. It was found that the thickness of the film was about 800 nm with round shaped particles, homogeneously distributed on the film surface. Electrophotochemical degradation of MB over the $BiVO_4$ film deposited on FTO exhibited a rate constant five times higher than carried out in the dark.

Metal-organic decomposition (MOD) for the $BiVO_4$ film preparation has also been studied. The MOD is a wet-chemical process that is employed to fabricate inorganic films without processing through a gel or powder step.[137] A starting materials is metal-organic compound, which is coated on a substrate by spraying, dip coating or spin coating, and then annealed to decompose the organic compound to form a final inorganic film.[164]

In 2000, Galembeck *et al.* fabricated $BiVO_4$ thin films via a MOD process, starting from dissolved bismuth 2-ethyl-hexanoate and vanadium (IV) (oxy) acetylacetonate precursors in acetylacetone, dip coated then on borosilicate glass substrates and annealed at 400°C.[157, 164] The thickness of films was in the range of 50–100 nm, depending on the number of deposition steps.

In 2010, Zhang *et al.* reported that a Si/$BiVO_4$ composite film was also fabricated by MOD process. The mixed solution of Bi and V sources, $Bi(NO_3)_3$ was dissolved in acetic acid (CH_3COOH), with vanadium (V) tri-isopropoxy and tetraethylorthosilicate (TEOS) dissolving in acetylacetone ($C_5H_8O_2$).[177] Si/$BiVO_4$ films were obtained by coating the above mixture on FTO substrate by a spin coater and then annealed in air at 500°C for 2 h. The results showed that the crystal size of the $BiVO_4$ film decreased from 32 nm to 24 nm by doping Si, which was confirmed by XRD analysis.

The photocatalytic decomposition rate of phenol on the Si/$BiVO_4$ film electrode was 1.8 times higher than the undoped $BiVO_4$ film electrode.

Slurry coating or doctor blading techniques, with a viscous paste of inorganic materials or colloidal suspensions is also used to fabricate the inorganic films.[178] This method allows simple preparation technique with varying experimental conditions, low production cost and low temperature preparation without processing in vacuum. However, the thickness of produced films is generally larger than a few microns and limited to the control of the thickness of films. In 2008, Long *et al.* reported the fabrication of $BiVO_4$ films by doctor blading for photoassisted water splitting applications.[164] The $BiVO_4$ film electrodes were prepared from the $BiVO_4$ powder synthesised via the hydrothermal method of $Bi(NO_3)_3$ and NH_4VO_3 in aqueous medium reported by Kohtani *et al.*. The film electrodes were coated with suspension of 200 mg of the powder in 1 mL of absolute ethanol on ITO glass, and then annealed at 400°C in air for 2 h.[179]

References

1. G. L. Baughman and E. J. Weber, *Environ. Sci. Technol.*, 1994, **28**, 267–276.
2. A. Ajmal, I. Majeed, R. N. Malik, H. Idriss and M. A. Nadeem, *RSC Adv.*, 2014, **4**, 37003–37026.
3. N. Muhd Julkapli, S. Bagheri and S. Bee Abd Hamid, *Scientific World J.*, 2014, **2014**, 25.
4. E. Forgacs, T. Cserháti and G. Oros, *Environ. Int.*, 2004, **30**, 953–971.
5. M. A. M. Salleh, D. K. Mahmoud, W. A. W. A. Karim and A. Idris, *Desalination*, 2011, **280**, 1–13.
6. D. Sara and K. S. Tushar, *J. Chem. Proc. Engg.*, 2014, **1**, 1–7.
7. J. S. Wu, C. H. Liu, K. H. Chu and S. Y. Suen, *J. Membrane Sci.*, 2008, **309**, 239–245.

8. E. Eren, *Journal of Hazard. Mater.*, 2009, **166**, 88–93.

9. T. S. Natarajan, M. Thomas, K. Natarajan, H. C. Bajaj and R. J. Tayade, *Chem. Eng. J.*, 2011, **169**, 126–134.

10. K. Yu, S. Yang, H. He, C. Sun, C. Gu and Y. Ju, *J. Phys. Chem. A*, 2009, **113**, 10024–10032.

11. H. Jiang, M. Nagai and K. Kobayashi, *J. Alloy. Compd.*, 2009, **479**, 821–827.

12. X. Meng, L. Zhang, H. Dai, Z. Zhao, R. Zhang and Y. Liu, *Mater. Chem.Phys.*, 2011, **125**, 59–65.

13. J. Tang, G. Cheng, H. Zhou, H. Yang, Z. Lu and R. Chen, *J. Nanosci. Nanotechnol.*, 2012, **12**, 4028–4034.

14. R. Jain, M. Mathur, S. Sikarwar and A. Mittal, *J. Environ. Manage.*, 2007, **85**, 956–964.

15. S. Horikoshi, H. Hidaka and N. Serpone, *Environ. Sci. Technol.*, 2002, **36**, 1357–1366.

16. A. Martínez-de la Cruz and U. M. G. Pérez, *Mater. Res. Bull.*, 2010, **45**, 135–141.

17. P. Wang, M. Cheng and Z. Zhang, *J. Saudi Chem. Soc.,* 2014, **18**, 308–316.

18. X. Zhang, Z. Ai, F. Jia, L. Zhang, X. Fan and Z. Zou, *Mater. Chem. Phys.*, 2007, **103**, 162–167.

19. A. L. Linsebigler, G. Lu and J. T. Yates, *Chem. Rev.*, 1995, **95**, 735–758.

20. J. M. Herrmann, *Catal. Today*, 1999, **53**, 115–129.

21. A. Houas, H. Lachheb, M. Ksibi, E. Elaloui, C. Guillard and J. M. Herrmann, *Appl. Catal., B*, 2001, **31**, 145–157.

22. J. Luan, W. Zhao, J. Feng, H. Cai, Z. Zheng, B. Pan, X. Wu, Z. Zou and Y. Li, *J. Hazard. Mater.*, 2009, **164**, 781–789.

23. S. van de Linde, I. Krstic, T. Prisner, S. Doose, M. Heilemann and M. Sauer, *Photochem. Photobiol. Sci.*, 2011, **10**, 499–506.

24. N. Liu, X. Chen, J. Zhang and J. W. Schwank, *Catal. Today*, 2014, **225**, 34–51.

25. J. Gamage McEvoy, W. Cui and Z. Zhang, *Catal. Today.*, 2013, **207**, 191–199.

26. L. Pan, X. Liu, Z. Sun and C. Q. Sun, *J. Mater. Chem. A*, 2013, **1**, 8299–8326.

27. J. Li and N. Wu, *Catal. Sci. Technol.*, 2015, **5**, 1360–1384.

28. A. Kudo, K. Omori and H. Kato, *J. Am. Chem. Soc.*, 1999, **121**, 11459–11467.

29. A. Kudo and Y. Miseki, *Chem. Soc. Rev.*, 2009, **38**, 253–278.

30. Z. F. Huang, L. Pan, J. J. Zou, X. Zhang and L. Wang, *Nanoscale*, 2014, **6**, 14044–14063.

31. N. Wang, X. Zhang, B. Chen, W. Song, N. Y. Chan and H. L. W. Chan, *Lab Chip*, 2012, **12**, 3983–3990.

32. D. S. Bhatkhande, V. G. Pangarkar and A. A. C. M. Beenackers, *J. Chem. Technol. Biotechnol.,* 2002, **77**, 102–116.

33. Y. Sun, C. Wu, R. Long, Y. Cui, S. Zhang and Y. Xie, *Chem. Commun.*, 2009, 4542–4544.

34. Y. Zhao, Y. Xie, X. Zhu, S. Yan and S. Wang, *Chem. Eur. J.*, 2008, **14**, 1601–1606.

35. R. S. R. Kalidindi and R. Subasri, in *Anti-Abrasive Nanocoatings*, ed. M. Aliofkhazraei, Woodhead Publishing, 2015, pp. 105–136.

36. A. K. Bhattacharya, K. K. Mallick and A. Hartridge, *Mater. Lett.*, 1997, **30**, 7–13.

37. A. Walsh, Y. Yan, M. N. Huda, M. M. Al Jassim and S. H. Wei, *Chem. Mater.*, 2009, **21**, 547–551

38. Z. Zhao, Z. Li and Z. Zou, *Phys. Chem. Chem. Phys.*, 2011, **13**, 4746–4753.

39. D. Lide, *CRC Handbook of Chemistry and Physics, 88th Edition (CRC Handbook of Chemistry & Physics)*, CRC Press, 2007.

40. R. Daghrir, P. Drogui and D. Robert, *Ind. Eng. Chem. Res.*, 2013, **52**, 3581–3599.

41. N. Guijarro, M. S. Prevot and K. Sivula, *Phys. Chem. Chem. Phys.*, 2015, **17**, 15655–15674.

42. F. F. Abdi, T. J. Savenije, M. M. May, B. Dam and R. van de Krol, *J. Phys. Chem. Lett.*, 2013, **4**, 2752–2757.

43. D. Bahnemann, *Sol. Energy*, 2004, **77**, 445–459.

44. A. Di Paola, E. García-López, G. Marcì and L. Palmisano, *J. Hazard. Mater.*, 2012, **211–212**, 3–29.

45. M. Pelaez, N. T. Nolan, S. C. Pillai, M. K. Seery, P. Falaras, A. G. Kontos, P. S. M. Dunlop, J. W. J. Hamilton, J. A. Byrne, K. O'Shea, M. H. Entezari and D. D. Dionysiou, *Appl. Catal., B*, 2012, **125**, 331–349.

46. H. Feng, M. H. Zhang and L. E. Yu, *Appl. Catal., A*, 2012, **413–414**, 238–244.

47. S. Ahmed, M. G. Rasul, W. N. Martens, R. Brown and M. A. Hashib, *Desalination*, 2010, **261**, 3–18.

48. Y. L. Pang, S. Lim, H. C. Ong and W. T. Chong, *Appl. Catal. A*, 2014, **481**, 127–142.

49. A. Zhang and J. Zhang, *J. Alloy. Compd.*, 2010, **491**, 631–635.

50. A. Y. Booshehri, S. Chun-Kiat Goh, J. Hong, R. Jiang and R. Xu, *J. Mater. Chem. A*, 2014, **2**, 6209–6217.

51. N. Myung, W. Lee, C. Lee, S. Jeong and K. Rajeshwar, *Chem. Phys. Chem.*, 2014, **15**, 2052–2057.

52. J. Liqiang, S. Xiaojun, S. Jing, C. Weimin, X. Zili, D. Yaoguo and F. Honggang, *Sol. Energy Mater. Sol. Cells*, 2003, **79**, 133–151.

53. G. Magesh, *Indian J. Chem., Sect. B: Org. Chem. Incl. Med. Chem.*, 2009, **48**, 480.

54. S. Gupta and M. Tripathi, *Chin. Sci. Bull.*, 2011, **56**, 1639–1657.

55. M. Long, W. Cai, J. Cai, B. Zhou, X. Chai and Y. Wu, *J. Phys. Chem. B*, 2006, **110**, 20211–20216.

56. L. Li and B. Yan, *J. Alloy. Compd.*, 2009, **476**, 624–628.

57. P. Madhusudan, J. Ran, J. Zhang, J. Yu and G. Liu, *Appl. Catal., B*, 2011, **110**, 286–295.

58. J. Su, X. X. Zou, G. D. Li, X. Wei, C. Yan, Y. N. Wang, J. Zhao, L. J. Zhou and J. S. Chen, *J. Phys. Chem. C*, 2011, **115**, 8064–8071.

59. Y. Hu, D. Li, Y. Zheng, W. Chen, Y. He, Y. Shao, X. Fu and G. Xiao, *Appl. Catal., B*, 2011, **104**, 30–36.

60. N. Wetchakun, S. Chaiwichain, B. Inceesungvorn, K. Pingmuang, S. Phanichphant, A. I. Minett and J. Chen, *ACS Appl. Mater. Interfaces*, 2012, **4**, 3718–3723.

61. D. K. Ma, M. L. Guan, S. S. Liu, Y. Q. Zhang, C. W. Zhang, Y. X. He and S. M. Huang, *Dalton Trans.*, 2012, **41**, 5581–5586.

62. L. Zhang, G. Tan, S. Wei, H. Ren, A. Xia and Y. Luo, *Ceram. Int.*, 2013, **39**, 8597.

63. P. Chatchai, A. Y. Nosaka and Y. Nosaka, *Electrochim. Acta*, 2013, **94**, 314–319.

64. L. Chen, Q. Zhang, R. Huang, S. F. Yin, S.-L. Luo and C. T. Au, *Dalton Trans.*, 2012, **41**, 9513–9518.

65. C. Li, P. Zhang, R. Lv, J. Lu, T. Wang, S. Wang, H. Wang and J. Gong, *Small*, 2013, **9**, 3951–3956.

66. R. Bajaj, M. Sharma and D. Bahadur, *Dalton Trans.*, 2013, **42**, 6736–6744.

67. F. P. Cao, C. H. Ding, K. C. Liu, B. Y. Kang and W. M. Liu, *Cryst. Res. Technol.*, 2014, **49**, 933–938.

68. S. Balachandran, N. Prakash, K. Thirumalai, M. Muruganandham, M. Sillanpää and M. Swaminathan, *Ind. Engi. Chem. Res.*, 2014, **53**, 8346–8356.

69. Z. He, Y. Shi, C. Gao, L. Wen, J. Chen and S. Song, *J. Phys. Chem. C*, 2014, **118**, 389–398.

70. T. Wang, C. Li, J. Ji, Y. Wei, P. Zhang, S. Wang, X. Fan and J. Gong, *ACS Sustainable Chem. Eng.*, 2014, **2**, 2253–2258.

71. Y. Yang, Y. Liu, B. Huang, R. Zhang, Y. Dai, X. Qin and X. Zhang, *RSC Adv.*, 2014, **4**, 20058–20061.

72. W. Zhang, M. Wang, W. Zhao and B. Wang, *Dalton Trans.*, 2013, **42**, 15464–15474.

73. Y. Tian, B. Chang, Z. Yang, B. Zhou, F. Xi and X. Dong, *RSC Adv.*, 2014, **4**, 4187–4193.

74. W. Wang, J. Wang, Z. Wang, X. Wei, L. Liu, Q. Ren, W. Gao, Y. Liang and H. Shi, *Dalton Trans.*, 2014, **43**, 6735–6743

75. Y. Geng, P. Zhang and S. Kuang, *RSC Adv.*, 2014, **4**, 46054-46059.

76. Y. Cheng, H. Wang, Y. Zhu, F. Liao, Z. Li and J. Li, *J. Mater. Sci. Mater. Electron.*, 2015, **26**, 1268–1274.

77. H. Huang, L. Liu, Y. Zhang and N. Tian, *RSC Adv.*, 2015, **5**, 1161-1167.

78. A. Fujishima and K. Honda, *Nature*, 1972, **238**, 37–38.

79. B. I. Kharisov, O. V. Kharissova and U. O. Méndez, *Microwave Hydrothermal and Solvothermal Processing of Materials and Compounds*, 2012.

80. O. Carp, C. L. Huisman and A. Reller, *Prog. Solid State Chem.*, 2004, **32**, 33–177.

81. X. Z. Li, H. Liu, L. F. Cheng and H. J. Tong, *Environ. Sci. Technol.*, 2003, **37**, 3989–3994.

82. C. B. Almquist and P. Biswas, *J. Catal.*, 2002, **212**, 145–156.

83. Y. Yang, G. Wang, Q. Deng, D. H. L. Ng and H. Zhao, *ACS Appl. Mater. Interfaces*, 2014, **6**, 3008–3015.

84. Z. Liu, D. D. Sun, P. Guo and J. O. Leckie, *Chem. Eur. J.*, 2007, **13**, 1851–1855.

85. S. Eiden-Assmann, J. Widoniak and G. Maret, *Chem. Mater.*, 2003, **16**, 6–11

86. Y. S. Lin, M. T. Chen, Y. F. Lin, S. J. Yang and J. L. Lin, *Appl. Surf. Sci.*, 2006, **252**, 5892–5899.

87. S. Chin, E. Park, M. Kim, G.-N. Bae and J. Jurng, *J. Colloid Interface Sci.*, 2011, **362**, 470–476.

88. N. Wetchakun, B. Incessungvorn, K. Wetchakun and S. Phanichphant, *Mater. Lett.*, 2012, **82**, 195–198.

89. E. Beyers, P. Cool and E. F. Vansant, *J. Phys. Chem. B*, 2005, **109**, 10081–10086.

90. Y. Lu, M. Hoffmann, R. S. Yelamanchili, A. Terrenoire, M. Schrinner, M. Drechsler, M. W. Möller, J. Breu and M. Ballauff, *Macromol. Chem. Phys.*, 2009, **210**, 377–386.

91. J. L. Hu, H. S. Qian, Y. Hu, Z. Q. Li, G. X. Tong, T. K. Ying, P. J. Gong, S. Y. Hao, H. B. Zhang and L. C. Li, *Cryst. Eng. Comm.*, 2012, **14**, 7118–7122.

92. X. Zhang, C. Hu, H. Bai, Y. Yan, J. Li, H. Yang, X. Lu and G. Xi, *Sci. Rep.*, 2013, **3**.

93. C. Hu, Z. Zhang, H. Liu, P. Gao and Z. L. Wang, *Nanotechnology*, 2006, **17**, 5983.

94. B. C. H. Steele and A. Heinzel, *Nature*, 2001, **414**, 345–352.

95. L. Liao, H. X. Mai, Q. Yuan, H. B. Lu, J. C. Li, C. Liu, C. H. Yan, Z. X. Shen and T. Yu, *J. Phys. Chem. C*, 2008, **112**, 9061–9065.

96. J. A. Rodriguez, J. C. Hanson, J.-Y. Kim, G. Liu, A. Iglesias-Juez and M. Fernández-García, *J. Phys. Chem. B*, 2003, **107**, 3535–3543.

97. S. Hu, F. Zhou, L. Wang and J. Zhang, *Catal. Commun.*, 2011, **12**, 794–797.

98. B. Zhou, X. Zhao, H. Liu, J. Qu and C. P. Huang, *Appl. Catal. B,* 2010, **99**, 214–221.

99. H. I. Chen and H. Y. Chang, *Colloids Surf., A*, 2004, **242**, 61–69.

100. D. Channei, B. Inceesungvorn, N. Wetchakun, S. Ukritnukun, A. Nattestad, J. Chen and S. Phanichphant, *Sci. Rep.*, 2014, **4**.

101. N. Guillou, L. C. Nistor, H. Fuess and H. Hahn, *Nanostruct. Mater.*, 1997, **8**, 545–557.

102 B. Elidrissi, M. Addou, M. Regragui, C. Monty, A. Bougrine and A. Kachouane, *Thin Solid Films*, 2000, **379**, 23–27.

103. H. Balavi, S. Samadanian-Isfahani, M. Mehrabani-Zeinabad and M. Edrissi, *Powder Technology*, 2013, **249**, 549–555.

104. L. Yin, Y. Wang, G. Pang, Y. Koltypin and A. Gedanken, *J. Colloid Interface Sci.*, 2002, **246**, 78–84.

105. T. N. Ravishankar, T. Ramakrishnappa, G. Nagaraju and H. Rajanaika, *Chemistry Open*, 2015, **4**, 146–154.

106. W. Morales, M. Cason, O. Aina, N. R. de Tacconi and K. Rajeshwar, *J. Am. Chem. Soc.*, 2008, **130**, 6318–6319.

107. N. Asim, M. F. Syuhami, M. Badiei and M. A. Yarmo, *APCBEE Procedia*, 2014, **9**, 175–180.

108. B. Zhou, X. Zhao, H. Liu, J. Qu and C. P. Huang, *Sep. Purif. Technol.*, 2011, **77**, 275–282.

109. G. R. Bamwenda and H. Arakawa, *Appl. Catal., A*, 2001, **210**, 181–191.

110. T. Siciliano, A. Tepore, G. Micocci, A. Serra, D. Manno and E. Filippo, *Sens. Actuators, B*, 2008, **133**, 321–326.

111. D. S. Lee, S. D. Han, J. S. Huh and D. D. Lee, *Sens. Actuators, B,* 1999, **60**, 57–63.

112. M. Sun, N. Xu, Y. W. Cao, J. N. Yao and E. G. Wang, *J. Mater. Res.*, 2000, **15**, 927–933.

113. J. Liu, S. Han, J. Li and J. Lin, *RSC Adv.*, 2014, **4**, 37556–37562.

114. S. Bai, K. Zhang, R. Luo, D. Li, A. Chen and C. C. Liu, *J. Mater. Chem.*, 2012, **22**, 12643–12650.

115. D. Xu, T. Jiang, D. Wang, L. Chen, L. Zhang, Z. Fu, L. Wang and T. Xie, *ACS Appl. Mater. Interfaces*, 2014, **6**, 9321–9327.

116. S. Q. Guo, M. M. Zhen, M. Q. Sun, X. Zhang, Y. P. Zhao and L. Liu, *RSC Adv.*, 2015, **5**, 16376–16385.

117. Q. Xiang, G. F. Meng, H. B. Zhao, Y. Zhang, H. Li, W. J. Ma and J. Q. Xu, *J. Phys. Chem. C*, 2010, **114**, 2049–2055.

118. S. M. Yong, T. Nikolay, B. T. Ahn and D. K. Kim, *J. Alloys Compd.*, 2013, **547**, 113–117.

119. C. G. Granqvist, *Sol. Energy Mater. Sol. Cells*, 2000, **60**, 201–262.

120. T. D. Senguttuvan, V. Srivastava, J. S. Tawal, M. Mishra, S. Srivastava and K. Jain, *Sens. Actuators, B*, 2010, **150**, 384–388.

121. A. R. Lim, S. H. Choh and M. S. Jang, *J. Phys. Condens. Matter*, 1995, **7**, 7309.

122. T. Lu and B. C. H. Steele, *Solid State Ionics*, 1986, **21**, 339–342.

123. Y.K. Taninouchi, T. Uda, T. Ichitsubo, Y. Awakura and E. Matsubara, *Solid State Ionics*, 2010, **181**, 719–723.

124. P. Wood and F. P. Glasser, *Ceram. Int.*, 2004, **30**, 875–882.

125. M. Gotić, S. Musić, M. Ivanda, M. Šoufek and S. Popović, *J. Mol. Struct.*, 2005, **744–747**, 535–540.

126. J. Yu, Y. Zhang and A. Kudo, *J. Solid State Chem.*, 2009, **182**, 223–228.

127. K. Hirota, G. Komatsu, H. Takemura and O. Yamaguchi, *Ceram. Int.*, 1992, **18**, 285–287.

128. H. Liu, R. Nakamura and Y. Nakato, *J. Electrochem. Soc.*, 2005, **152**, G856–G861.

129. J. Liu, H. Wang, S. Wang and H. Yan, *Mat. Sci. Eng. B-Solid*, 2003, **104**, 36–39.

130. L. Zhang, D. Chen and X. Jiao, *J. Phys. Chem. B*, 2006, **110**, 2668–2673.

131. S. Obregón, A. Caballero and G. Colón, *Appl. Catal., B*, 2012, **117–118**, 59–66.

132. H. Zhang, J. Liu, H. Wang, W. Zhang and H. Yan, *J. Nanopart. Res.*, 2008, **10**, 767–774.

133. W. Shi, Y. Yan and X. Yan, *Chem. Eng. J.*, 2013, **215–216**, 740–746.

134. Y. Zhang, G. Li, X. Yang, H. Yang, Z. Lu and R. Chen, *J. Alloy. Compd.*, 2013, **551**, 544–550.

135. G. Tan, L. Zhang, H. Ren, S. Wei, J. Huang and A. Xia, *ACS Appl. Mater. Interfaces*, 2013, **5**, 5186–5193.

136. Y. Lu, H. Shang, F. Shi, C. Chao, X. Zhang and B. Zhang, *J. Phys. Chem. Solids*, 2015, **85**, 44–50.

137. H. Hayashi and Y. Hakuta, *Materials*, 2010, **3**, 3794–3817.

138. I. Bilecka and M. Niederberger, *Nanoscale*, 2010, **2**, 1358–1374.

139. N. P. Herring, L. S. Panchakarla and M. S. El-Shall, *Langmuir*, 2014, **30**, 2230–2240.

139. K. Shantha and K. B. R. Varma, *Materials Sci. Eng. B-Solid*, 1999, **60**, 66–75.

140. H. Xu, C. Wu, H. Li, J. Chu, G. Sun, Y. Xu and Y. Yan, *Appl. Surf. Sci.*, 2009, **256**, 597–602.

141. L. Zhou, W. Wang, L. Zhang, H. Xu and W. Zhu, *J. Phys. Chem. C*, 2007, **111**, 13659–13664.

142. W. Yin, W. Wang, L. Zhou, S. Sun and L. Zhang, *J. Hazard. Mater.*, 2010, **173**, 194–199.

143. H. Golmojdeh and M. A. Zanjanchi, *Chem. Eng. Technol.*, 2013, **36**, 2080–2086.

144. Y. Guo, X. Yang, F. Ma, K. Li, L. Xu, X. Yuan and Y. Guo, *Appl. Surf. Sci.*, 2010, **256**, 2215–2222.

145. X. J. Wang, H. L. Liu, X. L. Wan, J. R. Wang and L. L. Chang, *Cryst. Res. Technol.*, 2013, **48**, 1066–1072.

146. A. Zhang, J. Zhang, N. Cui, X. Tie, Y. An and L. Li, *J. Mol. Catal. A-Chem.*, 2009, **304**, 28–32.

147. J. Q. Li, D. F. Wang, H. Liu, J. Du and Z. F. Zhu, *Phys. Status Solidi*, 2012, **209**, 248–253.

148. Y. Zhou, K. Vuille, A. Heel, B. Probst, R. Kontic and G. R. Patzke, *Appl. Catal., A*, 2010, **375**, 140–148.

149. X. Lin, H. Li, L. Yu, H. Zhao, Y. Yan, C. Liu and H. Zhai, *Mater. Res. Bull.*, 2013, **48**, 4424–4429.

150. F. Li, C. Yang, Q. Li, W. Cao and T. Li, *Mater. Lett.*, 2015, **145**, 52–55.

151. S. Sun, W. Wang, L. Zhou and H. Xu, *Ind. Eng. Chem. Res.*, 2009, **48**, 1735–1739.

152. H. Jiang, X. Meng, H. Dai, J. Deng, Y. Liu, L. Zhang, Z. Zhao and R. Zhang, *J. Hazard. Mater.*, 2012, **217–218**, 92–99.

153. Z. Zhu, J. Du, J. Li, Y. Zhang and D. Liu, *Ceram. Int.*, 2012, **38**, 4827–4834.

154. Z. Zhu, L. Zhang, J. Li, J. Du, Y. Zhang and J. Zhou, *Ceram. Int.*, 2013, **39**, 7461–7465.

155. A. Zhang and J. Zhang, *Spectrochim. Acta Mol. Biomo. Spectrosc.*, 2009, **73**, 336–341.

156. S. Dong, C. Yu, Y. Li, Y. Li, J. Sun and X. Geng, *J. Solid State Chem.*, 2014, **211**, 176–183.

157. X. Qi, X. Zhu, J. Wu, Q. Wu, X. Li and M. Gu, *Mater. Res. Bull.*, 2014, **59**, 435–441

158. L. Ren, L. Ma, L. Jin, J.-B. Wang, M. Qiu and Y. Yu, *Nanotechnology*, 2009, **20**, 405602.

159. S. Dong, J. Feng, Y. Li, L. Hu, M. Liu, Y. Wang, Y. Pi, J. Sun and J. Sun, *Appl. Catal., B*, 2014, **152–153**, 413–424.

160. L. Hu, S. Dong, Y. Li, Y. Pi, J. Wang, Y. Wang and J. Sun, *J. Taiwan Inst. Chem. Eng.*, 2014, **45**, 2462–2468.

161. G. Tan, L. Zhang, H. Ren, J. Huang, W. Yang and A. Xia, *Ceram. Int.*, 2014, **40**, 9541–9547.

162. L. Zhou, W. Wang, S. Liu, L. Zhang, H. Xu and W. Zhu, *J. Mol. Catal., A*, 2006, **252**, 120–124.

163. G. R. Patzke, Y. Zhou, R. Kontic and F. Conrad, *Angew. Chem. Int. Ed. Engl.*, 2011, **50**, 826–859.

164. S. Sarkar and K. K. Chattopadhyay, *Phys. E*, 2014, **58**, 52–58.

165. D. Barreca, L. E. Depero, V. D. Noto, G. A. Rizzi, L. Sangaletti and E. Tondello, *Chem. Mater.*, 1999, **11**, 255–261.

166. M. C. Neves and T. Trindade, *Thin Solid Films*, 2002, **406**, 93–97.

167. Y. Ma, S. R. Pendlebury, A. Reynal, F. Le Formal and J. R. Durrant, *Chem. Sci.*, 2014, **5**, 2964–2973.

168. M. Li, L. Zhao and L. Guo, *Int. J. Hydrogen Energy*, 2010, **35**, 7127–7133.

169. H. Luo, A. H. Mueller, T. M. McCleskey, A. K. Burrell, E. Bauer and Q. X. Jia, *J. Phys. Chem. C*, 2008, **112**, 6099–6102.

170. P. Chatchai, Y. Murakami, S. Y. Kishioka, A. Y. Nosaka and Y. Nosaka, *Electrochim. Acta*, 2009, **54**, 1147–1152.

171. R. Saito, Y. Miseki and K. Sayama, *J. Photochem. Photobiol., A*, 2013, **258**, 51–60.

172. J. Jiang, M. Wang, R. Li, L. Ma and L. Guo, *Int. J. Hydrogen Energy*, 2013, **38**, 13069–13076.

173. B. Xie, C. He, P. Cai and Y. Xiong, *Thin Solid Films*, 2010, **518**, 1958–1961.

174. B. Zhou, J. Qu, X. Zhao and H. Liu, *J. Environ. Sci.*, 2011, **23**, 151–159.

175. Q. Jia, K. Iwashina and A. Kudo, *Proc. Natl. Acad. Sci. U.S.A.*, 2012, **109**, 11564–11569.

176. M. R. da Silva, L. H. Dall'Antonia, L. V. A. Scalvi, D. I. dos Santos, L. O. Ruggiero and A. Urbano, *J. Solid State Electrochem.*, 2012, **16**, 3267–3274.

177. A. Galembeck and O. L. Alves, *Thin Solid Films*, 2000, **365**, 90–93

178. X. Zhang, X. Quan, S. Chen and Y. Zhang, *J. Hazard. Mater.*, 2010, **177**, 914–917.

179. M. Long and W. Cai, *Chin. J. Catal.*, 2008, **29**, 881–883

CHAPTER 3

EXPERIMENTAL AND TECHNIQUES

General experiment details including materials, techniques and instrument used in this research are described in this Chapter, with specific experimental details presented in each experimental Chapter. Most of the physical characterisation of the photocatalyst nanoparticles (X-ray diffraction, Raman spectroscopy, X-ray photoelectron spectroscopy and transmission electron microscopy) were undertaken at Chiang Mai University.

UV-vis absorption spectroscopy, scanning electron microscopy, all electrochemical characterizations and photocatalytic studies were carried out at the Intelligent Polymer Research Institute (IPRI) located at University of Wollongong. Additionally, Brunauer-Emmett-Teller (BET) for surface area and porosity analysis was performed at the University of Sydney using nitrogen adsorption-desorption experiment.

3.1 Chemicals and reagents

Table 3.1 All general chemicals and reagents used in this research.

Chemicals	**Purity**	**Molecular formula**	**Molecular Weight** (g mol^{-1})	**Company**
Acetic acid	99.0%	$C_2H_4O_2$	60.05	Ajax Finechem
Ammonium hydroxide	25.0% (w/v, aq.)	NH_4OH	17.00	Merck
Ammonium metavanadate	99.9%	NH_4VO_3	116.98	Aldrich
Bismuth (III)nitrate pentahydrate	98.0%	$Bi(NO_3)_3.5H_2O$	485.07	Sigma-Aldrich

Table 3.1 (continued) All general chemicals and reagents used in this research.

Chemicals	Purity	Molecular formula	Molecular Weight (g mol^{-1})	Company
Cerium(III)nitrate hexahydrate	99.9%	$Ce(NO_3)_3 \cdot 6H_2O$	434.22	Sigma-Aldrich
Citric acid	99.0%	$C_6H_8O_7$	192.12	Ajax
Ethanol absolute	100% (w/v)	C_2H_5OH	46.08	Ajax
Ethylene glycol	99.5% (w/v)	$C_2H_6O_2$	62.07	Fluka
Hydrochloric acid	37.0 wt.% in water	HCl	36.46	Merck
Potassiumhexacyano-ferrate(II)	98.5%	$K_4[Fe(CN)_6]$	422.39	Sigma-Aldrich
Methylene Blue	82%	$C_{16}H_{18}ClN_3S.3H_2O$	373.90	Fluka
Nitric acid	70.0% (w/v, aq.)	HNO_3	63.01	Ajax
Rhodamine B	90%	$C_{28}H_{31}ClN_2O_3$	479.01	Sigma-Aldrich
Sodium sulphate	99.0%	Na_2SO_4	142.04	Sigma-Aldrich
Sodium tungstate (VI)dihydrate	99.0%	$Na_2WO_4. 2H_2O$	329.85	Sigma-Aldrich
Titanium(IV) isopropoxide	97.0%	$C_{12}H_{28}O_4Ti$	284.22	Sigma-Aldrich
Octylphenoxypolyethoxyethanol (Triton™ X-100)	97.0%	$C_{14}H_{22}O(C_2H_4O)_n$ (n = 9-10)	647	Sigma-Aldrich

3.2 Synthesis of photocatalysts

The synthesis of all photocatalysts were carried out by solution phase synthetic methods. For the synthesis of Bismuth vanadate ($BiVO_4$) powders, Bismuth nitrate and ammonium vanadate in dilute nitric acid solution were used as starting precursors for three different preparation methods, namely precipitation at room temperature, hydrothermal synthesis and microwave synthesis. Details of this microwave based approach are explained in Chapter 5.

$CeO_2/BiVO_4$ and $TiO_2/BiVO_4$ composites were prepared by a two-step method. Firstly, $BiVO_4$ powder was synthesised by the precipitation method. Subsequently the $BiVO_4$ powder was added into cerium nitrate and titanium isopropoxide solutions to prepare composites by precipitation and sol-gel methods, respectively. $BiVO_4/WO_3$ composites were also synthesised by a two-step precipitation method, where WO_3 powder was firstly synthesised using tungsten nitrate as the starting material, then the $BiVO_4/WO_3$ composites were prepared by adding the WO_3 powder into the mixed precursors of Bi and V. Specific details of the synthesis of the $CeO_2/BiVO_4$, $TiO_2/BiVO_4$ and $BiVO_4/WO_3$ composites are presented in Chapter 6.

3.3 Thin film and electrode fabrication

All films for photocatalytic testing and electrochemical measurements were prepared by a doctor blading technique. Doctor blading, or tape coating, is widely used for fabricating thin films. A well-mixed slurry containing semiconductor photocatalysts and other additives (binders or plasticisers) is coated on substrate e.g., soda-lime glass, fluorine doped tin oxide (FTO) glass, tin doped indium oxide (ITO) glass, plastic foils, aluminium foils, titanium foils, etc.[1] As shown in Figure 3.1, the doctor blading process and slurry preparation are employed in this research. Briefly, 0.5 g of the photocatalytic powders ($BiVO_4$, CeO_2, TiO_2, WO_3, $BiVO_4/CeO_2$, $BiVO_4/TiO_2$ or

$BiVO_4/WO_3$ composites) were ground with 75 µL Triton X-100, 25 µL acetic acid and 4 mL ethanol. The slurry was ground with a mortar and pestle for 10 min with during which the ethanol was added in order to break up larger agglomerates. The paste was then sonicated for a further 30 min.

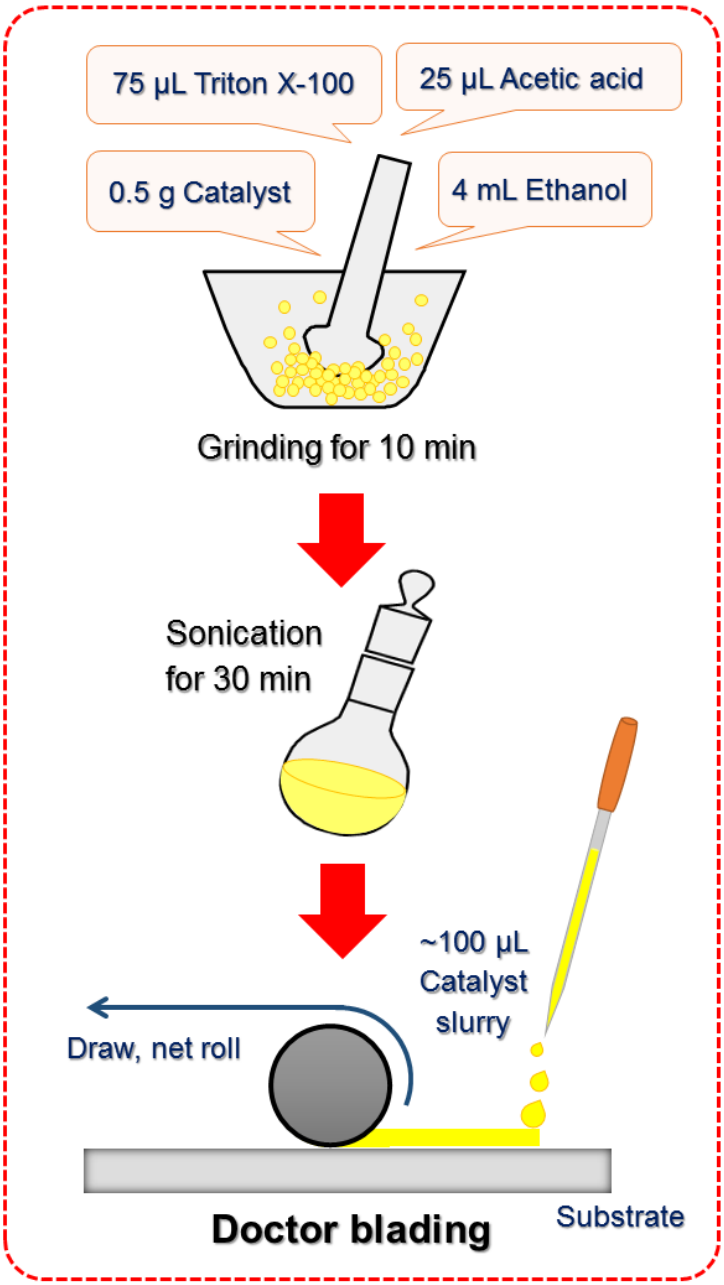

Figure 3.1 Diagram of the doctor blading technique used in fabrication of photocatalyst films.

Films were obtained by blading the slurry (~100 µL) on either glass slides (20 mm × 40 mm) for photocatalytic experiment or (~12.5 µL) on FTO glass working electrodes (10 mm × 10 mm) for electro-photocatalytic experiment. This was carried out on a heated (50°C) surface, using scotch tape as a spaces.

These films were then annealed in air at 450°C for 2 h, since annealing at this temperature provided a mechanically stable $BiVO_4$ film on glass substrate. The thickness of the resulting films was approximately 2.5 µm, as measured with a stylus profilometer (VeecoDektak 150). Typical examples of a $BiVO_4$ film and an electrode are shown in Figure 3.2.

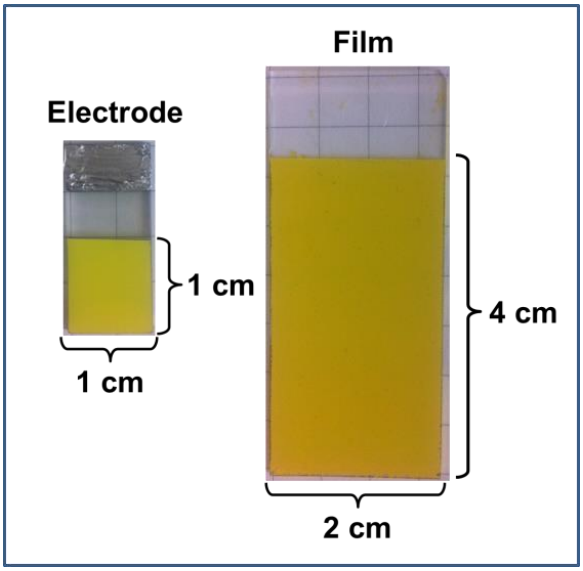

Figure 3.2 Photographs of a $BiVO_4$ electrode on FTO glass (left) and a $BiVO_4$ film on plain glass substrates (right) after annealing at 450°C for 2 h.

3.4 Photocatalytic degradation of dyes

3.4.1 Photocatalysis set up

Photocatalytic activities of the synthesised photocatalyst powder and films were studied by the degradation of either Rhodamime B (~25 µM, RhB) or methylene blue

(~50 µM, MB) in solution under simulated solar illumination (AM1.5G, 1 sun equivalent, 100 mW cm^{-2}) or visible light (a SOLUX Halogen lamp, with a 400 nm cut-off filter ~165 mW cm^{-2}) irradiation.

Photocatalyst films or powders (catalyst loading ~0.5 g per L of dye solution) were put in a reactor with the dye solution. A photocatalytic reactor is shown in Figure 3.3. Prior to irradiation, the films were left overnight in the dye solution under continuous stirring in order to attain an adsorption/desorption equilibrium. At irradiation time intervals of 30 min, the dye solution was collected and measured using a Shimadzu UV-1601 spectrophotometer. After that, the collected solution was put back into the reactor, and the photodegradation reaction resumed (< 3 min intermission).

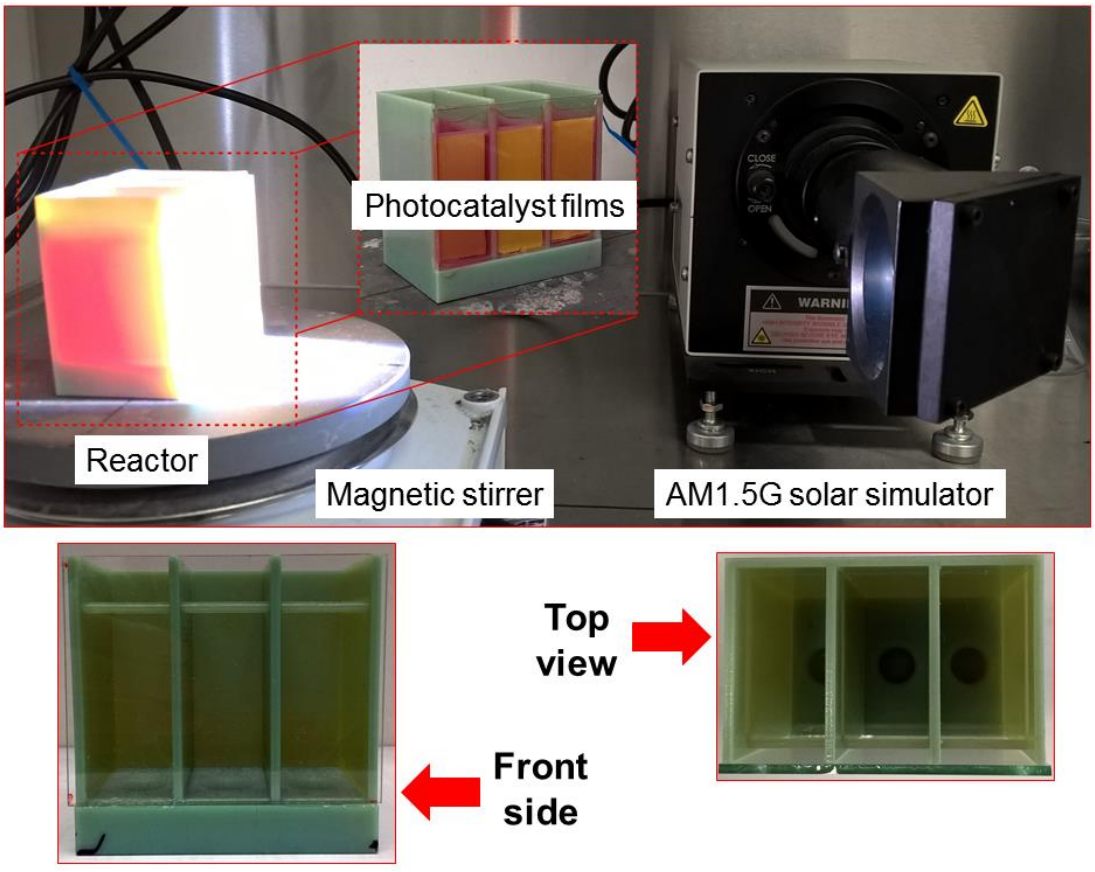

Figure 3.3 A photocatalytic reaction setup (top) with insert of the photocatalytic reactor and the front side (left bottom) and top view (right bottom) of reactor.

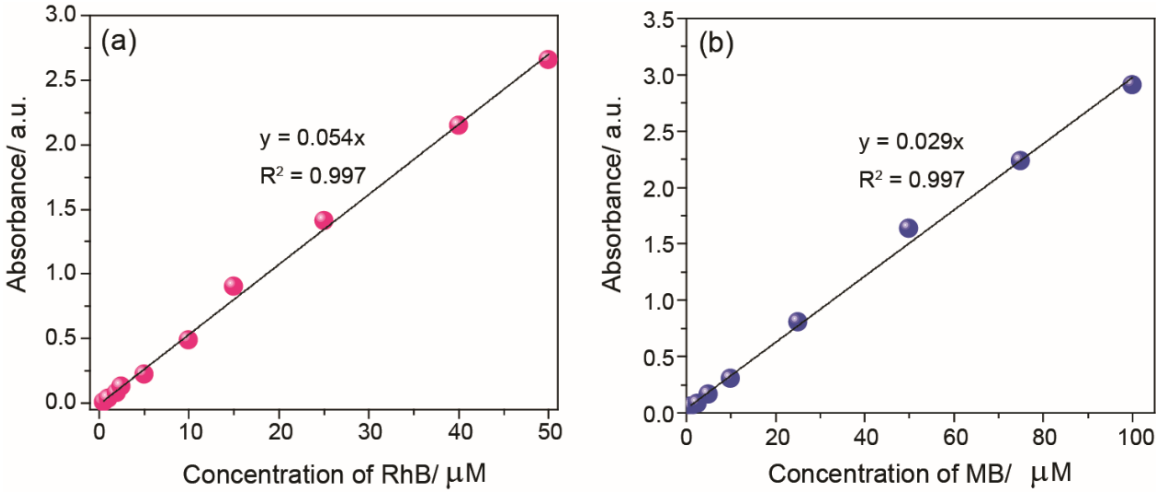

Figure 3.4 Calibration curves of (a) RhB and (b) MB in aqueous solution.

A calibration plot based on Beer-Lambert's law was established by relating the absorbance to the concentration as shown in Figure 3.4(a) for RhB dye and Figure 3.4(b) for MB dye.

3.4.2 Method and Kinetics analysis: photocatalytic degradation of dyes

While mass spectrometry has been widely used to determine photoreaction products, UV-vis spectrophotometry is commonly used to rapidly determine the concentration of the dyes and intermediates based on the Beer-Lambert's Law (Equation 3.1).[2,3]

$$A = \varepsilon bC \qquad (3.1)$$

Where A is absorbance, ε is the molar absorptivity ($cm^2.mol^{-1}$), b is the path length (cm), and C is the concentration of the coloured MB solution ($mol.L^{-1}$). When plotting calibration graph between A and C, the ε of each dye is the slope of the graph, which is used for converting the absorbance to the concentration of the dye.

A relationship between decreases of concentration dye as function of light irradiation time can be expressed as a linear equation represents Langmuir–Hinshelwood (LH)

kinetics. The LH kinetics is a kinetic model to explain the rate of a heterogeneous reaction, which is controlled by surface catalyst reaction, adsorption and desorption pressure of the adsorbed molecules are equilibrium.[4-6] Therefore, this model is possible to predict kinetics of photocatalytic degradation of dyes over the semiconductor metal oxide photocatalysts in this research. The LH kinetic expression is given by:

$$r = \frac{dC}{dt} = \frac{kKC}{(1+KC)} \qquad (3.2)$$

Where r represents the initial oxidation rate of organic substance, C is the concentration of the substrate at time (t), k and K are the oxidation rate constant and the adsorption coefficient of the reactant, respectively. The integration of Equation (32) gives Equation (3.3):

$$\ln\frac{C_t}{C_0} + K(C_0 - C_t) = kKt \qquad (3.3)$$

Where C_0 is the initial concentration of the RhB or MB dye and C_t is the concentration of the dye at time, t. When C_0 is very dilute concentrations ($C_0 < 10^{-3}$ mol.L^{-1}), and the reaction is of apparent first order kinetics.[4] Thus, the Equation (3.3) can be reduced to yield Equation (3.4).

$$\ln\frac{C_t}{C_0} = kKt = k_{app}t \qquad (3.4)$$

Where k_{app} is the apparent rate constant of a pseudo first order reaction. The plotting $\ln(C_0/C_t)$ as a function of irradiation time gives a straight line with slope corresponding to the first order constant.

3.4.3 Active species trapping study

An active species trapping study is an indirect chemical probe method using active specie scavengers, for studying photocatalytic reaction mechanism. Normally in the photocatalytic oxidation process, photo-induced active species, including holes (h^+), hydroxyl radicals ($^{\bullet}OH$) and superoxide anion radicals ($O_2^{\bullet-}$), oxidize organic molecules following the separation of electron-hole pairs created by photoexcitation. Therefore, the indirect chemical probe method is use to investigated the generated active species in photocatalysis reaction.

There is a few handful reports about detection of the main active species involved in photocatalytic oxidation process including hydroxyl radicals ($^{\bullet}OH$) and superoxide anion radicals ($O_2^{\bullet-}$) by using 5,5-dimethyl-1-pyrroline N-oxide (DMPO), where active intermediates are revealed by tracking active spin species such as DMPO-$^{\bullet}OH$ and DMPO-$O_2^{\bullet-}$.[7-9] Fang *et al.* employed an electron paramagnetic resonance (EPR) spin trapping techniques to analyse the photoreaction of organic compounds for BiOBr catalyst.[9] Xu *et al.* reported that Liquid chromatography-mass spectrometry (LC-MS) and LC-MS in the selected ion recording (SIR) mode were used to detect reaction products and intermediates, and proposed reaction pathways for the photocatalytic degradations of tetrabromobisphenol and carbamazepine.[10, 11] Table 3.2 presents a summary of scavengers use to study main reactive species for photocatalytic activity degradation of dyes.

Table 3.2 The scavengers use to study main active species for photocatalytic degradation of dyes.

Species	Scavengers	Ref.
$OH^{\bullet}$	Isopropanol (IPA)	12, 13
$O_2^{-\bullet}$	Benzoquinone (BQ)	12-19
h^+	Ethylenediaminetetraacetic acid (EDTA)	12, 13, 15, 16

3.5 Physical characterisation techniques

3.5.1 X-ray diffraction

X-ray diffraction (XRD) is a characterisation technique used to determine the crystalline phases and measure crystal size of the synthesised photocatalysts. The X-ray beam diffracts when crossing the crystal, and produces beams at different angles depending on the X-ray wavelength, the crystal orientation and the structure of the crystal. The structure can be described by the Bragg equation as shown in the following Equation (3.5):[20-22]

$$n\lambda = d_{hkl} \sin \theta_{hkl} \quad (3.5)$$

where is d_{hkl} the d-spacing; the interplanar distance between (hkl) planes, θ is the incidence angle, n is the order of diffraction, and λ is the wavelength of incident X-ray. [20-22]

The d_{hkl} spacing can be expressed though unite cell parameters and the Miller index by the following Equation (3.6): [20, 21]

$$\frac{1}{d_{hkl}^2} = \frac{h^2}{a^2} + \frac{k^2}{b^2} + \frac{l^2}{c^2} \quad (3.6)$$

where d_{hkl} is the d-spacing; a, b, c are the side lengths of the unit cell; and h, k, l are the Miller indices, which are used to describe the lattice planes and directions in a crystal. [20, 22] XRD was performed utilizing a GBC MMA XRD (Figure 3.5) employing Cu K_α X-rays of 1.542 Å radiation with the voltage and current kept at −40 kV and 25 mA, respectively. The broad scan analysis was typically conducted within the 2θ range of 15−55°.

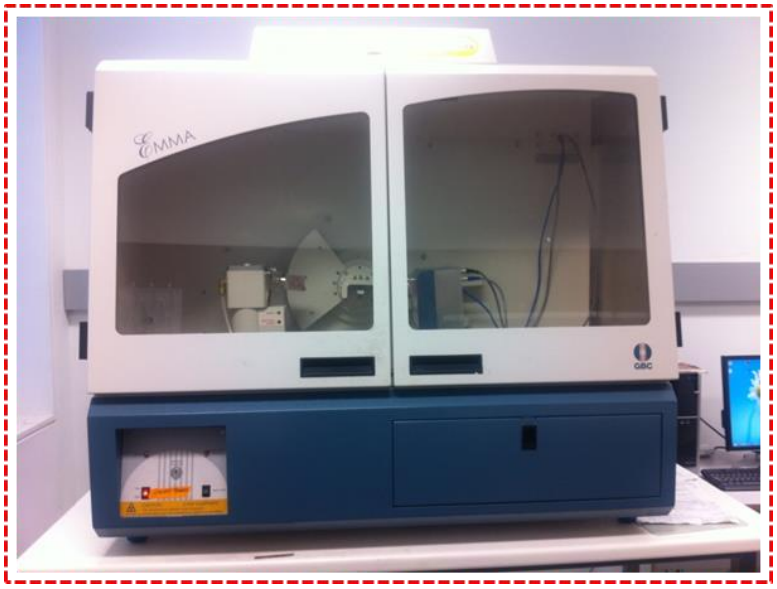

Figure 3.5 Photograph of a GBC MMA XRD machine.

XRD data is normally used for phase identification, whereby the XRD pattern of a sample being examined can be compared with Joint Committee Powder Diffraction Standards (JCPDS). In this research the main XRD patterns of monoclinic $BiVO_4$ (JCPDS no. 75–1688), tetragonal $BiVO_4$ (JCPDS no. 14–0133), tetragonal TiO_2 (JCPDS no. 21–1271), cubic CeO_2 (JCPDS no. 34–0394), and monoclinic WO_3 (JCPDS no. 72–0677) were identified.

The volume percentage of the monoclinic phase can be approximated by the relative intensities (XRD pattern) for the (112) peak of monoclinic and (200) peak of tetragonal and $BiVO_4$, as shown in Equation (3.7).[23]

$$\%V_{mono} = \frac{I_{mono(101)}}{I_{mono(101)} + I_{tetra(200)}} \times 100 \qquad (3.7)$$

where V_{mono} denotes as volume percentage of the monoclinic phase, and $I_{mono(121)}$ and $I_{tetra(200)}$ are relative intensity of the (121) peak for the monoclinic and that of the (200) peak for the tetragonal phases, respectively.

The average crystal sizes (D) of the synthesised $BiVO_4$ powders were calculated form their XRD patterns using the Scherrer equation as shown in Equation (3.8).[24, 25]

$$D = \frac{K\lambda}{\beta \cos \theta} \qquad (3.8)$$

where D is the crystal size, λ is the wavelength of the X-ray source ($\lambda_{Cu\,K\alpha}$ = 0.154 nm) and K usually is taken as 0.89 for spherical in shape, β is the peak width at half-maximum intensity (FWHM) and Bragg's diffraction angle (2θ). For $BiVO_4$ the peak at 2θ = 28.97 is used, corresponding to (121).

3.5.2 Raman spectroscopy

Raman spectroscopy is a characterisation technique which depicts specific vibrations and rotations of molecular bonds within the chemical structure of material as "Raman spectra" by scattering of an incident laser beam into separation frequencies.[26, 27] For metal oxide semiconductors, this technique can also give vibrational information about bulk mixed oxide molecular structures and surface structures of photocatalysts with high surface area. Furthermore, Raman spectroscopy has ability to detect amorphous phases and a greater sensitivity for detection of smaller nanoparticles (< 3 nm) than XRD technique. For qualitative determination, the sharpness of the Raman spectra relate to crystalline phases of photocatalysts

In this study the samples were analysed using a HORIBA Jobin Yvon Model T64000 with a laser generating radiation at 532 nm and 150 mW as shown in Figure 3.6, and the samples were recorded in the range of 100−1000 cm^{-1}..

Figure 3.6 Photograph of Raman spectroscopy equipment, JOBIN YVON HORIBA Model T64000.

3.5.3 X-ray photoelectron spectroscopy (XPS)

XPS is a quantitative technique that uses photons from an X-ray source (aluminium or magnesium) to excite the electronic states of the elements near the surface (1–10 nm depths) of a material.[21] The electrons emitted from the material are collected by an electron energy analyser which measure their kinetic energy. Hence, the electron binding energy of each of the emitted electrons can be determined from the following equation:[21, 22]

$$E_{binding} = E_{photon} - E_{kinetic} - \varphi \quad (3.9)$$

where $E_{binding}$ is the energy of the electron emitted from the material, E_{photon} is the energy of the X-ray photons, $E_{kinetic}$ is the kinetic energy of the emitted electron, and φ is the work function of the spectrometer.[21, 22] Each emitted electron from an element has its own characteristic binding energy at the peak position which can be used to identify the element and core level of the element.[22] Quantitative measurement of the elemental composition can be determined by using the peak intensities (with a

detection limit of ~1000 ppm for most elements), while oxidation states of the elements can be determined by the peak positions.[22]

In this research, surface compositions and oxidation states were determined by XPS using an AXIS Ultra DLD spectrometer (Figure 3.7) using a monochromatic Al K_{α} (150 W) source (15 mA, 14 kV). Survey and high-resolution spectra were obtained using an analysis area of ~300 x 700 microns and a pass energy of 80 eV. The binding energy of the C 1s transition at 285 eV was used as a reference to calibrate the binding energies of other species.

Figure 3.7 Photograph of X-ray photoelectron spectroscopy apparatus, AXIS Ultra DLD spectrometer.

3.5.4 UV-vis spectrophotometry

UV-visible spectroptotometry is a characterisation technique that obtains information about the electronic structure of semiconductor photocatalysts based on

their absorption and light scattering properties under light excitation in the range of 200–800 nm.[26, 28]

In this research, an ISR-3100 integrating sphere attachment (Figure 3.8(a)) was mounted in the UV-3600 UV-VIS-NIR spectrophotometer as shown in Figure 3.8(b), and diffuse reflectance and transmittance spectra of the films were recorded. Barium sulphate ($BaSO_4$) was used as a near perfect reflectance standard.

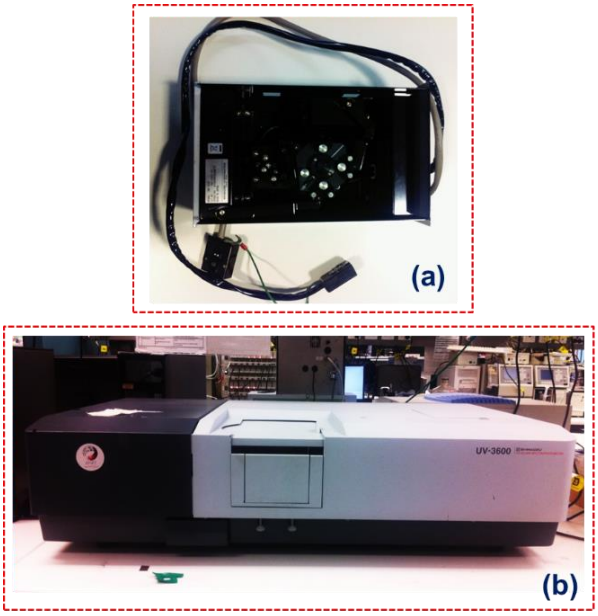

Figure 3.8 Photograph of (a) an ISR-3100 integrating sphere attachment and (b) UV-3600 UV-VIS-NIR spectrophotometer.

The following relational expression proposed by Tauc, Davis, and Mott, is used Equation (3.10) to determine direct electron transitions from absorbance spectra:[28, 29]

$$(\alpha h\nu) = A\,(h\nu - E_g)^{1/2} \qquad (3.10)$$

$$\alpha = 1 - (R + T) \qquad (3.11)$$

where A is a proportionality constant, E_g the direct band gap energy and $h\nu$ the incident photon energy (h is Plank's constant and ν is frequency of vibration). α is the absorption coefficient, which is related to the measured absorbance according to Equation (3.11).

3.5.5 Transmission electron microscopy (TEM)

Transmission electron microscopy (TEM) is an electron microscopy technique that uses a highly energetic beam of electrons that is transmitted through a thin specimen to provide a more penetrative and higher resolution image of the sample.[21, 30] TEM is a powerful tool for the morphological and structural analysis of samples and especially when these samples are mainly composed of two different materials in nanometric structures, as in the case of a two metal oxide composite.

Figure 3.9 Photograph of JEOL SM-2010 transmission electron microscope.

These TEM images were performed by a JEOL SM-2010 (Figure 3.9) with an acceleration voltage of 200 kV. For sample preparation, the powder samples were

dispersed in ethanol, dropped on carbon coated copper grids and dried at 60°C in a vacuum oven.

3.5.6 Scanning electron microscopy (SEM)

Scanning electron microscopy (SEM) is another electron microscope based technique that can provide the image of a specimens surface including surface topography, crystalline structure, chemical composition and electronic behaviour with high resolution and high magnification for samples with features in micro to nanoscale range.[21, 30]

Figure 3.10 Photograph of JEOL JSM-7500FA field emission scanning electron microscope.

A JEOL JSM-7500FA field emission SEM shown in Figure 3.10, was used to study the surface morphology of both powder and film samples, and to measure the thickness of the films (cross-sectional measurement). The accelerating voltage of this SEM was 5.0 kV with the emission current setting of 10 μA. For powdered sample

preparation, the catalyst powders were dispersed in ethanol, then dropped on the copper tape that attached the specimen holder, and dried overnight in a vacuum oven at 60°C. The catalyst film sample was cut into small pieces, then adhered the specimen with double sided copper tape. Both of prepared SEM samples were sputter coated with Pt coating (EDWARDS), to make the samples more conductive, before being placed in the SEM.

3.5.7 Surface area and porosity determination

3.5.7.1 Surface area determination

Specific surface area data was collected by N_2 physisorption at -195.6°C using a Quantachrome Instruments (Autosorb iQ). Prior to N_2 adsorption, the samples were degassed at 80°C for 6 h under vacuum in order to clean the surface and remove adsorbed water and other adsorbed species. During the adsorption process a relative pressure was increased from 0 to 1. The relative pressure (P/P_0) is defined as the absolute pressure of N_2 inside the adsorption chamber divided by the vapour pressure of N_2 at −195.6°C. A subsequent N_2 desorption profile was also carried out, where the relative pressure was decreased from 1 to 0. The analysis time for both adsorption and desorption isotherms was 24 hours in total.

Surface areas were obtained by the physical adsorption of monolayer of N_2 at −195.6°C from Brunauer-Emmett-Teller (BET) adsorption isotherm measurements. The BET equation can calculate the surface area of a solid sample from the number of N_2 molecules required to cover the solid surface in a monolayer, based on the cross-sectional area of N_2. The simple form of this equation can be written as Equation (3.11):[21, 22]

$$\frac{P}{V(P_0 - P)} = \frac{1}{V_{mol}\,C} + \frac{(C - 1)P}{CV_mP_0} \qquad (3.11)$$

where V is the volume, reduced to standard conditions (STP) of gas adsorbed per unit mass of adsorbent at a given pressure (P) and constant temperature, P_0 is the saturation pressure at the measurement temperature, V_m is the volume of gas adsorbed at STP per unit mass of adsorbent when the surface is covered by a monomolecule layer of adsorbate, and C is a constant, related to the free energy of adsorption.[21, 22]

According to Equation 3.12 a plot of $P/V(P_0-P)$ versus P/P_0 should yield a straight line. The surface area is then calculated using:

$$S_{BET} = \frac{V_m A_m N_a}{V_{mol}} \quad (3.12)$$

where N_a is Avogadro's number (6.02×10^{23}), V_{mol} is the molar volume of absorbate gas at STP (22.4 mol^{-1}), A_m is the cross-sectional area of absorbed gas ($A_m(N_2)$ = 0.162 nm^2). When nitrogen is the adsorbing gas this reduces to Equation (3.13):

$$S_{BET} = 4.353\ V_m \quad (3.13)$$

3.5.7.2 Pore size distribution

The International Union of Pure and Applied Chemistry (IUPAC) has classified pores into several size ranges. Pores with diameters less than 2 nm are termed "micropores", pores with a diameter greater than 2 nm but less than 50 nm are defined "mesopores", while pores with diameters greater than 50 nm are "macropores". In addition to the determination of the surface area of porous solids it is essential that the pore shape and size distributions are known to describe completely the textural properties of porous solids.

3.6 Electrochemical analysis techniques

Electrochemcal methods were used to estimate band energy of the semiconductor photocatalyts and study mechanism and reaction of photocatalytic degradation of dyes. Cyclic voltammetry (CV), Linear sweep voltammetry (LSV) and Mott-Schottky analysis were employed in this research.

For all measurements of electrical response, a conventional three-electrode system was used in 0.5 M Na_2SO_4 aqueous solution (pH 5.8) at room temperature. Before all testing, N_2 gas was bubbled into the electrolyte solution to displace O_2.

The coated sample on FTO conductive glass was used as the working electrode, a platinum mesh (approximately area of 1.7 cm^2) as the counter electrode and Ag/AgCl as the reference electrode. To convert the obtained potential (vs. Ag/AgCl) to reversible hydrogen electrode (RHE), the following Nernst equation (Equation 3.14) was used:

$$E_{RHE} = E_{Ag/AgCl} + 0.059\,pH + E^{\circ}_{Ag/AgCl} \quad (3.14)$$

where E_{RHE} is the converted potential vs. RHE, $E_{Ag/AgCl}$ is the experiment value of potential vs. Ag/AgCl, and $E^{o}_{Ag/AgCl}$ = 0.199 V at 25°C.[31, 32]

3.6.1 Cyclic voltammetry and Linear sweep voltammetry

To explore the surface electrochemistry of semiconductor materials and also understand the surface processes between the catalyst and dyes, cyclic voltammetry (CV) and linear sweep voltammetry (LSV) studies were used.

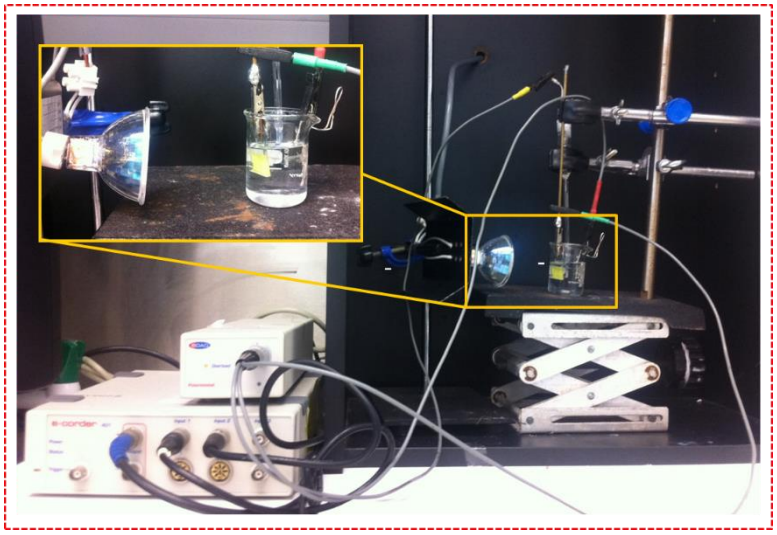

Figure 3.11 Photograph of CV and LSV measurements set up.

All of the voltametric measurements were performed on an EDAQ Australia™ potentiostat with Echem software (ADI Instrument Pty. Ltd.). The three-electrode set up was used in 0.5 M Na_2SO_4 solution as an electrolyte or a dye (25 µM RhB or 45 µM MB) solution with supported electrolyte (0.1 M Na_2SO_4). The potential was scanned from 0 V to -0.02 V. Furthermore, the oxidation and reduction potentials of RhB or MB solutions (as model dyes) were also investigated in a 0.1 M Na_2SO_4 supporting electrolyte.[32, 33] The CV measurement set up is shown in Figure 3.11.

3.6.2 Mott-Schottky analysis

Mott-Schottky plots were measured at a frequency of 1 kHz. A direct current (DC) potential was kept in the range −1 to 0 V vs Ag/AgCl for $BiVO_4$ and all composites and from -1 to 1 V vs Ag/AgCl for TiO_2, CeO_2 and WO_3. Both measurements were carried out using a GRAMRY Instrument Reference 600 Potentiostat/Galvanostate/ZRA. The Mott-Schottky equation (Equation 3.15) was used to calculate the flat-band potential (E_{fb}) of the semiconductors:[31, 34]

$$\frac{1}{C^2} = \frac{2}{e\varepsilon\varepsilon_0 N_d} \times \left(E - E_{fb} - \frac{kT}{e}\right) \qquad (3.15)$$

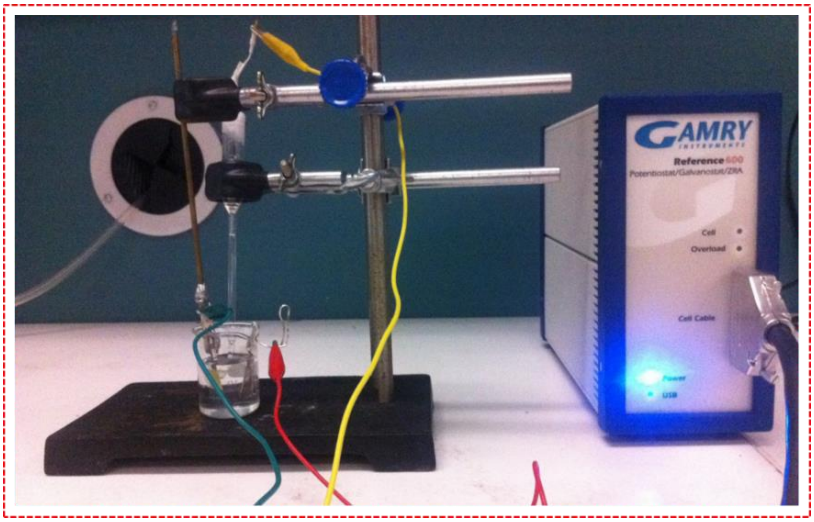

Figure 3.12 Photograph of Mott-Schottky measurement set up.

where C is the capacitance of the electrode, e is the elementary charge, ε is the dielectric constant of the electrode material, ε_0 is the permittivity of the vacuum, E is the applied potential, k is the Boltzmann constant and T is the temperature. E_{fb} is derived from the intercept of the potential axis, obtained by extrapolating the linear region of the plot.[31, 34] The Mott-Schottky set up for this research is presented in Figure 3.12.

References

1. A. Berni, M. Mennig and H. Schmidt, in *Sol-Gel Technologies for Glass Producers and Users*, eds. M. Aegerter and M. Mennig, Springer US, 2004, pp. 89–92.
2. J. Gamage McEvoy, W. Cui and Z. Zhang, *Catal. Today*, 2013, **207**, 191–199.
3. Y. J. Acosta-Silva, R. Nava, V. Hernández-Morales, S. A. Macías-Sánchez, M. L. Gómez-Herrera and B. Pawelec, *Appl. Catal., B*, 2011, **110**, 108–117.
4. J. M. Herrmann, *Catal. Today*, 1999, **53**, 115–129.
5. K. V. Kumar, K. Porkodi and F. Rocha, *Catal. Commun.*, 2008, **9**, 82–84.
6. A. Houas, H. Lachheb, M. Ksibi, E. Elaloui, C. Guillard and J. M. Herrmann, *Appl. Catal., B,*, 2001, **31**, 145-157.

7. Y. Chen, D. Li, X. Wang, L. Wu, X. Wang and X. Fu, *New J. Chem.*, 2005, **29**, 1514–1519.

8. M. Yin, Z. Li, J. Kou and Z. Zou, *Environ. Sci. Technol.*, 2009, **43**, 8361–8366.

9. Y. F. Fang, W. H. Ma, Y. P. Huang and G. W. Cheng, *Chem. Eur. J.*, 2013, **19**, 3224–3229.

10. J. Xu, L. Li, C. Guo, Y. Zhang and W. Meng, *Appl. Catal., B*, 2013, **130–131**, 285–292.

11. J. Xu, W. Meng, Y. Zhang, L. Li and C. Guo, *Appl. Catal., B*, 2011, **107**, 355–362.

12. Y. Park, Y. Na, D. Pradhan, B. K. Min and Y. Sohn, *Cryst. Eng. Comm.*, 2014, **16**, 3155–3167.

13. S. Xiao, Y. Li, J. Hu, H. Li, X. Zhang, L. Liu and J. Lian, *Cryst. Eng. Comm.*, 2015, **17**, 3809–3819.

14. J. Yang, C. Chen, H. Ji, W. Ma and J. Zhao, *J. Phys. Chem. B*, 2005, **109**, 21900–21907.

15. Z. W. Tong, D. Yang, Y. Y. Sun, Y. Tian and Z. Y. Jiang, *Phys. Chem. Chem. Phys.*, 2015, **17**, 12199–12206.

16. H. Huang, L. Liu, Y. Zhang and N. Tian, *RSC Adv.*, 2015, **5**, 1161–1167.

17. Y. Hu, D. Li, F. Sun, H. Wang, Y. Weng, W. Xiong and Y. Shao, *RSC Adv.*, 2015, **5**, 54882–54889.

18. L. Yuan, M. Q. Yang and Y. J. Xu, *Nanoscale*, 2014, **6**, 6335–6345.

19. D. Du, W. Li, S. Chen, T. Yan, J. You and D. Kong, *New J. Chem.*, 2015, **39**, 3129–3136.

20. P. L. Gai and E. D. Boyes, *Electron microscopy in heterogeneous catalysis,* Institute of Physics, Bristol, New York, 2003.

21. B. K. Hodnett, *Heterogeneous catalytic oxidationof organic compounds*, Department of Chemical and Environmental Sciences and The Materials and Surface Science Institute University of Limerick, Ireland, 2000.

22. S. Charles N., *Heterogeneous catalysis in industrial practice*, 2nd edn., McGraw Hill, New York, 1991.

23. A. K. Bhattacharya, K. K. Mallick and A. Hartridge, *Mater. Lett.*, 1997, **30**, 7–13.

24. Y. Wan, S. Wang, W. Luo and L. Zhao, *Int. J. Photoenergy*, 2012, **2012**, 7.

25. G. Li, D. Zhang and J. C. Yu, *Chem. Mater.*, 2008, **20**, 3983–3992.

26. H. H. Perkampus, *UV-VIS spectroscopy and its applications*, Springer Verlag, Berlin, New York, 1992.

27. S. Wartewig, *IR and Raman Spectroscopy*, Wiley VCH Verlag GmbH & Co. KGaA, 2005, pp. 27–33.

28. F. Wooten, *Optical Properties of Solids*, ed. F. Wooten, Academic Press, 1972, pp. 42–84.

29. E. A. Davis and N. F. Mott, *Philos. Mag. A*, 1970, **22**, 903–922.

30. C. Hammond, *J. Microsc., Oxford*, 1990, **159**, 123–124.

31. M. M. Khan, S. A. Ansari, D. Pradhan, M. O. Ansari, D. H. Han, J. Lee and M. H. Cho, *J. Mater. Chem. A*, 2014, **2**, 637–644.

32. A. Paracchino, V. Laporte, K. Sivula, M. Grätzel and E. Thimsen, *Nat. Mater.*, 2011, **10**, 456–461.

33. F. Fabregat Santiago, I. Mora Seró, G. Garcia Belmonte and J. Bisquert, *J. Phys. Chem. B*, 2002, **107**, 758–768.

34. N. Baram and Y. Ein Eli, *J. Phys. Chem. C*, 2010, **114**, 9781–9790.

CHAPTER 4

EFFECT OF OPERATIONAL PARAMETERS FOR PHOTOCATALYTIC DEGRADATION OF DYES

4.1 Introduction

Photocatalytic degradation of organic pollutants in wastewater, especially those from the textile and the photographic industries, has attracted a considerable attention from both academic researchers and industry as it offers the prospect of removing organic pollutants using sunlight as the driving force (thereby minimising operating costs, as well as other environmental impacts, such as is created by the generation of electricity from fossil fuels).[1-3] Most of the work in this field has used metal oxide photocatalysts in fine powder forms which have large surface areas leading to high photocatalytic activity.[3-6] However, suspensions of the photocatalyst, especially nano-sized particles, have two operating issues with the regard to the practicality of using powder catalysts: (1) a centrifugation or filtration process continuous stirring process, and (2) powder agglomeration during continuous stirring.[7-9] Photocatalysts in film form, rather than loose powder, are an attractive alternative for resolving these technical problems.[9-12]

Moreover, employing the photocatalyst in films has been demonstrated to be suitable for practical applications in wastewater purification with long-term photocatalytic stability, resistance to attack by reactive/oxidative radicals during irradiation, mechanical stability and comparable kinetics to powder systems all reported.[12] The photocatalyst films presented in this work show all these properties, and as such suitable for long term use. Methods available for the fabrication of photocatalytic films from powders include screen printing, dip-coating,[11, 13] and doctor blading.[14] Doctor blading is of particular interest due to the fact of readily applicable to industrial up-

scaling and of the fact that through changes to the ink formulation, speed of deposition and temperature, films can readily be produced with a range of thicknesses. This is particularly useful for optimization at the research and development levels.

Recently, Bismuth vanadate ($BiVO_4$) has become well-known as a semiconductor photocatalyst, which can be activated by visible light because of its band gap of ~2.4 eV ($\lambda < 517$ nm).[15, 16] It has successfully been used as photocatalyst for spitting water into hydrogen and oxygen gases[17, 18] and also for decomposition of organic and dye pollutants.[1, 24]

In addition to the comparison of photocatalytic properties between $BiVO_4$ powder and film forms as mentioned above this chapter explores the optimisation experimental parameters for suitably removal condition of organic dyes including thickness of the $BiVO_4$ films, initial concentration of dyes, reactor volume and intensity of light source were determinated. One of the limitations of $BiVO_4$ that is if it can only effectively degrade cationic dyes, it cannot be used for anion or neutral dyes.[19, 20] Rhodamine B (RhB) and methylene blue (MB) were chosen as model organic dyes in wastewater as discussed previously in Section 2.1 and are the most used model pollutants.[21]

4.2 Experiment section

$BiVO_4$ powder with a mean diameter of 50 nm and large surface area of 12.5 $m^2 g^{-1}$ was synthesised by a single step microwave method under 90°C (>300 W) for 1 h, as per Chapter 3. $BiVO_4$ films were fabricated on glass substrates by a doctor blading technique (details in Chapter 3), and then the photocatalytic activities for RhB and MB degradation of the $BiVO_4$ films were compared to those of powder. Furthermore, optimisation of photocatalytic parameters including thickness of catalyst film, initial concentration of organic dye, and light intensity were investigated using the $BiVO_4$ films for photodegradation of RhB and MB dyes under either solar simulator (an AM1.5 solar simulator, LCS-100™ ORIEL®) or visible light (a SOLUX Halogen lamp,

with a 400 nm cut-off filter) irradiation. All photocatalytic tests were performed as the same experimental set up in Chapter 3.

For the photocatalytic degradation of dyes, a solution containing a known concentration of each dye (20 mL) and $BiVO_4$ powder or film (for comparative studies both catalyst forms were used with the same mass of catalyst per reactor volume catalyst). These were allowed to equilibrate overnight in the dark, and then the above as-prepared batch was put and set up as per Figure 3.3 with the powder system, 1 mL of sample was withdrawn and centrifuged to separate catalyst particles from dye solution, while this separation process was not need for study of the catalyst film system. The remaining dye concentration of both systems were analysed with an UV-vis spectrophotometer (Shimadzu UV-1601) with concentrations of each dye determine based on absorption peak, which are at 553 nm for RhB and 664 nm for MB. Table 4.1 shows the ranges of parameters tested in this series of experiment.

Table 4.1 Ranges of operating parameters of photocatalytic experiment.

Parameters	Values
$BiVO_4$ film thickness/ µm	0.1–5.0
Dyes (RhB and MB) initial concentration/ µM	5–75
Light Intensity/ mW cm^{-2}	25–300
Reactor volume/ mL	10–30

Stability and recyclability of photocatalysis are important properties in water purification applications. $BiVO_4$ photocatalyst films and powders were repeatedly used without any treatment (annealing or washing process to remove absorbed dyes and contaminates on the catalyst surface).

4.3 Comparison of physical and photocatalytic properties between $BiVO_4$ powder and film

4.3.1 Physical properties

Figure 4.1 shows the XRD patterns of $BiVO_4$ film and powder. It was found both the film and the powder (after annealing at 450°C for 2 h) exhibited characteristic diffraction peak of the monoclinic $BiVO_4$ (JCPDS no. 75–1688) crystalline phase. There are no evidence of any second phase was observed. The XRD pattern of $BiVO_4$ film showed higher crystallinity, which exhibited sharper peaks (narrow width peaks) and higher intensity, than of $BiVO_4$ powder, which is expected as a result of the additional heat treatment process.

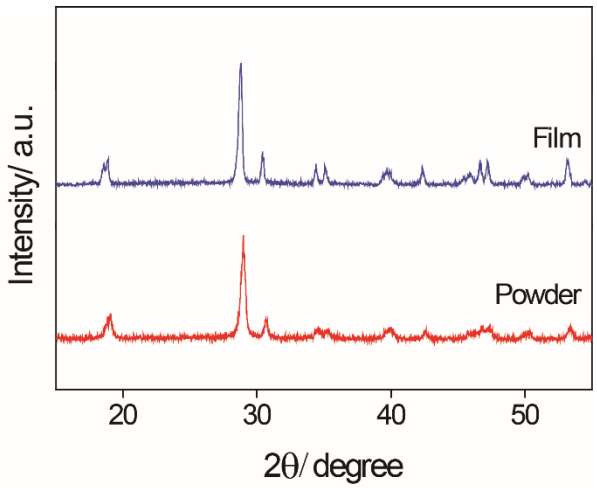

Figure 4.1 Comparison of XRD patterns of $BiVO_4$ powder and $BiVO_4$ film (annealed at 450°C for 2 h).

As shown in Figure 4.2(a), uniform, spherical, particles were observed with an average size in the range of 50–80 nm. The cross-sectional microstructure and surface topography of the $BiVO_4$ film deposited on glass plate after annealing at 450°C were examined by SEM as presented in Figures 4.2(c) and 4.2(d), respectively. The cross sectional SEM image revealed the thicknesses of $BiVO_4$ films (Figure 3.2(c)) to be about 2.3 µm and homogeneous throughout. The corresponding top

surface of $BiVO_4$ film (Figure 4.2(d)) showed similarly spherical particles with its cross section image as well as nano-sized spherical particles of its powder ((Figure 4.2(a)). Furthermore, a photograph of the $BiVO_4$ film is shown inset of Figure 4.2(d).

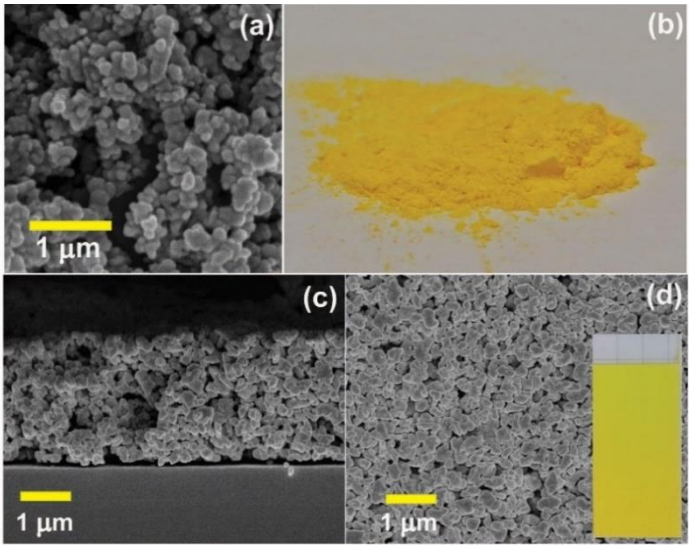

Figure 4.2 (a) morphology and (b) photograph of $BiVO_4$ powder, (c) cross-section and (d) top surface morphologies of $BiVO_4$ film (annealed at 450°C for 2 h) with inset of a photograph of the film.

The pore size distribution and surface area were obtained by N_2 adsorption analysis, as shown in Figure 4.3. The pore size distributions with inset adsorption/desorption isotherms of $BiVO_4$ powder and film samples. The pore size distribution of $BiVO_4$ powder, Figure 4.3(a), exhibits three major ranges of pores that are between 1.8–4.0 nm, 4.2–5.5 nm, and 7.6–10.7 nm. For comparison, the annealed $BiVO_4$ film contains less volume in pores between 2.0–3.8 nm and 4.0–5.0 nm in diameter. There is also almost nothing in the range of 8.0–10 nm as shown in Figure 4.3(b).

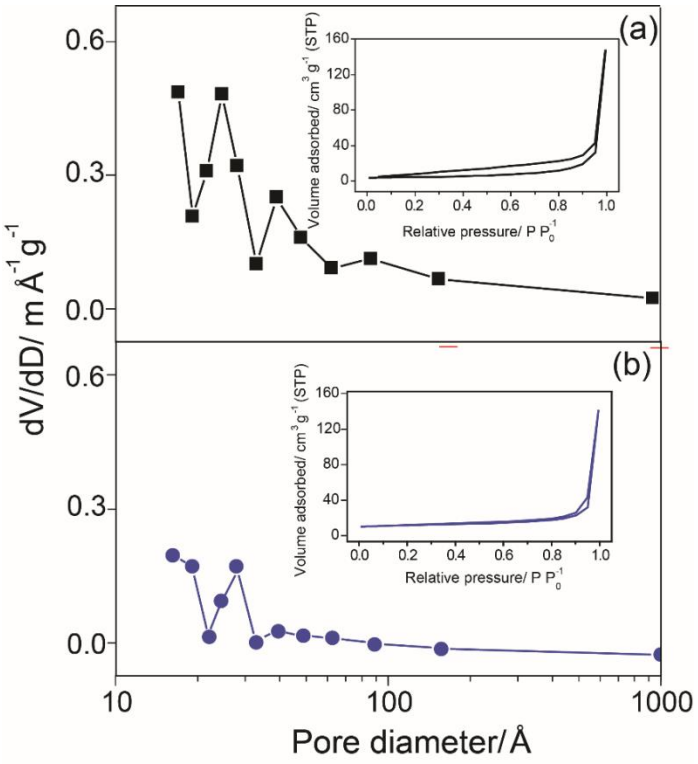

Figure 4.3 Pore size distribution plots with inset their corresponding BET nitrogen adsorption and desorption isotherm for (a) $BiVO_4$ powder and (b) $BiVO_4$ film (annealed 450°C for 2 h)

The inset of Figures 4.3(a) and 4.3(b) show the adsorption/desorption isotherms for $BiVO_4$ film and $BiVO_4$ powder, respectively. Both isotherms are characteristic of a type IV isotherm with their branches similar to the isotherm type II. A strong increase of N_2 adsorption isotherm of the $BiVO_4$ powder is observed up to a relative pressure (P/P_0) of 0.08, where a high surface area mesoporous structure is observed. While the adsorption branches of isotherm belonging to the $BiVO_4$ film presents a small increase up to 0.9, this probably due to the mesoporous formed an inter-particle pores and a consequence of the grain growth. This corresponds with the BET surface areas of $BiVO_4$ powder (22.5 m^2 g^{-1}) being larger than that of the $BiVO_4$ film (12.1 m^2 g^{-1}). As expected, the BET surface area and pore size of the $BiVO_4$ film decreased after annealing at 450°C for 2 h, since the pore volume formed by inter-particle pores.

Therefore, an effect of sintering process is reduction of surface area of $BiVO_4$ photocatalyst.

4.3.2 Photocatalytic properties for degradation of dyes

The photocatalytic activity of the $BiVO_4$ films were evaluated using the same mass loading of $BiVO_4$ power, based on weight of the coated catalysts on glass after annealing that is 0.5 g/L, in the same photocatalytic reactor set up.

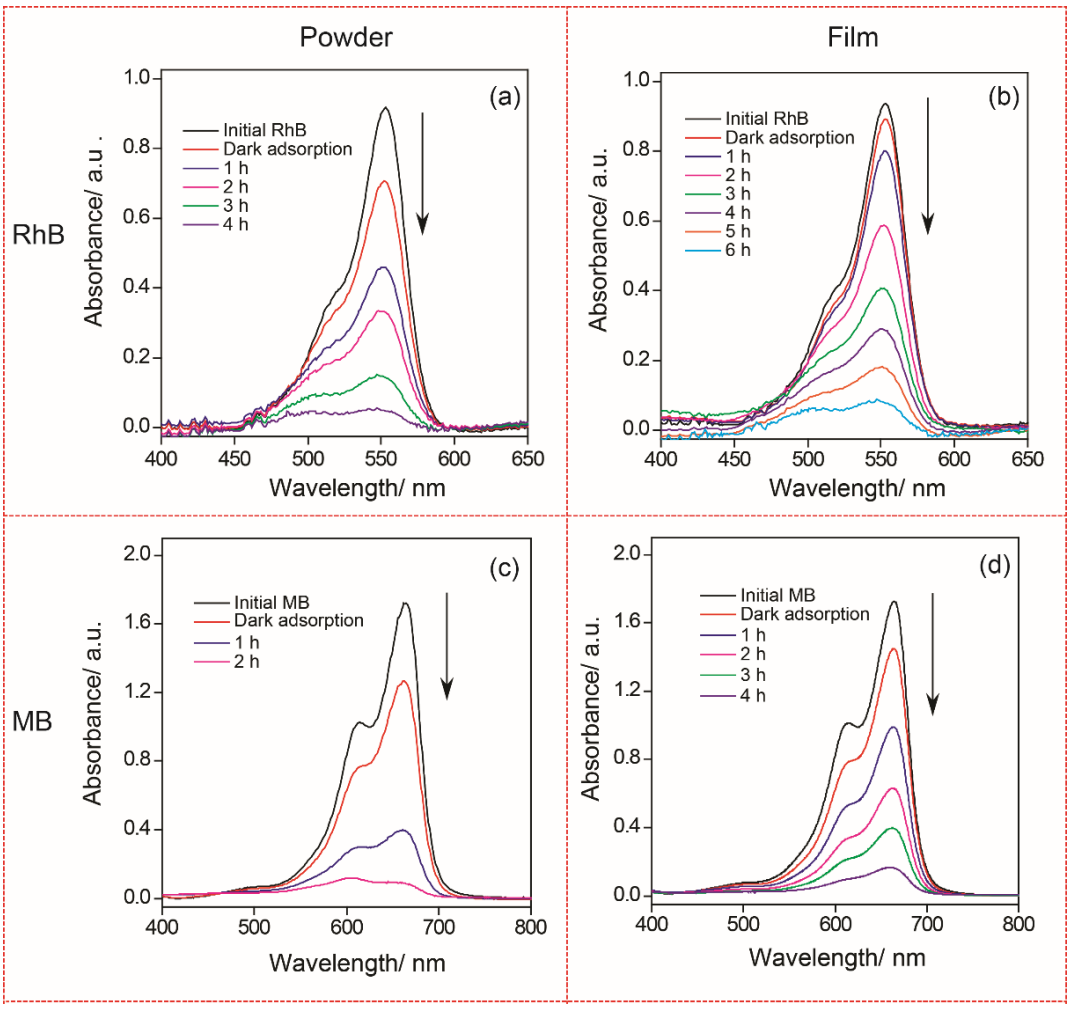

Figure 4.4 UV-vis spectra of dyes under different solar light irradiation times for RhB with (a) $BiVO_4$ powder and (b) $BiVO_4$ film, and visible light irradiation times for degradation of MB with (c) $BiVO_4$ powder and (d) $BiVO_4$ film, respectively.

Quantitative measurements of residual dye concentration were conducted by monitoring the height of the absorption peak at 553 nm for RhB 664 nm for MB dyes. Figures 4.4(a) and 4.4(c) show the adsorption spectra of RhB and MB dyes, respectively. Before photocatalysis testing, the catalyst powder and film were kept in solution (in the dark) overnight in order to attain an adsorption/desorption equilibrium of dyes bound to $BiVO_4$ and in solution. It was found that for both dyes, the loading was significantly higher on the catalyst powder than film. This might be due to the catalyst powder providing higher surface area that catalyst film form confirmed by BET results in Figure 4.3.

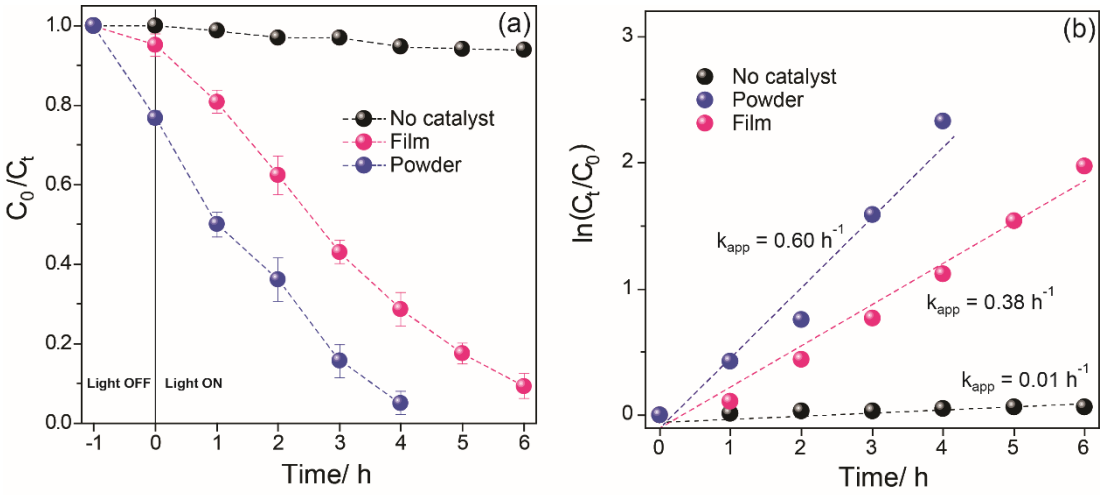

Figure 4.5 Comparison of (a) photocatalytic efficiencies and (b) their kinetic plots ($\ln(C_0/C_t)$ *vs.* t, $C_{ads/des} = C_0$) for degradation of RhB using $BiVO_4$ powder and $BiVO_4$ film under solar light irradiation.

Furthermore, the adsorption spectra of both RhB and MB dyes were decreased when increasing the solar light irradiation time. Obviously, the photodegradation of both dyes with the catalyst powder was faster than with the film form only trace amounts of MB were left after 2 h, whereas the film took nearly 4 h to reach this level. As a comparison, direct photolysis of MB and RhB performed under identical conditions.

As expected, the degradation of dyes (Figure 4.5(a)) appears to show a logarithmic relationship with respect to time, which the photocatalytic degradation rate of RhB can be fitted to the Langmuir-Hinshelwood (LH) kinetic model.[22, 23] By fitting the absorption data with Equation (3.4), as shown in Figure 4.5(b), which assumed that the dye concentration at adsorption/desorption equilibrium ($C_{ads/des}$) equals to the initial concentration of dye (C_0), the photodegradation rate can be determined. It was found that the $BiVO_4$ powder provided the highest photocatalytic activity of 0.60 h^{-1} while the $BiVO_4$ film showed a k_{app} of 0.38 h^{-1}.

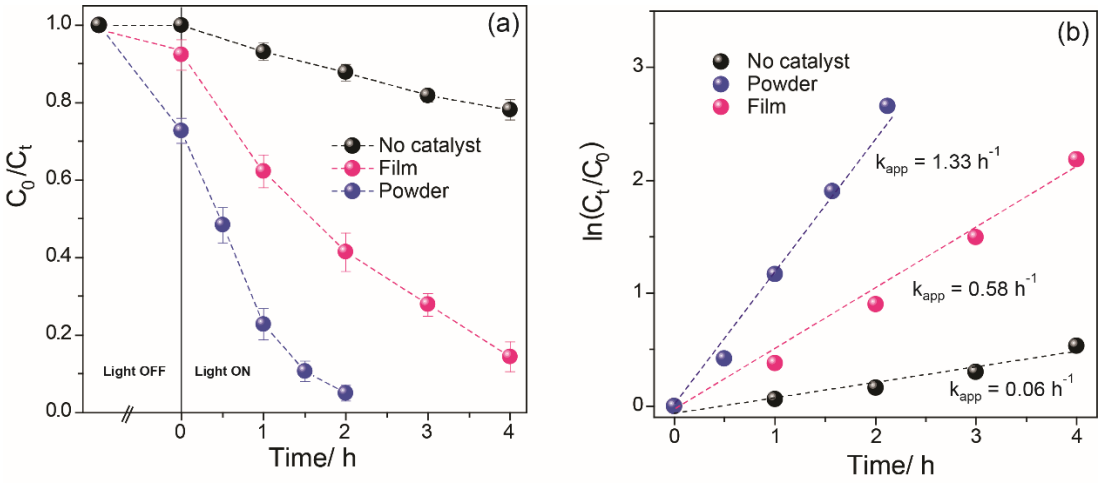

Figure 4.6 Comparison of (a) photocatalytic efficiencies and (b) their kinetic plots ($\ln(C_0/C_t)$ *vs*. t, $C_{ads/des} = C_0$) for degradation of MB using $BiVO_4$ powder and $BiVO_4$ film under visible light irradiation.

Similarly, the photocatalytic activities of $BiVO_4$ powder and film (0.5 g/L) were evaluated by measuring the decolouration of MB dye under visible light irradiation as presented in Figure 4.6(a). After 2 h of visible light irradiation, the MB solution with the $BiVO_4$ powder was colourless, while the MB solution was degraded by the $BiVO_4$ film nearly completed after light irradiation 4 h. It was concluded that the $BiVO_4$ powder also exhibited higher photocatalytic activity for degradation of MB than its film form, which could be attributed to its larger BET surface area. Furthermore, this results was

confirmed by fitting their absorption data to the LH model (Equation 3.4) as presented in Figure 4.6(b), which the pseudo-first order rate for photodegradation of MB using the $BiVO_4$ powder and $BiVO_4$ films were 1.33 h^{-1} and 0.58 h^{-1} respectively. The control sample, illuminated in the absence of a catalyst, showed only 0.06 h^{-1}.

The difference of photodegradation efficiency of MB and RhB dyes is attributed to their adsorption efficiencies. As MB has a cationic configuration, its adsorption would be favored on the negatively charged $BiVO_4$ surface. Although RhB is a cationic, the carboxyl acid group in RB would dissociate with increasing pH, so the dye molecule might be considered as negatively charged ($R–COO^-$).[24, 25] Hence, an electrostatic repulsion effect would take place leading to decreases of the adsorption behavior of RhB molecules on $BiVO_4$ surface, so that photodegradation rate of RhB is lower than of MB. Furthermore, another reason is that RhB is more stable to photolysis than MB, which photocatalysis and photolysis together occur in degradation of MB as confirmed by their no catalyst condition in Figure 4.6(a) and 4.6(b) of MB and RhB, respectively.

4.3.3 Stability and cyclability of catalyst

Stability and cyclability of the $BiVO_4$ catalysts is also important for their practical application. To investigate the recyclability of the catalyst powders and films, the $BiVO_4$ was reused for degradation of RhB and MB dyes under the same experimental conditions cycle length 4 h without any treatment process such as washing or annealing. In Figure 4.7, the comparison of recyclability between the $BiVO_4$ powder and film forms is presented for the two dyes as a function of photodegradation rate (k_{app}) over 5 cycles. After 5 runs, the photocatalytic efficiencies of the $BiVO_4$ film had dropped to 0.20 and 0.43 h^{-1} for degradation of RhB (Figure 4.7(a)) and MB dyes (Figure 4.7(b)), respectively.

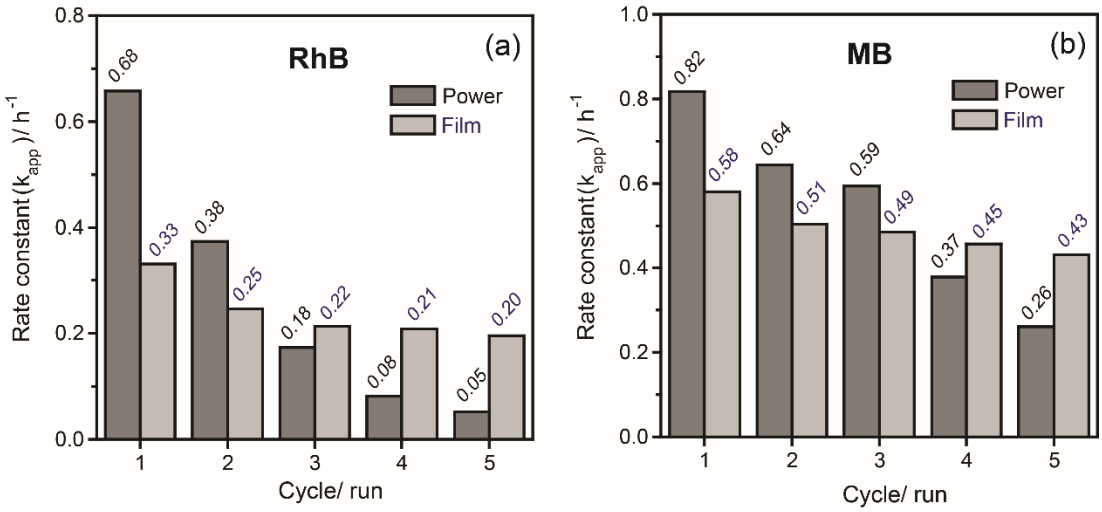

Figure 4.7 Comparison of recyclability between the $BiVO_4$ powder and film forms as a function of photodegradation rate (k_{app}) for (a) RhB and (b) MB dyes over number of cycle runs.

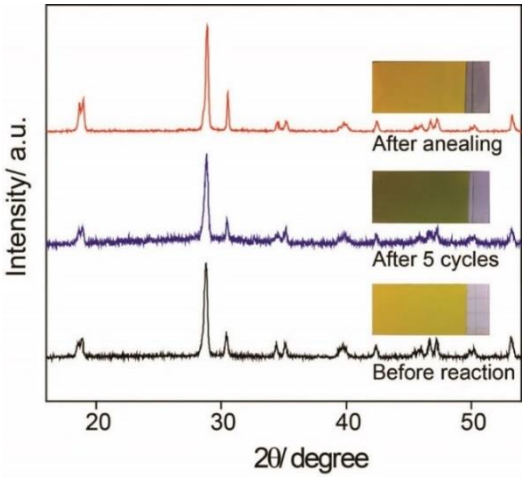

Figure 4.8 Comparison of XRD patterns of the $BiVO_4$ film (a) after annealing at 450°C for 2 h, (b) after using for MB photodegradation and (c) after treatment at 250°C for 2 h.

Under the same experimental condition, the $BiVO_4$ powder, which showed very high photodegradation efficiencies of both dyes for only the first run, decreased substantially. The fifth run k_{app} values of 0.05 h^{-1} and 0.26 h^{-1} for RhB and MB photodegradation, respectively were observed. Obviously, the photodegradation rate

of the film catalyst crossover of the powder catalyst after ~3 cycles. This can be attributed to a loss of the powder photocatalyst due to its incomplete recovery by centrifugation process.

The annealing temperature at 450°C in air was chosen since this temperature help to degrade some organic components in $BiVO_4$ film and provided a good mechanical stability with necking in $BiVO_4$ particles on glass substrate for photocatalytic testing compared to annealing at lower temperatures (250°C and 350°C). Further analysis of the $BiVO_4$ films, after photocatalytic testing over MB degradation, and treatment at 250°C for 2 h by XRD is shown in Figure 4.8. The crystal structure of the $BiVO_4$ film was not obviously change after the photocatalytic reaction (5 cycles), however the XRD pattern of $BiVO_4$ film after photocatalytic reaction is more noise, which correspond to the presence of adsorbed MB dye on film surface. This is seen in the photograph shown in inset Figure 4.8. The XRD pattern of the used $BiVO_4$ film after further treatment at 250°C for 2 h was one again, similar to the sample measured prior to the reaction. However it became slightly stronger, indicating that the crystallinity of the $BiVO_4$ film was slightly higher with the annealing treatment and confirmed by the change of crystallise size from 30 nm (before reaction) to 26 nm (after annealing). Additionally, this treatment also removed the adsorbed MB dye on the $BiVO_4$ film (see the photograph inset in Figure 4.8)

From these cyclability results, it could be concluded that the photocatalytic activity of the reused $BiVO_4$ film showed only a minor change after five cycles, indicating the recovered $BiVO_4$ film were stable and reusable since there was only a slight decrease in RhB or MB degradation efficiency over time. This might come from mechanical damage from turbulent flow and a degradation products blocking the surface (not easily removed). Therefore, catalyst in the film form would be applied to use for all photocatalytic studies in this research, which could be useful for the further real application in water purification.

4.4 Effect of thickness of $BiVO_4$ film

In order to study the effect of the film thickness on the optical properties, $BiVO_4$ films with various thicknesses (0.3–6 μm) were produced by doctor blading with multiple coatings and varying pressures (manual).

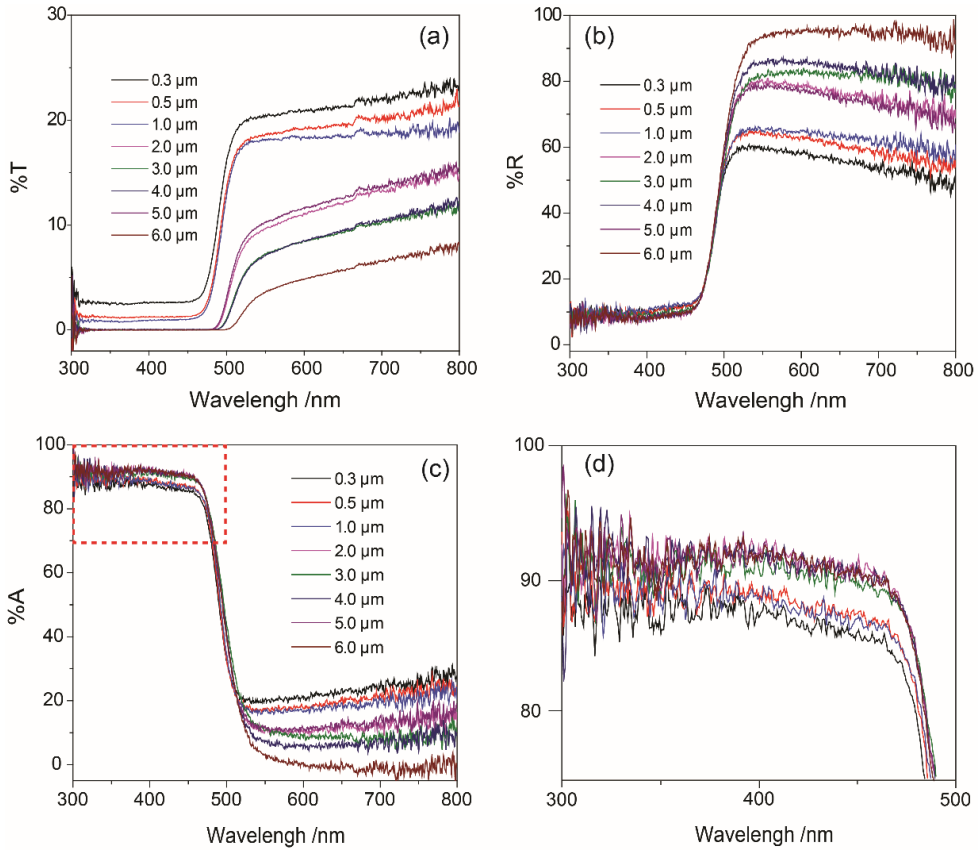

Figure 4.9 UV-vis diffuse (a) transmission, (b) refraction and (c) absorption spectra in the range of 500–800 nm and (d) the interesting area as marked from Figure 3.9(c).

A transmittance, reflectance and absorption spectra of the $BiVO_4$ films with different thickness were measured by an integrating-sphere spectrophotometer as shown in Figures 4.9(a), (b), and (c), respectively. The results showed that light harvesting efficiency in the wavelength between 300 and 500 nm is similar. As Figure 4.9(d), the wavelength more than 550 nm, the thin films (0.3–1 μm) shows a high transmittance and low reflectance, while the thick film (2–6 μm) shows a high reflectance and low transmittance. This suggests that integrating sphere does not account for all light. The

thickness of $BiVO_4$ films in the range of 0.3−6 µm had minimal effect on the optical properties, which this range of film thickness was controlled in the part of photocatalytic study. In this study, the 0.3 µm is minimum thickness of catalyst film because it is difficult to make thinner film (especially with catalyst particle size of 50–80 nm).

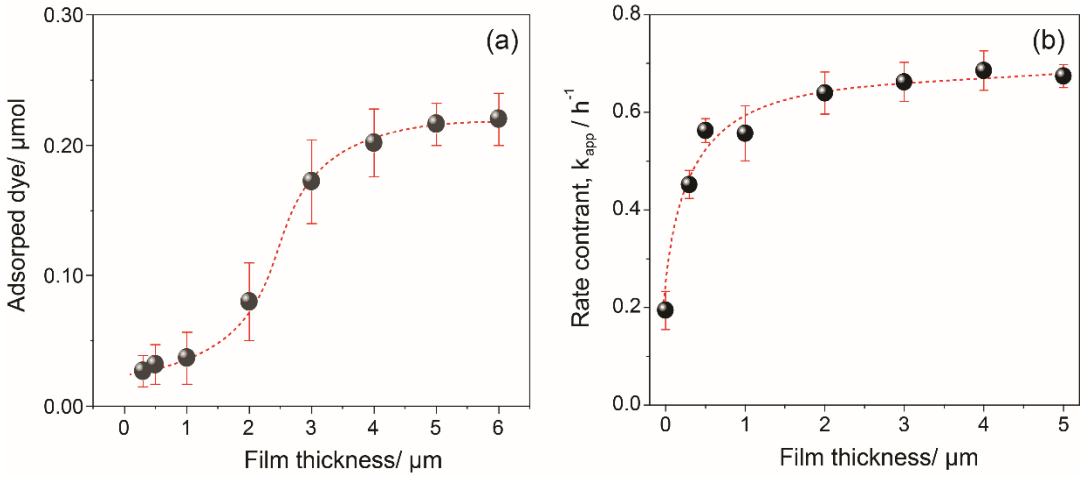

Figure 4.10 Effect of thickness of the $BiVO_4$ film on (a) adsorption efficiency, and (b) photocatalytic degradation of MB (C_0 = 50 µM, 165 mW cm^{-2} of visible light irradiation).

The effect of the thickness of catalyst films on the adsorption and photodegradation of dye were investigated from 0.3−6.0 µm with controlled concentration of MB (50 µM), and light intensity of 165 mW cm^{-2} (visible light), as shown in Figures 4.10(a) and 4.10(b), respectively. The adsorption test in dark was carried out in order to evaluate the adsorption and desorption equilibrium between an adsorbed dyes on catalyst surface. The $BiVO_4$ films with different thicknesses were put in MB solution and kept in the dark condition, then measured the remaining dye concentration by a UV-vis spectrophotometer. Generally, the adsorbed dyes on catalyst films should linearly increase with increasing the film thickness, since the surface area available for dye adsorption increased. However, the amount of adsorbed MB dye in this work, as in Figure 4.10(a), has increased as an S-shaped curve when the film thickness

increased. This is need more experiments such as BET analysis and Thermo-gravimetric analysis to confirm the surface area and amount of adsorbed dye on surface of each catalyst film.

The influence of the thickness of $BiVO_4$ film on the measured rate constant for photodegradation of MB is shown in Figure 4.10(b). As the thickness of the catalyst films increased to 2.0 µm, the rate constant for photodegradation of MB was showed significant improvement. This was probably due to the increase in the thickness of catalyst film which increased in catalyst particles in the area of light irradiation. Further increase of the $BiVO_4$ film thickness resulted in only a slight increase of the photodegradation rate of MB. As the results of dye adsorption properties of $BiVO_4$ film in dark condition in Figure 4.10(a) rise with increasing of the thickness of films, so this means a total surface area of $BiVO_4$ was increased when the thickness increased.[26] Although increasing the film thickness increases the surface area, the amount of light harvested is nearly the same (close to 100% below 520 nm), hence it cannot act as a photocatalyst. This may also explain that not only the high surface area of $BiVO_4$ powder but also more even light distribution in the system leading its high photocatalytic activity for degradation of dyes. Moreover, increasing film thickness with increasing adsorptive dyes on catalyst surface would possibly prevent light harvesting of the catalyst (the adsorbed dye can absorb light instated) leading to decrease of photodegradation rate.[27] Therefore, the thickness of $BiVO_4$ in the range of 2.0–3.0 µm would be used with all photocatalytic studies in this research since above thicknesses provided high photocatalytic degradation of MB and there is manual benefit making film.

4.5 Effect of dye concentration

The effect of various initial concentration of RhB and MB dyes upon their adsorption ability and photodegradation rate were investigated from 5 µM to 100 µM in the

presence of ~2.5 μm film thickness of $BiVO_4$ film (20 mm x 40 mm) and under solar light irradiation (100 mW cm^{-2}).

The adsorption efficiencies of $BiVO_4$ films over RhB and MB dyes are shown in Figures 4.11(a) and 4.11(b), respectively. It was found that the adsorption efficiencies of both dyes decreased when increasing initial concentration dyes from 5 to 50 μM, then slightly decreased with the further increasing of initial concertation from 75 to 100 μM. This results are probably reasonable with the increase in dye concentration, also increasing the amount of dye molecules in system, but surface area of film is the same, hence this does not make further contribution for its adsorption ability.

To study the adsorption behaviour of dyes, the Langmuir and Freundlich adsorption isotherms were used to apply here. The Langmuir isotherm model assumes that the formation of adsorbed dye molecules act as monolayer on surface of catalysts, while the Freundlich isotherm assumes that a multilayer adsorption can be formed.[26, 28]

Figure 4.11(c) shows the relationship between the amounts of adsorbed dye on the surface of catalyst as function of dye concentration that are fitted with the Langmuir and Freundlich adsorption isotherms. The Langmuir and Freundlich adsorption equation are expressed as Equation (4.1) and (4.2), respectively.[26, 28]

$$\frac{C_e}{X_e} = \left(\frac{1}{k_L X_m}\right) + \frac{C_e}{X_m} \quad (4.1)$$

$$\ln X_e = \ln k_L + \frac{1}{n} \ln C_e \quad (4.2)$$

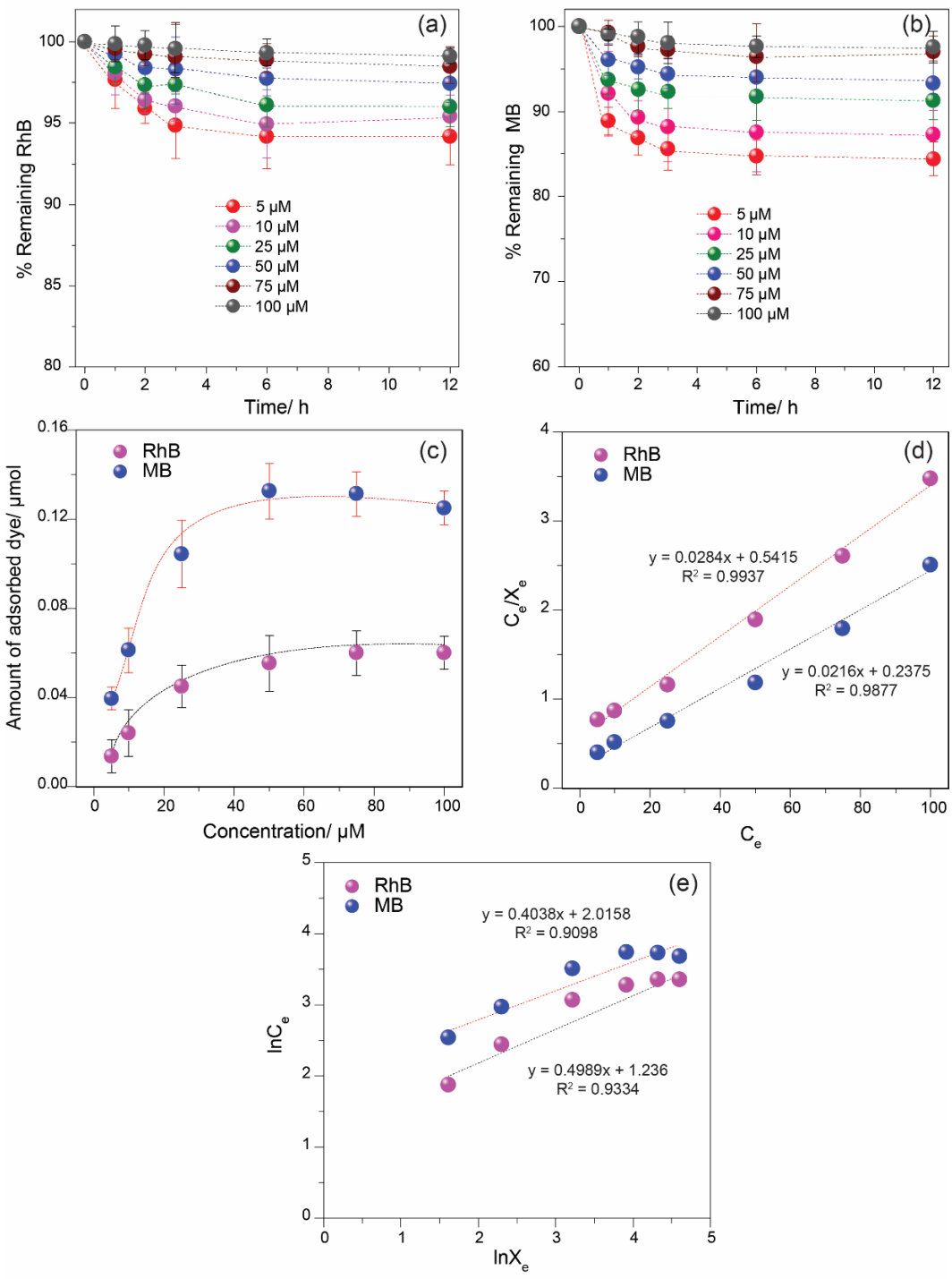

Figure 4.11 The relationship of initial concentration of dyes over the $BiVO_4$ film on adsorption efficiency of (a) RhB, and (b) MB dyes (~2.5 μm film thickness and 100 mW cm^{-2}), (c) adsorption isotherms of RhB and MB on the $BiVO_4$, (d) Langmuir plots for RhB and MB adsorption and (e) Freundlich plots for RhB and MB adsorption.

where, X_e is the amount of adsorbed dye per gram weight of catalysts; C_e is the equilibrium concentration of dye solution; k_L the adsorption constant; X_m the amount of adsorbed dye at saturation; and n is a constant depicting the adsorption intensity.

Table 4.2 The constants and correlation coefficients of Langmuir and Freundlich isotherms for MB and RhB adsorption.

Dyes	Langmuir isotherm			Freundlich isotherm		
	k_L	X_m	R^2	k_L	n	R^2
RhB	0.0525	35.2	0.993	0.291	2.00	0.933
MB	0.0909	46.3	0.988	0.133	2.48	0.910

The evaluated adsorption constants and correlation coefficients from the Langmuir and Freundlich isotherms were summarised in Table 2. It could be seen from Figure 11(d) and 11(e) that the Langmuir isotherm provided better fits than the Freundlich isotherm, which represented that the adsorption of the two dyes on the surface of $BiVO_4$ film was a monolayer adsorption. As the charge of $BiVO_4$ surface is negative, RhB and MB adsorption would be favoured. However, the adsorption through carboxylic groups of RhB would reasonably provide weak (at neutral pH=5.5) electrostatic interactions with the catalyst.[24, 25]

The influence of the initial concentration of RhB and MB dyes to their pseudo-first rate constants of photodegradation are summarised and presented in Figure 4.12. For RhB, high photodegradation rates were observed at the low initial concentrations (less than 25 μM) that the degradation rate was rapidly decreased and then slightly decreased with the further increasing of initial concentration. As similarly result, the photodegradation rate of MB gradually increased when the initial concentration increased from 5 to 50 μM, the photodegradation rate was slower when increasing the dye concentration from 50 to 100 μM. This is probably due to the photodegradation efficiencies of both dyes over the fixed thickness and amount of $BiVO_4$ catalyst film.

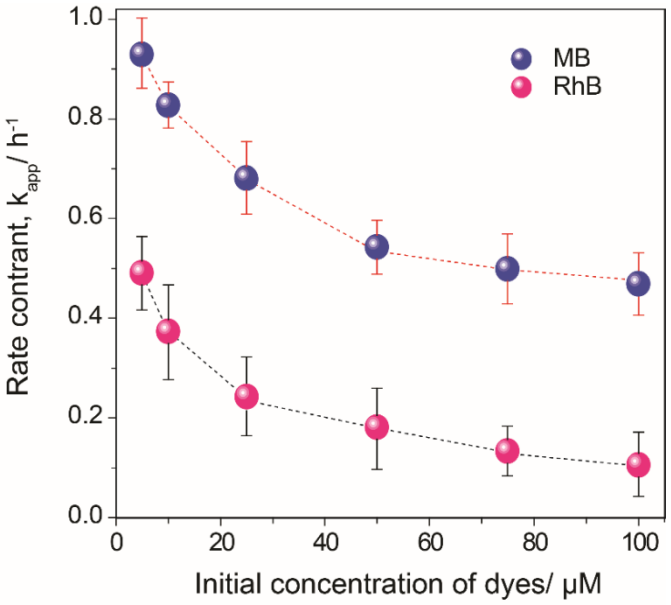

Figure 4.12 The relationship of initial dye concentration over the $BiVO_4$ film on the photoreaction rate (k_{app}) for degradation of RhB and MB dyes (~2.5 µm film thickness and 100 $mW.cm^{-2}$).

Moreover, the increasing of dye concentration will increase the adsorbed dyes on catalyst surface so that the adsorbed oxygen and hydroxyl ion will be decreased. Additionally, the route of photons going into dye solution, which dye molecules might absorb a significant of light irradiation rather than the photocatalyst. This cause a reduced production of hydroxyl and superoxide anion radicals leading to a decrease of photodegradation efficiency. Therefore, the concentration of 25 µM and 50 µM were chosen as the suitable initial concentration of RhB and MB dyes for this research due to their providing good duration to study photodegradation process.

4.6 Effect of solar light intensity

The effect of light intensity from a solar simulator (LCS-100™ ORIEL®) on photodegradation of 25 µM RhB and 50 µM MB dyes was examined using the $BiVO_4$ film (~2.5 µm thickness).

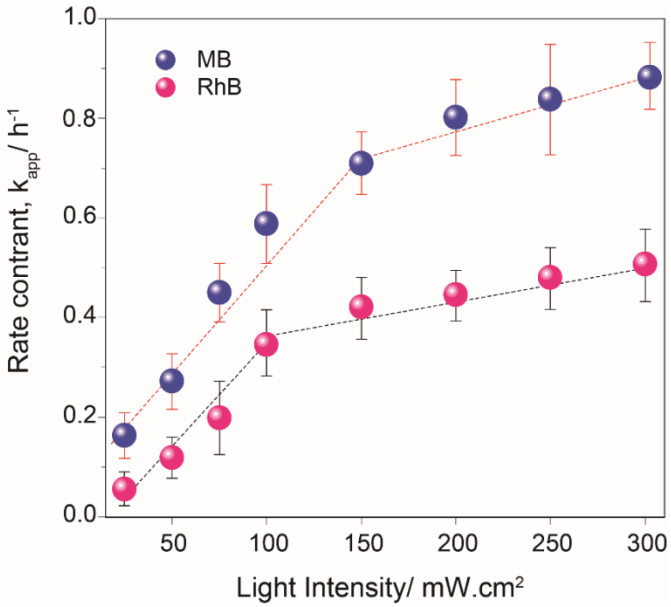

Figure 4.13 Effect of light intensities over the $BiVO_4$ films on photocatalytic degradation of RhB (C_0 = 25 µM) and MB (C_0 = 50 µM).

As Figure 4.13, the results clearly show that the pseudo-first order rate constants for dye photodegradation increase linearly with light intensity up to 100 and 150 mW.cm^{-2} for RhB and MB, respectively and higher intensity (~200 to 300 mW cm^2) this tails off, however does not plateau for MB due to its photolysis. Since the light intensity determines the amount of absorbed by the photocatalyst film. At lower intensity of light irradiation, the amount of photons is not enough to excite the availably active sites of $BiVO_4$ films, hence, insufficient electron and hole pairs are generated on the catalyst surface. Therefore, an increase in the light intensity the photocatalyst absorbs more photons producing more photogenerated electron and hole pairs on the surface of photocatalyst, then this would increase the concentration of active species and consequently increases the photodegradation rate of dyes. However, as increasing the light intensity beyond 100 mW cm^2, the photodegradation rate of MB slightly increased. This suggested that the intensity of about 100 mW cm^2 provided enough photon production for this system with a fixed photocatalyst, and an effect of direct photolysis were observed upon this intensity. This corresponded to the results of

controlled experiment (without catalyst) in Figures 4.5 and 4.6, MB showed high photolysis rate than RhB.

4.7 The effect of reactor volume

In order to study the effect of reactor volume on photodegradation rate of dyes, experiment was carried out by varying the volume of reactor as 10, 20 and 30 mL with the same size of the irradiated side. Concentration of RhB dye, catalyst film thickness average and lamp power were kept constant at 25 µM of RhB, ~2.5 µm, 20 mm x 40 mm and 100 mW cm^{-2}, respectively.

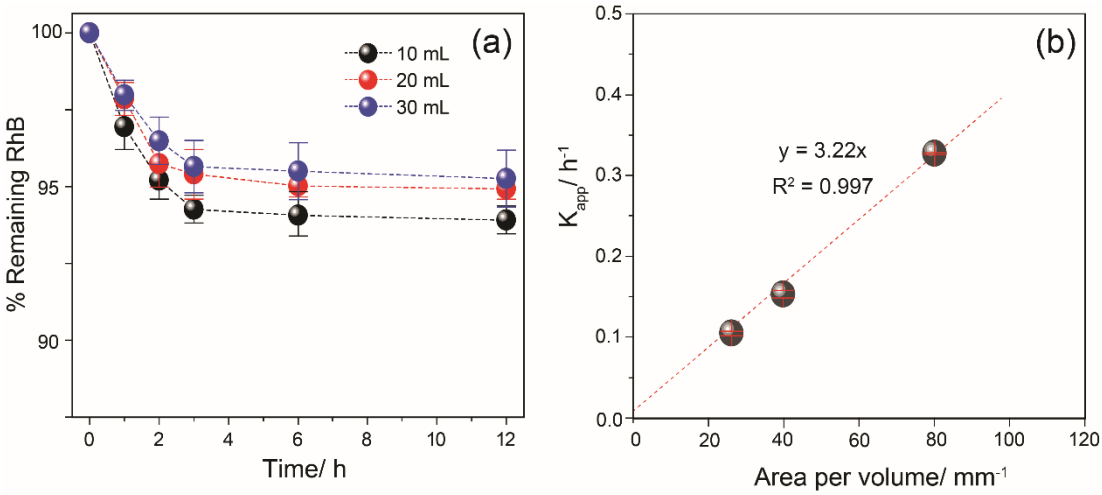

Figure 4.14 The relationship of (a) reactor volume on adsorption efficiency, and (b) on photodegradation rate (k_{app}) with inset the plot of k_{app} and aperture to volume per area ratio, (~2.5 µm $BiVO_4$ film thickness, 100 mW cm^{-2} and 25 µM RhB).

The adsorption efficiency of dye over $BiVO_4$ film is shown in Figure 4.14(a). A slight decrease of adsorption efficiency was observed with increasing of reactor volume. It is because the presence of amount of RhB molecules increases, but the amount of photocatalyst is constant. In contrast, the photodegradation rate of RhB over the $BiVO_4$ film increased with decreasing reactor volume, which was probably due to decrease of light penetration into the dye solution. Furthermore, the relationship of

aperture area per volume ratio (A/V) on the photodegradation rate were calculated and illustrated Figure 4.14(b). It was clearly seen that the increasing of reaction rate and the A/V ratios was attribute to a linear relationship. This means that the reaction rate increases when increasing surface area of dye solution, which can be increasing by decreasing reactor volume and keeping aperture constant. Since, the path length of photons entering the dye solution increases leading to high formation of active species such as hydroxyl radicals. This results agreed well to the literature reported by Klausner and Goswami that the photodegradation rate of 4-chlorophenol depended on A/V ratio, and it increased when increasing in A/V ratio.[29] This suggests that flow through reactor should be flexible, large area to volume ratio, short reaction time, and offer a promising prospect for large-volume production of photocatalytic water treatment with long durability.

4.8 Figures of Merit

The International Union of Pure and Applied Chemistry (IUPAC) has proposed various figures of merit for advanced oxidation processes (AOPs), which can directly use for comparison between different AOPs systems and for a cost estimation in a full scale-up design. For a low pollutant concentration, the appropriate figures of merit based on electric energy consumption is the electrical energy per order (E_{EO}) reported by Bolton *et al.* will apply here.[30] E_{EO} is the electrical energy (kW h) required to reduce the concentration of pollutant in wastewater in a unit volume (L) by one order of magnitude in a time. The E_{EO} (kWh m^{-3}) can be calculated from Equation 4.1:

$$E_{EO} = \frac{P}{V \times k_{app}} \qquad (4.1)$$

where P is the lamp power (kW) of operating system, V is the volume (m^{-3}), and k_{app} is the pseudo first order rate constant (h^{-1}) for degradation of the pollutant concentration. Thus, the lower E_{EO} value means the lower electricity costs will be

required for operating AOPs system. The E_{EO} required to degrade RhB (25 μM) and MB (50 μM) dyes in this system were obtained as 4,286 and 2,875 kWh m^{-3} $order^{-1}$, respectively.

However, in the case of using solar energy (real application), where the cost of incident solar radiation should be zero. Therefore, an illuminated collector area is considered as the main factor so that the suitable figures of merit based on solar energy is the illuminated collector area per order (A_{CO}). The A_{CO} (h m^{-3} sun^{-1}) can be calculated as following equation:

$$A_{CO} = \frac{A_r}{V \times k_{app}} \tag{4.2}$$

where Ar is the illuminated collector area (m^2). The A_{CO} index for this operating system were 105 and 69 h m^{-1} sun^{-1} of photodegradation of RhB and MB dyes, respectively.

4.9 Conclusion

Initial, photocatalytic activity of the powder systems were better than films due to higher surface area, however the cyclibility of the photocatalytic films was superior, leading to better photocatalytic performance after 3–4 cycles. The application of the catalyst in film form helps overcome some of the major technical problems associated with photocatalytic dye degradation, specifically separation of the catalyst particles from suspension by centrifugation, which leads to loss of the catalyst material is both time and energy consuming.

The effects of thickness of film, concentration of dyes, intensity of solar light and reactor volume on the photocatalytic activities of the $BiVO_4$ photocatalyst were studied in this Chapter. Photocatalytic efficiency of the thicker films is better than thin films, but marginal improvement is obtained past 2 μm thick. Dye concentration is a test of the applicability of the Langmuir isotherm for dye adsorption and Langmuir-

Hinshelwood kinetics for dye photodegradation. Concentration of dye and intensity of light are important factors for reactor design. In this system, the suitable concentration of RhB and MB are 25 μM and 50 μM, respectively, and intensity of light 100 mW cm^{-2} is used, where corresponds to standard illumination of one sun. The photocatalytic degradation of dyes over the fixed catalyst film is obtained with reactor volume independent that is a high collector area to reactor volume ratio facilitates a good capture of incident photons. The chosen reactor volume in this work is 20 mL with fixed light collector area. The figure of merit based on electrical energy consumption for photocatalytic degradation of dyes was calculated and the related electricity costs of MB photodegradation was lower than of RhB. Furthermore, in the case of solar photocatalysis, the figure of merit is an illuminated collector area per order indicates a loss in photocatalytic efficiency of dye degradation with increasing value of the collector area per order.

References

1. A. Fujishima, T. N. Rao and D. A. Tryk, *J. Photochem. Photobiol., C*, 2000, **1**, 1–21.
2. A. Fujishima, X. Zhang and D. A. Tryk, *Int. J. Hydrogen Energy*, 2007, **32**, 2664–2672.
3. J. M. Herrmann, *Catal. Today*, 1999, **53**, 115–129.
4. N. Wetchakun, S. Chaiwichain, B. Inceesungvorn, K. Pingmuang, S. Phanichphant, A. I. Minett and J. Chen, *ACS Appl. Mater. Interfaces*, 2012, **4**, 3718–3723.
5. D. K. Ma, M. L. Guan, S. S. Liu, Y. Q. Zhang, C. W. Zhang, Y. X. He and S.M. Huang, *Dalton Trans.*, 2012, **41**, 5581-5586.
6. R. Bajaj, M. Sharma and D. Bahadur, *Dalton Trans.*, 2013, **42**, 6736–6744.
7. A. Yasumori, H. Shinoda, Y. Kameshima, S. Hayashi and K. Okada, *J. Mater. Chem.*, 2001, **11**, 1253–1257.
8. S. Choudhury, R. Sasikala, V. Saxena, D. K. Aswal and D. Bhattacharya, *Dalton Trans.*, 2012, **41**, 12090–12095.
9. R. T. Sapkal, S. S. Shinde, M. A. Mahadik, V. S. Mohite, T. R. Waghmode, S. P. Govindwar, K. Y. Rajpure and C. H. Bhosale, *J. Photochem. Photobiol., B,* 2012, **114**, 102–107.
10. P. Jongnavakit, P. Amornpitoksuk, S. Suwanboon and T. Ratana, *Thin Solid Films*, 2012, **520**, 5561–5567.
11. C. M. Malengreaux, A. Timmermans, S. L. Pirard, S. D. Lambert, J. P. Pirard, D. Poelman and B. Heinrichs, *Chem. Eng. J.*, 2012, **195–196**, 347–358.
12. Y. Zhiyong, E. Mielczarski, J. Mielczarski, D. Laub, P. Buffat, U. Klehm, P. Albers, K. Lee, A. Kulik, L. Kiwi Minsker, A. Renken and J. Kiwi, *Water Res.*, 2007, **41**, 3186.
13. S. K. Bhar, S. Jana, A. Mondal and N. Mukherjee, *J. Colloid Interface Sci.*, 2013, **393**, 286–290.
14. A. Nattestad, M. Ferguson, R. Kerr, Y. B. Cheng and U. Bach, *Nanotechnology*, 2008, **19**, 295304.

15. Z.-F. Huang, L. Pan, J.-J. Zou, X. Zhang and L. Wang, *Nanoscale*, 2014, **6**, 14044–14063.

16. A. K. Bhattacharya, K. K. Mallick and A. Hartridge, *Mater. Lett.*, 1997, **30**, 7–13.

17. A. Kudo, K. Omori and H. Kato, *J. Am. Chem. Soc.*, 1999, **121**, 11459–11467.

18. A. Kudo and Y. Miseki, *Chem. Soc. Rev.*, 2009, **38**, 253–278.

19. J. Zhao, T. Wu, K. Wu, K. Oikawa, H. Hidaka and N. Serpone, *Environ. Sci. Technol.*, 1998, **32**, 2394–2400.

20. R. Li, F. Zhang, D. Wang, J. Yang, M. Li, J. Zhu, X. Zhou, H. Han and C. Li, *Nat. Commun.*, 2013, **4**, 1432.

21. K. Liu, Z. Chang, W. Li, P. Che and H. Zhou, *Sci. China. Chem.*, 2012, **55**, 1770–1775.

22. K. V. Kumar, K. Porkodi and F. Rocha, *Catal. Commun.*, 2008, **9**, 82–84.

23. A. Houas, H. Lachheb, M. Ksibi, E. Elaloui, C. Guillard and J. M. Herrmann, *Appl. Catal., B*, 2001, **31**, 145–157.

24. S. Obregón and G. Colón, *Journal of Molecular Catalysis A: Chemical*, 2013, **376**, 40-47.

25. Y. Na, Y.I. Kim, D. Won Cho, D. Pradhan and Y. Sohn, *Mater. Sci. Semicond. Process*, 2014, **27**, 181–190.

26. W. F. Chen, P. Koshy, B. Zhu and C. C. Sorrell, in *Ceramic Materials for Energy Applications IV*, John Wiley & Sons, Inc., 2014, pp. 51–60.

27. I. Langmuir, *J. Am. Chem. Soc.*, 1918, **40**, 1361–1403.

28. A. Kumar Paul, G. Madras and S. Natarajan, *Phys. Chem. Chem. Phys.*, 2009, **11**, 11285–11296

29. J. F. Klausner, A. R. Martin, D. Y. Goswami and K. S. Schanze, *J. Sol. Energy Eng.*, 1994, **116**, 19–24.

30. J.R., Bolton, K.G. Bircher, W. Tumas, C.A. Tolman, *Pure Appl. Chem.,* 2001, **73**, 627–637.

CHAPTER 5

MICROWAVE SYNTHESIS OF BISMUTH VANADATE NANOPARTICLES FOR PHOTOCATALYSIS

5.1 Introduction

As mentioned in the literature review (Chapter 1), various synthetic methods such as solid-state reactions,[1, 2] precipitation reactions,[1-5] sol-gel processes,[6-8] and hydrothermal methods[9-12] have previously been employed to prepare $BiVO_4$ powder.

Apart from the hydrothermal methods a high-temperature, calcination is usually required to crystallise the structure. Thus, hydrothermal treatments have become popular for the preparation of crystalline metal oxide semiconductors in a single step, without any post processing requirements. Furthermore, crystal structure, size and particle morphology of the metal oxide semiconductor can be controlled by solvent, precursor composition, temperature and pressure. Note well: Teflon lined stainless steel is the most common design, but other do exist. However, the preparation of crystalline metal oxide nanoparticles through these hydrothermal methods has some disadvantages such as (1) the fact that it requires high temperatures (more than 100°C) and pressures (5 kbar),[13] (2) it is limited to batch processing, (3) there are difficulties in achieving uniform size, (4) requiring a long reaction time, and (5) the impossibility of observing the reaction in the reactor. Therefore, microwave synthesis has been studied to prepare the $BiVO_4$ nanoparticles and counteract the above mentioned issues in this research.[14]

The definition of “Microwave irradiation” is electromagnetic radiation with frequency in the range of 0.3 to 300 GHz corresponding to wavelengths of 1 m down to 1 mm in air.[15, 16] The most commercial microwave systems for chemical synthesis operate at

a frequency of 2.45 GHz (1.0×10^{-5} eV) to avoid the frequency of direct water heating.[15] This energy is lower than Brownian motion and much too low to cleave chemical bonds, only affects molecular rotations.[16]

In inorganic chemistry, the microwave synthesis can be defined as a method of synthesis of single crystals that depends on the solubility of minerals in hot solvent under microwave irradiation, which provides uniform heating in the reactor, this energy is more likely to be transferred to ionic species (such as precursor salts).[15, 17] These ionic molecules oscillate and quickly collide with their neighbouring molecules allowing an enhanced reaction rate compared to if other heating mechanism employed. This can be modelled according to an Arrhenius equation as follows, ($k = A_{exp}\ (-E_a/RT)$),[15] where microwave energy increases the pre-exponential factor (A_{exp}) or the activation energy (E_a) associated to the reaction rate (k) at temperature (T) and gas constant (R).[15] Thus, this microwave synthesis only accelerate nucleation and crystal growth processes by heating materials, but cannot directly induce chemical reactions such as photochemistry process.

The heating mechanism of microwaves includes two processes, dipolar polarisation (solvent) and ionic conduction (precursor). In the dipolar polarisation mechanism, the applied microwave irradiation provides the energy for rotations of polar molecules (such as water), consequently heating the medium as energy loss.[16, 18]

Similarly, in ionic conduction mechanism, the ionic molecules oscillate by the influence of microwave irradiation so well that there is no random motion generated, and then they collide with neighbouring molecules, creating heat.[16, 18] However, the ionic conduction mechanism is a much stronger interaction than dipolar polarization mechanism causes providing higher heat generation.[16]

The loss tangent (tan d), the ratio of the dielectric constant to dielectric loss provides a measure for the ability of a material to convert electromagnetic energy into heat at

a given frequency and temperature. Therefore, a high loss factor will give a high tan d value, which is required for efficient absorption and rapid heating in synthetic processes. Generally, solvents can be classified as high (tan d > 0.5), medium (tan 0.1< d <0.5), and low microwave absorbing (tan d < 0.1) solvents.[15-18] In spite of having a medium tan d (0.123), water was used as solvent in this research.

In recent years, there have been four reports on the synthesis of $BiVO_4$ using a microwave: In 2008, Zhang *et al*. reported that pure tetragonal and monoclinic $BiVO_4$ were synthesised by a rapid microwave-assisted method from $Bi(NO_3)_3$ and $NaVO_3$ with different microwave irradiation time and power.[14] Tetragonal $BiVO_4$ with small particle sizes or monoclinic $BiVO_4$ with highly crystallised and large sheets was observed after 10 or 40 min irradiation time, respectively with mixed results for intermediated time. The photocatalytic rate of RhB degradation with the various $BiVO_4$materials increased with increasing content of the monoclinic phase. Shi *et al*. synthesised $BiVO_4$ nanocrystal photocatalyst using $Bi(NO_3)_3$ and NH_4VO_3 as precursors with the operating power of 800W and temperature of 100°C for 5 h.[19] These results showed that they have a strawberry-like structure with 5 nm particles scattered on the 200 nm particle surfaces and photocatalytic activity exhibited excellent in degradation of ciprofloxacin under visible light irradiation. Recently, Zhang *et al.* synthesised monoclinic $BiVO_4$ micro-/nanostructures with different sizes and morphologies via a combination of microwave and ultrasonic techniques.[20] The mixture $Bi(NO_3)_3.5H_2O$ and NH_4VO_3 in diethylene glycol and deionized water was heated to 110°C for 27 min under the microwave irradiation power at 500 W and the ultrasonic irradiation power at 800 W (two second sonication and one second interruption). The results showed that the solvent and pH value had a significant influence on morphology, size and crystalline structure of the product. In addition, monoclinic $BiVO_4$ nanoparticles with small crystal exhibited high photocatalytic activity for degradation of Rhodamine B (RhB).

Microwave synthesis of other semiconductor metal oxides have also been reported due to its advantages especially in short processing time. In generally, a metal salt and an additive in aqueous solution were used as the metal source and the product morphology and size control, respectively for preparation of metal oxide nanostructures by microwave synthesis. Some examples of metal oxides prepared by the microwave method include ZnO,[21, 22] SnO_2,[23] Fe_2O_3,[24, 25] Fe_3O_4,[24, 26] TiO_2,[27-29] CuO,[30] and MnO_2.[31]

In this research, a solution phase synthetic method using a single step microwave process with power less than 300 W was developed. The physical properties of $BiVO_4$ synthesised by this method along with those produced by hydrothermal and precipitation methods were compared. In particular, the photocatalytic performances of the products from those methods were investigated through monitoring RhB and Methylene Blue (MB) degradation under simulated sun light illumination. Furthermore, to improve the photocatalytic performance, electrophotocatalysis for degradation of both dyes over the $BiVO_4$ synthesised by microwave method was studied.

5.2 Experimental section

$BiVO_4$ nanoparticles were prepared by an aqueous-microwave synthesis using an advanced microwave system (APEX, China) as shown in Figure 5.1 with control over power, time and temperature programming. The photographs of microwave apparatus (left) and the reactor (right) used in this is presented in Figure 5.1. The setup consists of (1) a multimode microwave magnetron (APEX), (2) a stirring system, (3) two inert gas (Ar or N_2) flowing tubes, (4) a water cooling condenser, (5) a thermocouple, (6) a funnel for adding precursor or adjusting pH, (7) a parameters setup screen, and (8) CCTV system to observe the reaction inside the microwave oven.

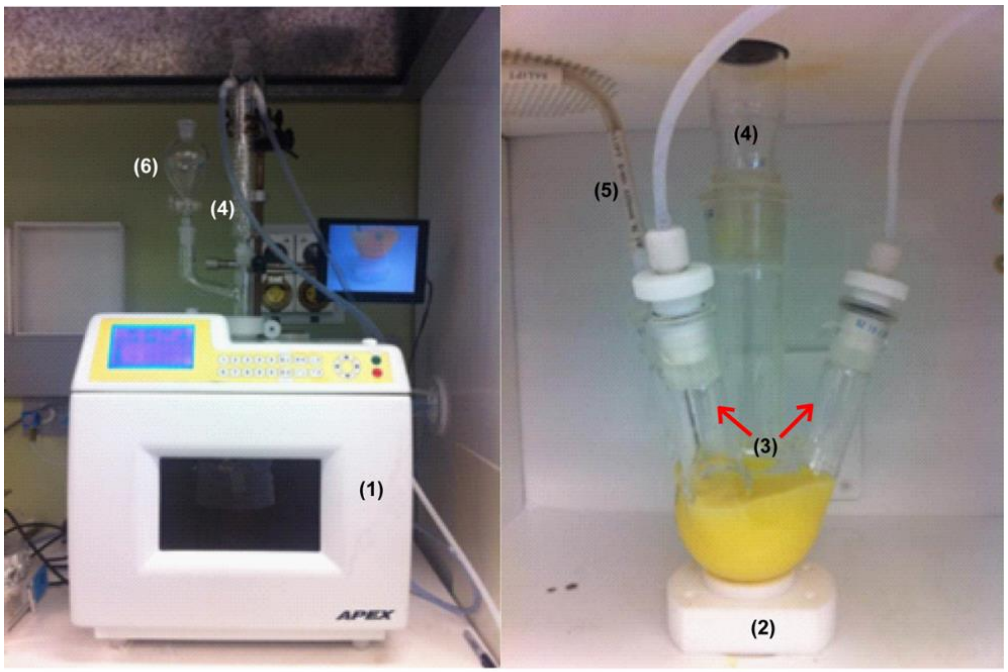

Figure 5.1 Photographs of (Left) microwave heating system setup; (1) a microwave magnetron, (2) a stirring system, (3) two inert gas flowing tubes, (4) a water cooling condenser, (5) a thermocouple, and (Right) reactor in microwave box; (6) a funnel for adding solution, (7) a parameters setup screen, and (8) CCTV system.

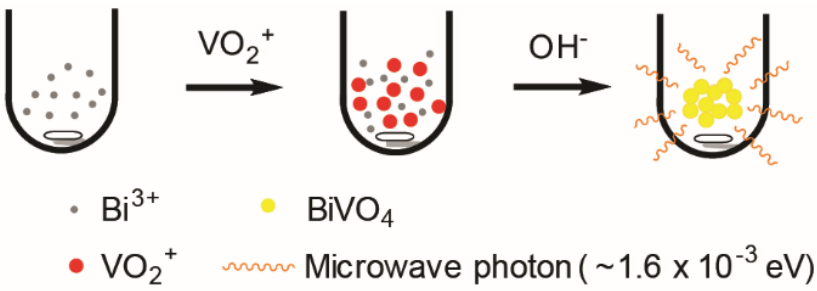

Figure 5.2 Schematic illustration of microwave synthesis of $BiVO_4$ nanoparticles.

As shown in Figure 5.2, 0.125 M each of precursors were separately prepared by dissolving each of $Bi(NO_3)_3{\cdot}5H_2O$ and NH_3VO_4 in 1 M nitric acid respectively. Briefly, the bismuth nitrate solution was transferred to a reactor (Quartz glass, 100 mL), then vanadium precursor was added into this bismuth solution, and 3 M ammonium

hydroxide solution was slowly added until the desired pH was attained (1, 3, 5, 7, 9 or 12). The above mixture was stirred under a maximum power of 300 W microwave irradiation with different temperature (60°C or 90°C) and holding time (5, 15, 30 or 60 min), after which it was allowed to cool to room temperature. Then the resultant precipitate was washed with deionized water, centrifuged and dried at 60°C for 12 h.

For comparison, $BiVO_4$ powder was synthesised by hydrothermal and precipitation methods form the same precursors and reaction temperature. For hydrothermal $BiVO_4$ synthesised, the above mixture of precursor solution was adjusted using the ammonia solution until the pH was 7 before being transferred to Teflon-lined stainless autoclave reactor and then treated at 90°C for 1 h (HT-60-90-7) or at 120°C for 6 h (HT-360-120-7). The precipitation method was conducted at 90°C for 1 h (PC-60-90-7) and at room temperature with a subsequent calcination at 450°C for 2 h (PC-120-450-7). Both of these alternate synthetic methods were employed with optimal conditions for photocatalytic performances, as reported previously.[32, 33]

The physical properties of the $BiVO_4$ photocatalysts from above three methods were compared and carried out by X-ray diffraction (XRD), Raman spectroscopy, scanning electron microscope (SEM), transmission electron microscopy (TEM), Brunauer-Emmett-Teller (BET) analysis and UV-visible spectrophotometry. For electrochemical and photoelectrochemical properties, cyclic voltammetry (CV) and Mott-Schottky analysis were carried out in a three electrode set up as mentioned in Chapter 3. The synthesised $BiVO_4$ powder was coated FTO as working electrode, a Pt-wire as counter electrode, and Ag/AgCl was used as reference electrode. Furthermore, the photocatalytic and electrophotocatalytic tests of the $BiVO_4$ synthesised by this microwave method were also compared and studied though degradation of both dyes RhB and MB solutions under the illumination of AM 1.5 G (one sun), which all synthesised photocatalysts were fabricated into films by doctor blading technique as also described in Chapter 3.

5.3 Influence of precursor solution pH on physical and photocatalytic properties of microwave synthesised $BiVO_4$

5.3.1 Physical characterisation of $BiVO_4$ powder

The first parameter optimised in the microwave synthesis was the pH value of reaction solution. An aqueous solution of ammonium hydroxide was employed to adjust the pH values to 1, 3, 5, 7, 9 or 12, in order to produce MW-60-90-1, MW-60-90-3, MW-60-90-5, MW-60-90-7, MW-60-90-9 and MW-60-90-12, respectively. These reactions were all completed at a temperature of 90°C (>300 W) with a duration of 60 min. The temperature for the microwave synthesis was set to 90°C to avoid boiling the aqueous solutions.

The morphologies of the microwave synthesised $BiVO_4$ powder with various pH value were investigated by SEM, as shown in Figure 5.3. In Figure 5.3(a), the SEM image of MW-60-90-1 sample shows $BiVO_4$ microspheres composed of small irregular nanoparticles and some irregular polyhedra. The obtained microspheres had an average diameter of 3.8 μm, while the smooth surfaced polyhedra were ~1.5 μm. As shown in Figure 5.3(b), the morphology of MW-60-90-3 sample was predominantly large (~300 nm) plates with rough surfaces. Given that analysis of the XRD patterns suggested the crystal size to be ~61 nm. It can be assumed that each of these is comprised of a number of highly aggregated crystals. The aggregates in MW-60-90-5, MW-60-90-7, MW-60-90-9 and MW-60-90-12 were quite different from those of MW-60-90-1 and MW-60-90-3. The MW-60-90-5 sample (Figure 5.3(c)) contained mixture of larges spheres and small spherical particles with average size of 120 nm and 50 nm, respectively. Small spherical particles, in the range of 50–80 nm, are also seen in the SEM images of both MW-60-90-7 (Figure 5.3(d)) and MW-60-90-9 (Figure 5.3(e)). The average particle size of MW-60-90-12 (Figure 5.3(f)), was however once

again quite large. Here it can clearly be seen that these particles are aggregates, composed larger irregular particles with diameters of about 250 nm.

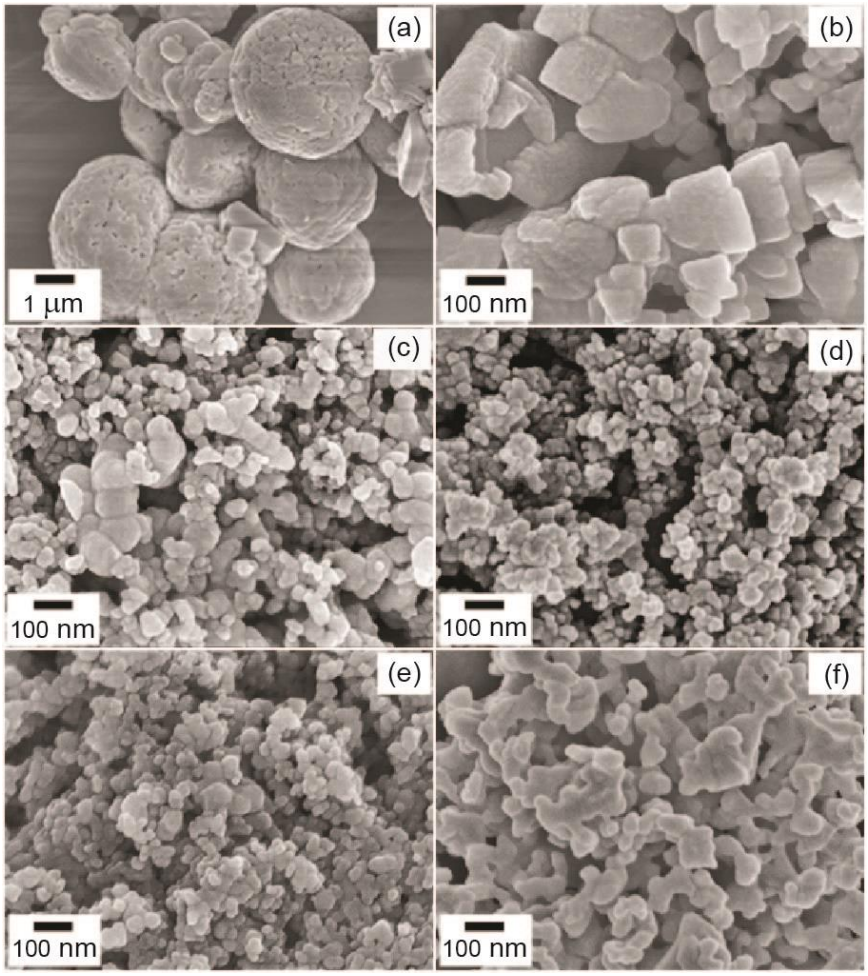

Figure 5.3 SEM images of $BiVO_4$ powder synthesised by the microwave method as a function of pH values: (a) MW-60-90-1, (b) MW-60-90-3, (c) MW-60-90-5, (d) MW-60-90-7, (e) MW-60-90-9 and (f) MW-60-90-12 at 90°C (>300 W) for 60 min.

Crystal structures of the $BiVO_4$ synthesised by microwave irradiation with different pH values were investigated by a GBC MMA XRD (λ = 0.154 nm) with Cu K_α radiation in the range of 10−70° as shown in Figure 5.4. The diffraction peaks of monoclinic $BiVO_4$ were located at 2θ = 28.8°, 30.55°, 34.5°, 35.2°, 39.8°, and 42.5°, corresponding to (112), (004), (200), (020), (211), and (015) planes of monoclinic $BiVO_4$ (JCPDS No. 75-1866, space group: *I2/b*, unit cell parameters: *a* = 5.194 Å, *b* = 5.090 Å, *c* = 11.697

Å, γ = 90.39°), respectively, which was crystallised as main structure for all of the as-synthesised $BiVO_4$ samples.

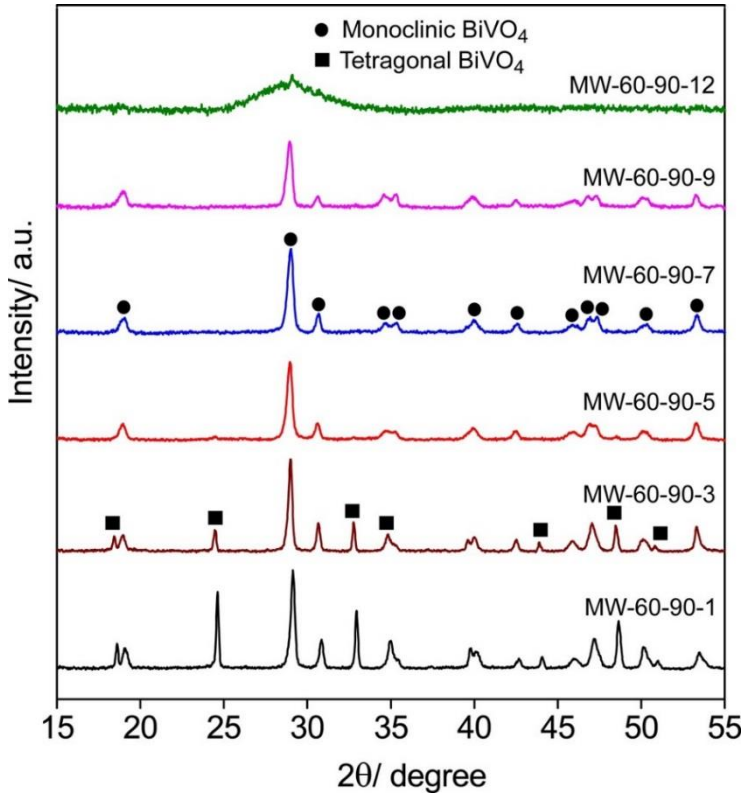

Figure 5.4 XRD patterns of pure $BiVO_4$ powder synthesised by microwave process at different pH value, prior to calcination.

The XRD patterns for MW-60-90-7 and MW-60-90-9 samples exhibited a single phase of the monoclinic $BiVO_4$. However, at pH lower than 7 (MW-60-90-1, MW-60-90-3 and MW-60-90-5), a mixture of tetragonal (JCPDS no. 14−0133, space group: *I41/amd*, unit cell parameters: *a* = 7.300 Å, *c* = 6.457 Å) and monoclinic phases was observed with the proportion of the tetragonal phase decreased with increasing pH. For the MW-60-90-12 sample, no signals of crystalline diffraction peaks were observed in the XRD pattern demonstrated an amorphous characteristic. This is possibly due to a strong dissolution ability of ammonium hydroxide that affect to phase transformation from tetragonal to monoclinic phases via a dissolution-recrystallization process.[34, 35]

The volume percentage (Equation 3.7) of the monoclinic phase and average crystalline size (determined by Scherrer equation, Equation 2.8) of the $BiVO_4$ powder are summarised in Table 5.1. It was found that with acidic conditions mixed phases of monoclinic and tetragonal $BiVO_4$ were produced with relatively coarse microstructure. Increasing the pH to 7 yielded a single phase of monoclinic $BiVO_4$ with nano-size spherical particles. The crystallinity of monoclinic $BiVO_4$ decreased and become amorphous at more basic condition (pH more than 9). Moreover, the sharpness of diffraction peaks became and the intensities decreased gradually when the pH value increased from 3 to 12, indicating lower crystallises formed corresponding to the calculated crystal sizes of the $BiVO_4$ samples from the Scherrer equation.

Table 5.1 The relationship between final pH values for synthesis of $BiVO_4$ powder with percentage of monoclinic $BiVO_4$ phase ($\%V_{mono}$), crystalline size (Scherrer equation) and particle size from SEM images.

Samples	$\%V_{mono}$	Crystallite size (XRD, nm)	Particles size (SEM, nm)	$I_{(011)}/I_{112}$	$I_{(004)}/I_{112}$
MW-60-90-1	56	61	3800	0.234	0.309
MW-60-90-3	80	66	300	0.186	0.325
MW-60-90-5	90	50	80–100	0.209	0.216
MW-60-90-7	100	47	30–60	0.212	0.252
MW-60-90-9	100	46	50–80	0.188	0.254
MW-60-90-12	Amorphous	-	200–300	-	-

The relative intensities of (011)/(112) from XRD results (Table 5.1), spherical particles were 0.252. Obviously, the sheet-like $BiVO_4$ synthesised at 3 by the microwave method (Figure 5.3(c)) provided higher the (004)/(112) relative intensity of 0.325. It was found that the growing orientation of (011) and (004) planes are clearly associated with the rod-like and sheet-like morphologies of monoclinic $BiVO_4$, respectively, which crystal growing of the spherical particle probably has similarly relative intensities of both planes as seen in the synthesised $BiVO_4$ at pH 7.

Raman spectroscopy provided further information on the local structure of the $BiVO_4$ powder after synthesis by microwave processing, as shown in Figure 5.5. The Raman bands at 320, 367, 637, and 820 cm^{-1}, observed for each of the $BiVO_4$ samples, were characteristic bands of monoclinic $BiVO_4$ similarly to the reports by Gotić *et al.*[3] and Zhang *et al*..[14] The Raman band at 210 cm^{-1} could be assigned to the external modes (rotation/translation) of $BiVO_4$. The bands at 320 and 367 cm^{-1} were attributed to the asymmetric and symmetric V–O bending modes of the VO_4 tetrahedron, respectively. The bands at 637 and 820 cm^{-1} were ascribed to asymmetric and symmetric V−O stretching modes, respectively.

For MW-60-90-3 and MW-60-90-5, not only the Raman bands of monoclinic $BiVO_4$ observed, but also were the three bands of tetragonal $BiVO_4$ appeared at 398, 517 and 831 cm^{-1}.The bands at 398 and 517 cm^{-1} were attributed to the antisymmetric and symmetric V–O bending modes, respectively as reported by Zhang *et al*.[14] The shift from 820 cm^{-1} to 831 cm^{-1} for the main band of monoclinic $BiVO_4$, were described as the symmetric V–O stretching mode, which was also reported by Obregón *et al*..[36]

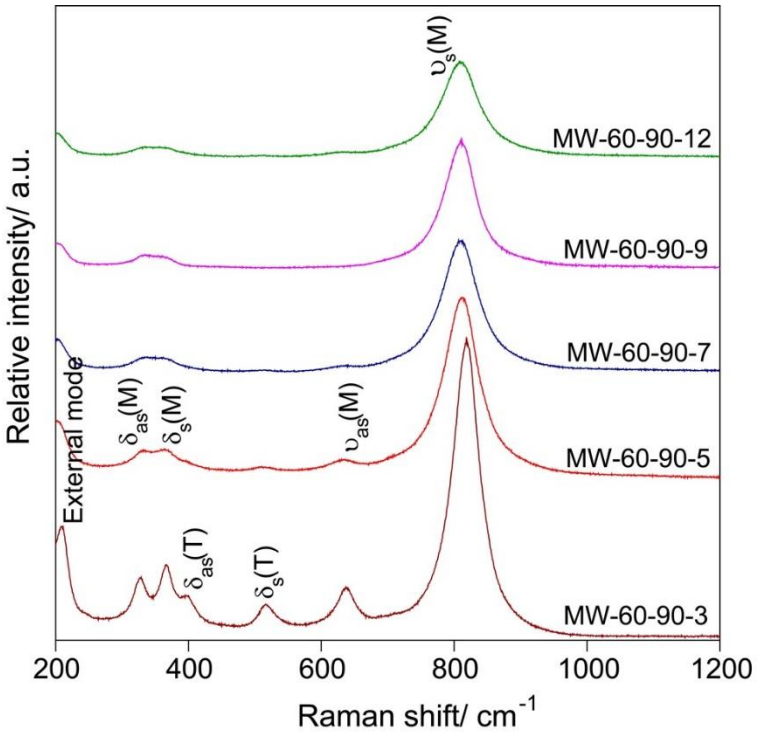

Figure 5.5 Raman spectra of pure $BiVO_4$ powder synthesised by microwave process at different pH values.

Moreover, in the result from Figure 5.5 it was observed that the intensity of the Raman bands for the mixed phases of tetragonal and monoclinic $BiVO_4$ (MW-60-90-3 and MW-60-90-5) were stronger than that of the single phase of monoclinic $BiVO_4$ (MW-60-90-7, MW-60-90-9 and MW-60-90-12) due to the percentage of the monoclinic phase in the $BiVO_4$ at MW-60-90-3 and MW-60-90-5 being 80% and 90%, respectively. Additionally, the intensity of Raman spectra decreased when the percentage of monoclinic increase corresponding with the percentages of monoclinic increased with increasing pH value. Compared to XRD results (Figure 5.4), it could be assumed that Raman spectroscopy is more sensitive to the presence of the tetragonal $BiVO_4$ in the mixture of both monoclinic and tetragonal phases.[14, 32, 37]

From XRD and SEM results, it should be noted that all of the synthesised $BiVO_4$ powder by microwave method obtained different crystalline, morphologies and particle sizes, which were formed simply by changing the pH of the synthesis.

Therefore, the pH of the microwave synthesis is clearly an important impact on crystalline, morphologies and particle size of $BiVO_4$ powder.

In this experiment, based on a one-pot reaction, probable mechanism growth mechanism of $BiVO_4$ nanoparticles could be explained by the amount of the generated nuclei, which depends on the adjustment of pH with ammonium hydroxide solution (NH_4OH), and remaining precursors introduced into the reaction environment. The proposed mechanism could be explained together with the reaction processes as follow (Equations 5.1–5.3).[17, 35, 38, 39]

$$Bi(NO_3)_3 + H_2O \longrightarrow BiO(NO_3) + 2H^+ + 2NO_3^- \quad (5.1)$$

$$2NH_4VO_3 + 4HNO_3 \longrightarrow 2VO_2^+ + 4NO_3^- + 2NH_4^+ + 2H_2O \quad (5.2)$$

$$BiO(NO_3) + VO_2^+ + OH^- \longrightarrow BiVO_4 + NO_3^- + H^+ \quad (5.3)$$

When the precursor solutions were mixed together, no precipitate was observed. After NH_4OH was slowly added to the mixture (to give final pH of 1, 3, 5, 7, 9 and 12) and irradiated by microwave, $BiVO_4$ precipitates with different of crystal structures and morphologies were obtained as Equation 5.3. Regarding to the reported by Tan *et al.*[35], the monoclinic $BiVO_4$ polyhedral was firstly formed before adjusting pH, and after adding NH_4OH this the monoclinic $BiVO_4$ then suddenly dissolved and transformed to be tetragonal $BiVO_4$ microspheres by recrystallization process. Hence, a mixture of $BiVO_4$ monoclinic polyhedral and tetragonal $BiVO_4$ microsphere was obtained at pH 1. However, when increasing higher than 1 the higher OH^- concentration gradually forces all the tetragonal $BiVO_4$ microspheres again to dissolve and recrystallise to monoclinic $BiVO_4$ with small grains. This trend continued with increase pH, with nucleation rate increasing hence the pure monoclinic $BiVO_4$ nanoparticles was obtained at pH 7. At highly basic condition (pH 12), it was assumed that the $BiVO_4$ nanoparticles gradually dissolved, and finally enabled amorphous phases ($Bi(OH)_3$)

to be formed as an irregular dendritic morphology. Thus, the synthesised $BiVO_4$ at pH 7 appeared to be optimal for the formation of a single monoclinic phase and nano-size particles with large surface area under the microwave conditions tested.

5.3.2 Physical characterisation of $BiVO_4$ films

In this study, films made from the $BiVO_4$ powder synthesised at different pH by microwave process were fabricated in film form by a doctor blading technique on glass substrates. Figure 5.6 shows pictures of $BiVO_4$ films after annealing at 450°C for 1 h in air.

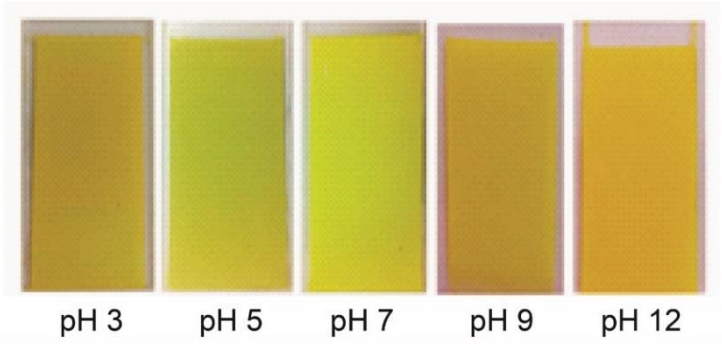

Figure 5.6 Photographs of the $BiVO_4$ films synthesised at different pH on plain glass substrates after being fired at 450°C for 2 h.

Figure 5.7 shows the XRD patterns of the $BiVO_4$ films fabricated on glass substrates by doctor blading, using the above synthesised $BiVO_4$ powders and annealed at 450°C for 2 h. As clearly seen from the XRD patterns, the tetragonal phase, previously observed in MW-60-90-3 and MW-60-90-5 is transferred to the monoclinic $BiVO_4$ after annealing at 450°C for 2 h. The calculated percentage of the monoclinic phases is shown in Table 5.2. For MW-60-90-12 film, the peaks of monoclinic $BiVO_4$ could be seen along with the peaks of tetragonal $BiVO_4$, bismuth oxide (Bi_2O_3, JCPDF no. 41–1449), and indicating that after annealing at 450°C for 2 h this amorphous sample was converted to the mixture of tetragonal $BiVO_4$, monoclinic $BiVO_4$ and Bi_2O_3.

However, the XRD peaks of monoclinic $BiVO_4$ in this mixed phases slightly shifted towards a lower angles. This observation showed that transformation of the monoclinic phase was not complete from the tetragonal phase during cooling temperature process it is assumed that at 450°C the amorphous $BiVO_4$ was firstly transferred to a tetragonal form (orange in colour) and then converted to a monoclinic phase when cooled (yellow in colour).[1, 34]

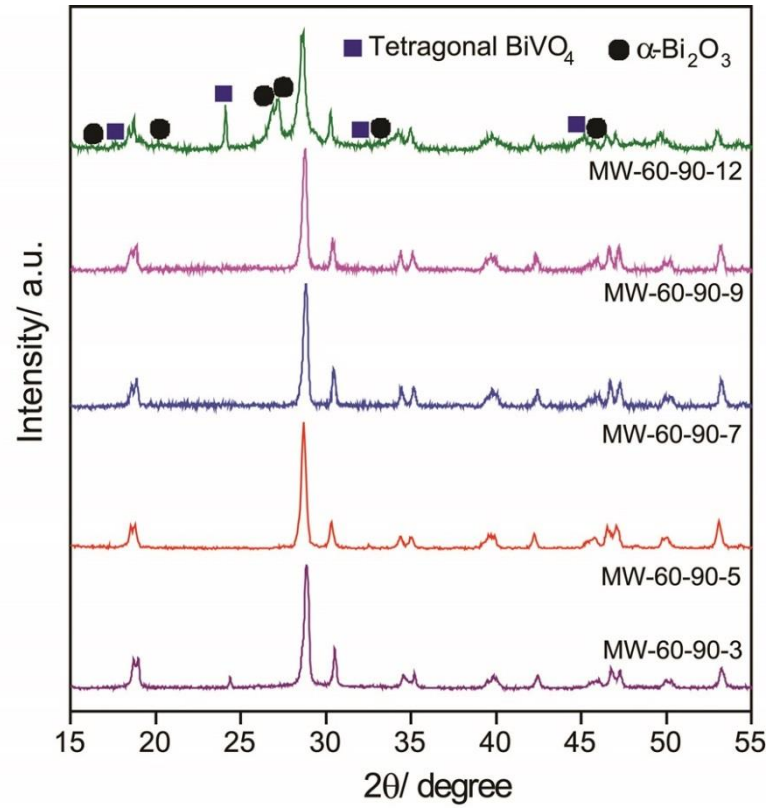

Figure 5.7 XRD patterns of $BiVO_4$ films annealed at 450°C for 1 h, which used the synthesised $BiVO_4$ powder by microwave process at different pH values.

Table 5.2 The relationship of $BiVO_4$ films after annealing at 450°C for 2 h to their percentage of monoclinic $BiVO_4$ phase ($\%V_{mono}$), band gap energy (E_g), specific surface area (S_{BET}) and first order rate constant (k_{app}) for dye degradation.

Samples	$\%V_{mono}$	E_g (eV)	S_{BET} (m^2/g)	Pore radius (nm)	k_{app}RhB (h^{-1})	k_{app} MB (h^{-1})
MW-60-90-3	98	2.36	4.9	1.5	0.25	0.39
MW-60-90-5	100	2.40	6.6	1.9	0.36	0.50
MW-60-90-7	100	2.44	25.5	8.5	0.39	0.60
MW-60-90-9	100	2.44	12.5	2.4	0.30	0.44
MW-60-90-12	65	2.42	5.1	1.6	0.20	0.51

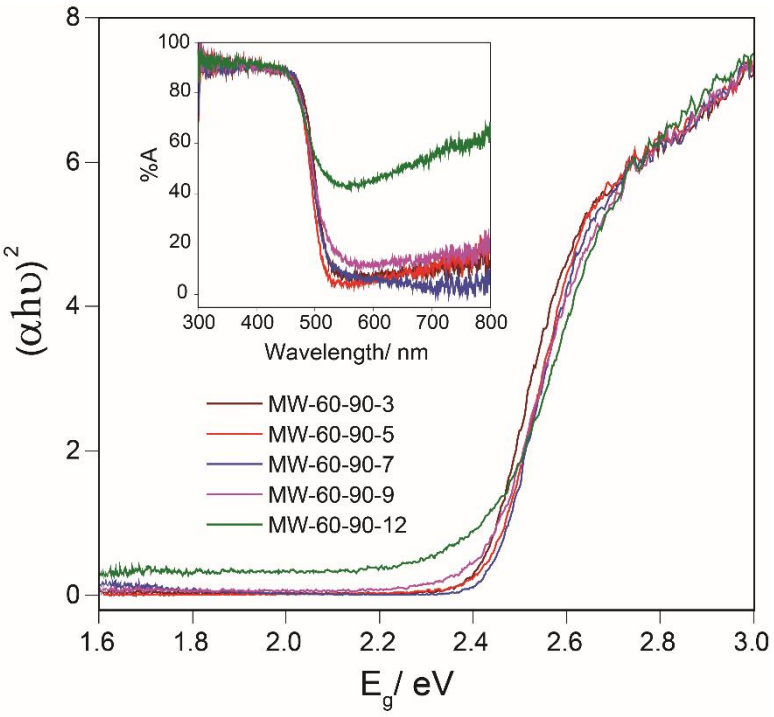

Figure 5.8 UV-vis diffuse absorption in the range of 500–800 nm spectra and inset the plots of $(\alpha h\nu)^2$ versus photon energy ($h\nu$) of the $BiVO_4$ films synthesised by microwave process with different pH values after annealing at 450°C for 2 h.

After annealing at 450°C for 2 h, the band gap energies (E_g) were estimated from the absorption, as illustrated in Figure 5.8, which used the Equation (3.10) as discussed in Chapter 3. The band gap energies of the synthesised $BiVO_4$ films were all 2.45 ± 0.03 eV, summarised in Table 5.2. Thus, the annealing process for the $BiVO_4$ films led to similar optical band gap energies as a result of a change in phase structure from tetragonal to monoclinic $BiVO_4$ confirmed by the XRD results (Figure 5.7).

To observe surface and porosity of the photocatalyst films, the comparison of top surface and cross-section morphologies of the as-prepared films was investigated using SEM, as shown in Figure 5.9. The top view images of the MW-60-90-3 and MW-60-90-12 films show aggregated particles (Figure 5.9(a) and Figure 5.9(e), respectively), which MW-60-90-3 appears more compact, with extensive aggregation, a smooth surface and low porosity, while the MW-60-90-12 film was less aggregated and comprised of smaller particles leading to a rougher surface and more porosities than MW-60-90-3. For MW-60-90-5 (Figure 5.9(b)) an MW-60-90-7 (Figure 5.9(c)), the morphologies of the films were composed of uniformly sized $BiVO_4$ nanoparticles. Both of the annealed MW-60-90-5 and MW-60-90-7 films had similar particle shape, and slightly larger particle size as compared to when unannealed. However, the particles in the MW-60-90-5 film were much larger than those of the MW-60-90-7 film. The morphology of the MW-60-90-9 film was nearly identical to the unannealed, with a uniformly porous surface and a slight porous (Figure 5.9(d)). From these SEM results, it is suggested that the sintering process had a minor effect (with some particle growth observed) for powder which were already monoclinic, while tetragonal or amorphous materials changed more dramatically.

Additionally, the cross-section of $BiVO_4$ films were also measured as presented in Figures 5.9(f)-(j). It was found that all samples had uniform morphology and porosity throughout. Film thicknesses were determined to confirm all be 2.42 ±0.14 μm. SEM give qualitative information about morphology and porosity of the photocatalyst films,

but also Brunauer Emmett Teller (BET) of N_2 adsorption/desorption analysis can quantify the values of specific surface area and porosity of the films.

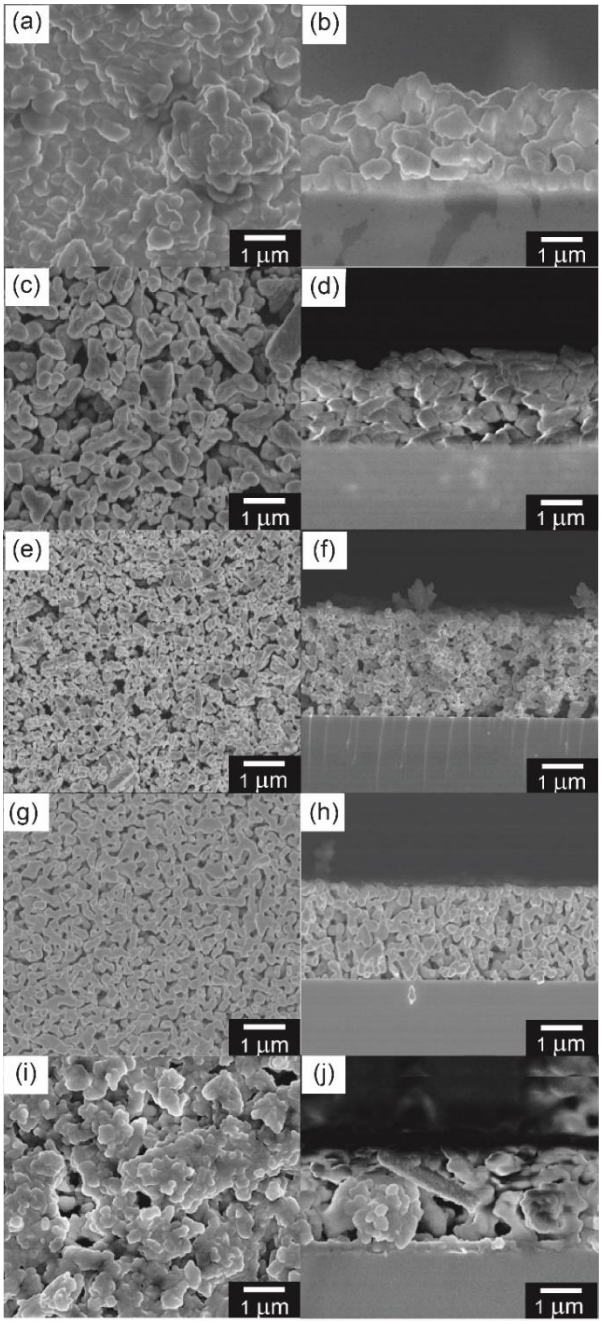

Figure 5.9 SEM images of top surfaces (a), (c), (e), (g) and (i); and cross sections (b), (d), (f), (h) and (j) corresponding of MW-60-90-3, MW-60-90-5, MW-60-90-7, MW-60-90-9 and MW-60-90-12 films, respectively, after annealing at 450°C for 2 h.

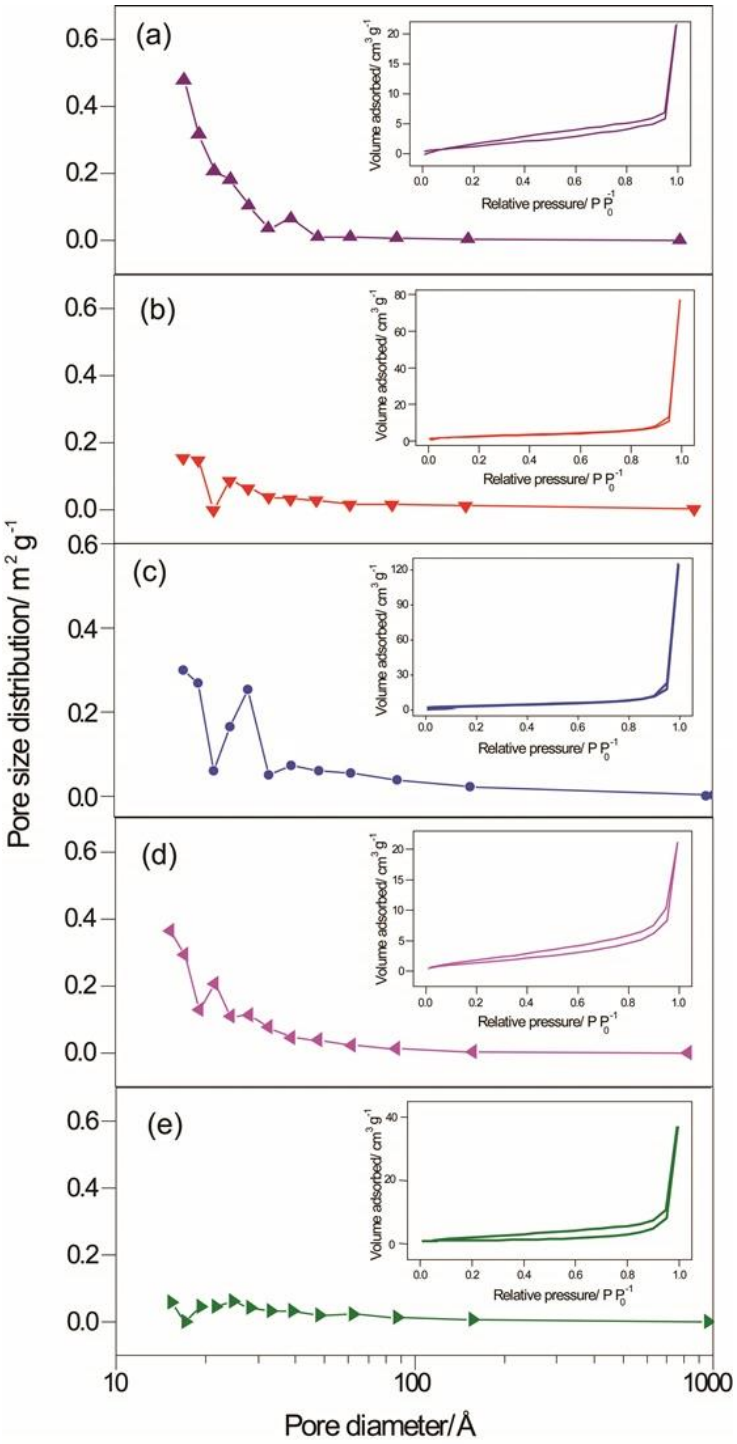

Figure 5.10 Pore size distribution plot for MW-60-90-3, MW-60-90-5, MW-60-90-7, MW-60-90-9 and MW-60-90-12 films with inset their corresponding BET nitrogen adsorption and desorption isotherm.

The adsorption and desorption isotherms were evaluated at -195.6°C after the samples were degassed at 80°C for 6 h. The BJH (Barrett Joyner Halenda) method

of analysing nitrogen adsorption-desorption isotherms, as shown inset Figure 5.10 was used to determine the pore-size distribution (Figure 5.10) of the $BiVO_4$ films (summarised in Table 5.2). All these isotherm plots could be identified as a type IV pattern with a type H2 hysteresis loop, which is indicative of mesoporous materials according to IUPAC classification. From both results of SEM and BET analyses, it could be confirmed that the MW-60-90-7 film had the highest specific surface area (25.5 m^2 g^{-1}) and porosity (16 nm), which provided a larger number of reaction sites corresponding to its highest photocatalytic activity for degradation of RhB and MB dyes.

Based on XRD and SEM results of both $BiVO_4$ powder and their films with different pH synthesis condition, it is suggested that the sintering process had a minor effect on the $BiVO_4$ powder at pH 7. The monoclinic $BiVO_4$ powder with nanoparticle size was already obtained from this condition while tetragonal or amorphous materials of the synthesised $BiVO_4$ powder at lower and higher than pH 7 changed more dramatically due to crystal phase transfer and necking particles during the sintering process.

5.3.3 Photocatalytic performance

RhB and MB dyes in aqueous solution were chosen as a model pollutant dye to study the photocatalytic activities of the $BiVO_4$ films fabricated on glass substrate by doctor blading technique.[4, 40] In this study, photocatalyst films with catalyst loading of ~0.50 g per L (50 μM of MB and 25 μM of RhB solution) was used to study photocatalytic performance of the films under the illumination of simulated sunlight (AM 1.5 G, 100 mW cm^{-2}).

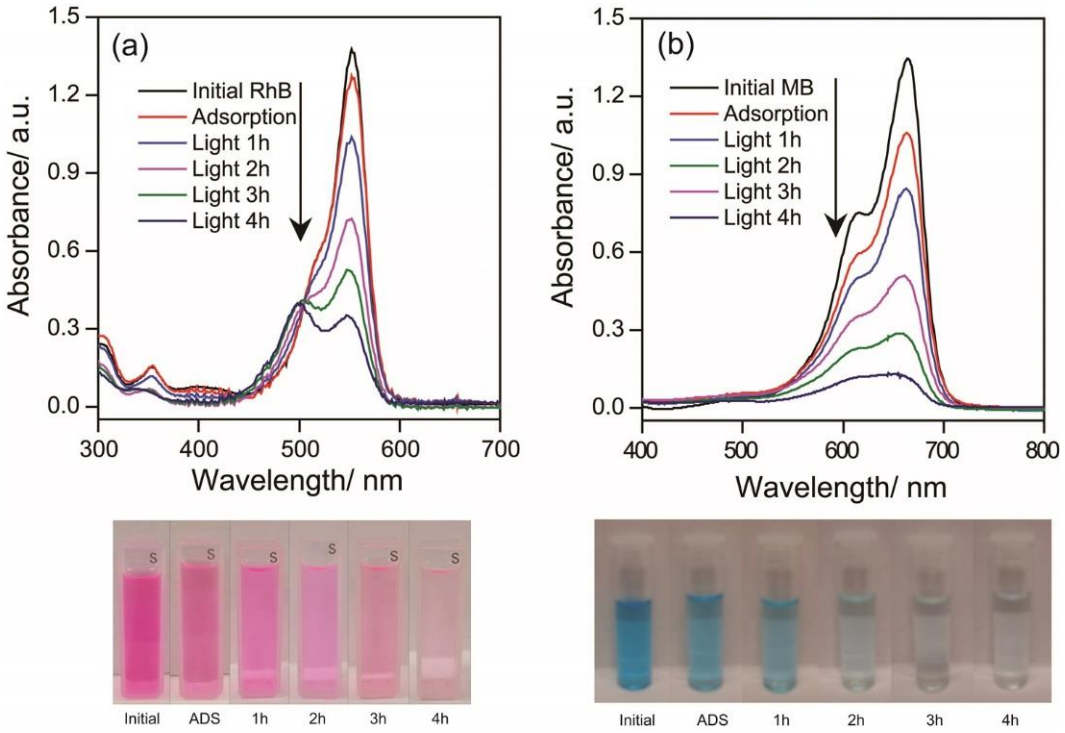

Figure 5.11 Absorption spectra of (a) RhB and (b) MB aqueous solutions at different time intervals in the presence of MW-60-90-7 film under sun light irradiation.

The change in the absorption spectra of RhB and MB aqueous solution after sun light irradiation with different time intervals over the MW-60-90-7 film is shown in Figure 5.11. It was found that the absorption band at 553 nm of the RhB (Figure 5.11(a)) and 664 nm of MB solutions (Figure 5.11(b)) decreased gradually with 4 h irradiation time, demonstrating that the chromophoric structure RhB and MB were destroyed.[5, 40-42]

Before sun light irradiation, each dye solution with catalyst film was kept overnight in the dark in order to attain an adsorption/desorption equilibrium and to study the adsorption of the dyes on the films. Adsorption of each dye in the dark on the $BiVO_4$ films synthesised as a function of time are shown in Figure 5.12(a) for RhB and Figure 5.12(b) for MB dyes. The results showed that the adsorption/desorption equilibrium of both dyes were as much as 10–20% (~ 0.08 and 0.20 μmol of adsorbed RhB and MB, respectively) of the total dyes from the reactor.

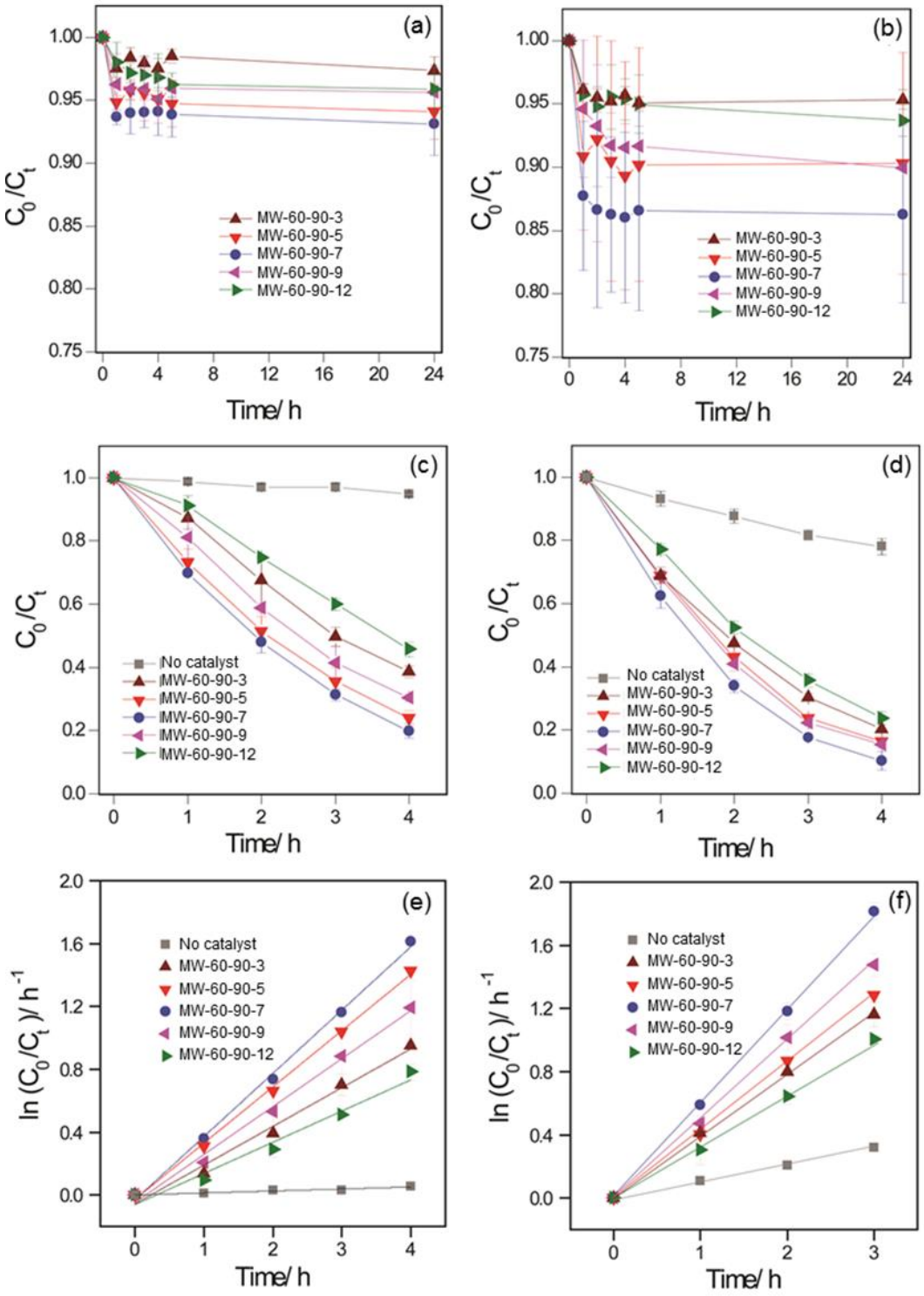

Figure 5.12 (a) and (b) adsorption/desorption equilibrium;(c) and (d) dye degradation; and (e) and (f) fittings for degradation of RhB and MB dyes, respectively, over the $BiVO_4$ films synthesised by microwave with different pH values of precursor (at 90°C for 60 min).

Furthermore, a control, without photocatalyst, was carried out under the same experimental conditions. The adsorption and degradation efficiencies of the $BiVO_4$ films made with different synthetic conditions were normalised as C_t/C_0, where C_0 is the initial concentration of each dye (after equilibrium adsorption) and C_t its concentration at a given time, t.

Dye loading on the $BiVO_4$ film is one of the most important factors, which could subsequently influence its photocatalytic activity. The adsorption efficiencies of RhB and MB on the MW-60-90-3, MW-60-90-5, MW-60-90-7 and MW-60-90-9 films with the similar thickness of 2.4 μm are shown in Figure 5.12(a) and Figure 5.12(b), respectively. It was clearly seen that the adsorption/desorption equilibrium of RhB and MB on all of these films, is reached rapidly with little change. After about three hours, the adsorption of the films was in equilibrium, could be attributed to the sufficient adsorption sites for the dyes (dye loading molecules/nm^2). This could be explained by the Fick's law of diffusion that the adsorption amount of dye was equivalent to adsorption time and the adsorption reaction rate is limited by the mass transport of the dye. According the BET and porosity results (Figure 5.10), the surface area and porous volume of the $BiVO_4$ films directly affected on their adsorption behaviours.

Figures 5.12(c) and 5.12(d) show photocatalytic degradation of RhB and MB under sun light irradiation of the $BiVO_4$ films as a function of time, along with a control (without photocatalyst). As expected, the degradation efficiencies of RhB and MB dyes appear to show logarithmic relationship with respect to time. Thus, the photocatalytic degradation rates of RhB and MB can be fitted to the Langmuir-Hinshelwood (LH) model with pseudo-first order kinetics ($\ln C_t/C_0 = k_{app}\, t$, k_{app} is pseudo-first order rate constant) as presented in Figure 5.12(e) and Figure 5.12(f), respectively.[16] The apparent rate constants for photocatalytic degradation of RhB and MB by the $BiVO_4$ films prepared with different pH value precursors are also presented in Table 5.3. It was found that high specific surface areas of the catalyst films,

calculated by using BET results (Table 5.2), were also related to their high photocatalytic activity, since, their high surface area will enhance the adsorption of photons and dye molecules and offer a large number of reactive sites.[39]

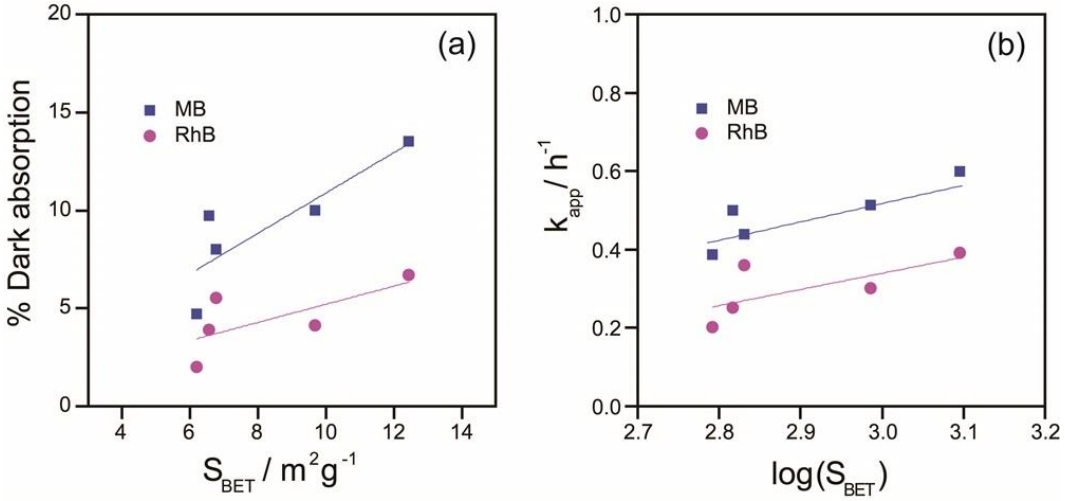

Figure 5.13 (a) Plot of adsorption capacity of dyes *vs.* specific surface area of the films, and (b) Plot of k_{app} for photocatalytic degradation of dyes *vs.* the logarithm of specific surface area of catalyst films.

The relationship between specific surface area of the catalyst films and the percentage of RhB and MB dyes absorbed on the catalyst films with fixed thickness (~2.5 μm) is shown in Figure 5.13(a). The linear relationship in Figure 5.13(a) suggests that the adsorption capacity of RhB and MB dyes on the catalyst films are proportional to the specific surface area of the films. This means that the adsorption capacity can be increased by increasing the surface area. Additionally, the effect of the total surface area of catalyst films on the photocatalytic rates for degradation of RhB and MB dyes is illustrated in Figure 5.13(b). This suggests that there is a logarithmic relationship between the apparent rate constant and the total surface area of catalyst films although further investigation, such as bulk and surface recombination analysis, is required. This could be explained that simple producing

larger surface area in unlikely to help k_{app}, in spite of the increase area, as light will only penetrate a short distances.

5.4 Influence of microwave treatment time

As further steps of optimisation, the effects of the reaction time and temperature on morphology, crystallinity and photocatalytic ability were studied. Times of 5, 15, 30, 45 and 60 min, corresponding with samples MW-05-90-7, MW-15-90-7, MW-30-90-7, MW-45-90-7 and MW-60-90-7, respectively, were used in this series of experiments.

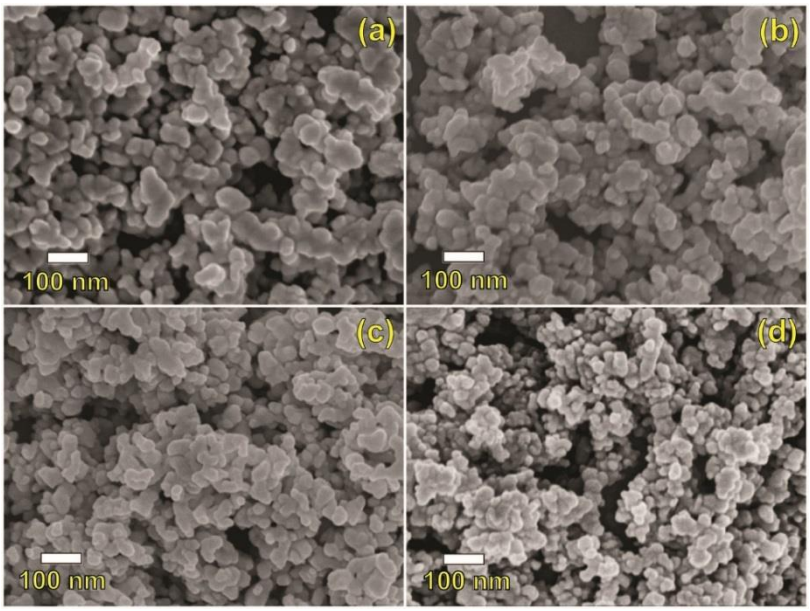

Figure 5.14 SEM images of $BiVO_4$ powder synthesised by the microwave method as a function of time (a) MW-15-90-7, (b) MW-30-90-7, (c) 4 MW-45-90-7and (d) MW-60-90-7.

As Figure 5.14 highlights for the effect of time, the morphology of the $BiVO_4$ products produced are similarly with irregular in shape and particle size in the range of 80–120 nm. XRD results (Figure 5.15) however reveal more marked differences in crystallinity and phase purity, in opposition with the more or less consistent morphology observed by SEM. This also reveals additional information about the manner in which

monoclinic $BiVO_4$ is formed. The product of the short reaction time is a mixture of monoclinic and tetragonal phase along with substantial amorphous material. With 15min processing this amorphous material is no longer observed, giving way to more of the both the monoclinic and tetragonal phases. From 30 min onward there is a notable decrease in the quantity of tetragonal $BiVO_4$, however it is not until 60 min that the material can be considered phase pure. This is highlighted with the percentage of monoclinic structure in Table 5.3.

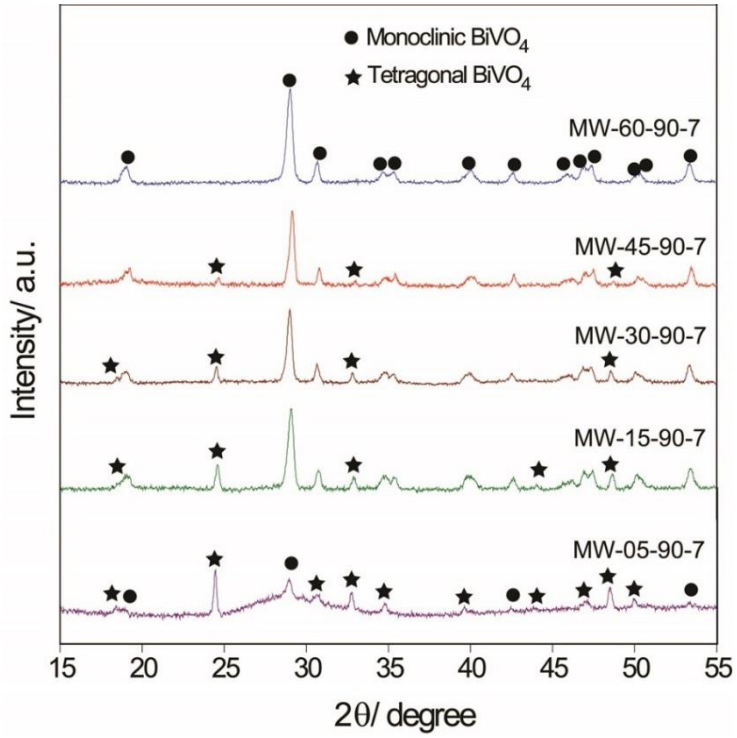

Figure 5.15 XRD patterns of pure $BiVO_4$ powder synthesised by microwave process at different treatment time of microwave irradiation.

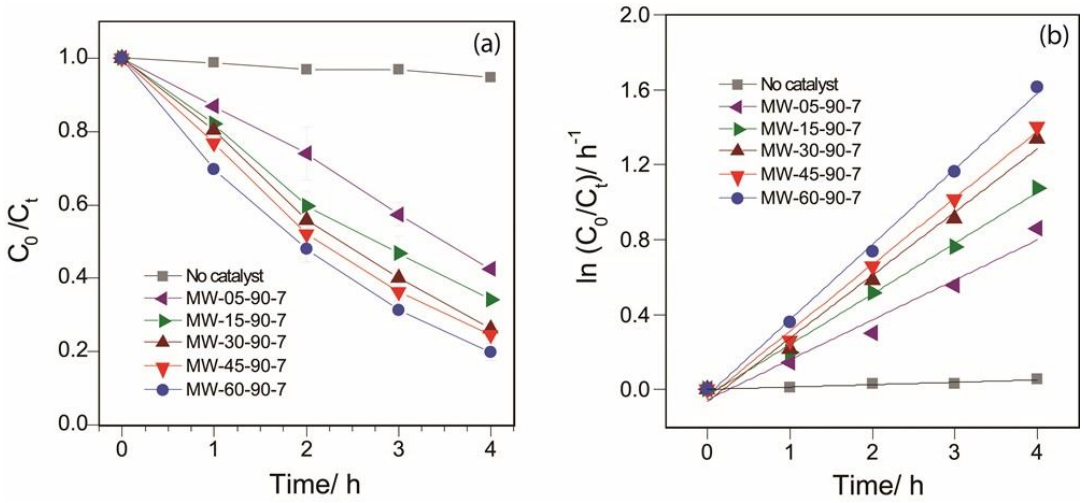

Figure 5.16 (a) photocatalytic efficiencies; and (b) kinetic studies for degradation of RhB dye over the $BiVO_4$ films synthesised by microwave method with different microwave treatment time (at pH 7 and 90°C).

Comparison their photocatalytic properties (Figure 5.16), the $BiVO_4$ treated by microwave irradiation for 60 min (MW-60-90-7) showed the highest performance, since this condition provided phase pure monoclinic materials with the smallest particle size.

Table 5.3 The relationship between microwave irradiation time for synthesis of $BiVO_4$ powder and the percentage of monoclinic $BiVO_4$, crystallite size, particle size from SEM images and their rate constant (k_{app}) for degradation of RhB.

Samples	$\%V_{mono}$	Crystallite size (XRD, nm)	Particles size (SEM, nm)	k_{app} (h^{-1})
MW-5-90-3	30	106	80–100	0.21
MW-15-90-5	75	50	100–200	0.27
MW-30-90-7	80	57	80–200	0.32
MW-45-90-9	88	54	80–150	0.35
MW-60-90-7	100	47	50–80	0.39

5.5 Influence of microwave temperature

The effect of the processing temperature with respect to crystalline structure, morphologies and photocatalytic properties of $BiVO_4$ was also studied with pH fixed at 7 and reaction time of 60 min. Figure 5.17 shows the SEM images of $BiVO_4$ samples synthesised at two different reaction temperatures of 60°C and 90°C.

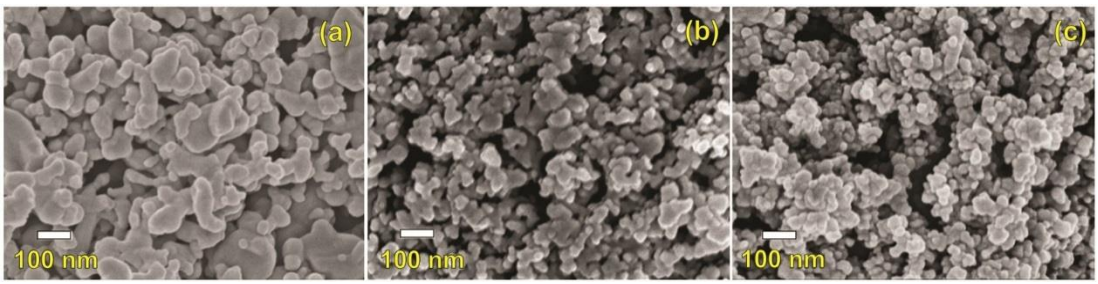

Figure 5.17 SEM images of $BiVO_4$ powder synthesised by the microwave method as a function of temperature: (a) RT-60-25-7, (b) MW-60-60-7and (c) MW-60-90-7.

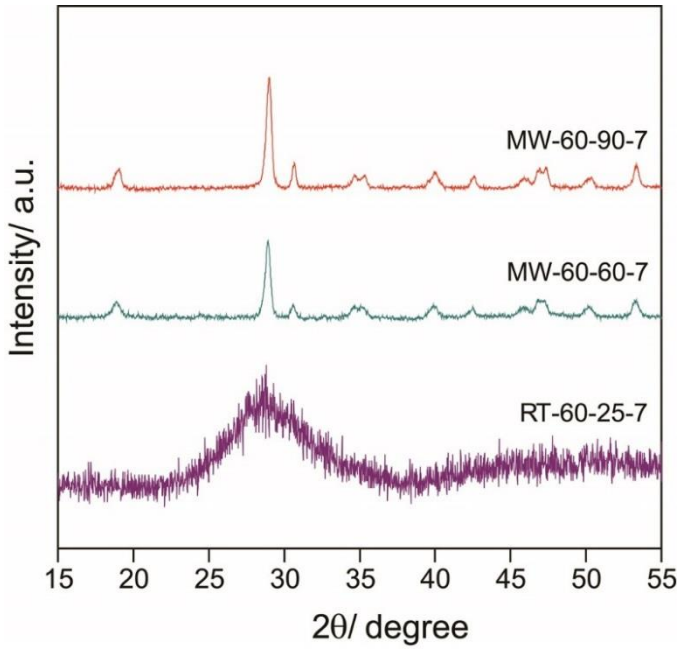

Figure 5.18 XRD patterns of pure $BiVO_4$ powder synthesised by microwave process at different temperature by microwave synthesis.

The temperature of 90°C was chosen as to avoid boiling the aqueous solution. At 60°C, the particle size and morphology of the samples was almost the same in the sample prepared at 90°C, which were mainly composed of spherical particles about 50–80 nm in size and slightly small in size when increasing reaction temperature. Control experiments at room temperature (RT-60-25-7) indicated that the crystalline $BiVO_4$ could not form without microwave treatment, as the XRD of this sample showed an amorphous structure (Figure 5.18). The XRD results also shown both of the synthesised $BiVO_4$ powders with different temperature had monoclinic structures. It is seen that the reaction temperature for microwave synthesis of $BiVO_4$ (pH 7, 90°C and >300 W) had a minor effect to its morphology and crystallinity.

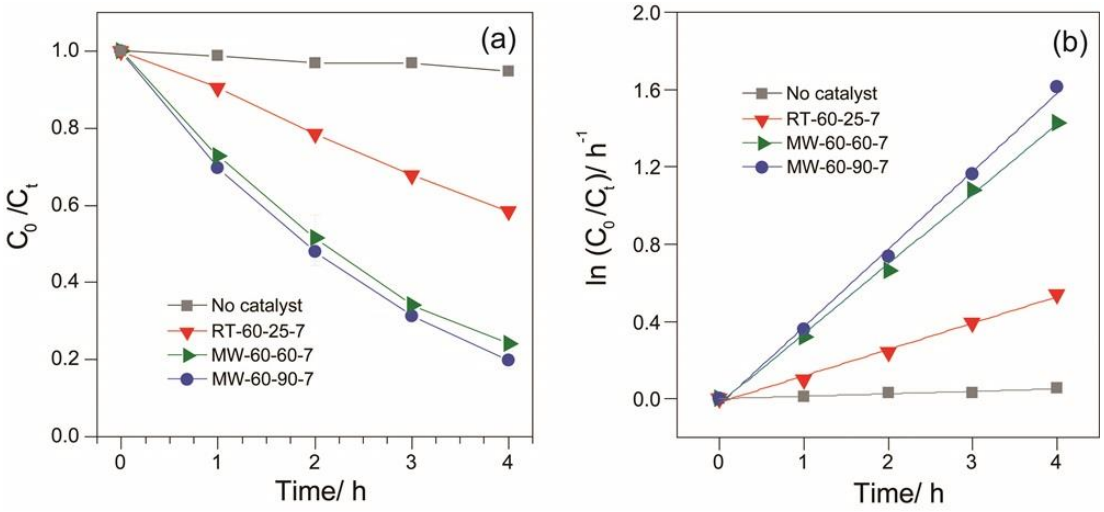

Figure 5.19 (a) photocatalytic efficiencies; and (b) kinetic studies for degradation of RhB dye over the $BiVO_4$ films synthesised by microwave method with different microwave treatment time (at pH 7 and 60 min).

As Figure 5.19 shows the photocatalytic properties for degradation of RhB dye over the $BiVO_4$photocatalyst prepared with different temperature by microwave synthesis, the $BiVO_4$ sample synthesised at temperature of 90°C showed slightly higher photocatalytic activity than the 60°C sample. This is likely to be due to its higher crystallinity of monoclinic phase as summarised in Table 5.4.

Table 5.4 Percentage of monoclinic $BiVO_4$ phase, crystalline size, particle size from SEM images and their rate constant (k_{app}) for degradation of RhB for $BiVO_4$ produced by microwave synthesis performed at different temperatures.

Samples	$\%V_{mono}$	Crystalline size (nm)	Particles size (SEM, nm)	k_{app} (h^{-1})
RT-60-25-7	Amorphous	-	150–200	0.24
MW-60-60-7	100	46.0	50–80	0.35
MW-60-90-7	100	47.0	80–100	0.39

Based on the experimental results, it could be concluded that the crystal phase and morphology of $BiVO_4$ are strongly dependent on the pH of the solution, and minor dependent on time and temperature for microwave synthesis. $BiVO_4$ synthesised by microwave treatment at pH 7 and 90°C for 60 min (MW-60-90-7) was seen to be the optimal condition to produce single phase of monoclinic $BiVO_4$ and small spherical particles with high specific surface area, leading to high photocatalytic degradation of dyes under simulated sunlight irradiation.

5.6 Comparison of microwave synthesis with other methods

5.6.1 Comparison of controlled experiment to the optimised microwave

The microwave synthesised $BiVO_4$ material was compared to state of the hydrothermal and precipitation methods, the XRD patterns of samples produced by precipitation (PC-60-90-7) and hydrothermal (HT60-90-7) methods, using the same experimental conditions (same precursors, pH 7, temperature of 90°C and 60 min holding time) were studied and compared as shown in (Figure 5.20). While MW-60-90-7 sample was clearly monoclinic, PC-60-90-7 and HT-60-90-7 samples had an amorphous structure. This could is explained by the microwave energy being applied

directly to ions in the solution providing a higher probability of collision and subsequent reaction, allowing enhanced reaction rates.[17]

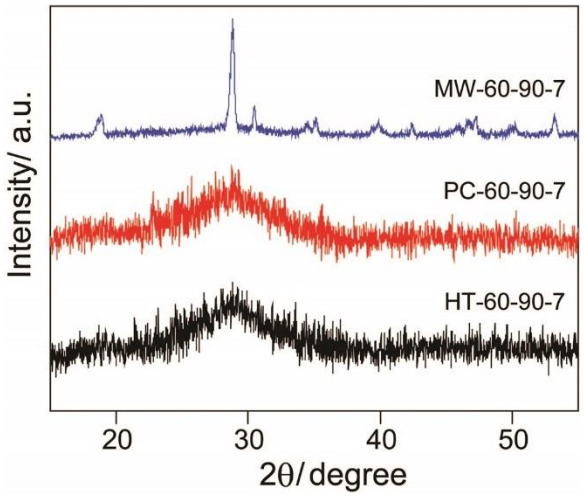

Figure 5.20 XRD patterns of $BiVO_4$ powder synthesised by hydrothermal (HT-60-90-7), precipitation (PC-60-90-7) and microwave (MW-60-90-7) methods with conditions of pH 7, 90°C and 60 min unannealed.

5.6.2 Comparison of physical characterisation $BiVO_4$ powder

The crystal structures of the $BiVO_4$ powder synthesised with different methods were investigated by X-ray diffraction and the resulting patterns are shown in Figure 5.21. It was found that all $BiVO_4$ samples provided single phase of monoclinic structure corresponding to JCPDS No. 75–1866. The calculated crystalline size of them also is presented in Table 5.5, which could be seen that the synthesised $BiVO_4$ by precipitation and hydrothermal methods showed higher crystallinity than by microwave methods.

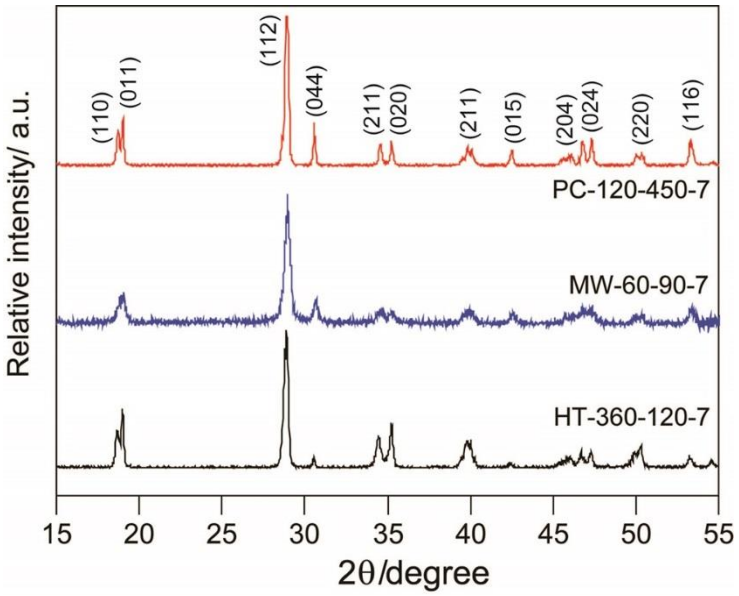

Figure 5.21 XRD patterns of $BiVO_4$ synthesised at pH 7 by an optimised hydrothermal method (HT-360-120-7), microwave method (MW-60-90-7); and precipitation method (PC-120-450-7).

Table 5.5 Comparison of the percentage of monoclinic $BiVO_4$ phase ($\%V_{mono}$), crystalline size (Scherrer equation), relative intensities of (011)/(112) and (004)/(112), as a function of preparation methods.

Samples	$\%V_{mono}$	Crystalline size of powder (nm)	Particles size (SEM, nm)	$I_{(011)}/I_{112}$	$I_{(004)}/I_{112}$
HT-360-120-7	100%	28	Length 1000 Width 100	0.430	0.067
PC-120-450-7	100%	34	200	0.317	0.279
MW-60-90-7	100%	19	30	0.230	0.195

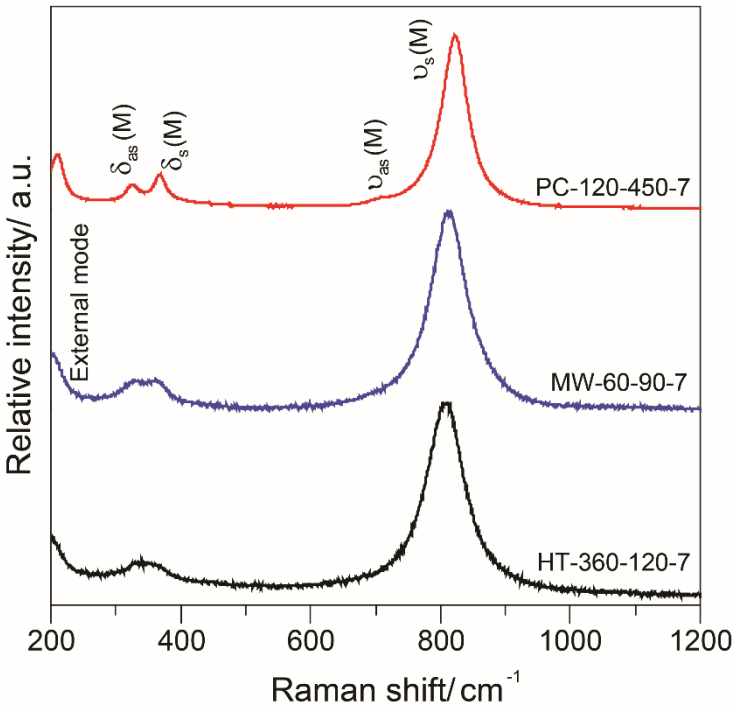

Figure 5.22 Raman of $BiVO_4$ synthesised at pH 7 by hydrothermal method (HT-360-120-7), microwave method (MW-60-90-7); and precipitation method (PC-120-450-7).

The Raman spectra of the $BiVO_4$ powders synthesised by different methods, namely HT-360-120-7, MW-60-90-7 and PC-120-450-7 under the same pH and experimental conditions are presented in Figure 5.22. It was found that all synthesised samples had the same position of Raman bands at 320, 367, 637, and 820 cm^{-1}, which were attributed to the Raman bands of monoclinic $BiVO_4$.[3, 14].The PC-120-450-7 showed strong intensity Raman bands, ten times stronger compared to HT-360-120-7 and MW-60-90-7 samples. This is due to its high crystallinity and crystalline size that corresponding with XRD result and calculated crystalline size as shown in Figure 5.21 and Table 5.5, respectively.

Clearly different morphologies of HT-360-120-7, PC-120-450-7 and MW-60-90-7 samples are presented in Figure 5.23. The rod-like $BiVO_4$ particles with particle size of about 100 nm in width and 1 μm in length are observed for the HT-360-120-7 sample (Figures 5.23(a) and 5.23 (d)). The ellipsoidal particles for the PC-120-450-7

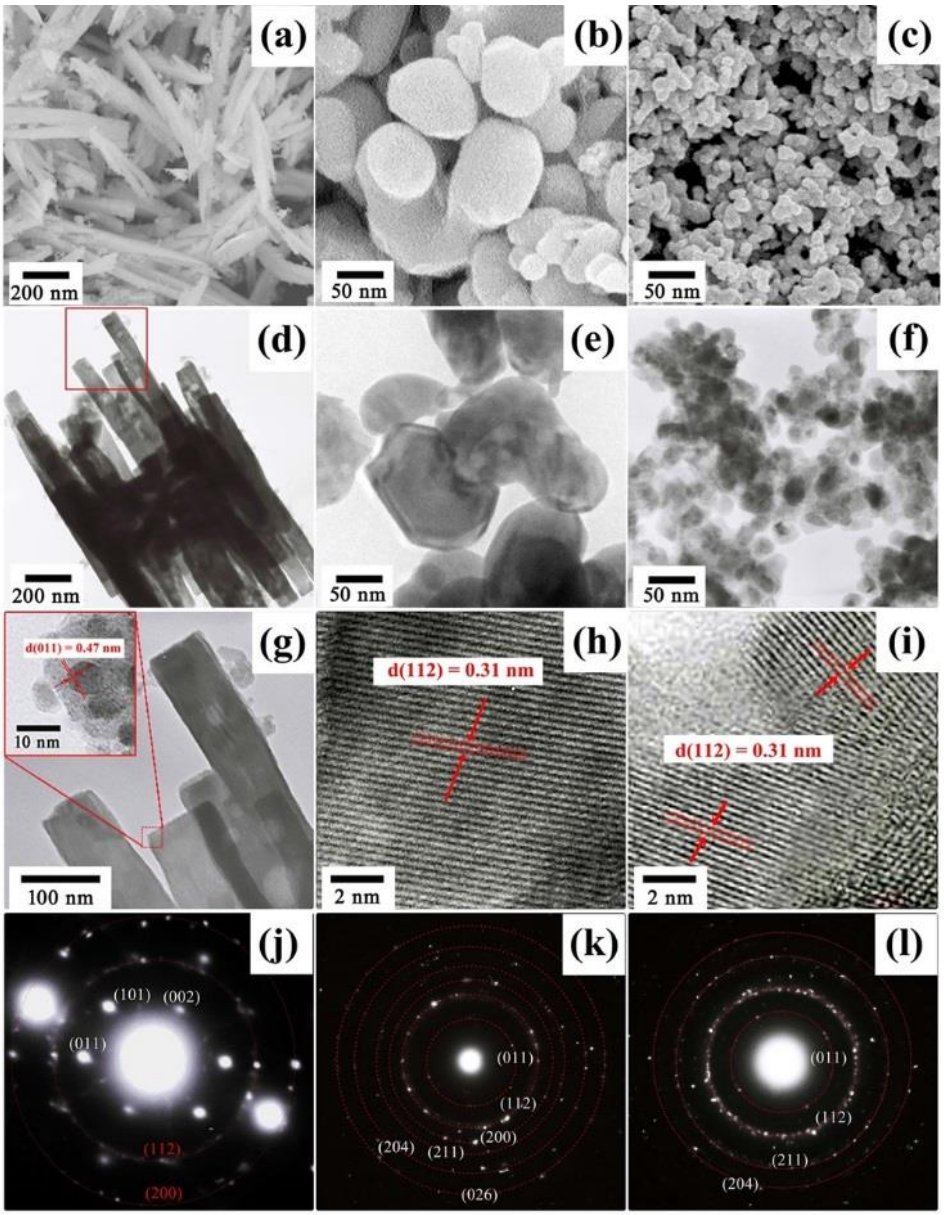

Figure 5.23 (a)-(c) SEM images, (d)-(f) TEM images, (g)-(i) HRTEM images and (j)-(l) its SAED of synthesised $BiVO_4$ powder, HT-360-120-7, PC-120-450-7 and MW-60-90-7, respectively.

sample were found to be ~200 nm in size, as shown in Figures 5.23(b) and 5.23(e). In the MW-60-90-7 sample, spherical $BiVO_4$ particles with an average size of 40 nm are observed, as seen in Figures 5.23(c) and 5.23(f). HRTEM images obtained from

the area marked with red rectangles in Figures 5.23(d)-(f) are shown in Figures 5.23(g)-(i). The fringes of 0.31 nm (Figures 5.23(h) and 5.23(i)) and 0.49 (Figure 5.23(g)) are in good agreement with the known spacings of the (112) and (011) lattice planes of monoclinic $BiVO_4$. It could be assumed that the rod-like $BiVO_4$ grows along with (011) plane, corresponding to the lattice fringe of (011) plane in HRTEM image and its higher of XRD relative intensities of (011)/(112) as shown in Table 5.5 which agreed well with the results by Obregón *et al.*[12] and Tan *et al.*.[35] For the relative intensities of (011)/(112), the ellipsoidal (0.317) and spherical (0.230) particles were lower than the rod-like particles (0.430). It has been suggested that the growing orientation of (011) and (004) planes are associated with the rod-like and plate-like morphologies of monoclinic $BiVO_4$ respectively.[12, 35] Spherical results in similarly relative intensities of both planes, as seen in the case of the MW-60-90-7 sample. Moreover, the corresponding SAED patterns (Figures 5.23(j)-(l)) of the HRTEM images confirmed that all synthesised $BiVO_4$ samples had polycrystalline monoclinic structure, which is in agreement with XRD results in Figure 5.21.

5.6.3 Comparison of physical properties $BiVO_4$ films after annealing

XRD was also employed to examine the phase structure and crystallinity of the films after annealing at 450°C for 1h as shown in Figure 5.24, these films were from the synthesised powder with different methods. It was found that all the patterns in Figure 5.24 can be once again indexed to monoclinic $BiVO_4$. Compared to the unannealed sample the crystallinity is much higher.

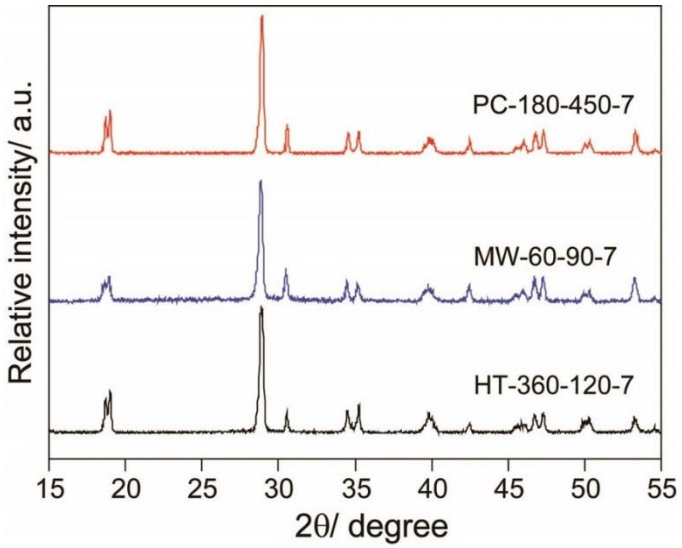

Figure 5.24 XRD patterns of $BiVO_4$ films annealed at 450°C for 1 h, which used the synthesised $BiVO_4$ powder by different methods.

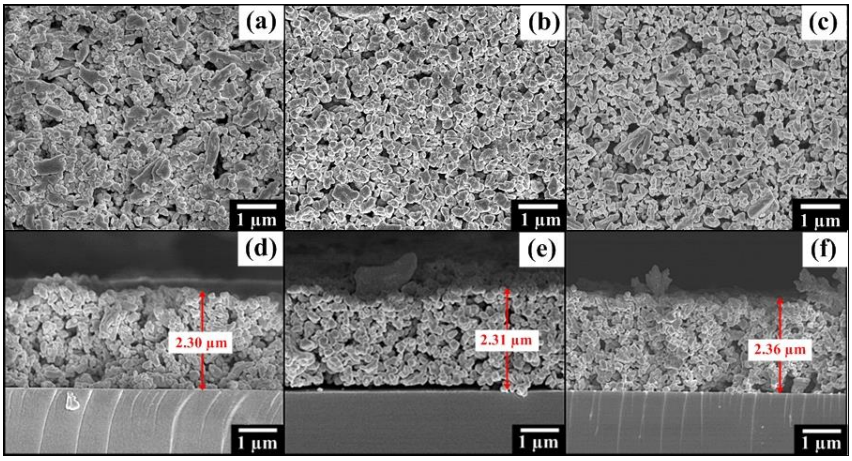

Figure 5.25 SEM images for top surfaces (a), (b) and (c), and cross sections (d), (e) and (f) of BVO_4 films synthesised by hydrothermal (HT-360-120-7), precipitation (PC-120-450-7) and microwave (MW-60-90-7) methods, respectively.

The comparison of SEM top surface and cross section images of the $BiVO_4$ films from the three methods is shown in Figure 5.25. The SEM top surfaces of the $BiVO_4$ films synthesised by hydrothermal, precipitation and microwave methods as presented in Figures 5.25(a), 5.25(b) and 5.25(c), respectively and the corresponding cross-sectional images (Figures 5.25(d)-(f)) of $BiVO_4$ films could be measured the thickness

to be 2.30, 2.31 and 2.36 μm, respectively. As Figure 5.25, the surface and cross-section SEM images of those three catalyst films show the porous $BiVO_4$ film of a uniform spherical shape in the MW-60-90-7 but a mixture of large irregular and spherical shapes in HT-360-120-7 and PC-120-450-7. In comparison, all $BiVO_4$ films synthesised by three different methods had a bigger particle size than their powders this is probably due to aggregation of small particles from film fabrication and annealing processes

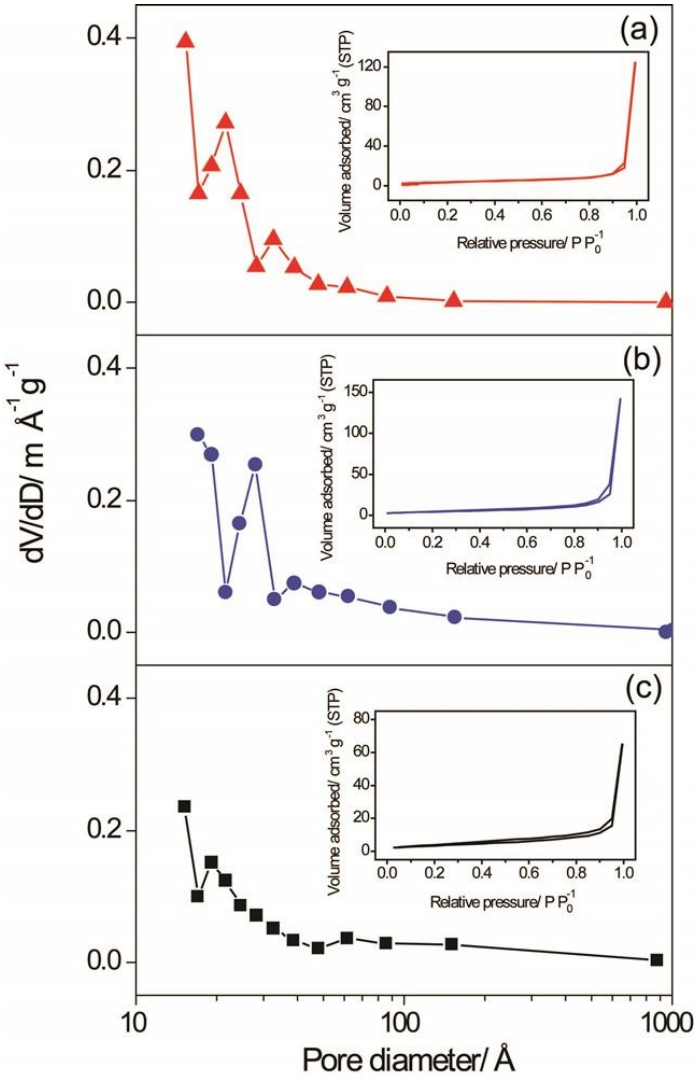

Figure 5.26 Pore size distribution plots with inset their corresponding BET nitrogen adsorption and desorption isotherm for the annealed (a) PC-120-450-7, (b) MW-60-90-7and (c) HT-360-120-7 films.

Table 5.6 Comparison of the percentage of monoclinic $BiVO_4$ phase (%V_{mono}), crystalline size (Scherrer equation), relative intensities of (011)/(112) and (004)/(112) as for various synthetic methods.

Samples	S_{BET} (m^2/g)	Pore radius (nm)	Pore volume (cm^3/g)	d_{BET} (nm)
HT-360-120-7	9.7	15.5	0.19	67
PC-120-450-7	22.0	3.0	0.22	28
MW-60-90-7	25.5	16.0	0.19	20

Table 5.6 shows the comparison of S_{BET}, d_{BET} and pore volume of the $BiVO_4$ nanoparticles synthesised by hydrothermal precipitation and hydrothermal methods after annealing at 450°C for 2 h and their BET nitrogen adsorption and desorption isotherm (Figure 5.26) and corresponding to pore size distribution plot also presented inset Figure 5.26. The $BiVO_4$ films with powder synthetic methods of hydrothermal and microwave obtained mesoporous structures with main pore size of 15.5 and 16.0 nm, respectively. However, the $BiVO_4$ film synthesised by the precipitation and microwave methods showed high surface area of 22.0 and 25.5 $m^2\,g^{-1}$, respectively corresponding to their high photocatalytic performance of degradation of dyes.

5.6.4 Comparison of the photocatalytic properties of the $BiVO_4$ films

Again the adsorptive performances and photocatalytic activities of $BiVO_4$ produced by different synthetic method were evaluated using 25 μM RhB and 50 μM MB aqueous solutions, as model organic compounds, under sun light irradiation. The relative dyes remaining, C/C_0, for the adsorptive and photocatalytic efficiencies of the $BiVO_4$ films synthesised by different methods as a function of irradiation times are presented in Figure 5.27 and summarised in Table 5.7.

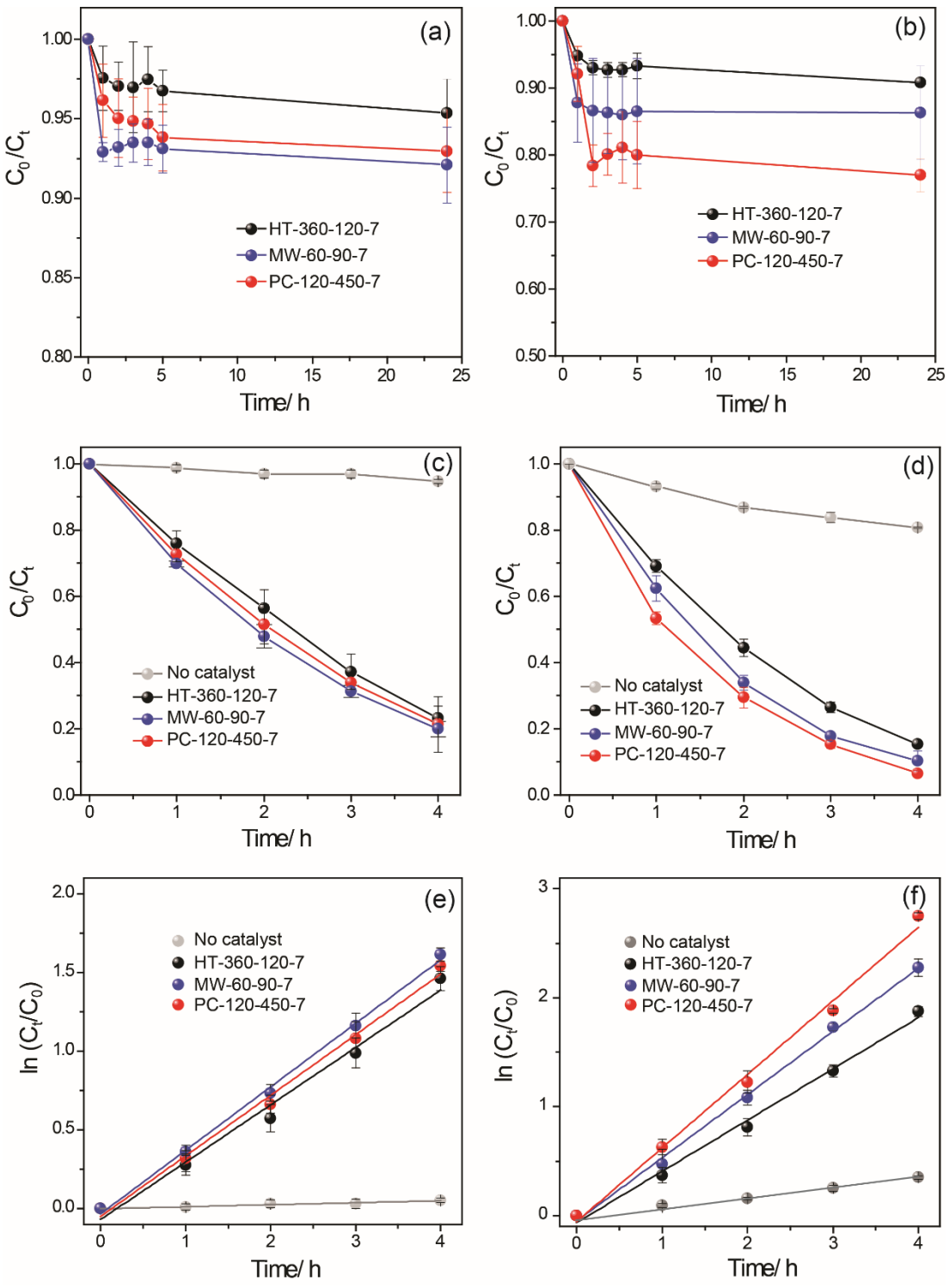

Figure 5.27 (a) and (b) dark adsorption; (c) and (d) photocatalytic efficiencies; and (e) and (f) kinetic studies for degradation of RhB and MB dyes, respectively, over the $BiVO_4$ films synthesised with different synthetic methods under simulated sun light irradiation.

The results showed that about 7% of RhB (~0.05 µmol) and 14% of MB (~0.15 µmol) dyes in reactor were adsorbed on the MW-60-90-7 film. For RhB, the average adsorption percentage of the PC-120-450-7 film was found to be almost the same value for the MW-60-90-7 film corresponding to their similarly specific surface area from BET results (Table 5.6). MB showed a higher affinity for the $BiVO_4$ surface than RhB did, in line with previous reports in the literature.[43, 44] This because both dyes have positive charges, while $BiVO_4$ has a surface charged at above a pH 5.6 in RhB solution and pH 5.0 in MB solution shown in Figure 5.28, the Zeta potential of the $BiVO_4$ nanoparticles synthesised by different methods, will interact with the dyes by electrostatic forces. [43, 45] Furthermore, the adsorption efficiencies of dyes on the $BiVO_4$ films also correspond to their surface area of catalyst films, high surface area of the catalyst provide a large number of reactive sites. The difference of isoelectric point (IEP) for $BiVO_4$ particles with three different synthetic methods may be correspond to amount of hydroxyl anion (^{-}OH) functional group on surface of catalyst, which also related to their surface area.

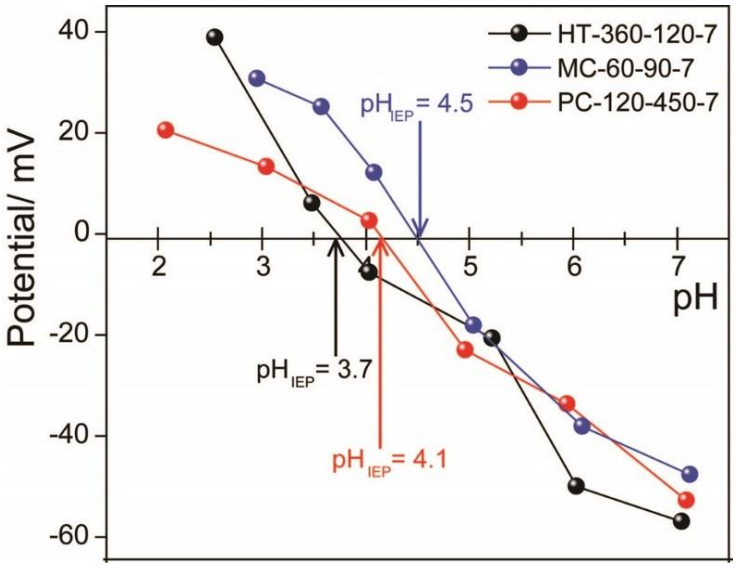

Figure 5.28 Zeta potentials and isoelectric points (IEPs) of the $BiVO_4$ nanoparticles synthesised by different methods plotted against pH.

The $BiVO_4$ film samples with their corresponding adsorption performances and photocatalytic reaction rate constant (k_{app}) for degradation of dyes are listed in Table 5.8. Figures 5.27(c) and 5.27(d) show the photocatalytic degradation performance of RhB and MB dyes, respectively in the presences of the $BiVO_4$ films with different synthesis methods along with the control (without photocatalyst). As shown in Figure 5.27(c), both of the PC-120-450-7 and MW-60-90-7 films exhibited similarly photocatalytic activities for RhB degradation following by the HT-360-120-7 film. However, the PC-120-450-7 film showed slightly better photocatalytic activity for degradation of MB than either the MW-60-90-7 or HT-360-120-7 films, (Figure 5.27(d)).

Table 5.7 Relationship between synthetic methods (powder) of the $BiVO_4$ films and average adsorption percentage and photocatalytic degradation performances of dyes.

Samples	RhB		MB	
	Adsorbed dye (μmol)	k_{app} (h^{-1})	Adsorbed dye (μmol)	k_{app} (h^{-1})
No catalyst	-	0.013	-	0.04
HT-360-120-7	0.02	0.36	0.09	0.48
PC-120-450-7	0.05	0.38	0.14	0.66
MW-60-90-7	0.06	0.40	0.20	0.59

The Langmuir-Hinshelwood kinetic model was also used to analyse the kinetics of these photodegradation experiments,[46] as presented in Figures 5.27(e) and 5.27(f), respectively. The calculated values for apparent rate constant (k_{app}) of all samples are summarised in Table 5.7. It was found that the MW-60-90-7 film exhibited the highest k_{app} value (0.40 h^{-1}) for RhB degradation, but for MB degradation the PC-120-450-7 film had the highest value of 0.66 h^{-1}. However, the MW-60-90-7 and PC-120-450-7 film samples presented not much different of the k_{app} values for degradation of both RhB and MB dyes. Hence, it could be concluded that the MW-60-90-7 film exhibited

as good photocatalytic behaviour as PC-120-450-7 film. This is largely due to these films providing high crystallinity of the monoclinic structure and high surface areas. The microwave method has the added bonus that is can be conducted rapidly and with less input energy.

5.7 Band structure and photocatalytic mechanisms

To study the possible mechanisms of photocatalytic degradation of the RhB and MB dyes by $BiVO_4$ photocatalysis, the optical and electronic properties of the $BiVO_4$ film were investigated by UV-vis absorption spectroscopy and the conduction band edge estimated from a Mott-Schottky experiment. The optical properties of the $BiVO_4$ films prepared by different synthesis methods were comparing using the UV-vis spectroscopy, as shown in Figure 5.29(a). It was shown that all samples have very strong absorption at ultraviolet and visible light regions. Furthermore, the band gap energies of three film samples were determined as shown in Figure 5.29(b), following the Equation 2.10 in Chapter 2, to once again be 2.44 ± 0.02 eV, as one would anticipate for monoclinic $BiVO_4$. All three condition should harvest a similar number of photons.

Additionally, Mott-Schottky experiments determine the position of the conduction band (CB) edge of the $BiVO_4$ synthesised by microwave irradiation (presented in Figure 5.30(a)) to be -0.50 V (vs. Ag/AgCl, or 0.03V *vs.* NHE).[47] From these measurements the valance band (VB) edge can be determined to be about -2.36 V (*vs.* NHE). Mott-Schottky plots also confirm (Figure 5.30(a)) the MW sample to be n-type semiconductors due to showing the positive slope corresponding the previously reported works by Hong *et al.*[48] and Luo *et al.*[49] Considering the redox potentials of RhB(0.95 V vs. NHE) and RhB* (−1.42 V vs. NHE)[50-52] and MB (1.17 V vs. NHE) MB*

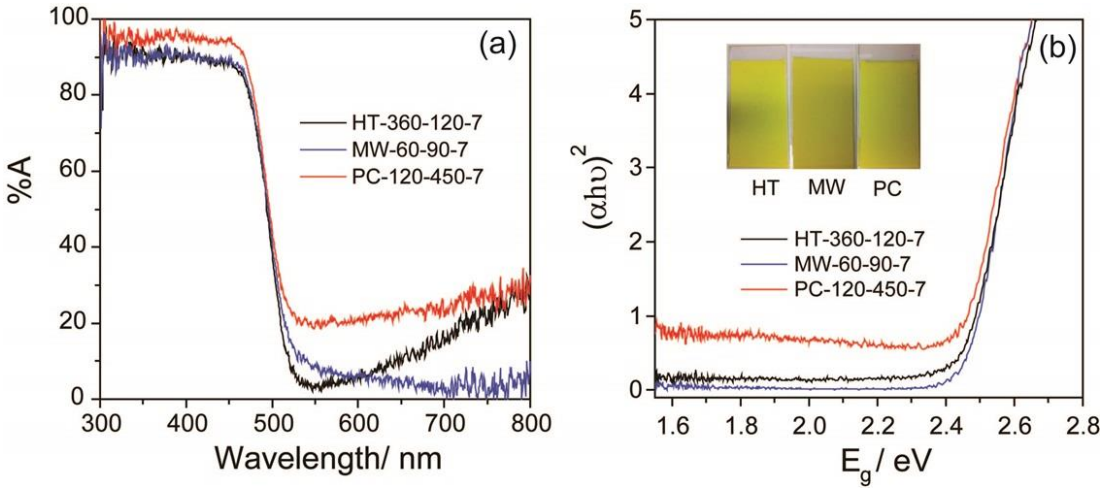

Figure 5.29 (a) absorption spectra in the range of 500–800 nm and (b) the corresponding plots of $(\alpha h\nu)^2$ versus photon energy ($h\nu$) of the $BiVO_4$ films annealed at 450°C for 1 h by different synthetic methods.

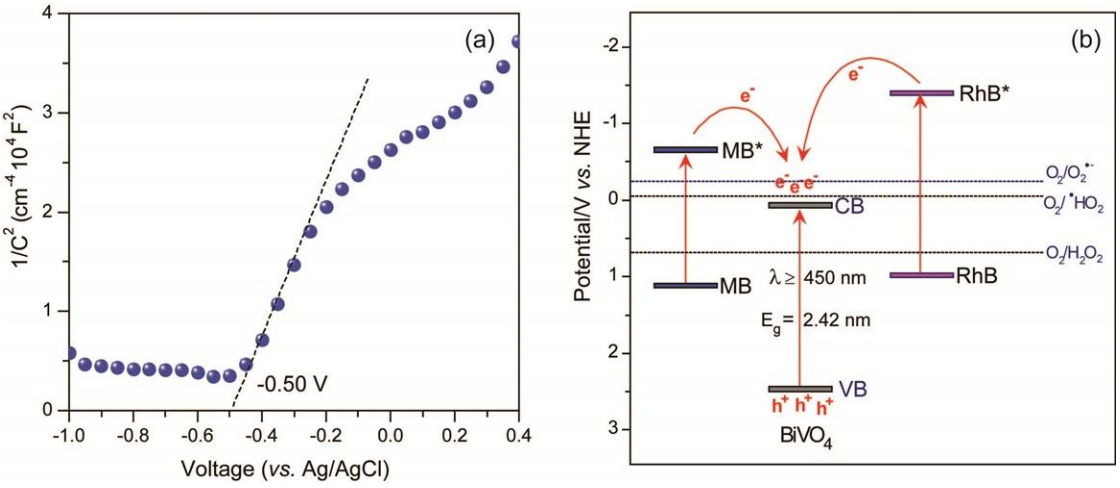

Figure 5.30 (a) Mott–Schottky plot of the $BiVO_4$ film synthesised by microwave irradiation, and (b) proposed $BiVO_4$ band diagram and electron and hole transfer reactions for the photocatalytic degradation of dyes. The Mott–Schottky plots were measured in 0.5 M Na_2SO_4 solution (pH 5.5) at a frequency of 1 kHz.

(−0.69V vs. NHE),[53, 54] which can be activated by the wavelength of light as 553 nm and 664 nm, respectively. Thus the possible mechanisms for degradation of both dyes by $BiVO_4$ photocatalyst are shown as inset Figure 5.30(b). Under sunlight irradiation, dyes can adsorb the visible light and then generate the excited dyes*. Thus, high rates of photocatalytic dye degradation were recorded. This is probably due to the increase of electron transfer from the excited dyes* to the CB of $BiVO_4$, the reduction of dissolved O_2 at the dyes* can also yield $\cdot O_2^{-\bullet}$ radicals ($O_2 + e^- = O_2^{-\bullet}$, −0.248 V vs. NHE) and/or $^{\bullet}HO_2$ radicals ($O_2 + H^+ + e^- = {}^{\bullet}HO_2$, −0.046 V vs. NHE).[55, 56]

Simultaneously, $BiVO_4$ also can be activated by visible light and generated electron-hole pairs. The electrons in the CB of $BiVO_4$ will then be transferred to the oxygen moles (O_2) adsorbed on the surface of $BiVO_4$ to produce hydrogen peroxide (H_2O_2), since the CB level of $BiVO_4$ is more negative than its standard redox potential ($O_2 + 2e^- + 2H^+ = H_2O_2$, 0.682 V vs. NHE).[56, 57] Finally, these H_2O_2 molecule can react with electrons to generate active hydroxyl radicals ($^{\bullet}OH$).

Therefore, the possible reaction to produce strong oxidizing radicals in this system is the reduction of surface chemisorbed O_2 to active species such as $O_2^{-\bullet}$, $^{\bullet}HO_2$ and $^{\bullet}OH$ by the electron at the exited of both dyes* and CB of $BiVO_4$, and then these strong oxidizing radicals can degrade the RhB molecules.[5, 58]

5.8 Electrophotocatalytic degradation of RhB and MB

As mentioned briefly in Chapter 3, photoelectrochemical measurement was performed using a three-electrode system composed of the microwave synthesised $BiVO_4$ film on FTO glass, Pt mesh and Ag/AgCl as working, counter, reference electrodes, respectively. Cyclic voltammetry (CV) and Linear sweep voltammetry (LSV) were employed to study the electrophotocatalysis for degradation of RhB and MB dyes of the $BiVO_4$ film upon light and no light irradiation. Figures 5.31 and 5.32

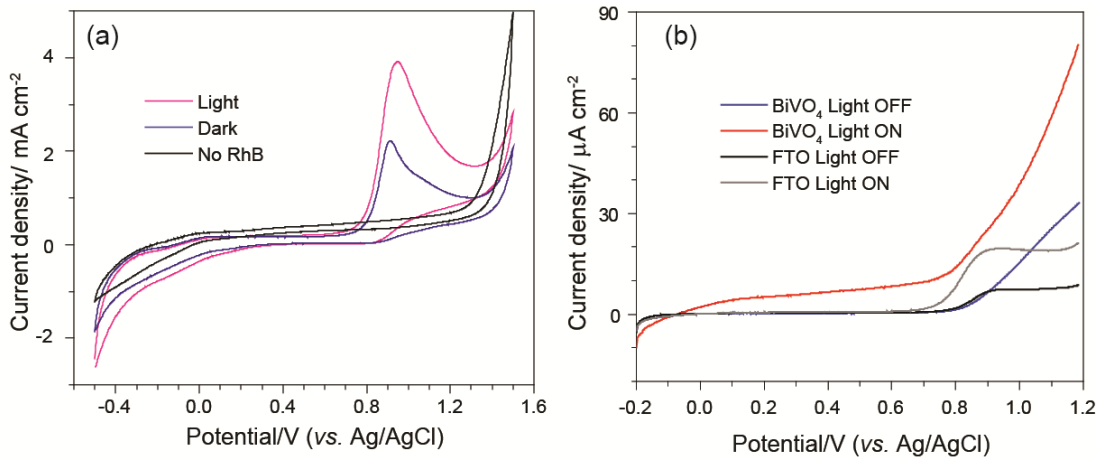

Figure 5.31 (a) CVs and (b) LSVs of the $BiVO_4$ electrode in 0.1M Na_2SO_4 containing 25 µM RhB solution (pH 5.0) at scan rate of 100 and 2 mV s^{-1}, respectively.

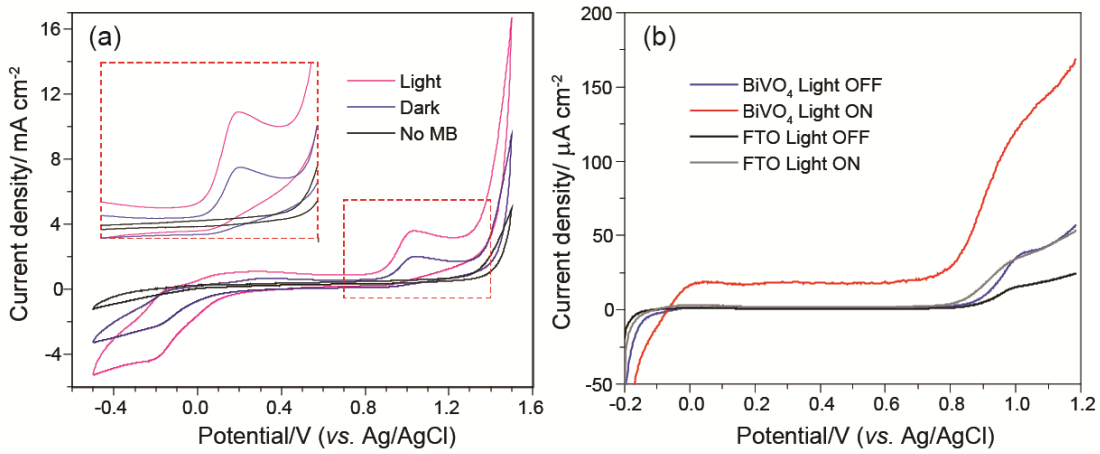

Figure 5.32 (a) CVs and (b) LSVs of the $BiVO_4$ electrode in 0.1M Na_2SO_4 containing 50 µM MB solution (pH 5.6) at 100 and 2 mV s^{-1}, respectively.

show CVs and LSVs of the $BiVO_4$ electrode with 25 µM RhB and 50 µM MB solution with supporting electrolyte (0.1M Na_2SO_4), respectively. The applied potential was in the range of -0.5 to 1.5 V (*vs.* Ag/AgCl) with scan rate 100 mV s^{-1} for the CV measurement, and of -0.2 to 1.2 V with scan rate 2 mV s^{-1} for the LSV measurement. As shown in Figure in Figure 5.31(a), an semi-reversible peak at about 0.90 V (vs Ag/AgCl) was observed, which was contributed to oxidative decomposition of RhB.[59, 60]

In the presence of MB (Figure 5.32(a)), two peaks of anodic and catholic currents appear at 1.0 V and -0.25V, respectively.[61] The peak current increased when the $BiVO_4$ electrode was irradiated by sun light for both dye.

Control experiments without any dye solution were performed, where an anodic current sharply increase at about 1.4 V (*vs.* Ag/AgCl) corresponding to water oxidation. In RhB (Figure 5.31(b)) and MB (Figure 5.32(b)) solutions, the LSVs results over the $BiVO_4$ film exhibited significantly higher anodic current and lower onset potential than that of a FTO substrate under both light and no light irradiation. Upon light irradiation, the onset potentials of the $BiVO_4$ film with RhB and MB dyes were found to be 0.68 and 0.78 V (vs. Ag/AgCl), respectively, which corresponded to the CVs results their onset of oxidation peaks. Furthermore, it should be noted that there is no peak at 0.60–0.90 V for CV the voltammogram of FTO substrate in the absence of dyes, but the onset potentials were observed at about 0.70 and 0.80 V for its LSV voltammogram with slower scan rate (2 mV s^{-1}) in the presence of RhB and MB dyes, respectively. This is confirming that the anodic current peak at 0.90 V (Figure 5.31(a)) and 1.0 V (Figure 5.32(a)), and the corresponded onset potentials at 0.70 V (Figure 5.31(b)) and 0.80 V (Figure 5.32(b)) belong to oxidative decomposition of RhB and MB, respectively.[61]

To further investigate the photoinduced behaviours and improve photocatalytic properties of the MW film, the chronoamperometric responses (I–t curves) were measured upon the on-off sun light at bias potentials of 0.70 V and 0.80 V (*vs.* Ag/AgCl) for RhB and MB solutions, respectively as shown in Figure 5.33. Both applied voltages were chosen due to being oxidative decomposition of both dyes form their CVs and LSV results (Figures 5.31 and 5.32).

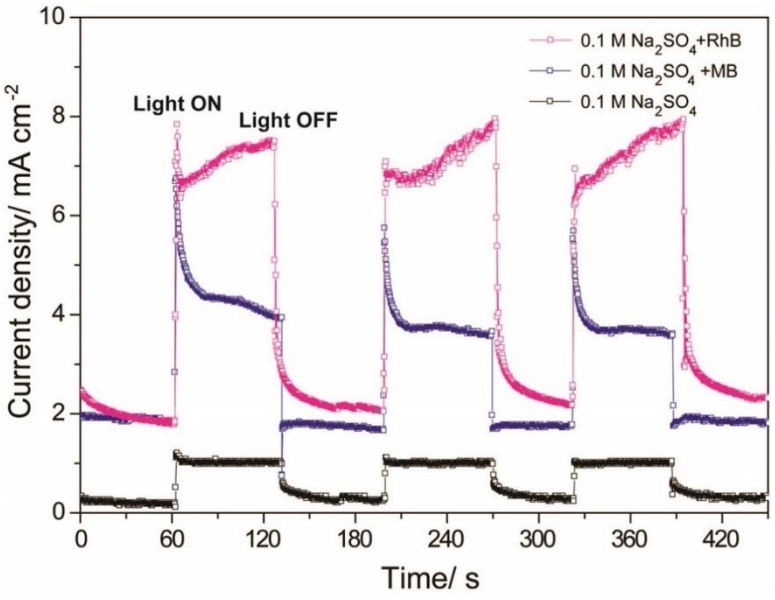

Figure 5.33 Photocurrent produced by the $BiVO_4$ electrode (MW-60-90-7) for three on-off cycles of sun light irradiation at an applied potential of 0.70 V (*vs.* Ag/AgCl) for RhB and 0.8 V (*vs.* Ag/AgCl) for MB solution.

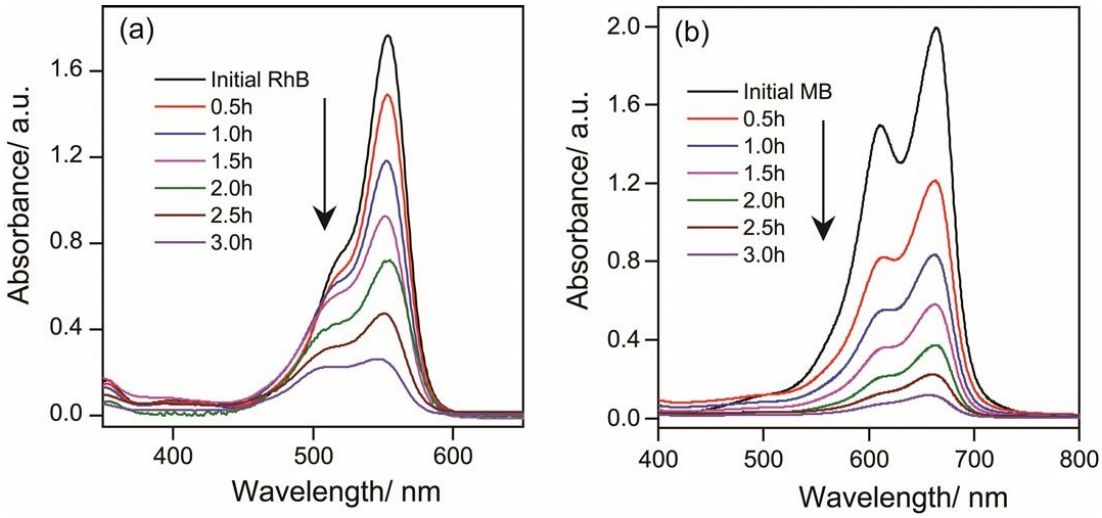

Figure 5.34 (a) RhB and (b) MB spectra from electrophotocatalytic process at 0.70 V and 0.80 V (*vs.* Ag/AgCl), respectively under sun light irradiation.

In the dark, photocurrent of the $BiVO_4$ film (microwave synthesis) with applied bias potentials in RhB and MB dye solutions were observed, and were found to be stable

at around 2.35 and 1.98 mA cm^{-2}, respectively. It could be assumed that decomposition process of both dyes was occurred in the system. Moreover, the photocurrent densities of both dye solutions were higher (7.23 and 4.08 mA cm^{-2}, respectively) when the light was on, and then promptly decreased as the light was turned off. The trend agrees with the CVs and LSVs results that more photocurrent density leads to high degradation process due to reducing recombination between electrons (e^-) at CB and holes (h^+) at VB. This could be confirmed from the reduction of UV-vis spectra of RhB (Figure 5.34(a)) and MB (Figure 5.34(b)) during electro photocatalytic process.

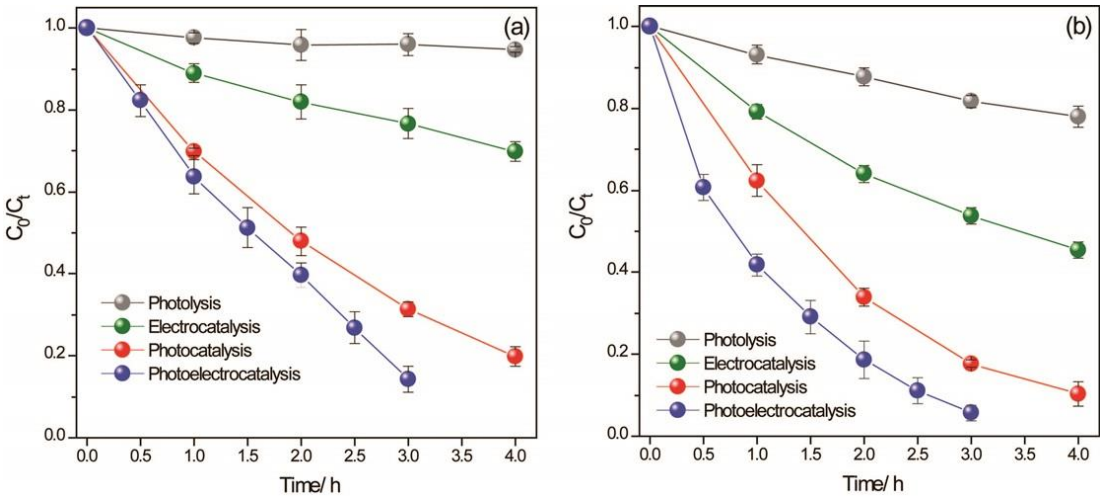

Figure 5.35 Electrophotocatalytic efficiencies for degradation of (a) RhB and (b) MB dyes with applied 0.70 V and 0.80 V (*vs.* Ag/AgCl), respectively under solar irradiation for 3 h.

It could be suggested that, under sun light and then the e^- separation under an anode bias can restrain the rapid recombination of the photogenerated charge carriers under sun light irradiation. Thus, the two processes are balanced as the recombination of e^- and h^+ is saturated, leading to enhance photocatalytic activity for degradation of both dyes over the $BiVO_4$ film even used the smaller cell.[62, 63] Figure 5.35 shows

comparison of the photocatalytic, electrocatalytic and electrophotocatalytic degradation of RhB (Figure 5.35(a)) and MB (Figure 5.35(b)) dyes for the $BiVO_4$ film synthesised by microwave. After 3 h solar irradiation, 0.48 h^{-1} and 0. 98 h^{-1} for degradation rate of RhB and MB, respectively were obtained at an applied bias potentials of 0.70 V and 0.80 V (*vs.* Ag/AgCl), respectively; while only 0.006 h^{-1} of RhB and 0.047 h^{-1} of MB were self-degraded and 0.38 $h^{-1}$of RhB and 0.58 $h^{-1}$of MB were degraded with the same photocatalyst of $BiVO_4$ film in the absence of an applied bias potentials. This result indicated that the degradation activities of both dyes were improved extremely by electrophotocatalysis.

5.9 Conclusions

A single-step microwave method has been developed to synthesise high-purity $BiVO_4$ nanoparticles. The pH of the precursor solution and microwave treatment time had significant influences on the crystal structure and morphology of the obtained $BiVO_4$ powder. At precursor pH values lower than 7, mixture of monoclinic and tetragonal structures were obtained. $BiVO_4$ synthesised at pH ≥ 7 provided only monoclinic phase material, with the crystallinity of $BiVO_4$ decreasing as pH increased. In spite of this decrease in crystal size surface area also goes down due to heavy agglomeration.

$BiVO_4$ with small spherical particles of 40 nm, band energy of 2.44 eV and pure monoclinic structure was obtained using a pH 7 solution, microwave power less than 300 W, at low temperature (90°C), and short reaction time (60 min). The photocatalytic properties of all synthesised $BiVO_4$ films for degradation of dyes were determinated by fitting with Langmuir-Hinshelwood kinetic model, which the $BiVO_4$ film synthesised from above condition exhibited high photocatalytic activity for degradation of RhB and MB under sunlight irradiation due to their provision of high surface area.

The crystallinities, morphologies and photocatalytic properties of the synthesised $BiVO_4$ by microwave were further compared to of synthesised $BiVO_4$ by the

precipitation and hydrothermal methods under the same starting precursors ($Bi(NO_3)_3$and NH_4VO_3), solvents (H_2O and dill. HNO_3), pH control agent (NH_4OH) and pH of final solution (pH7). The crystalline structure of synthesised $BiVO_4$ from all methods showed a single structure of monoclinic $BiVO_4$. On the other hand, each method yielded radically different morphologies. The $BiVO_4$ synthesised by microwave had small spherical particles, while the $BiVO_4$ synthesised by hydrothermal and precipitation methods were rod-like particles and ellipsoidal particles, respectively.

The photocatalytic properties of the synthesised $BiVO_4$ films with different methods for degradation of RhB and MB dyes were similarly due to their providing similarly high surface area after making the films. The photocatalytic mechanism was validated by electrochemical methods of the $BiVO_4$ synthesised by microwave method, including cyclic voltammetry, chronoamperometry (I-t curves) and Mott-Schottky analysis.

Furthermore, electrophotocatalytic degradation of RhB and MB over the $BiVO_4$ film were carried out with an applied voltage of 0.70 V and 0.80 V (*vs.* Ag/AgCl), respectively since the electron separation under an anode bias can restrain the rapid recombination of the photogenerated charge carriers under sun light irradiation, then the photocatalytic ability was improved.

References

1. A. K. Bhattacharya, K. K. Mallick and A. Hartridge, *Mater. Lett.*, 1997, **30**, 7–13.
2. P. Wood and F. P. Glasser, *Ceram. Int.*, 2004, **30**, 875–882.
3. M. Gotić, S. Musić, M. Ivanda, M. Šoufek and S. Popović, *J. Mol. Struct.*, 2005, **744–747**, 535–540.
4. J. Yu, Y. Zhang and A. Kudo, *J. Solid State Chem.*, 2009, **182**, 223–228.
5. A. Martínez-de la Cruz and U. M. G. Pérez, *Mater. Res. Bull.*, 2010, **45**, 135–141.
6. A. Kudo, K. Omori and H. Kato, *J. Am. Chem. Soc.*, 1999, **121**, 11459–11467.
7. K. Hirota, G. Komatsu, H. Takemura and O. Yamaguchi, *Ceram. Int.*, 1992, **18**, 285–287.
8. H. Liu, R. Nakamura and Y. Nakato, *J. Electrochem. Soc.*, 2005, **152**, G856–G861.
9. J. Liu, H. Wang, S. Wang and H. Yan, *Mater. Sci. Eng., B*, 2003, **104**, 36–39.
10. L. Zhang, D. Chen and X. Jiao, *J. Phys. Chem. B*, 2006, **110**, 2668–2673.
11. A. Zhang and J. Zhang, *Mater. Lett.*, 2009, **63**, 1939–1942.
12. S. Obregón, A. Caballero and G. Colón, *Appl. Catal., B*, 2012, **117–118**, 59–66.
13. R. Roy, *J. Solid State Chem.*, 1994, **111**, 11–17.
14. H. Zhang, J. Liu, H. Wang, W. Zhang and H. Yan, *J. Nanopart. Res.*, 2008, **10**, 767–774.
15. I. Bilecka and M. Niederberger, *Nanoscale*, 2010, **2**, 1358–1374.
16. L. Pan, X. Liu, Z. Sun and C. Q. Sun, *J. Mater. Chem. A*, 2013, **1**, 8299–8326.
17. M. Baghbanzadeh, L. Carbone, P. D. Cozzoli and C. O. Kappe, *Angew. Chem. Int. Ed.*, 2011, **50**, 11312–11359.
18 S. Dong, J. Feng, M. Fan, Y. Pi, L. Hu, X. Han, M. Liu, J. Sun and J. Sun, *RSC Adv.*, 2015, **5**, 14610–14630.
19. W. Shi, Y. Yan and X. Yan, *Chem. Eng. J.*, 2013, **215–216**, 740–746.

20. Y. Zhang, G. Li, X. Yang, H. Yang, Z. Lu and R. Chen, *J. Alloy. Compd.*, 2013, **551**, 544–550.

21. Z. Jing and J. Zhan, *Adv. Mater.*, 2008, **20**, 4547–4551.

22. S. Cho, S. H. Jung and K. H. Lee, *J. Phys. Chem. C*, 2008, **112**, 12769–12776.

23. H. J. Ahn, H. C. Choi, K. W. Park, S. B. Kim and Y. E. Sung, *J. Phys. Chem. B*, 2004, **108**, 9815–9820.

24. W. W. Wang, Y. J. Zhu and M. L. Ruan, *J. Nanopart. Res.*, 2007, **9**, 419–426.

25. X. Hu, J. C. Yu and J. Gong, *J. Phys. Chem. C*, 2007, **111**, 11180–11185.

26. T. Muraliganth, A. Vadivel Murugan and A. Manthiram, *Chem. Commun.*, 2009, **1**, 7360–7362.

27. T. Suprabha, H. Roy, J. Thomas, K. Praveen Kumar and S. Mathew, *Nanoscale Res. Lett.*, 2009, **4**, 144–152.

28. K. Manseki, Y. Kondo, T. Ban, T. Sugiura and T. Yoshida, *Dalton Trans.*, 2013, **42**, 3295–3299.

29. D. Zhang, G. Li, F. Wang and J. C. Yu, *Cryst. Eng. Comm.*, 2010, **12**, 1759–1763.

30. H. T. Zhu, C. Y. Zhang, Y. M. Tang and J. X. Wang, *J. Phys. Chem. C*, 2007, **111**, 1646–1650.

31. L. X. Yang, Y. J. Zhu, H. Tong, W. W. Wang and G. F. Cheng, *J. Solid State Chem.*, 2006, **179**, 1225–1229.

32. N. Wetchakun, S. Chaiwichain, B. Inceesungvorn, K. Pingmuang, S. Phanichphant, A. I. Minett and J. Chen, *ACS Appl. Mater. Interfaces*, 2012, **4**, 3718–3723.

33. K. Pingmuang, N. Wetchakun, W. Kangwansupamonkon, K. Ounnunkad, B. Inceesungvorn and S. Phanichphant, *Int. J. Photoenergy*, 2013, **2013**, 7.

34. S. Tokunaga, H. Kato and A. Kudo, *Chem. Mater.*, 2001, **13**, 4624–4628.

35. G. Tan, L. Zhang, H. Ren, S. Wei, J. Huang and A. Xia, *ACS Appl. Mater. Interfaces*, 2013, **5**, 5186–5193.

36. S. Obregon and G. Colon, *Catal. Sci. Tech.*, 2014, **4**, 2042–2050.

37. R. Venkatesan, S. Velumani and A. Kassiba, *Mater. Chem. Phys.*, 2012, **135**, 842–848.B.

38. X. Lei, L. L. Zeng, P. Zhang, Z. F. Sun, W. Sun and X. X. Zhang, *Adv. Powder Technol.*, 2014, **25**, 946–951.

39. L. Zhou, W. Wang, L. Zhang, H. Xu and W. Zhu, *J. Phys.Chem. C*, 2007, **111**, 13659–13664.

40. B. Xie, C. He, P. Cai and Y. Xiong, *Thin Solid Films*, 2010, **518**, 1958–1961.

41. Z. Zhu, L. Zhang, J. Li, J. Du, Y. Zhang and J. Zhou, *Ceram. Int.*, 2013, **39**, 7461–7465.

42. A. Houas, H. Lachheb, M. Ksibi, E. Elaloui, C. Guillard and J. M. Herrmann, *Appl. Catal., B*, 2001, **31**, 145–157.

43. K. Liu, Z. Chang, W. Li, P. Che and H. Zhou, *Sci. China Chem.*, 2012, **55**, 1770–1775.

44. J. Zhao, T. Wu, K. Wu, K. Oikawa, H. Hidaka and N. Serpone, *Environ. Sci. Technol.*, 1998, **32**, 2394–2400.

45. R. Li, F. Zhang, D. Wang, J. Yang, M. Li, J. Zhu, X. Zhou, H. Han and C. Li, *Nat. Commun.*, 2013, **4**, 1432.

46. K. V. Kumar, K. Porkodi and F. Rocha, *Catal. Commun.*, 2008, **9**, 82–84.

47. M. Kaneko, H. Ueno and J. Nemoto, *Beilstein J. Nanotechnol.*, 2011, **2**, 127–134.

48. S. J. Hong, S. Lee, J. S. Jang and J. S. Lee, *Energy Environ. Sci.*, 2011, **4**, 1781–1787.

49. W. Luo, Z. Yang, Z. Li, J. Zhang, J. Liu, Z. Zhao, Z. Wang, S. Yan, T. Yu and Z. Zou, *Energy Environ. Sci.*, 2011, **4**, 4046–4051.

50. J. Tang, D. Li, Z. Feng, Z. Tan and B. Ou, *RSC Adv.*, 2014, **4**, 2151–2154.

51. X.X. Wei, C.M. Chen, S.Q. Guo, F. Guo, X.M. Li, X.X. Wang, H. T. Cui, L.F. Zhao and W. Li, *J. Mater. Chem. A*, 2014, **2**, 4667–4675.

52. D. Du, W. Li, S. Chen, T. Yan, J. You and D. Kong, *New J. Chem.*, 2015, **39**, 3129–3136.

53. Z. Xiong and X. S. Zhao, *RSC Adv.*, 2014, **4**, 61960–61967.

54. T. Shen, Z.G. Zhao, Q. Yu and H.J. Xu, *J. Photoch. Photobio., A*, 1989, **47**, 203–212.

55. S. Nishimoto, T. Mano, Y. Kameshima and M. Miyake, *Chem. Phys. Lett.*, 2010, **500**, 86–89.

56. W. Liu, M. Wang, C. Xu, S. Chen and X. Fu, *Mater. Res. Bull.*, 2013, **48**, 106–113.

57. P. Wang, Y. Xia, P. Wu, X. Wang, H. Yu and J. Yu, *J. Phys. Chem. C*, 2014, **118**, 8891–8898.

58. J. Xia, S. Yin, H. Li, H. Xu, L. Xu and Y. Xu, *Dalton Trans.,* 2011, **40**, 5249–5258.

59. Z. Han, L. Liao, Y. Wu, H. Pan, S. Shen and J. Chen, *J. Hazard. Mater.*, 2012, **217–218**, 100–106.

60. O. Zhang, B.Z. Lin, Y.L. Chen, B.F. Gao, L.M. Fu and B. Li, *Electrochim. Acta*, 2012, **81**, 74–82.

61. F. Manea and A. Pop, *Decontamination of Wastewaters Containing Organics by Electrochemical Methods*, 2013.

62. M. Wang, L. Sun, Z. Lin, J. Cai, K. Xie and C. Lin, *Energy Environ. Sci.*, 2013, **6**, 1211–1220.

63. B. Ntsendwana, S. Sampath, B. B. Mamba and O. A. Arotiba, *Photochem. Photobiol. Sci.*, 2013, **12**, 1091–1102.

CHAPTER 6

BISMUTHVANADATE COMPOSITES WITH CERIUM DIOXIDE TITANIUM DIOXIDE AND TUNGSEN TRIOXIDE

6.1 Introduction

Bismuth vanadate ($BiVO_4$) has attracted much attention as a highly responsive visible-light driven photocatalyst due to its narrow band gap energy of 2.4 eV. Thus, it has been used in the photocatalytic degradation of organic dyes in aqueous solution and splitting of water for oxygen evolution under sunlight irradiation.[1-4] However, one of limitations of the photocatalytic efficiency in pure $BiVO_4$ is the fast recombination of photogenerated electrons and holes, with the free carrier life time reported to be about 40 ns by Abdi *et al.*.[5] In order to enhance the photocatalytic activity of $BiVO_4$, an essential requirement is to fabricate an electronic barrier, which facilities spatial separation of the photogenerated electrons and holes. This charge separation prevents the electrons and holes from recombination. Thus, the electrons and holes have more opportunities to participate in reduction and oxidation reactions for the degradation of organic materials. [4, 6] Many attempts have been made in order to improve the photocatalytic performance via enhancing an electron hole separation, such as doping these semiconductors with metal and non-metals, and sensitising composite with other metal oxide semiconductors.[4, 6, 7]

Recently, some publications of coupled $BiVO_4$ with other metal oxides such as Bi_2O_3,[8, 9] V_2O_5,[10, 11] TiO_2,[12, 13] WO_3,[11, 14-16] CdS,[17] $CuCr_2O_4$ [18] and $CuWO_4$ [19] have been reported in water purification and water spitting applications (coupling the different materials will create a heterostructured photocatalyst, which can facilitate electron-hole transport and separation if the band energy differ.

Li *et al.* reported a $Bi_2O_3/BiVO_4$ nanocomposite, synthesised by a two-step process. This synthesis included a simple decomposition reaction to produce monoclinic Bi_2O_3 (600°C for 6 h) and a homogeneous precipitation method at room temperature to decorate these sphere with tetragonal $BiVO_4$.[8] Another report, desorbs the synthesis of a porous peanut-like $Bi_2O_3/BiVO_4$ composite by a one-step mixed solvothermal method with the assistance of a L-lysine template.[9] Photocatalytic degradation of organic dyes include Rhodamine B (RhB) and Methylene blue (MB), were also investigated, and the composite catalysts exhibited higher photocatalytic activities.

Jiang *et al.* reported a $V_2O_5/BiVO_4$ composite photocatalyst with orthorhombic and monoclinic structures of V_2O_5 and $BiVO_4$, respectively, synthesised by a one-step solution combustion synthesis method.[10] The 9 mol% $V_2O_5/BiVO_4$ composite photocatalyst annealed at 500°C for 4 h exhibited the best photocatalytic degradation activities of MB.

Hu *et al.* reported that the $BiVO_4/TiO_2$ heterostructure was synthesised by a sol-gel method with optimum content of $BiVO_4$:TiO_2 as 1:200 (mass ratio), which could enhanced photocatalytic degradation of benzene under visible light irradiation.[12] Zhang *et al.* also synthesised $BiVO_4/TiO_2$ composite photocatalysts with heterojunction structures of monoclinic $BiVO_4$ and anatase TiO_2 by a one-step of combined microwave and hydrothermal method at 200°C, and the 20%$TiO_2/BiVO_4$ showed the best photocatalytic activity for degradation of RhB.[13] Recently, a ternary $Er^{3+}/BiVO_4/TiO_2$ composite synthesised by a simple impregnation method was reported by Obregon and Colon for degradation of phenol.[20] The result showed that the best photocatalytic performance was attained for the samples of 1 wt% $Er^{3+}/BiVO_4$ content with respect to TiO_2, since this composite provided different band position leading to effective charge pair separation which induced higher photocatalytic activities. Furthermore, Chatchai *et al.* studied the photocatalytic and electrophotocatalytic properties of $WO_3/BiVO_4$ photoanode for the degradation of

methylene blue, in which the composite electrode was fabricated by an electrodeposition technique.[15] The photo-electrocatalytic system of $WO_3/BiVO_4$ photoanode with a Cu_2O photocathode modified with Ag showed higher performance for MB degradation under visible light irradiation than the individual photocatalytic system.

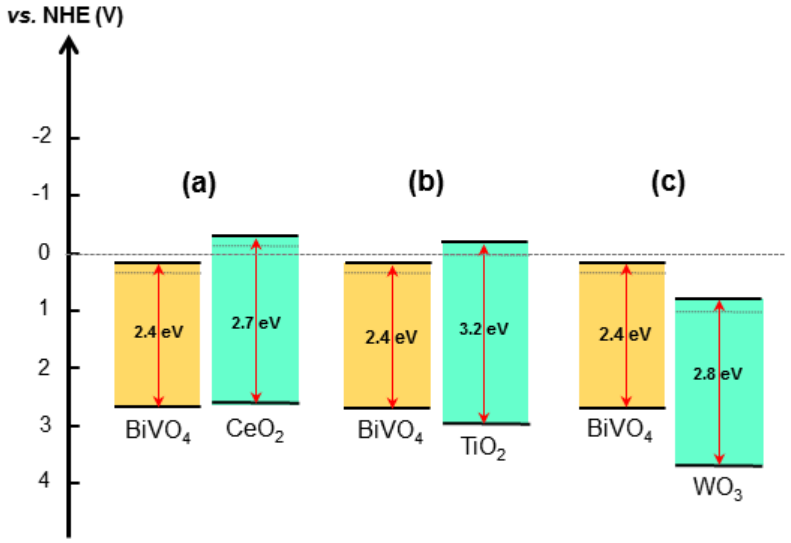

Figure 6.1 Schematic diagrams of the possible energy band structures of coupling (a) $CeO_2/BiVO_4$, (b) $TiO_2/BiVO_4$ and (c) $BiVO_4/WO_3$ composites at pH 0 based on the literature reviews.

It could be observed that the composite semiconductor photocatalysts were more photocatalytically active than its individual catalysts for all photocatalytic degradation of organic pollutants of the above composites. Therefore, $BiVO_4$ based composites, $CeO_2/BiVO_4$, $TiO_2/BiVO_4$ and $BiVO_4/WO_3$ with different valence band (VB) and conduction band (CB) offsets were chosen to study for photodegradation of RhB and MB dyes in this research. The composites were selected since the CB and VB potential edges of $BiVO_4$ are more positive than of CeO_2, in between those of TiO_2, and more negative than of WO_3, as shown in Figure 6.1.[6, 7, 21, 22] The photodegradation mechanisms of RhB and MB dyes in aqueous solution, under solar light irradiation of

above three composites were studied and investigated using an indirect chemical probe method (active species trapping), monochromatic illumination and Mott-Schottky experiments. Additionally, X-ray photoelectron spectroscopy (XPS) and Transmission electron microscopy (TEM) were also employed to characterise these composite photocatalysts.

6.2 Experimental section

6.2.1 Preparation of $BiVO_4$ powder

Pure $BiVO_4$ was synthesised by the homogeneous precipitation method using bismuth nitrate pentahydrate ($Bi(NO_3)_3{\cdot}5H_2O$, Sigma-Aldrich) and ammonium meta-vanadate (NH_4VO_3, Aldrich) as bismuth and vanadium precursors, respectively. In a typical procedure, 0.125 M each of Bi^{3+} and V^{5+} precursors were separately prepared by dissolving $Bi(NO_3)_3{\cdot}5H_2O$ in 3 M nitric acid (HNO_3) solution and NH_4VO_3 in 3 M ammonium hydroxide (NH_4OH) solution. The vanadium precursor solution was slowly added to the bismuth nitrate solution under stirring over 30 min. Then 3 M ammonia solution was added drop wise until pH 7 was attained. The resultant precipitate was washed with deionized water, centrifuged and dried at 60°C for 12 h. Finally, the dried powder was then calcined at 450°C for 2 h to obtain $BiVO_4$ powder.

6.2.2 Preparation of CeO_2 and $CeO_2/BiVO_4$ composite powder

Pure CeO_2 and $BiVO_4/CeO_2$ nanocomposite catalysts were prepared with different mole ratios (4:1, 3:2, 1:1, 2:3 and 1:4.) by a precipitation process. Briefly, Cerium(III)nitrate hexahydrate ($Ce(NO_3)_3{\cdot}6H_2O$, Sigma-Aldrich) was dissolved in 100 mL of 80% v/v ethylene glycol solution. The solution was kept under constant stirring and heated at 50°C until a homogeneous solution was obtained. The $BiVO_4$ powder was subsequently added to the above cerium precursor solution to prepare $BiVO_4/CeO_2$ composite with the desired mole ratio. After that, 25 mL of 3 M ammonium

hydroxide (NH_4OH) was slowly added into the above solution, and the transparent solution changed to a yellowish suspension. The suspension was kept under stirring at 50°C for a further 24 h and the precipitate was finally collected by centrifugation, washed 3 times with deionised water and then dried at 60°C for 24 h. The obtained powder was subsequently calcined at 450°C for 2 h. The as-synthesised composites were characterised and actual the ratio of $BiVO_4$:CeO_2 was confirmed by elemental analysis of Bi (from to $BiVO_4$) and Ce (CeO_2). For control experiments, pure CeO_2 was also prepared by the procedure described above, without the $BiVO_4$ addition step.

6.2.3 Preparation of TiO_2 and TiO_2/$BiVO_4$ composite powder

$BiVO_4$/TiO_2 nanocomposite catalysts with different mole ratios (4:1, 3:2, 1:1, 2:3 and 1:4.) between $BiVO_4$ and TiO_2 were synthesised by coupling a precipitation and sol-gel methods. Firstly, pure $BiVO_4$ powder was synthesised as per section 6.2.1. The sol-gel method of anatase TiO_2 synthesis reported by Wetchakun *et al.*[23], was chosen to produce pure TiO_2 and the TiO_2/$BiVO_4$ nanocomposites. Firstly, 20 mL titanium tetraisopropoxide (TTIP, Sigma-Aldrich) was dissolved in 250 mL 6 M nitric acid solution and mixed until a homogeneous solution was obtained. The mixture of TTIP and nitric acid solution was put into a cellophane membrane and then placed in solution containing a 1:1 v/v ratio (350 mL) of absolute ethanol and deionized water with 0.5–1.0 vol% concentrated (25%) ammonia. The $BiVO_4$ powder was subsequently added to the above mixture in the cellophane pouch to synthesise $BiVO_4$/TiO_2 composite powders. The mixture inside the cellophane pouch was kept stirring with magnetic stirrer bar and heated to 80°C for 1 h. After the completion of the dialysis process, the suspension was centrifuged at 5000 rpm for 10 min, washed with deionised water and then dried in an oven at 60°C for 24 h. The obtained powder was finally calcined in a furnace at the temperature of 450°C for 2 h. For control

experiments, pure TiO_2 photocatalyst was also synthesised by the procedure described above, without any $BiVO_4$ added.

6.2.4 Preparation of WO_3 and $BiVO_4/WO_3$ composite powder

$BiVO_4/WO_3$ nanocomposite photocatalysts with different mole ratios between were synthesised by a two step precipitation processes, because the $BiVO_4$ powder is not stable in acidic condition, WO_3 powder was first synthesised by dissolving 5 g of sodium tungstate dihydrate ($Na_2WO_4 \cdot 2H_2O$, Sigma-Aldrich) in a solution containing 10 g of citric acid, 75 mL of ethylene glycol and 25 mL of deionized water under continuous stirring. The solution was heated at 70°C, and then 25 mL of 1M hydrochloric acid (HCl) was added to the above solution (pH ~1). The mixed solution was kept under continuous stirring and maintaining a constant temperature until the formation of a yellow-green precipitate. This powder was separated by centrifugation, washed with deionized water and ethanol several times, dried at 60°C for 24 h, and then calcined at 450°C for 2 h. This WO_3 powder was mixed into precursor solution used in BiVO4 synthesis by precipitation (see section 6.2.1).

6.2.5 Fabrication of photocatalyst films and photocatalyst test

All synthesised catalysts described above were used to produce photocatalyst film by the doctor blading onto glass substrates. The photocatalytic activities these also investigated by degradation of RhB and MB under solar light irradiation as described in Chapter 2. According to the results of thickness optimisation study in Chapter 4, the thicknesses of all fabricated films in this research were controlled to be about ~2.5 μm. The films were measured by using a stylus profilometer (Veeco Dektak 150).

An indirect chemical probe method was employed to investigate the mechanisms of dye degradation. Scavengers of various possible active species, including

isopropanol (IPA, $^{\bullet}OH$), benzoquinone (BQ, $O_2^{-\bullet}$) and ethylenediamine tetra acetic acid (EDTA, h^+), were added during the photoreaction, after which the dye degradation rate was measured.

6.3 Physical properties of composited photocatalysts

6.3.1 Structural characterisation

Table 6.1 shows percent yield of the synthesised $CeO_2/BiVO_4$ composites with different mole ratios by the two-steps precipitation method. It was found that the percent yield of the $CeO_2/BiVO_4$ composites decreased when increased the amount of CeO_2 loading, this probably because of lost CeO_2 nanoparticles during the washing process. As the crystal size calculated by Scherrer equation (Equation (3.8) of CeO_2 particles had about 5 nm was much smaller than $BiVO_4$ particles (~20 nm).

Table 6.1 Percent yield of the synthesised $CeO_2/BiVO_4$ composite powders with different mole ratios by the two-steps precipitation method.

Samples	Yield (%)
CeO_2	88
4:1$CeO_2/BiVO_4$	83
3:2$CeO_2/BiVO_4$	91
1:1$CeO_2/BiVO_4$	93
2:3$CeO_2/BiVO_4$	90
1:4$CeO_2/BiVO_4$	89
$BiVO_4$	92

The phase crystallinity of all composite powders and films synthesised in this research were analysed by X-ray diffraction using CuKα radiation (λ= 0.154 nm) at 2θ = 15–55° with a step size of 0.06 and a scanning speed of 0.72° per min.

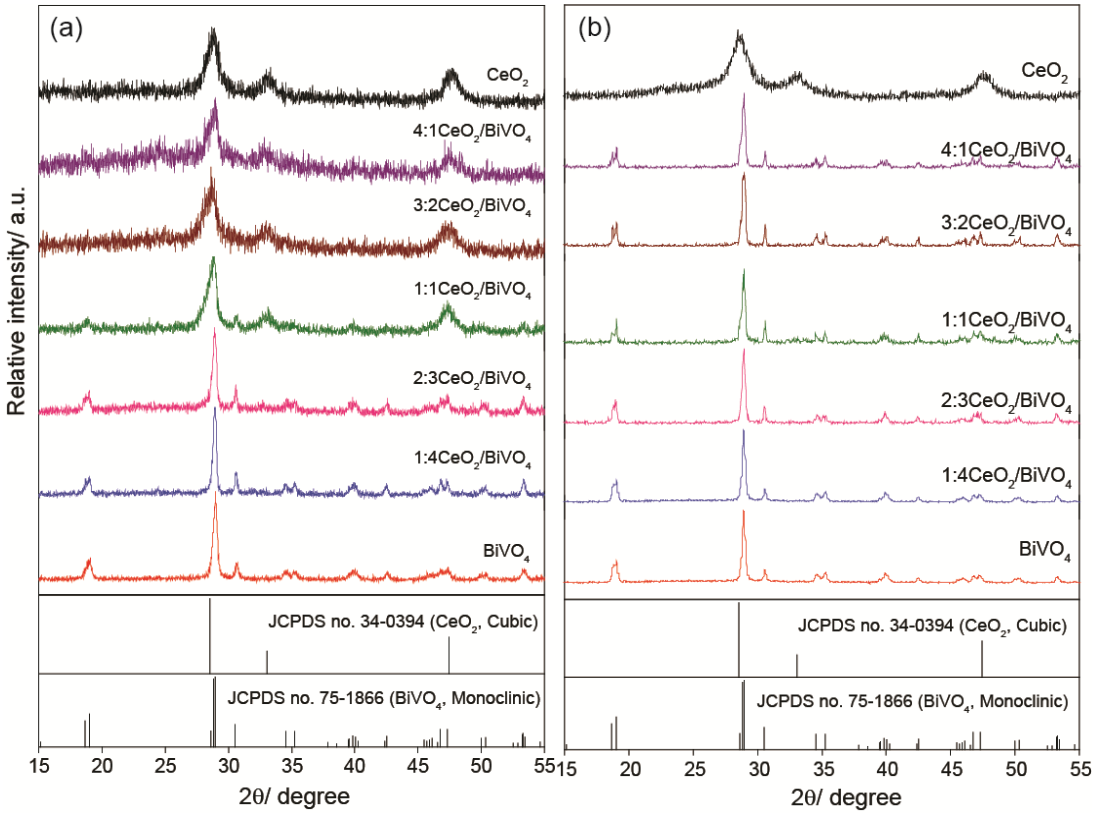

Figure 6.2 XRD patterns of pure $BiVO_4$, pure CeO_2 and $CeO_2/BiVO_4$ composite with different mole ratios: (a) powder and (b) film forms after annealing at 450°C for 2 h.

Figure 6.2(a) shows the XRD patterns of $CeO_2/BiVO_4$ composite powders with mole ratios of 4:1, 3:2, 1:1, 2:3 and 1:4 in comparison with those of pure $BiVO_4$ and pure CeO_2. The diffraction peaks of pure $BiVO_4$ at 2θ of 28.8°, 30.55°, 34.5°, 35.2°, 39.8°, and 42.5° were respectively indexed as (112), (004), (200), (020), (211), and (015) planes of monoclinic $BiVO_4$ according to the Joint Committee Powder Diffraction Standards (JCPDS) file no. 75−1866. Diffraction peaks of pure CeO_2 at 2θ of 28.8°, 33.3° and 47.6° can be indexed as the (111), (200) and (220) planes of fluorite CeO_2 with JCPDS file no. 34−0394. The XRD patterns of $BiVO_4/CeO_2$ composites exhibited characteristic diffraction peaks of both $BiVO_4$ and CeO_2 crystalline phases. It can be clearly seen from Figure 6.2(a) that, the $CeO_2/BiVO_4$ composites with mole ratio of 4:1, 3:2 and 1:1 showed the diffraction patterns of both cubic CeO_2 and monoclinic

$BiVO_4$. However, upon increasing the mole ratio of $BiVO_4$ in the composite sample, the diffraction pattern was more similar to that of pure $BiVO_4$. This is possibly due to the low crystallinity of the CeO_2 phases, thus being difficult to differentiate from the peaks of $BiVO_4$, which are at similar angles to the major CeO_2 peak.

Photocatalyst films were fabricated by a doctor blading technique on glass substrates. Figure 6.2(b) shows the XRD patterns of the $CeO_2/BiVO_4$ composite films fabricated on glass substrates after annealing at 450°C for 2 h. It was found that the XRD pattern of $CeO_2/BiVO_4$ composite films also exhibited characteristic diffraction peaks of both cubic fluorite CeO_2 and monoclinic $BiVO_4$ crystalline phases of the mole ratios as 4:1, 3:2 and 4:14, similarly with the XRD results of the composite powders and no evidence of any third phase.

Figure 6.3(a) shows the XRD patterns of pure $BiVO_4$, TiO_2 and $TiO_2/BiVO_4$ composite powders with different mole ratios. The XRD patterns of pure TiO_2 powder could be identified as the JCPDS file no. 21−1272, and the diffraction peaks correspond to tetragonal TiO_2 (anatase) are at 2θ = 25.3°, 37.8°, 48.0°, 53.9°, 55.0° and 62.7°. In XRD patterns of composite powders, it was obviously seen that the $TiO_2/BiVO_4$ composites with 4:1, 3:2, 1:1 and 2:3 mole ratios showed the formation of two phases of monoclinic $BiVO_4$ and tetragonal TiO_2. With increasing TiO_2 ratios, the diffraction peaks of the $BiVO_4$ continued to be the major phase with higher crystallinity, while the TiO_2 was seen as a minor phase. However, the TiO_2 phase was not be observed in the 4:1 $TiO_2/BiVO_4$ composite, possibly because that the amount of TiO_2 was too low and the size of TiO_2 particles was too small. Again the crystallinity of the $BiVO_4$ phase was high which may have masked the broad peak of this TiO_2 phase.

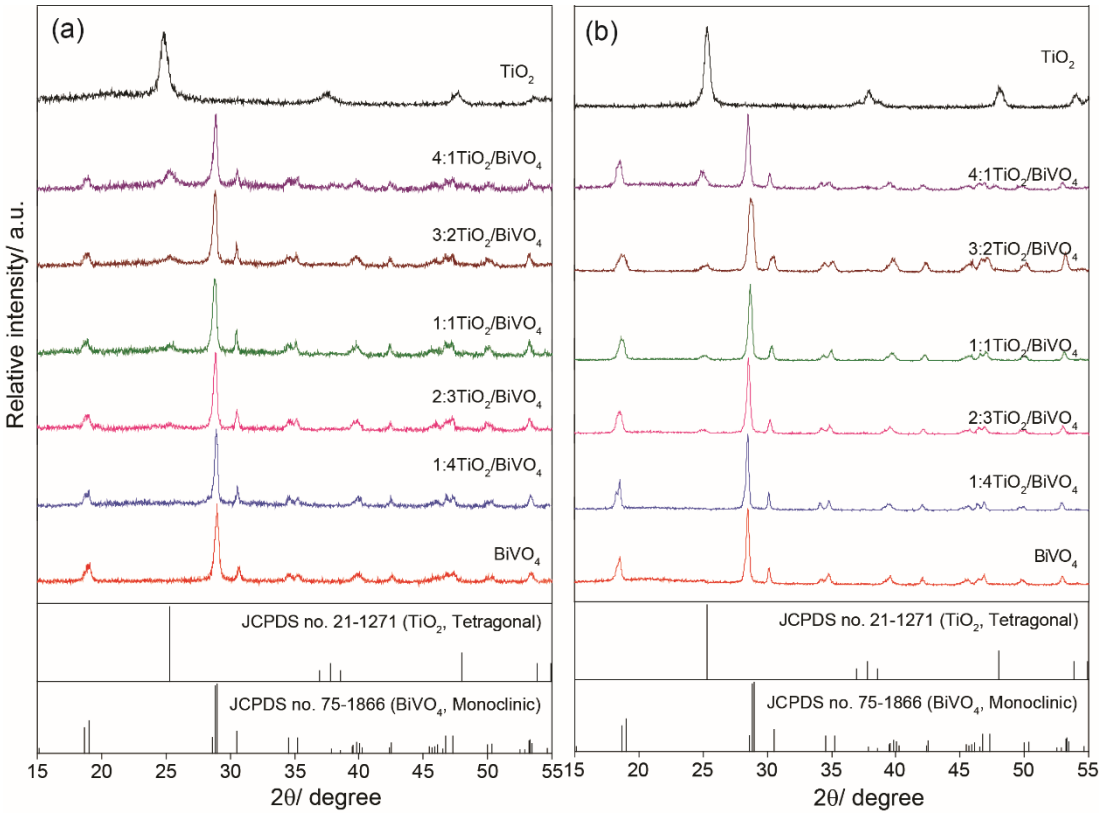

Figure 6.3 XRD patterns of pure $BiVO_4$, pure TiO_2 and $TiO_2/BiVO_4$ composite with different mole ratios: (a) powder and (b) films form after annealing at 450°C for 2 h.

The XRD pattern of the $TiO_2/BiVO_4$ composite films after annealing at 450°C for 2 h (Figure 6.3(b)) showed characteristic diffraction peaks of both monoclinic $BiVO_4$ and tetragonal TiO_2 crystalline phases similarly with the XRD results of the composite powders and no evidence of any third phase. Moreover, the XRD patterns of all prepared films (TiO_2, $BiVO_4$, and $TiO_2/BiVO_4$ composites) obtained sharper than the XRD patterns of their respecting powders (Figure 6.3(a)) indicating higher crystalline sizes as shown in Tables 6.2 and Table 6.3 for the samples before and after annealing.

Table 6.2 Comparison of phase composition and crystalline size of $TiO_2/BiVO_4$ composite powders with different mole ratios.

Samples	Yield (%)	Crystalline phase composition (%)		Crystalline size (nm)	
		$BiVO_4$	TiO_2	$BiVO_4$	TiO_2
TiO_2	84	-	100	-	10
4:1$TiO_2/BiVO_4$	87	80	20	14	9
3:2$TiO_2/BiVO_4$	82	87	13	15	7
1:1$TiO_2/BiVO_4$	90	92	8	17	8
2:3$TiO_2/BiVO_4$	93	95	5	17	9
1:4$TiO_2/BiVO_4$	89	100	0	18	-
$BiVO_4$	92	100	0	20	-

Table 6.3 Comparison of phase composition and crystalline size of $TiO_2/BiVO_4$ composite films with different mole ratios after annealing at 450°C for 2 h.

Samples	Crystalline phase composition (%)		Crystalline size (nm)	
	$BiVO_4$	TiO_2	$BiVO_4$	TiO_2
TiO_2	0	100	-	7
4:1$TiO_2/BiVO_4$	81	19	24	8
3:2$TiO_2/BiVO_4$	91	9	17	6
1:1$TiO_2/BiVO_4$	94	6	19	7
2:3$TiO_2/BiVO_4$	96	4	18	7
1:4$TiO_2/BiVO_4$	100	0	20	-
$BiVO_4$	100	0	22	-

The percentage of tetragonal TiO_2 and monoclinic $BiVO_4$ in the composites could be estimated by the relative intensities of the main XRD peaks of tetragonal TiO_2 (101) and monoclinic $BiVO_4$ (200), as shown in Equation (3.7). The average crystalline sizes of the composites were also calculated from the Scherrer equation. The summarised phase compositions and crystalline sizes of the TiO_2/$BiVO_4$ composites, with different mole ratios, are shown in Table 6.2. It was found that the monoclinic $BiVO_4$ in all the TiO_2/$BiVO_4$ composites showed as the predominant crystalline structure, and the percentage of tetragonal TiO_2 increased with increasing the mole ratio of TiO_2. Additionally, the percentages of crystalline phase compositions in the TiO_2/$BiVO_4$ composite films after annealing were not charged much compared to of the composite powders before annealing. Again the percent yield of the TiO_2/$BiVO_4$ composites decreased with increasing the amount of TiO_2 loading, since the crystal size of TiO_2 particles were much smaller compared to of $BiVO_4$.

The crystalline structure of the $BiVO_4$/WO_3 composite powders were also determined using XRD and compared to pure WO_3 and $BiVO_4$ as shown in Figure 6.4(a). The XRD pattern of pure WO_3 powder revealed diffraction peaks at 23.6°, 24.2°, 26.6°, 28.7°, 34.1°, 42.0° and 49.7° which could be indexed to (020), (200), (120), (112), (202), (222) and (400) of the monoclinic WO_3 phase, respectively in good agreement with JCPDS no. 72–0677. In the XRD patterns of the $BiVO_4$/WO_3 composite powders, it was obviously seen that the peaks belonging to monoclinic $BiVO_4$ were the major phase in all composites. Peaks belonging to monoclinic WO_3 increased when increasing mole ratio of WO_3 as corresponded with the calculated percentage of phase composition and crystalline size in Table 6.4. It was revealed that the percentage of phase composition of $BiVO_4$ in the $BiVO_4$/WO_3 composites with mole ratios of 4:1, 3:2, 1:1 and 2:3 had higher than of WO_3 indicating larger size in $BiVO_4$ than WO_3.

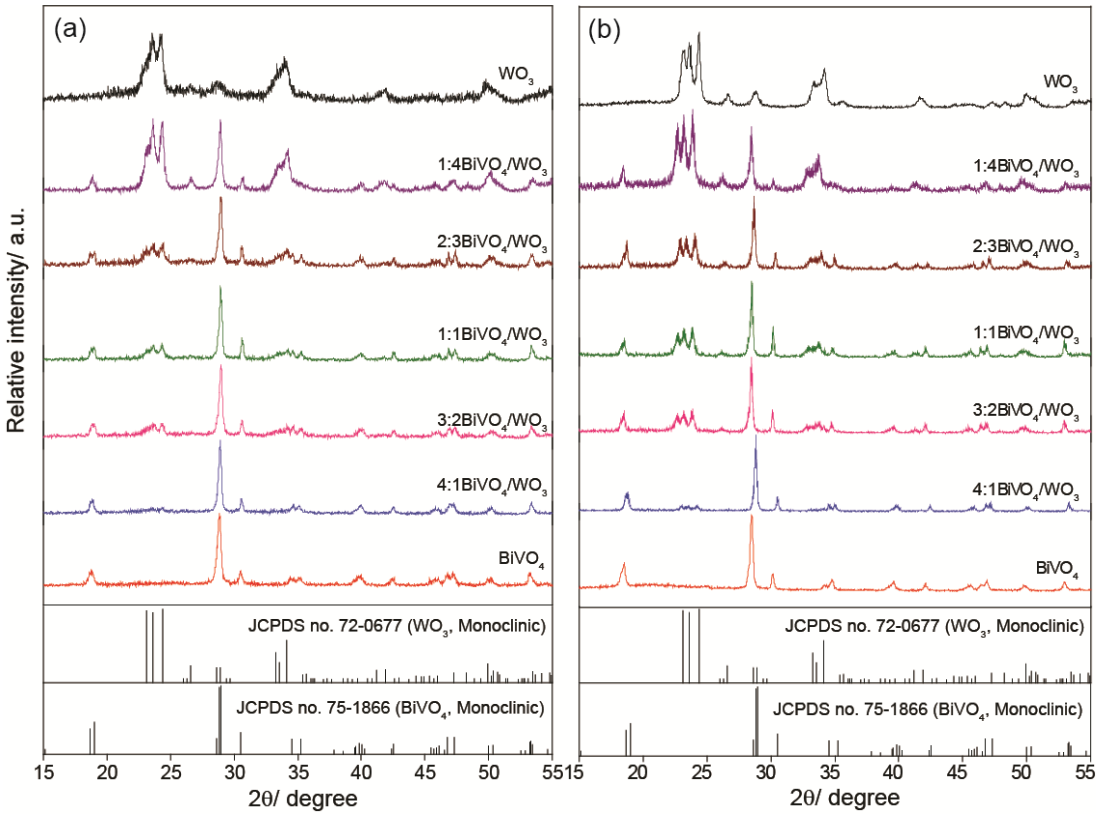

Figure 6.4 XRD patterns of pure $BiVO_4$, pure WO_3 and $BiVO_4/WO_3$ composite with different mole ratios: (a) powder form and (b) film form after annealing at 450°C for 2 h.

XRD patterns of $BiVO_4/WO_3$ composite films, along with pure $BiVO_4$ and WO_3, were also investigated as shown Figure 6.4(b). It could be observed that XRD patterns of all $BiVO_4/WO_3$ composite films showed peaks corresponding to both $BiVO_4$ and WO_3, and that these peaks were sharper than for their respective powder based measurements relating to the crystal size for a smaller size of the samples before annealing compared to after annealing as calculated and presented in Table 6.4 and Table 6.5, respectively.

Table 6.4 Comparison of phase compositions and crystalline sizes of $BiVO_4/WO_3$ composite powders with different mole ratios.

Sample	Yield (%)	Crystalline phase composition (%)		Crystalline size (nm)	
		$BiVO_4$	WO_3	$BiVO_4$	WO_3
$BiVO_4$	92	100	0	20	-
4:1$BiVO_4/WO_3$	89	94	6	25	18
3:2$BiVO_4/WO_3$	90	84	16	29	20
1:1$BiVO_4/WO_3$	92	81	19	31	24
2:3$BiVO_4/WO_3$	90	74	26	28	21
1:4$BiVO_4/WO_3$	93	49	51	32	20
WO_3	82	0	100	-	18

Table 6.5 Comparison of phase compositions and crystalline sizes of $BiVO_4/WO_3$ composite films with different mole ratios.

Sample	Crystalline phase composition (%)		Crystalline size (nm)	
	$BiVO_4$	WO_3	$BiVO_4$	WO_3
$BiVO_4$	100	-	22	-
4:1$BiVO_4/WO_3$	93	7	38	24
3:2$BiVO_4/WO_3$	76	24	40	23
1:1$BiVO_4/WO_3$	72	28	40	21
2:3$BiVO_4/WO_3$	67	33	42	23
1:4$BiVO_4/WO_3$	47	53	43	22
WO_3	-	100	-	27

From the XRD analysis, it can be concluded that the XRD patterns of the three composites including $CeO_2/BiVO_4$, $TiO_2/BiVO_4$ and $BiVO_4/WO_3$ composites reveal their two phase hybrid of each composite, however the disappearance of characteristic peaks of CeO_2 in 2:3 and 1:4$CeO_2/BiVO_4$ composites, and TiO_2 in 1:4$TiO_2/BiVO_4$ composite suggests a low amount of loading in the. Furthermore, it is noticed that percent yield of products especially in the composited $CeO_2/BiVO_4$ and $TiO_2/BiVO_4$ series decreased with increasing the amount of CeO_2 and TiO_2, respectively, this is probably due to the particles lose during washing process.

6.3.2 Raman spectroscopy

In order to investigate the composition of $CeO_2/BiVO_4$ composites, XRD was found to be ineffective technique, as both materials posed similar different peaks. Coupled with small particles size these peals were not able to be resolved. As such Raman spectroscopy was employed as an alternation. Figure 6.5 shows Raman spectra of the $CeO_2/BiVO_4$ composites with different mole ratios. The vibrational peaks at 121.9, 220.1, 322.3, 378.0, 720.9, and 831.1 cm^{-1} observed from the pure $BiVO_4$ sample were in good agreement with those from the work by Gotić *et al.*[24] and Zhang *et al.*[25]. The peaks at 720.9 and 831.1 cm^{-1} were ascribed to asymmetric and symmetric V−O stretching modes, respectively. The peaks at 322.3 and 378.0 cm^{-1} reflected the asymmetric and symmetric bending vibrations of VO_4^{3-}. Another two vibrational peaks at lower wave numbers (121.9 and 220.1 cm^{-1}) were assigned to external vibration modes. For the pure CeO_2 sample, only one main vibrational band at 463.7 cm^{-1} is observed, originating from the Ce−O bond vibration.[25]

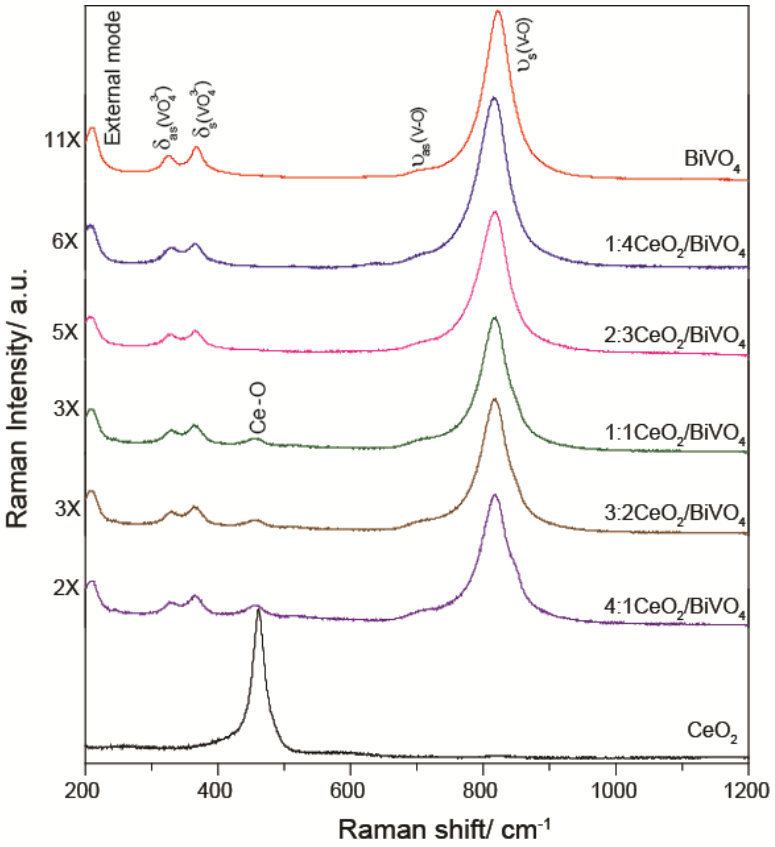

Figure 6.5 Raman spectra of pure $BiVO_4$, pure CeO_2 and $CeO_2/BiVO_4$composite powders with different mole ratios.

In the case of composited materials, characteristic Raman peaks for both $BiVO_4$ and CeO_2 were found in 4:1, 3:2 and $1{:}1CeO_2/BiVO_4$ samples. The composite spectra also clearly showed a decreasing CeO_2 peak intensity when the mole ratio of CeO_2 to $BiVO_4$ was decreased, which disappeared in 2:3 and $1{:}4CeO_2/BiVO_4$ samples. This suggested a less sensitivity of the CeO_2 nanoparticles with lower crystallinity and small crystal size than $BiVO_4$.[21] Furthermore, the dominate $BiVO_4$ peak (at 810.5 cm^{-1} in the pure materials) gradually shifted to higher wavenumber with increase CeO_2 content. This could possibly suggest that it was not a simple metal oxide mixture but that chemical interactions between the $BiVO_4$ and CeO_2 leads to a decrease in the symmetry of the $BiVO_4$.[20, 26]

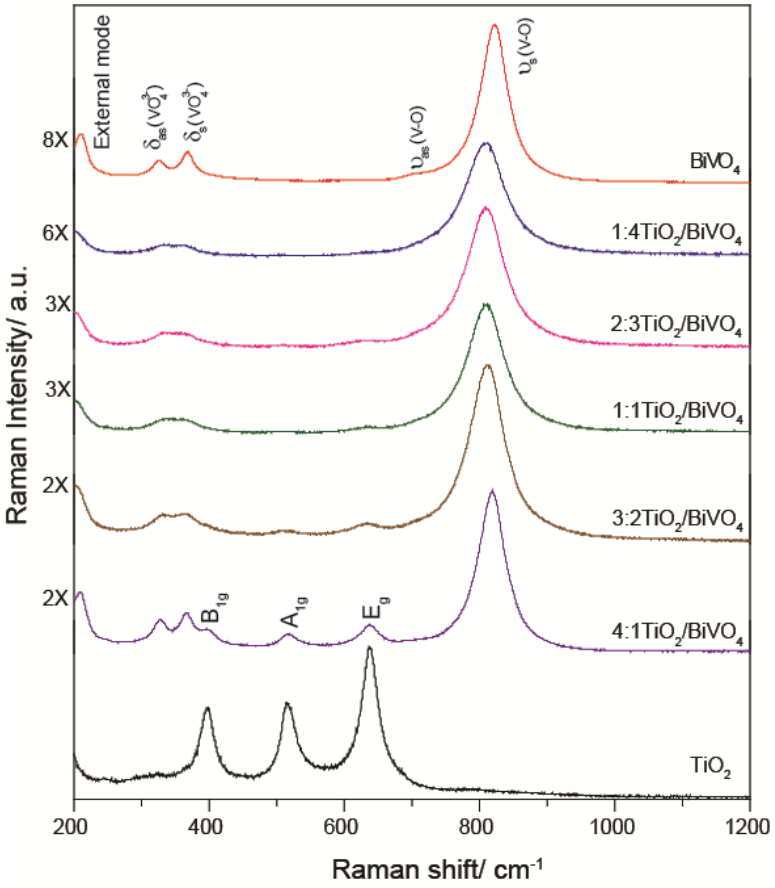

Figure 6.6 Raman spectra of pure $BiVO_4$, pure TiO_2 and $TiO_2/BiVO_4$ composite powders with different mole ratios.

The Raman spectra for the $TiO_2/BiVO_4$ composite with different mole ratios compared to bare TiO_2 and $BiVO_4$ photocatalysts are shown in Figure 6.6. The characteristic spectra of the pure TiO_2 powder at 398.2 (B_{1g}), 516.5 (A_{1g}), 634.1 cm^{-1} (E_g) were attributed to the Raman active bands of the anatase TiO_2, similar to the results reported by Miao *et al.*[27] and Xue *et al.*[28]

For the $TiO_2/BiVO_4$ composites, characteristic Raman spectra for both $BiVO_4$ and TiO_2 were found in 3:2 and 4:1 $TiO_2/BiVO_4$ composites. Similar to the results of $CeO_2/BiVO_4$ composites, all $TiO_2/BiVO_4$ composites has a tendency to shift the main Raman peak to higher wavenumber with increasing amount of TiO_2 mole ratios.

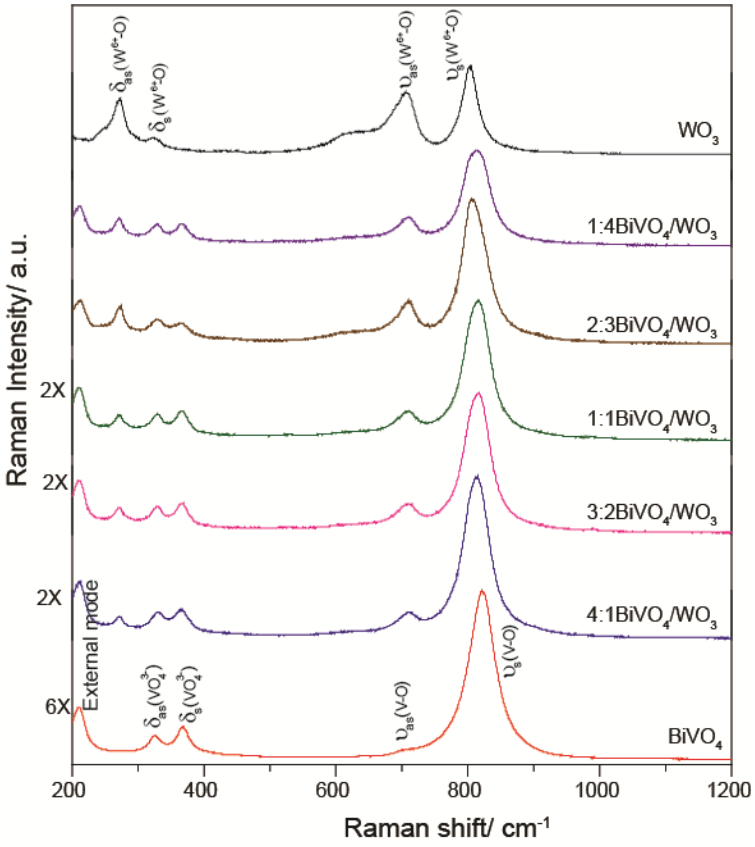

Figure 6.7 Raman spectra of pure $BiVO_4$, pure WO_3 and $BiVO_4/WO_3$ composite powders with different mole ratios.

Figure 6.7 shows Raman spectra the $BiVO_4/WO_3$ composites with different mole ratios of 4:1, 3:2, 1:1, 2:3 and 1:4 compared to pure $BiVO_4$ and WO_3. The pure WO_3 powder shows characteristic vibration modes of Raman spectra at 271.4, 324.0, 705.9 and 806.8 cm^{-1}.[29] The observed spectra at 271.4 and 324.0 cm^{-1} were attributed to the asymmetric and symmetric bending vibration of O–W–O, respectively, whereas, the spectra at 705.9 cm^{-1} and 806.8 cm^{-1} were attributed to the asymmetric and symmetric O–W–O stretching vibrations respectively.[29, 30] All these spectra were the characteristic features of monoclinic WO_3.

Obviously in the $BiVO_4/WO_3$ composites, the peak belonging to $BiVO_4$ at 810.5 cm^{-1} overlapped with WO_3 at 806.8 cm^{-1}, which lead to the boarded spectrum in this position. However, the domain peak of $BiVO_4/WO_3$ composites have slightly shifted

to lower wavenumber when increased the amount of WO_3 mole ratios due to mixed signal or chemical interaction of the $BiVO_4/WO_3$ composites.

The Raman spectra of all composite photocatalysts, that is $CeO_2/BiVO_4$, $TiO_2/BiVO_4$ and $BiVO_4/WO_3$, provide the following insights: (1) Raman spectra shows both the fundamental Raman vibrations of each materials in its composite agreeing with the XRD results, confirming each materials presence as a separate crystalline phase; (2) in all composites, the shift of the dominate $BiVO_4$ peak suggests a strong interaction between two materials in each composite; and (3) the tendency increases in the Raman intensities of those three composites with increasing amount of $BiVO_4$ suggests that $BiVO_4$ is more sensitive with Raman spectroscopy than other the used metal oxide in this research. These above Raman observations are consistent with the XRD analysis.

6.3.3 XPS analysis

The XRD and Raman analyses do not give any information about the surface structure of the composite materials. The surface structure of photocatalyst materials is an important factor for their photocatalytic activities, since the reaction generally occur on the surface of catalyst. According to the $2:3CeO_2/BiVO_4$, $1:1TiO_2/BiVO_4$ and $4:1BiVO_4/CeO_2$ composites exhibited the highest photocatalytic degradation of MB under visible light irradiation compared to their series with different mole ratios (more details in section 6.4). Hence, XPS analysis was carried out to study the surface chemical composition and the chemical state of the above composites, and take a more detailed look at the interactions between CeO_2 and $BiVO_4$ in the 2:3 $CeO_2/BiVO_4$ composites, as well as to confirm the composition of TiO_2 and $BiVO_4$ in the 1:1 $TiO_2/BiVO_4$, and of $BiVO_4$ and WO_3 in the 4:1 $BiVO_4/WO_3$ composites.

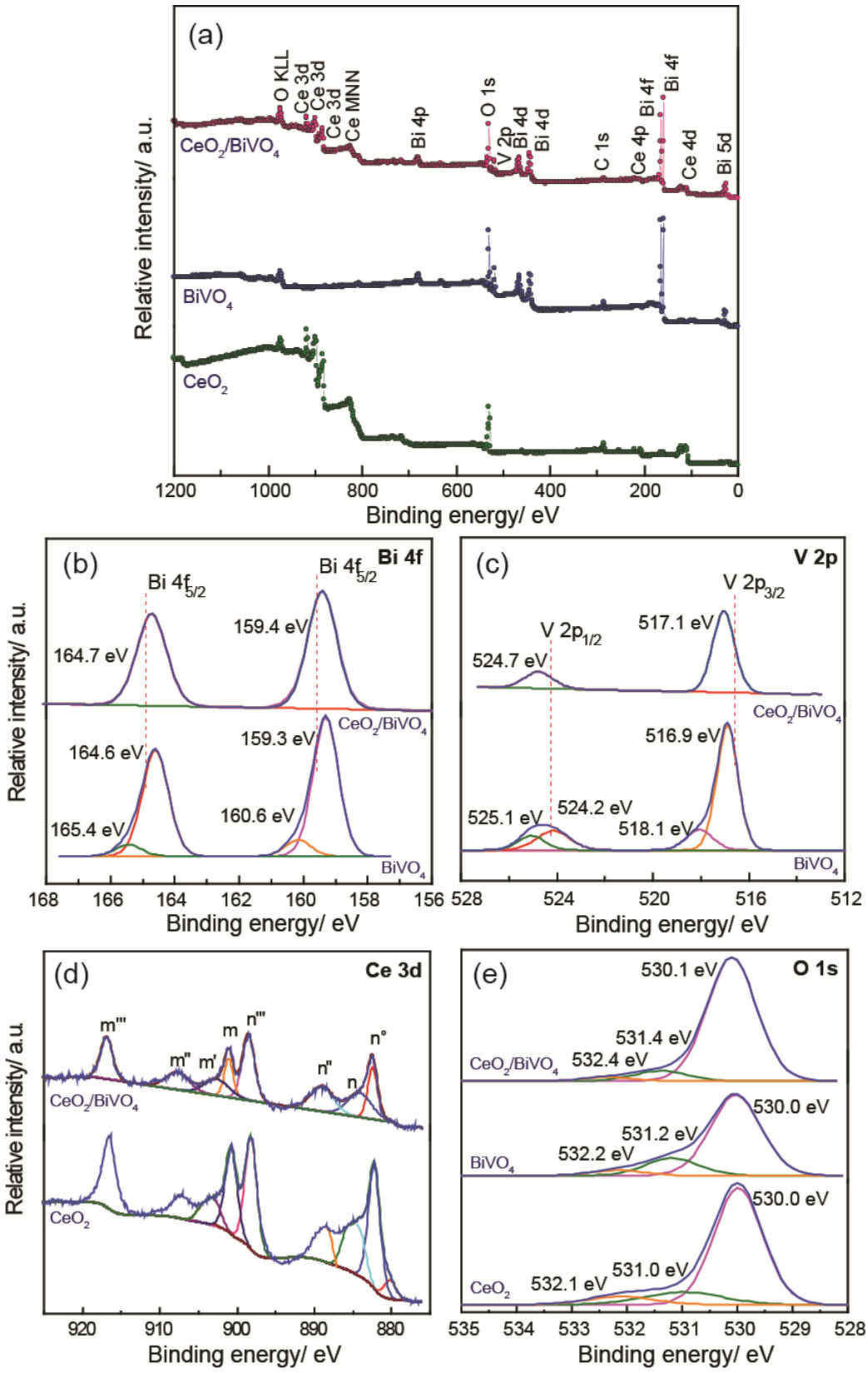

Figure 6.8 XPS survey spectra of $BiVO_4$, CeO_2 and 2:3 $CeO_2/BiVO_4$ composite, high-resolution XPS spectrum of (b) Bi 4f, (c) V 2p, (d) Ce 3d and (e) O 1s regions.

In the XPS survey of 2:3CeO_2/$BiVO_4$, Bi, O, Ce and C were detected shown in Figure 6.8(a). The binding energy of the C 1s transition at 284.6 eV was used as a reference to calibrate the binding energies of other elements. In Figure 6.8(b), the comparison of high resolution splitting of Bi $4f_{7/2}$ and Bi $4f_{5/2}$, are assigned to Bi^{3+} of $BiVO_4$ present physical distortion.[31] Moreover, a negative shift of about 0.2 eV as compared with pure $BiVO_4$ (159.2 and 159.4 eV) suggests that there are electrical interactions between Bi and Ce in the CeO_2/$BiVO_4$ composite.[31]

The two symmetric spectra of V $2p_{1/2}$ and V $2p_{3/2}$ in the CeO_2/$BiVO_4$ composite, at binding energies of 524.7 and 517.1 eV respectively (shown in Figure 6.8(c)), are characteristic of V^{5+} ions.[9, 31] When compared with pure $BiVO_4$, the V 2p peaks of the composite shifted to high binding energies which indicates again that CeO_2 altered the chemical environment around the V species.

Interpretation of Ce is significantly more complex than the other elements investigated here. The labels of the Ce 3d spectra in Figure 6.8(d) follow the convention established by Burroughs *et al.,*[32] where n and m indicate the spin-orbit coupling $3d_{5/2}$ and $3d_{3/2}$, respectively. The six peaks labelled as n, n″, n‴, m, m″ and m‴ represent the $3d^{10}4f^0$ initial electronic state, corresponding to Ce^{4+} cations. In the composite catalysts, the peaks attributed to Ce^{4+} are dominant. Ce^{3+} is distinguishable, however observed at significantly lower quantities in the composite than pure CeO_2. In CeO_2 the n′ and m′ feature peaks are seen, but the intensities of two peaks are very weak. The presence of Ce^{3+} can create a charge imbalance, leading to vacancies, and unsaturated chemical bonds on the catalyst surface,[33, 34] which may lead to increase of chemisorbed oxygen on the surface.[35, 36] Moreover, the increase in binding energies of Ce 3d in the composite catalysts, as compared to the pure CeO_2, again indicates that the electrons are transferred from CeO_2 to $BiVO_4$ system.[34]

The O 1s XPS spectrum of pure $BiVO_4$ is found to have two peaks, as shown in Figure 6.8(e). The peak at binding energy of 530.0 eV corresponds to O in $BiVO_4$ bulk and other peak at binding energy of 531.0 eV may be assigned to surface hydroxyl groups such as Bi—OH. The O 1s spectrum of the $CeO_2/BiVO_4$ composite includes a peak at a binding energy of 530.2 eV, characteristic of metallic oxides and in agreement with the O 1s electron binding energy arising from the $BiVO_4$ and CeO_2 lattices. The shoulder at binding energy of 531.4 and 532.4 eV may be assigned to surface species such as Ce—OH and Bi—OH resulting from the reaction of chemisorbed water or/and oxygen molecules with Ce^{3+} and Bi^{3+} on the surface.[31, 37]

The three O 1s peaks of the CeO_2 catalyst also are observed at binding energies of 530.0, 531.0 and 532.1 eV corresponding with the results of the composite catalysts. Furthermore, the binding energy of O 1s (530.2 eV) was slightly shifted after coupling $BiVO_4$ and CeO_2 (530.0 and 530.0 eV), indicating that Bi and Ce electronically interact with each other in the $CeO_2/BiVO_4$ composite.

Figure 6.9(a) represents typical XPS survey spectra for the TiO_2, $BiVO_4$ and $TiO_2/BiVO_4$ composite, which can be observed the spectra belonging to Bi 4f, V 2p, and O 1s in the $BiVO_4$, Ti 2p and O 1s in the TiO_2, and Bi 4f, V 2p, Ti 2p and O 1s in the $TiO_2/BiVO_4$ samples. The high resolution XPS spectra of $TiO_2/BiVO_4$ composite showed the binding energy spectra splitting of Bi $4f_{7/2}$ and Bi $4f_{5/2}$ at 159.4 and 164.7 eV, respectively (Figure 6.9(b)), which was assigned to Bi^{3+} in $BiVO_4$.[9] The two symmetric spectra of V $2p_{1/2}$ and V $2p_{3/2}$ in the $TiO_2/BiVO_4$ composite at binding energies of 524.4 and 516.9 eV, respectively (shown in Figure 6.9(c)), were characteristic of V^{5+} ions.[9]

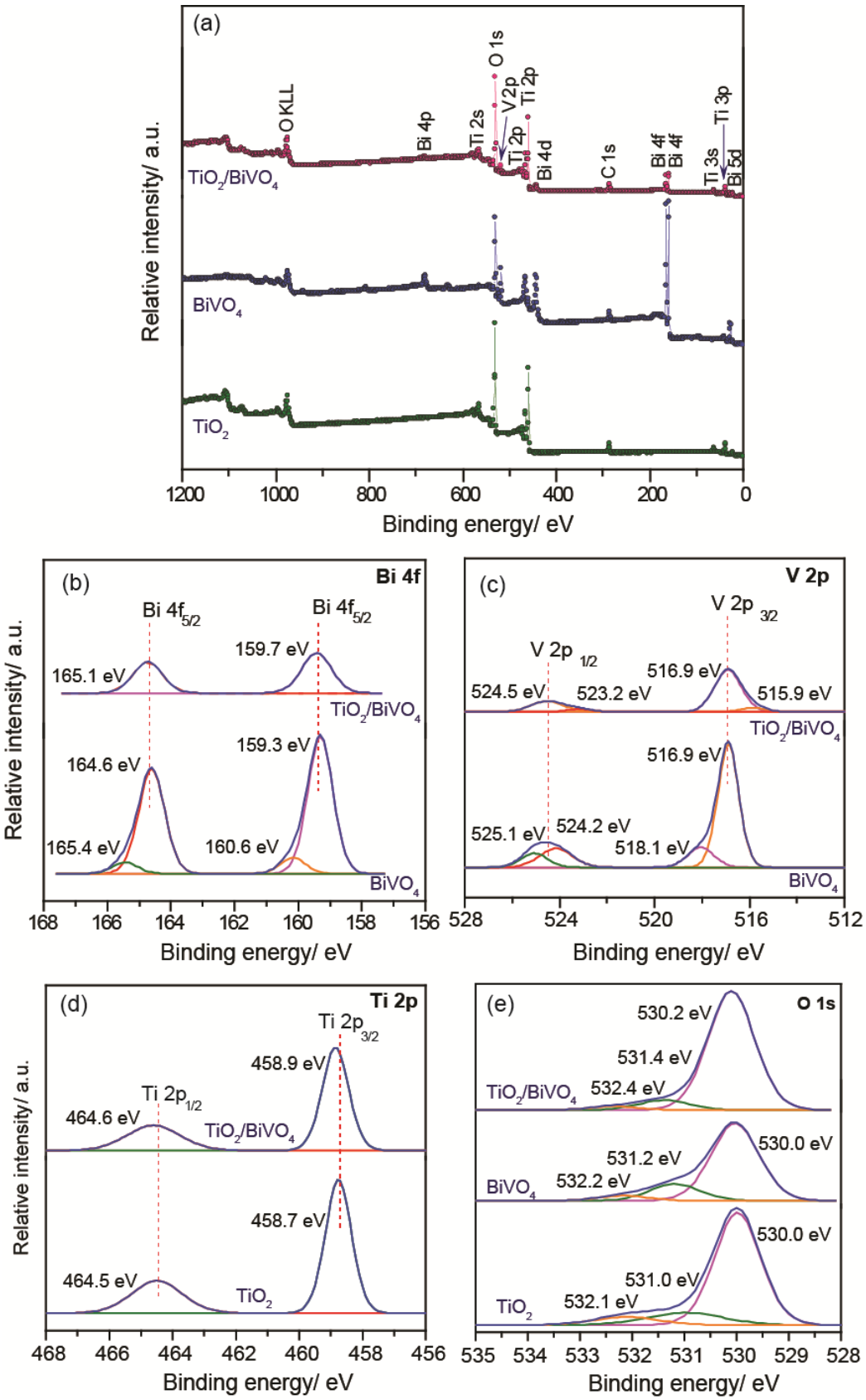

Figure 6.9 XPS survey spectra of $BiVO_4$, TiO_2 and 1:1 $TiO_2/BiVO_4$ composite, high-resolution XPS spectrum of (b) Bi 4f, (c) V 2p, (d) Ti 2p and (e) O 1s regions.

In Figure 6.9(d), the $TiO_2/BiVO_4$ composite presented two spectra of Ti 2p at 458.9 and 464.6 eV assigned to Ti $2p_{3/2}$ and Ti $2p_{1/2}$, respectively. The spectrum separation between Ti 2p3/2 and Ti 2p1/2 was 5.7 eV, which has been shown previous to be characteristic of Ti^{4+}.[28, 38] None of the peaks observed suggested the presence of Ti^{3+}. The O spectrum was located at 530.1 eV with an asymmetric pattern as in showed Figure 6.9(e). The primary peak at 530.1 eV indicated the O^{2-} ion, while the additional shoulders at higher energies assigned to surface OH^- groups and/or chemisorbed H_2O.

Figure 6.10(a) shows the comparison of survey XPS spectra of pure WO_3 and pure $BiVO_4$ and $BiVO_4/WO_3$ composite, which can observe the spectra corresponding to Bi, W, C, V and O. For the $BiVO_4/WO_3$ composite, the Bi 4f spectra with the binding energy peaks splitting at 159.7 and 167.1 eV were attributed to be o Bi $4f_{7/2}$ and Bi $4f_{5/2}$, respectively, which is assigned to Bi^{3+} of $BiVO_4$ present in separate phase (Figure 6.10(b)).[9] The two symmetric spectra of V $2p_{1/2}$ and V $2p_{3/2}$ in the 4:1$BiVO_4/WO_3$ composite at binding energies of 525.0 and 517.4 eV respectively (shown in Figure 6.10(c)), are characteristic of V^{5+} ions.[9]

The spectra of W at 35.9 and 38.0 eV which are shown in Figure 6.10(d) can be attributed to the W $4f_{7/2}$ and W $4f_{5/2}$ binding energies, respectively. When compared with the pure $BiVO_4$ and pure WO_3 the Bi 4f, V 2p and W 4f spectra of the $BiVO_4/WO_3$ composite slightly shifted to the high binding energies, indicating an interaction between the $BiVO_4$ and WO_3 on the surface of the composite.

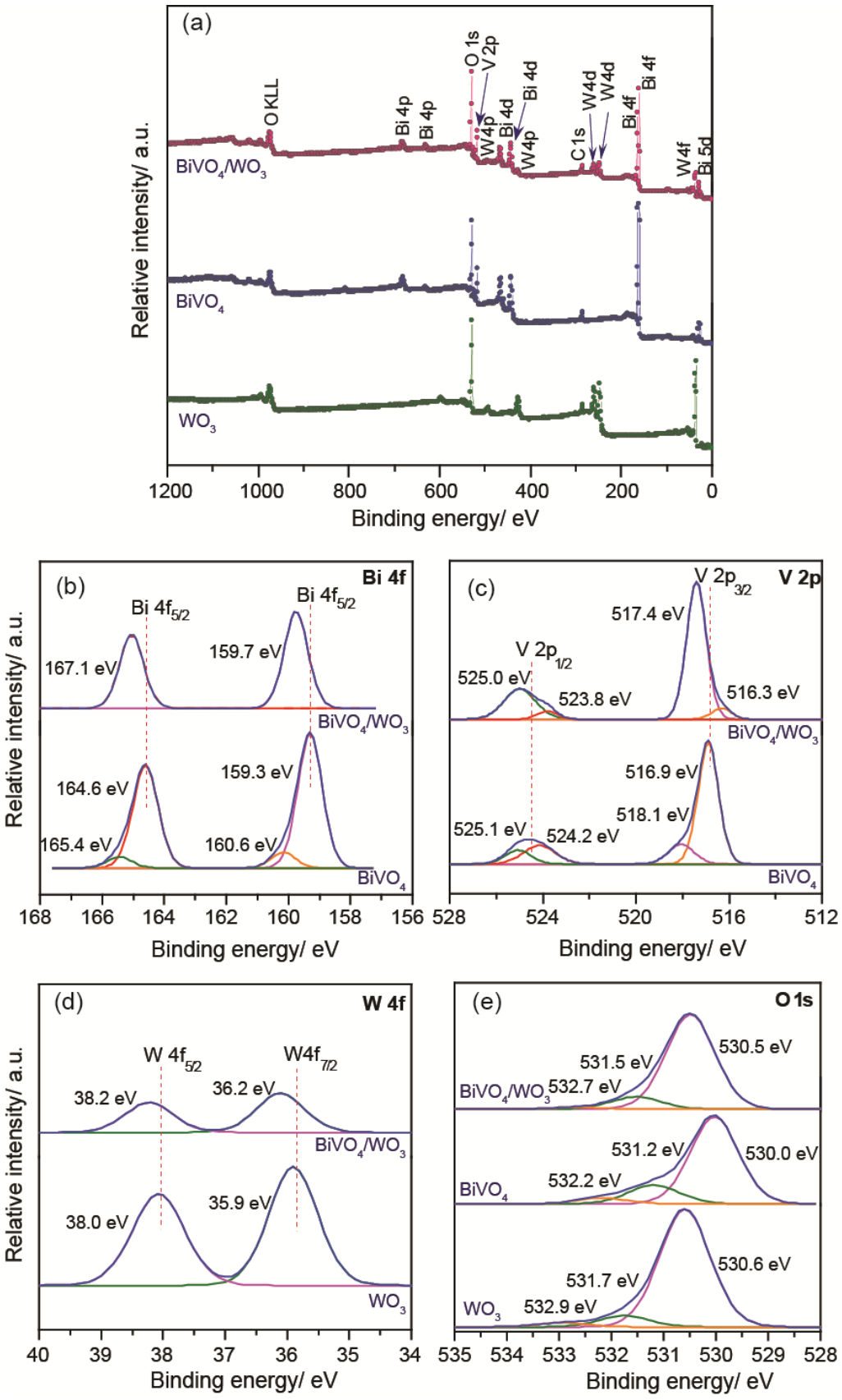

Figure 6.10 XPS survey spectra of $BiVO_4$, WO_3 and 4:1 $BiVO_4/WO_3$ composite, high resolution XPS spectrum of (b) Bi 4f, (c) V 2p, (d) W 4f and (e) O 1s regions.

The O1s binding energies of the pure $BiVO_4$, pure WO_3, and $BiVO_4/WO_3$ composite are shown in Figure 6.10(e) located at 529.9, 529.9 and 530.0 eV, respectively. Compared to the pure $BiVO_4$ and pure WO_3, the O1s became broader and there was a slight increase in binding energy in the 1:1$BiVO_4/WO_3$ composite. This positive shift inferred the W–O–Bi linkage which contains contributions from both the Bi–O and W–O bonds, respectively.[39, 40]

As well as the shifting of all Bi 2f, V2p, O 1s, Ce 3d, Ti 2p and W 4f from their original values confirm the electrical interaction between $BiVO_4$ and CeO_2 or TiO_2 or WO_3 in their composites. In comparison, the $BiVO_4/WO_3$ composite compared to its individual materials showed more shifts in XPS spectra than $CeO_2/BiVO_4$ and $TiO_2/BiVO_4$ suggested that the interaction between $BiVO_4$ and WO_3 was stronger than between $BiVO_4$ and CeO_2 or TiO_2.

Thus, it can be concluded from both XRD, Raman and XPS results that those three composite did not contain any significant doping in either phase, nor did it contain a mixed oxide phase.[31, 34, 36, 37] However, due to proximity, electronic interaction were observed using XPS.

6.3.4 TEM and SEM analyses

The morphologies of $CeO_2/BiVO_4$, $TiO_2/BiVO_4$ and $BiVO_4/WO_3$ composite powders and films were investigated using TEM and SEM as shown in Figures 6.11 and 6.12, respectively. Nanoparticles of $BiVO_4$ with irregular shapes (80–100 nm size) can be clearly observed in Figures 6.11(a) and 6.11(b). A TEM image of the $CeO_2/BiVO_4$ composite is shown in Figure 6.11(c), where many small spherical particles (2–5 nm) are observed over the surface of a larger $BiVO_4$ particles which are similar to those observed for $BiVO_4$ that is the secondary process does alter the structure of $BiVO_4$.

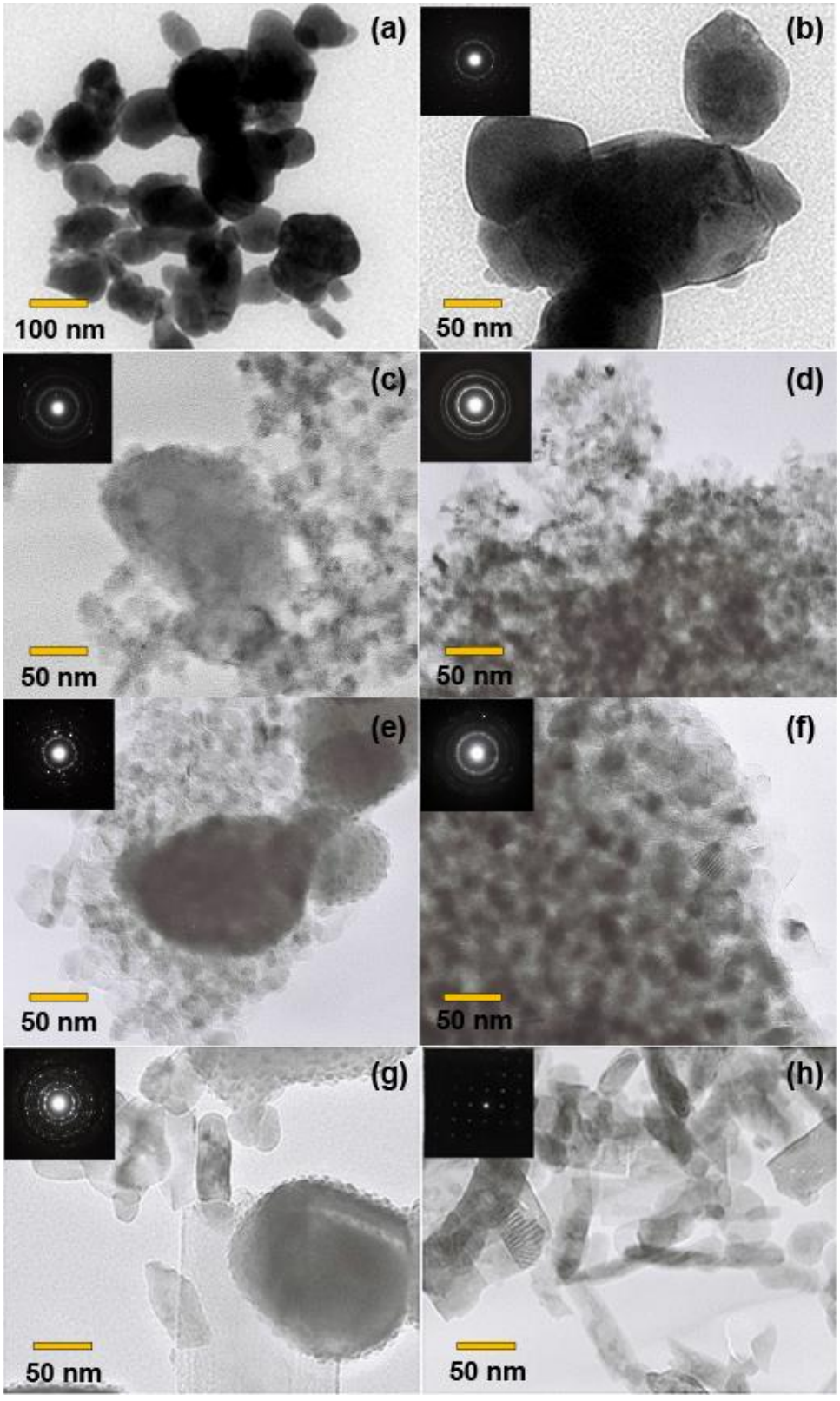

Figure 6.11 TEM images inset its SAED of (a) and (b) $BiVO_4$, (c) 2:3 $CeO_2/BiVO_4$, (d) CeO_2, (e) 1:1 $TiO_2/BiVO_4$ (f) TiO_2, (g) 4:1 $BiVO_4/WO_3$, and (h) WO_3 nanoparticles.

The small spherical nanoparticles in the composite sample (Figure 6.11(c)) were strong reasonably to the morphology of the CeO_2 as shown in Figure 6.11(d). The uniform fringes (inset Figure 6.11(c)) with spacings of 0.25 nm, and 0.27 nm were in good agreement with the (020) and (200) lattice planes of monoclinic $BiVO_4$ and cubic CeO_2, respectively. Moreover, the distance of 0.31 nm corresponds with both the lattice spacing at the (112) plane of the monoclinic $BiVO_4$ (inset Figure 6.11(b)) and the (100) plane of the cubic CeO_2 (inset Figure 6.11(d)). This also corresponded to the highest XRD peaks, which both appeared at about 28.8° as seen in Figure 6.2.

Figure 6.11(e) shows TEM image of 1:1 $TiO_2/BiVO_4$ composite, it was found that small nanoparticles of TiO_2, with an average size of 10–30 nm, completely cover the surface of the $BiVO_4$ (~100 nm). The SAED pattern (inset Figure 6.11(e)) shows the mixture of lattice planes indexed to the monoclinic $BiVO_4$ and tetragonal TiO_2. The TEM image of pure TiO_2 (Figure 6.11(f)) revealed a small nanoparticle with similar sizes as in Figure 6.11(e). The SAED patterns of the TiO_2 (inset Figure 6.11(e)) indicated that they were polycrystalline and could be indexed to tetragonal TiO_2, which related with of the $TiO_2/BiVO_4$ composite and agreed well with the XRD results in Figure 6.3.

The $BiVO_4/WO_3$ composite in Figure 6.11(g) revealed $BiVO_4$ particles with diameter of 100 nm, which related to the particles of pure $BiVO_4$ in Figure 6.11(a). Additionally, there were some uninform particles (rod- and plate-like) with particle size in the range of 60–120 nm, corresponded to the obtained particles of pure WO_3 in Figure 6.11(h). The corresponding SAED of $BiVO_4/WO_3$ composite (inset Figure 6.11(g)) was composed of two sets of diffraction patterns including the monoclinic $BiVO_4$ and monoclinic WO_3, which agreed well with the XRD results.

TEM results confirmed the formation of composites where a heterojunction structure of two metal oxides is formed. In each case these phases are effectively interspersed. The SEM images for surface topology and cross section of the $CeO_2/BiVO_4$ composite

film (annealed at 450°C for 2 h) are shown in Figures 6.12(a) and 6.12(b), respectively. It was found that a homogeneous distribution of the small CeO_2 particles on surface of the large $BiVO_4$ particles and the existence of porosity distribution were observed, which related to the morphology of its cross section image.

The $TiO_2/BiVO_4$ composite film, the SEM top surface (Figure 6.12(c)) and corresponding cross section (Figure 6.12(d)) represented a mixture of large aggregates and smaller uniformly dispersed particles were observed.

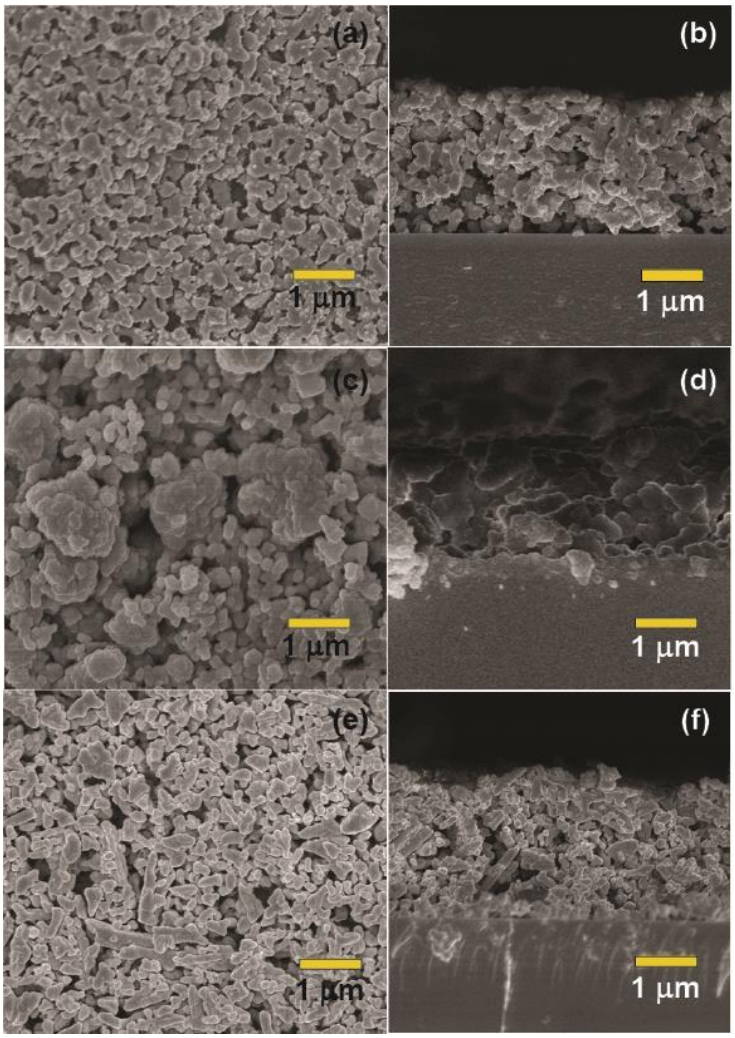

Figure 6.12 Surface topology and cross-sectional images: (a) and (b) of the 2:3 $CeO_2/BiVO_4$, (c) and (d) of 1:1 $TiO_2/BiVO_4$, (e) and (f) 4:1 $BiVO_4/WO_3$ composite films, respectively after annealing at 450°C for 2 h.

Figure 6.12(e) and Figure 6.12(f) show the SEM images of the top surface view and cross section of the $BiVO_4/WO_3$ film. A porous film with a dispersion of spherical and rod-like particles were observed. It is assumed that there are $BiVO_4$ and WO_3 particles respectively, as per TEM results. Furthermore, the thickness of the three composite films could be determined to be ~2.8 μm from their SEM cross section images.

6.3.5 Light absorption properties and band structures

Light harvesting of the composite films with $BiVO_4$ and either CeO_2, TiO_2 and WO_3 different mole ratios, along with pure oxide photocatalysts were investigated by UV-vis spectroscopy with an attached integrating sphere in transmission and/or reflection modes. Figure 6.13(a) shows the absorption spectra, calculated from Equation (3.11), in the range of 350–600 nm for $CeO_2/BiVO_4$ composites with different mole ratios, which are presented a slightly red shift of absorption band compared with of pure CeO_2. However, the absorption bands of $CeO_2/BiVO_4$ composites exhibited did not change too much when comparing with of pure $BiVO_4$ this demonstrated presence of $BiVO_4$ in all composites.

The band gap energies of the above photocatalyst films were estimated from the plots of $(\alpha h\nu)^2$ versus photon energy ($h\nu$) by using the intercept of the two tangent to the plots (Equation (3.10)), as illustrated in Figure 6.13(b) of the $CeO_2/BiVO_4$ composites. The band gap energies of the CeO_2 and $BiVO_4$ films were determined to be 2.71 and 2.40 eV, respectively, while all the $CeO_2/BiVO_4$ composite films were similar to be 2.40 eV, as $BiVO_4$ absorption masked the absorption onset of CeO_2.[35] The absence of any major change in the absorption onset of $BiVO_4$ (either pure or in the composite) is further evidence against doping taking place.

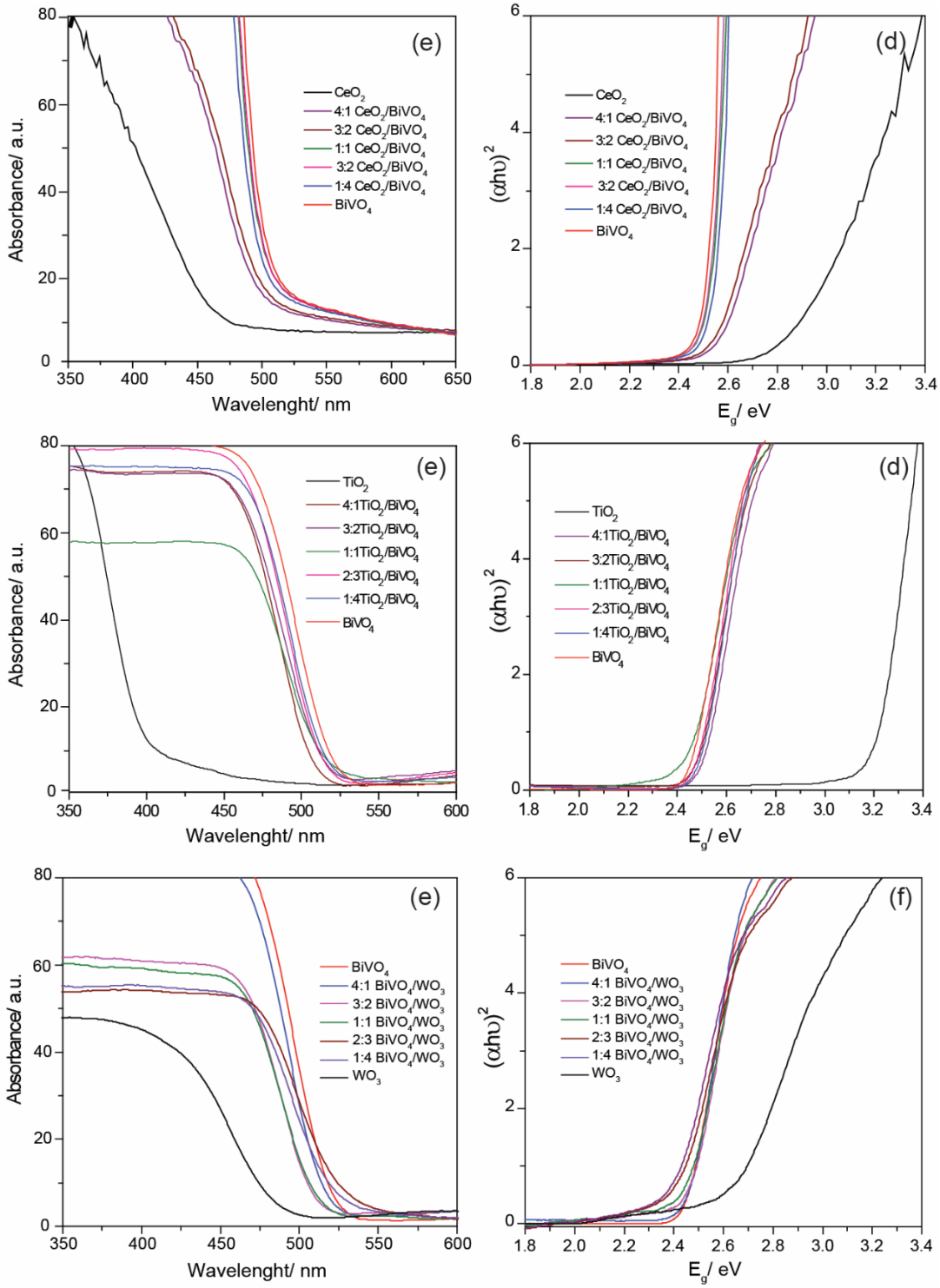

Figure 6.13 UV-vis absorption spectra and the plots of $(\alpha h\nu)^2$ versus photon energy ($h\nu$): (a) and (b) of $CeO_2/BiVO_4$, (c) and (d) $TiO_2/BiVO_4$, and (e) and (f) $BiVO_4/WO_3$ composite films, respectively, (annealed at 450°C for 2 h).

For the $TiO_2/BiVO_4$ composite films, the absorption edges were observed at the wavelengths of about 510−530 nm as shown in Figure 6.13(c). In Figure 6.13(d), the band gap energies of all $TiO_2/BiVO_4$ composite films was ~2.40 eV, which was close to pure $BiVO_4$ (2.40 eV). Figure 6.13(e) shows absorption spectra of $BiVO_4/WO_3$ composites compared to pure $BiVO_4$ and WO_3. It was found that the absorption edges of all $BiVO_4/WO_3$ composite films were similar to the $BiVO_4$ with in the range of 500–560 nm. Moreover, it was showed that the band gap energies of all $BiVO_4/WO_3$ composite and $BiVO_4$ films were similar (Figure 6.13(f)) with the average of 2.43±0.04 eV, while the band gap energy of WO_3 film was 2.63 eV.

From all absorption results, it could be concluded that the absorption values obtained being similar and closeness to of the pure $BiVO_4$. This is the observed band gap energy is that of the lowest E_g component in the composites. Hence, monochromatic illumination experiments will be used to clarify the mechanisms of light harvesting of theses composites for photodegradation of dyes.

Mott-Schottky measurements were performed in the dark using impedance spectroscopy techniques. The Mott-Schottky curves of pure $BiVO_4$, CeO_2, TiO_2 and WO_3 films were shown in Figures 6.14(a), 6.14(b), 6.14(c) and 6.14(d), respectively, measured in 0.5 M Na_2SO_4 solution at frequency of 1 kHz. The flat band potentials of all above photocatalysts were obtained by extrapolation of the Mott-Schottky plots between C^{-2} and Voltage (*vs.* Ag/AgCl) using the Equation 3.15.

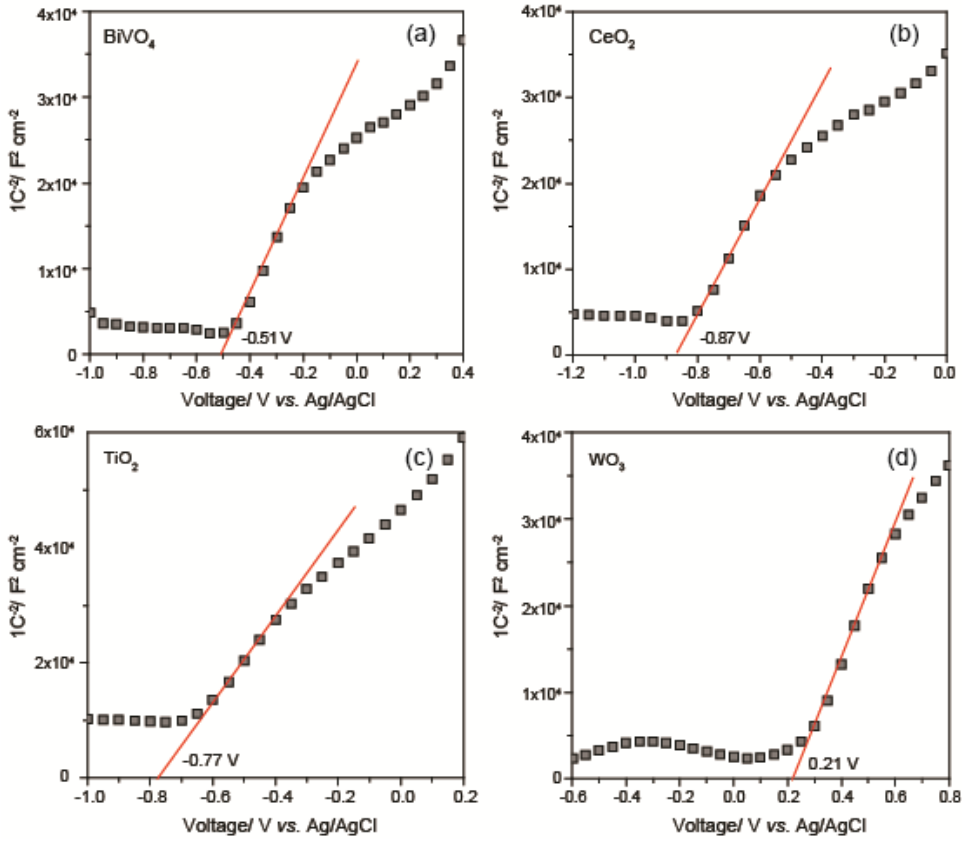

Figure 6.14 Mott-Schottky plots of (a) $BiVO_4$, (b) CeO_2, (c) TiO_2 and (d) WO_3 films on FTO substrates were carried out in 0.5 M Na_2SO_4 solution (pH 5.5) at frequency 1 kHz.

Figure 6.14(a), it can be seen that the flat band energy of $BiVO_4$ is about -0.51 V (vs. Ag/AgCl), which is more positive than that of pure CeO_2 (-0.87 V *vs.* Ag/AgCl, Figure 6.14(b)), TiO_2 (-0.78 *vs.* Ag/AgCl, Figure 6.14(c)), or WO_3 (0.21 V *vs.* Ag/AgCl, Figure 6.14(d)). Furthermore, these flat band values of the pure $BiVO_4$, TiO_2 and WO_3 in this research are good agreement with the data reported in the literatures[16, 41-45] It is tropically assumed that for n-type semiconductor the flat the potential measured according to the Mott-Schottky relationship approximates the bottom of the conduction band (VB = CB - E_g). Thus, the possible position of conduction band (CB) and valence band (VB) edges of the $CeO_2/BiVO_4$, $TiO_2/BiVO_4$ and $BiVO_4/WO_3$ composite photocatalysts are mentioned previously as summarised in Table 6.6. Nernst equation

(Equation 3.14) was used to convert the obtained potentials (*vs.* Ag/AgCl) to reversible hydrogen electrode (RHE).[11, 46]

Table 6.6 The wavelength of the monochromic light and the corresponding intensity used in the photocatalytic test.

Samples	E_g (eV)	CB (V *vs.* NHE)	VB (V *vs.* NHE)
$BiVO_4$	2.40	0.01	2.39
CeO_2	2.71	-0.35	2.36
TiO_2	3.20	-0.26	2.94
WO_3	2.63	0.73	3.36

6.4 Photocatalytic properties of composited photocatalysts

The photocatalytic activities of the composite films were evaluated by measuring the degradation of RhB and MB dyes in aqueous solution under visible-light and simulated solar light irradiation, respectively. The degradation of dyes were monitored by examining in decreases of its concentration, which measured the changes in maximal absorption of UV-vis spectra of RhB (553 nm) and MB (664 nm).

Quantitative measurements were conducted by monitoring the height of the absorption peak of RhB and MB dyes. By fitting these absorption data with Equation (2.4) as previously mentioned in Chapter 2, the reaction rate constant of photocatalytic activates over 1:4, 3:2, 1:1, 2:3 and 4:1 mole of the CeO_2/$BiVO_4$ films thought comparison with pure CeO_2 and $BiVO_4$ films could be determined as shown in Figure 6.15. It was found that optimum condition for synthesis the composite photocatalyst of CeO_2/$BiVO_4$ for degradation of both RhB and MB was 2:3 mole ratio.

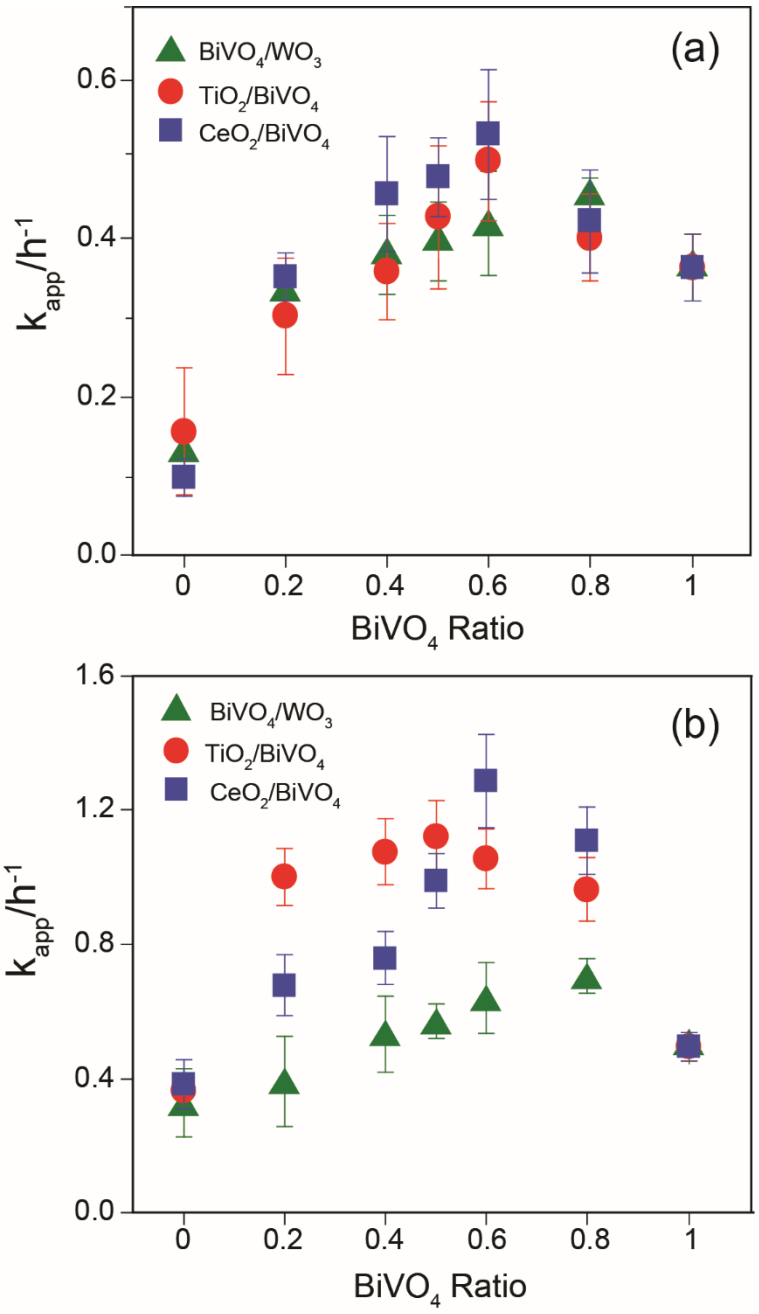

Figure 6.15 Pseudo first order rate constants of photodegradation of (a) RhB and (b) MB dyes by using various composite films with different mole ratio under irradiation of solar light for RhB and visible light for of MB.

The pseudo first order rate constants for photo-degradation of dyes over all $TiO_2/BiVO_4$ composite films (along with pure $BiVO_4$ and TiO_2 films) are shown in Figure 6.15(a) for RhB and Figure 6.15(b) for MB. From the comparison of the pseudo first order rate constants, it could be observed that the 2:3 $TiO_2/BiVO_4$ and 1:1

$TiO_2/BiVO_4$ composite films showed the highest photocatalytic activities for degradation of RhB (0.498 h^{-1}) and MB (1.12 h^{-1}) dyes, respectively. Moreover, all results for $TiO_2/BiVO_4$ composites (20–80% TiO_2 in $BiVO_4$) in photodegradation of MB are equal within uncertainties. This suggests a robust system.

The comparison of the pseudo-first order rate constants for degradation of RhB and MB dyes for pure $BiVO_4$, pure WO_3 and $BiVO_4/WO_3$ composite films were summarised in Figure 6.15. It was found that the rate constant for degradation of RhB and MB dyes of $BiVO_4/WO_3$ composite films was increased when increasing the mole ratio of $BiVO_4$, which the $BiVO_4/WO_3$ composite films with mole ratio of 3:2 and 4:1 exhibited the highest photocatalytic activities of RhB (0.454 h^{-1}) and MB (0.693 h^{-1}) dyes, respectively. Since, visible light can be harvested by the $BiVO_4$, corresponding to the estimated band gap of 2.44 eV, which thus leads to higher harvest efficiency of sunlight, compared to the WO_3.

Time dependent absorption spectra of RhB solution during overnight adsorption/ desorption and solar light irradiation in the presence of 2:3 $CeO_2/BiVO_4$, 1:1 $TiO_2/BiVO_4$ and 4:1 $BiVO_4/WO_3$ films are compared and displayed in Figures 6.16(a) and (b), Figures 6.16(c) and (d), and Figures 6.16(e) and (f), respectively.

It was observed that the absorption of the solution decreased over time in the dark, with the $BiVO_4/WO_3$ film exhibited the greatest surface adsorption followed by the $TiO_2/BiVO_4$ and $CeO_2/BiVO_4$ films. There is no dark process driving degradation, it is assumed the decrease in solution absorbance can be directly correlated with adsorption on the films, and that the photocatalytic reactions only occur on photoactivated catalysts.

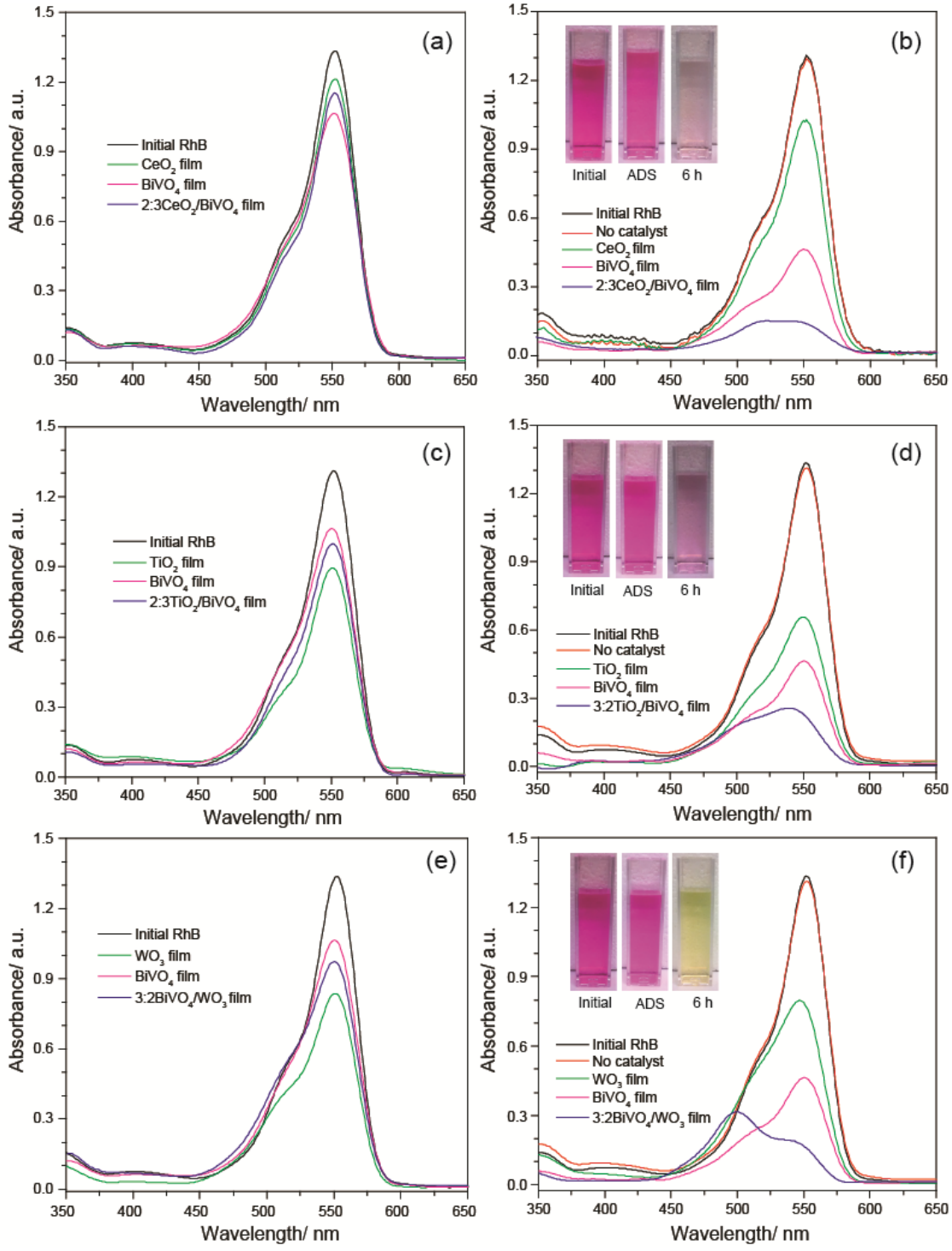

Figure 6.16 Absorption spectra of RhB with function of time (under adsorption in the dark and solar light irradiation, respectively): (a) and (b) of 2:3 $CeO_2/BiVO_4$, (c) and (d) of 1:1 $TiO_2/BiVO_4$, and (e) and (f) of 3:2 $BiVO_4/WO_3$ composite films.

Under simulated solar irradiation for 6 h, the concentration of RhB gradually decreased in the presence of each photocatalyst film. As Figure 6.16, the system containing the 2:3 $CeO_2/BiVO_4$ composite film was distinctly lower than those for the systems containing other composite catalysts meaning that presented highest photocatalytic activity. Furthermore, the maximum absorption band of the RhB solution gradually shifted to lower wavelength as clearly seen in Figure 6.16(f) owing to the formation of de-ethylated RhB, similar to that was observed by Guan *et al.*[47] and Zhuang *et al.*.[48]

The absorption spectra of MB solutions after being stored in the dark and then illuminated over three catalyst composites including 2:3 $CeO_2/BiVO_4$, 1:1 $TiO_2/BiVO_4$ and 4:1 $BiVO_4/WO_3$ composite films are presented in Figures 6.17(a) and (b)), Figures 6.17(c) and (d), and Figures 6.17(e) and (f), respectively. For adsorption in the dark, results showed similarly the $BiVO_4/WO_3$ composite film also exhibited the highest surface adsorption (largest decrease in solution absorbance).

After 4 h of visible light irradiation, the 2:3 $CeO_2/BiVO_4$ composite film (the dye solution catalysed by the presence of a 2:3 CeO_2:$BiVO_4$ film) yielded the lowest peak intensity at 664 nm, that is the highest photocatalytic activity for MB degradation, followed by the 1:1 $TiO_2/BiVO_4$ and 4:1 $BiVO_4/WO_3$ composite films respectively. Furthermore, the peak became very broad and weak, and also no obvious new band was observed, which suggested nearly complete degradation of MB. However, some degradation intermediates have no visible absorption such as benzyl compounds may remain, hence it need to do more testing to confirm.

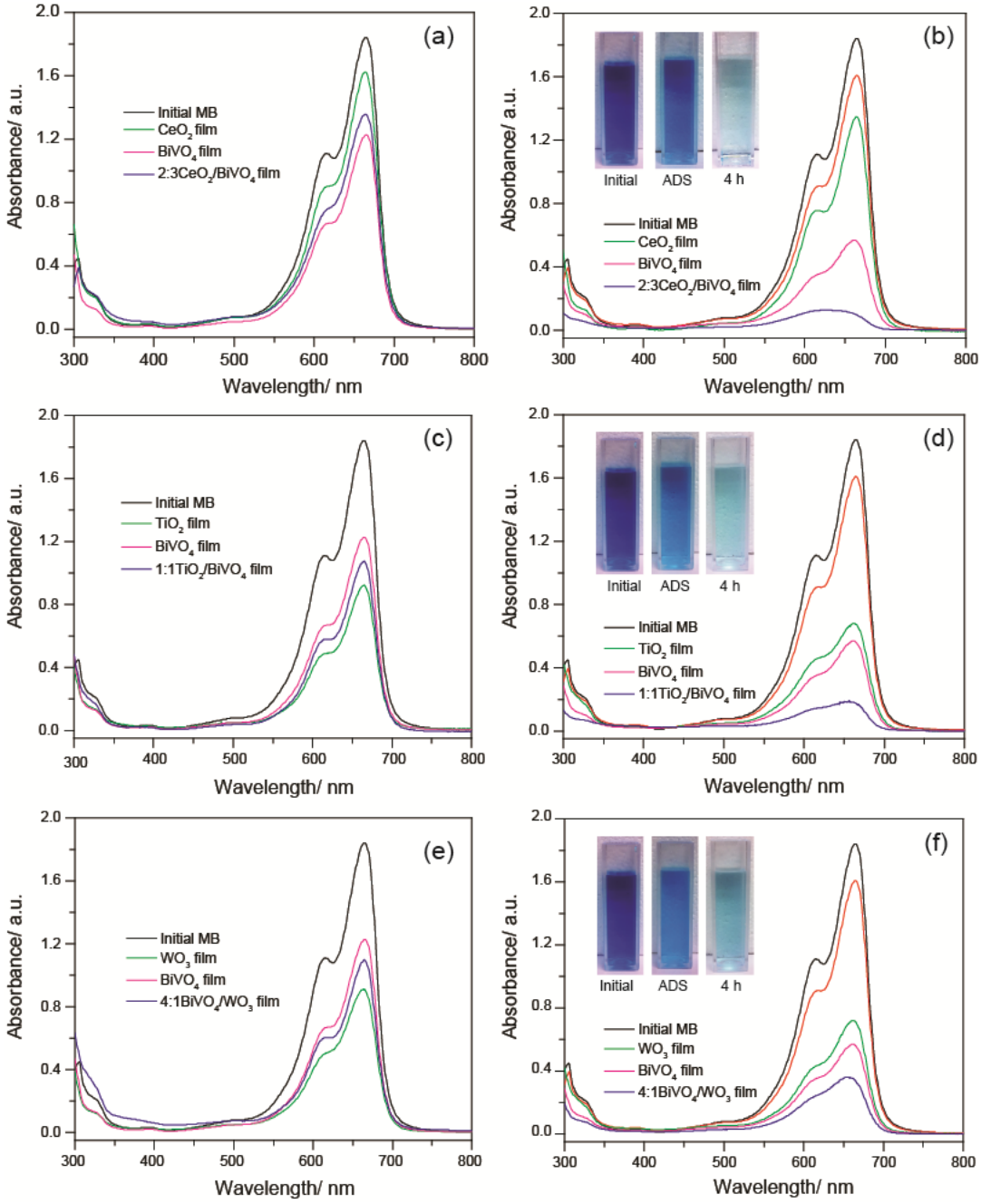

Figure 6.17 Absorption spectra of MB with function of time under adsorption in the dark and solar light irradiation: (a) and (b) of 2:3 $CeO_2/BiVO_4$, (c) and (d) of 1:1 $TiO_2/BiVO_4$, and (e) and (f) of 3:2 $BiVO_4/WO_3$ composite films.

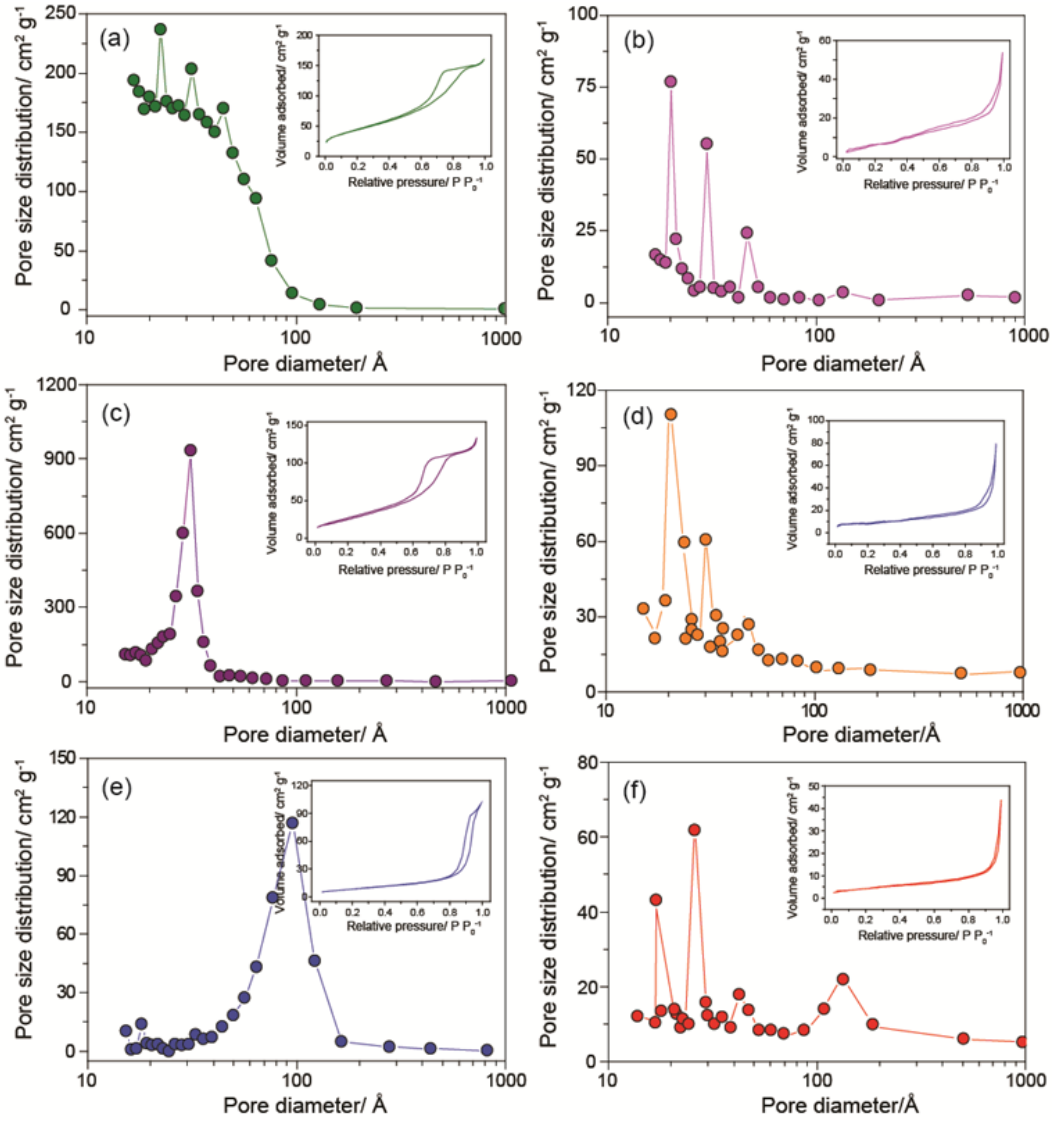

Figure 6.18 Pore size distribution plots inset their corresponding BET nitrogen adsorption and desorption isotherm: (a) CeO_2, (b) 2:3 CeO_2/$BiVO_4$, (c) TiO_2, (d) 1:1TiO_2/$BiVO_4$ (e), WO_3 and (f) 4:1 $BiVO_4$/WO_3 films.

The BET nitrogen adsorption and desorption isotherm and pore size distribution of the different composite catalysts, 2:3 CeO_2/$BiVO_4$, 1:1 TiO_2/$BiVO_4$ and 4:1 $BiVO_4$/WO_3 films, is shown in Figure 6.18. Surface and pore size were considered the RhB and MB in aqueous solution with Bohr radius of 1.7 nm[49] and 0.80 nm,[50] respectively, should be able to infiltrate on 2:3 CeO_2/$BiVO_4$ with larger pores (2–5 nm) and a higher surface (49.2 m^2 g^{-1}) than 1:1 TiO_2/$BiVO_4$ (~ 3 nm and 27.9 m^2 g^{-1}) and, 4:1 $BiVO_4$/WO_3 (~8 nm and 14.6 m^2 g^{-1}), respectively as shown in Figure 6.18.

Table 6.7 BET surface areas (S_{BET}) and degradation rate constant (k_{app}) of dyes over $CeO_2/BiVO_4$ composite films with different mole ratios.

Sample films	Properties		
	S_{BET} ($m^2 g^{-1}$)	k_{app} (h^{-1})	
		RhB	MB
CeO_2	147	0.098	0.383
4:1$CeO_2/BiVO_4$	93.9	0.363	0.678
3:2$CeO_2/BiVO_4$	62.7	0.460	0.758
1:1$CeO_2/BiVO_4$	49.2	0.458	0.989
2:3$CeO_2/BiVO_4$	33.8	0.528	1.29
1:4$CeO_2/BiVO_4$	31.8	0.410	1.11
$BiVO_4$	13.6	0.354	0.495

Table 6.8 BET surface areas (S_{BET}) and degradation rate constant (k_{app}) of dyes over $TiO_2/BiVO_4$ composite films with different mole ratios.

Sample films	Properties		
	S_{BET} ($m^2 g^{-1}$)	k_{app} (h^{-1})	
		RhB	MB
TiO_2	102.8	0.126	0.363
4:1$TiO_2/BiVO_4$	54.0	0.350	1.00
3:2$TiO_2/BiVO_4$	49.9	0.398	1.08
1:1$TiO_2/BiVO_4$	32.0	0.470	1.12
2:3$TiO_2/BiVO_4$	27.9	0.498	1.06
1:4$TiO_2/BiVO_4$	14.8	0.452	0.964
$BiVO_4$	13.6	0.354	0.495

Table 6.9 The relationship between BET surface areas (S_{BET}) and degradation rate constant (k_{app}) of dyes over $BiVO_4/WO_3$ composite films with different mole ratios.

Sample films	Properties		
	S_{BET} ($m^2 g^{-1}$)	k_{app} (h^{-1})	
		RhB	MB
$BiVO_4$	13.6	0.354	0.495
4:1$BiVO_4/WO_3$	18.1	0.423	0.693
3:2$BiVO_4/WO_3$	21.0	0.454	0.628
1:1$BiVO_4/WO_3$	24.1	0.396	0.558
2:3$BiVO_4/WO_3$	26.0	0.359	0.521
1:4$BiVO_4/WO_3$	28.6	0.320	0.380
WO_3	36.5	0.108	0.314

It is well know that the surface area of a photocatalyst greatly affects its adsorption and photocatalytic properties for degradation of dyes.[51] The relationship between pseudo first order rate constants for photo-degradation of dyes over $CeO_2/BiVO_4$, $TiO_2/BiVO_4$ and $BiVO_4/WO_3$ with different mole ratios, and their specific surface area were summarised and shown in Tables 6.8, 6.8 and 6.9, respectively.. This suggested that active size and light harvesting of composited photocatalysts play important roles to their photocatalytic degradation of dyes.

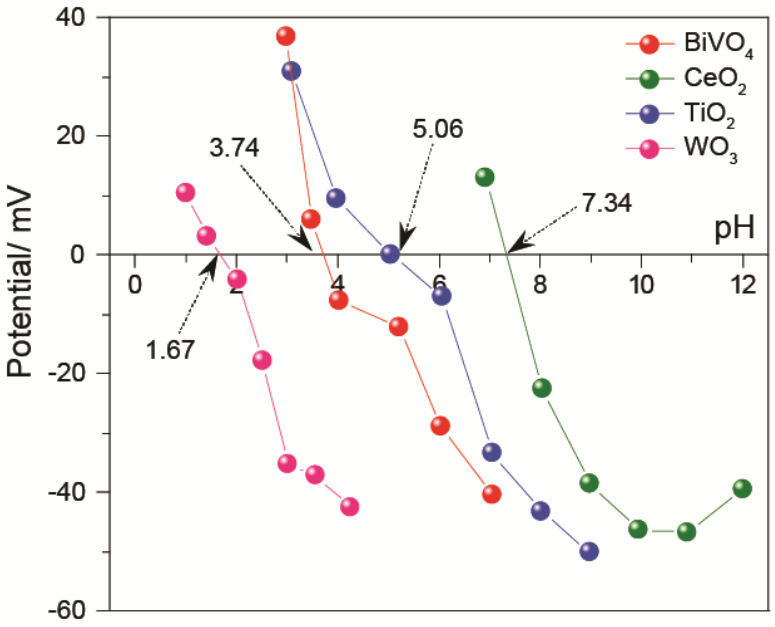

Figure 6.19 pH dependence of zeta potentials of $BiVO_4$, CeO_2, TiO_2 and WO_3 in aqueous solution.

Although, the $BiVO_4/WO_3$ film had low surface area them either $CeO_2/BiVO_4$ or $TiO_2/BiVO_4$, it exhibited higher loading of RhB or MB dyes in the dark. These differing levels of dye loading can be explained in term of Zeta potentials. Both RhB and MB are cationic dyes due to the positively charged amino groups of RhB and sulfonate groups of MB, which preferentially adsorb on the negatively charged catalyst surfaces. As shown in Figure 6.19, the point of zero charge (PZC) of WO_3 is more negative than $BiVO_4$, TiO_2 and CeO_2, respectively at pH neutral. Together with the mesoporous characteristics (pore size 5–50 nm) of WO_3 and TiO_2, this leads to showing an order of adsorption properties for the $BiVO_4/WO_3$, $TiO_2/BiVO_4$ and $CeO_2/BiVO_4$ composites, respectively. Hence, the major factor for adsorption behaviour of RhB and MB on the composite films in this research also can be reasonably understood based on the negatively charged surface and also high surface area, respectively.

It has been observed that all composite photocatalysts exhibit higher photocatalytic activity compared with individual components alone, and an order of the photocatalytic activity for the composites was $CeO_2/BiVO_4$, $TiO_2/BiVO_4$, and $BiVO_4/WO_3$, respectively. The obtained photocatalysis of those three composites could be attributed to the synergetic effect in the heterostructures under light excitation. This is probably because charge carriers will be spatially separated more readily due to band energy offsets in the composite, which will in turn lead to longer lived free charges, capable of degrading organic materials such as RhB and MB dyes.

To more understand about the mechanism of the three different band energy offsets of the composites for dye degradation, monochromatic light measurement was studied together with active species trapping to confirm mechanism path ways of each composite catalyst. These all studies and results would be discussed next session.

6.5 Photocatalytic mechanisms of composited catalysts

Monochromatic illumination, active species trapping studies and Mott-Schottky measurements were used to determine the mechanisms of photocatalytic degradation for the various systems (pure materials and composites with either RhB or MB).

6.5.1 Monochromatic photocatalysis

According the closeness of light adsorption onset of all composites compared to $BiVO_4$ (Figure 6.13) so that white light is simultaneously exciting $BiVO_4$ and other component. To determine how to these three composited photocatalysts work and improve their photodegradation of MB, monochromatic light experiment in visible range (400–700 nm) were applied and the wavelength specific photocatalytic performance examined. Comparison of absorption spectra for degradation of MB dye in the presence of different photocatalysts under solar light irradiation with and without various band pass filters is shown in Figure 6.20. The MB dye under solar light

irradiation without a band pass filter showed the greatest degradation, which the order were 2:3CeO_2/$BiVO_4$ > 1:1TiO_2/$BiVO_4$ > 4:1$BiVO_4$/WO_3 > $BiVO_4$ > TiO_2 > CeO_2 > WO_3, respectively.

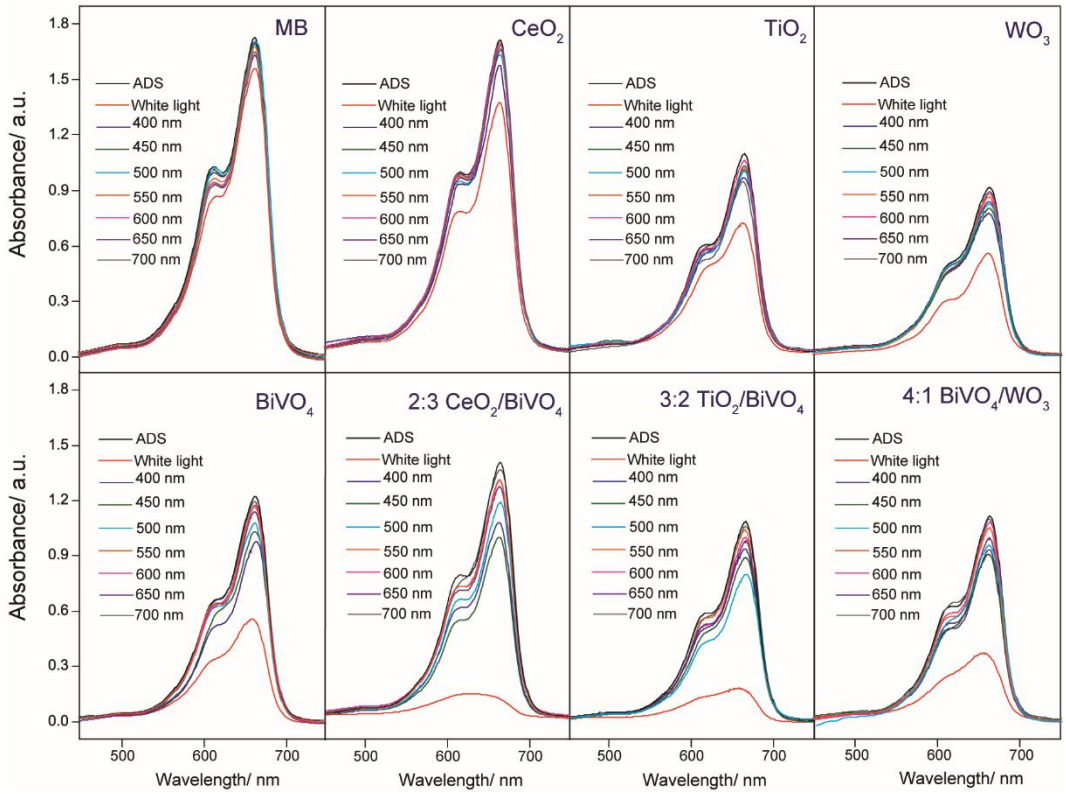

Figure 6.20 Absorption spectra of MB photodegradation by using different catalyst films under solar light irradiation with and without various band pass filters.

Table 6.10 The wavelength of the monochromic light and the corresponding intensity used in the photocatalytic test.

Wavelength (nm)	400 (382–424)	450 (436–478)	500 (484–522)	550 (536–577)	600 (586–623)	650 (640–676)	700 (684–723)
Intensity (mW/cm^2)	5.6	11.6	12.8	12.4	8.0	3.2	1.4

The monochromatic photocatalysis presented as pseudo first order rate constants for photodegradation of MB dye over various photocatalysis. There were versus different wavelength as shown in Figure 6.20. The intensities of each wavelength of monochromatic light were also measured and controlled as reported in Table 6.10.

After the light is filtered by each filter, main absorption spectrum of MB decreased a little by comparing to without filter (Figure 6.20). This suggest that the photon energy of each filtered light (band pass filter) was quite low compared to white light (without filter), thus a small degradation rate was obtained. However, it could be noticed that the absorption spectra of MB over all catalyst increased a little by comparing with that under a longer wavelength filter than the absorption onset of each photocatalyst, this means the MB is still degraded. Herein, a controlled experiment (without catalysts) was also investigated.

As shown in Figure 6.20, MB was degraded under 600 and 650 nm filters as a results of photolysis. These wavelengths are closed to maximum absorption, at 664 nm and suggested that some dye radiate at other wavelength.[52-54] Since the adsorbed MB on the catalyst surface can be excited by visible light irradiation and then undergo a one electron reduction by other MB molecules to produce *Leuco*-methylene blue ($MB/MB^{\bullet-}$ = -0.23 V *vs.* NHE),[52] as seen in a decreases of MB spectra at 650 nm for all system. This electron can then be transferred to the conduction band of semiconductor photocatalysts, leading to increase photocatalytic degradation of dye.

The monochromatic photocatalysis presented as the normalised pseudo first order rate constants for photodegradation of MB dye over various photocatalysts were plotted versus different band pass filters thought comparison to their absorption spectra as shown in Figure 6.21

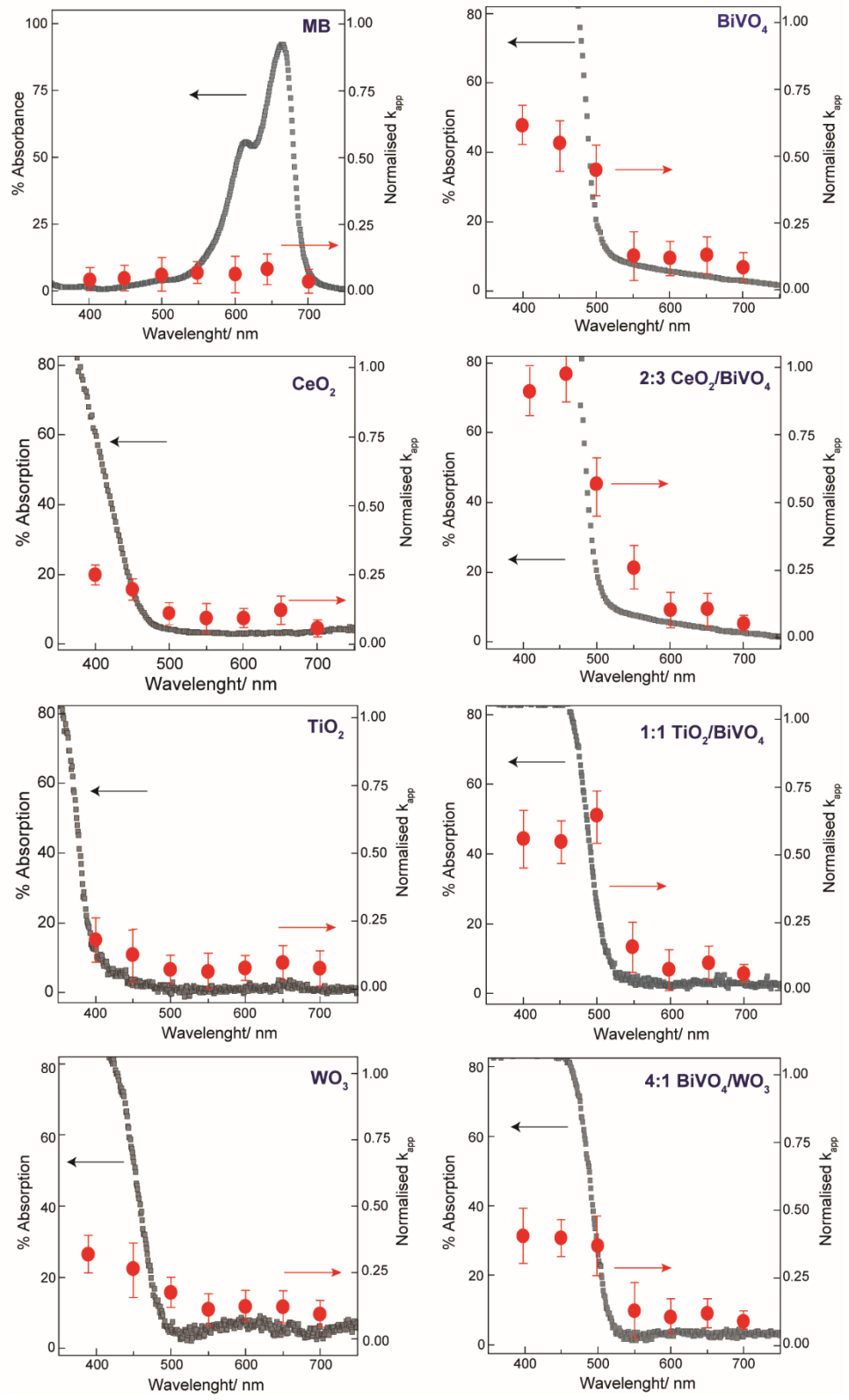

Figure 6.21 Absorption spectra of photocatalyst as a function of wavelength, and normalised photocatalytic rate for MB degradation as a function of bandpass filter cut off wavelength.

For the three composited catalysts, similar results were obtained for photodegradation rate of MB dye that the high degradation rate was observed close to its absorption onset, then dramatically dropped at the longer wavelength filters than this, and slightly increased again at about 650 nm filter, which the adsorption onsets of the 3:2 $CeO_2/BiVO_4$, 1:1 $TiO_2/BiVO_4$ and 4:1 $BiVO_4/WO_3$ films were found to be 532, 420 nm and 435 nm, respectively. This suggests that the high rates for MB photodegradation of the all composites where $BiVO_4$, but other component could not clearly observed which need more analysis to confirm. Therefore, from these monochromatic light experiments, it was believed that the degradation processes of MB over each composite were synergistic degradation by photolysis and photocatalysis under the simulated solar irradiation.

Further experiment in determining active species trapping was also studied and discussed together with Mott-Schottky results in order to clarify the mechanisms of each composited photocatalysts.

6.5.2 An indirect chemical probe method (active species trapping)

The mechanisms of photocatalytic degradation of RhB and MB, by $BiVO_4$, CeO_2, TiO_2 and WO_3 were investigated by an indirect chemical probe method with active species scavengers.[55, 56] Normally in the photocatalytic oxidation process, photoinduced active species, including holes (h^+), hydroxyl radical ($^{\bullet}OH$) and/or superoxide anion radical ($^{\bullet-}O_2$), oxidize organic molecules following the separation of electron-hole pairs created by photoexcitation.

As shown in Table 6.11, a $^{\bullet}OH$ scavenger, isopropanol (IPA) was added to the reaction system, benzoquinone (BQ) was introduced as the scavenger of $^{\bullet-}O_2$, and ethylenediamine tetra acetic acid (EDTA) was adopted to quench h^+. Each scavenger solution was added to RhB or MB solution at a concentration of 1 mM prior to addition

of the photocatalyst film. All other conditions remained the same as in the photocatalytic test as mentioned in Chapter 3.

Table 6.11 The scavengers use to study main active species for photocatalytic degradation of dyes.[57, 58]

Species	Scavengers
$OH^{\bullet}$	IPA
$^{\bullet-}O_2$	BQ
h^+	EDTA

The photocatalytic degradation of RhB with 2:3 $CeO_2/BiVO_4$, 3:2 $TiO_2/BiVO_4$ and 3:2 $BiVO_4/WO_3$ films compared to their bare photocatalyst films in the absence and presence of scavengers (IPA, BQ and EDTA) under solar light irradiation for 6 h is presented in Figure 6.22, and the changed spectra for MB degradation with different scavengers of 2:3 $CeO_2/BiVO_4$, 1:1 $TiO_2/BiVO_4$ and 4:1 $BiVO_4/WO_3$ films under solar light irradiation for 4 h is shown in Figure 6.23.

In the added EDTA system, all photocatalysts showed almost no effect on the degradation of RhB and MB dyes compared to the control experiment (without any scavengers). This is probably those photocatalysts are sensitive to EDTA, suggesting that there is no effective mechanism involving degradation of RhB and MB by h^+.

In the RhB and MB spectra of the $CeO_2/BiVO_4$ composite systems with BQ and IPA, were all decreased less than without scavenger. Obviously, the slight decrease in RhB degradation is observed in the added BQ system, which acted as scavengers for $^{\bullet-}O_2$ radical species. Thus, the active species trapping experiments demonstrated that the $^{\bullet-}O_2$ is the main active specie in the degradation process of both RhB and MB dyes, and $^{\bullet}OH$ may be play as the second active species for degradation of RhB and MB dyes.

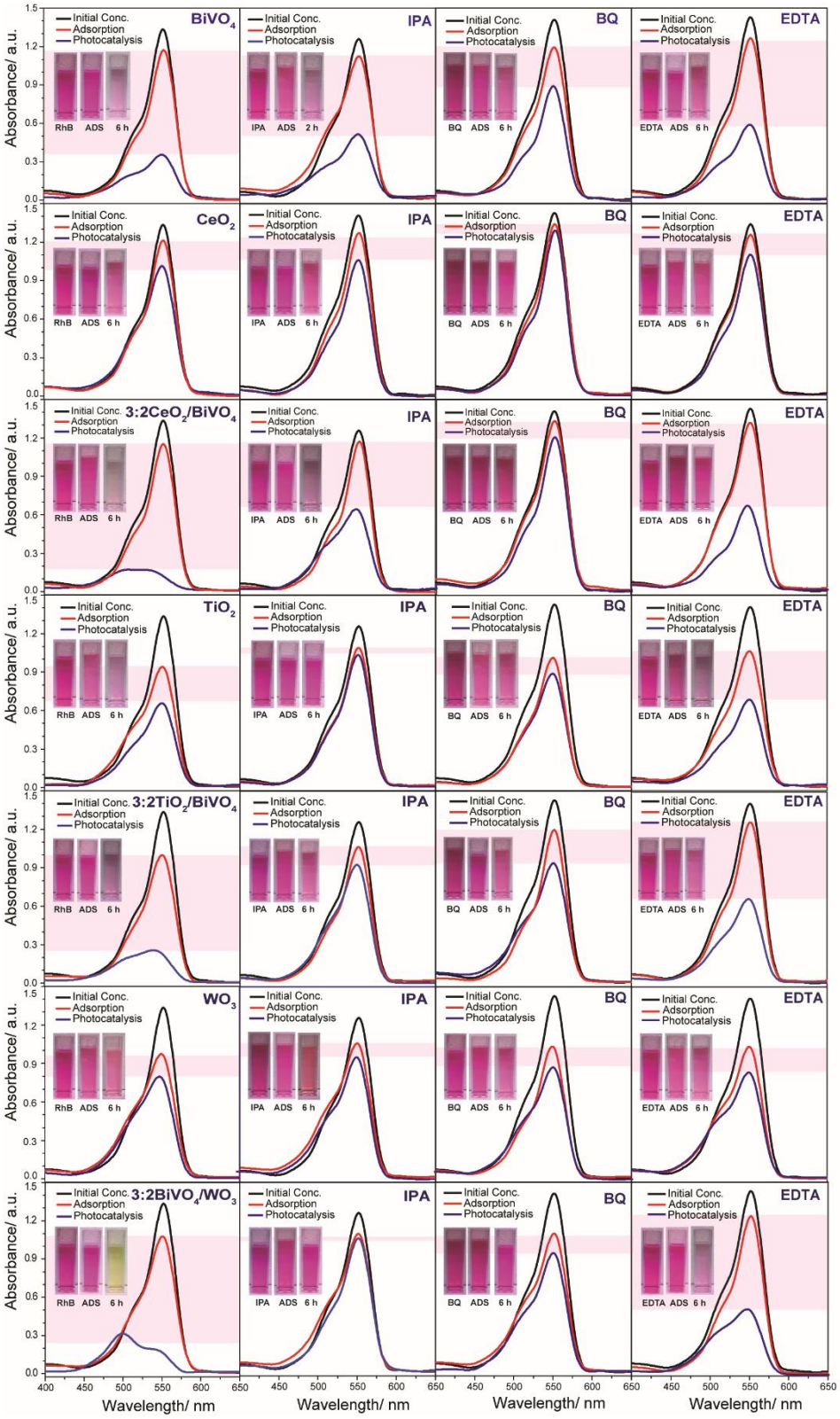

Figure 6.22 Photodegradation of RhB (change of UV-vis spectra) with different composite films in the absence and presence of IPA, BQ and EDTA scavengers under solar light irradiation for 6 h.

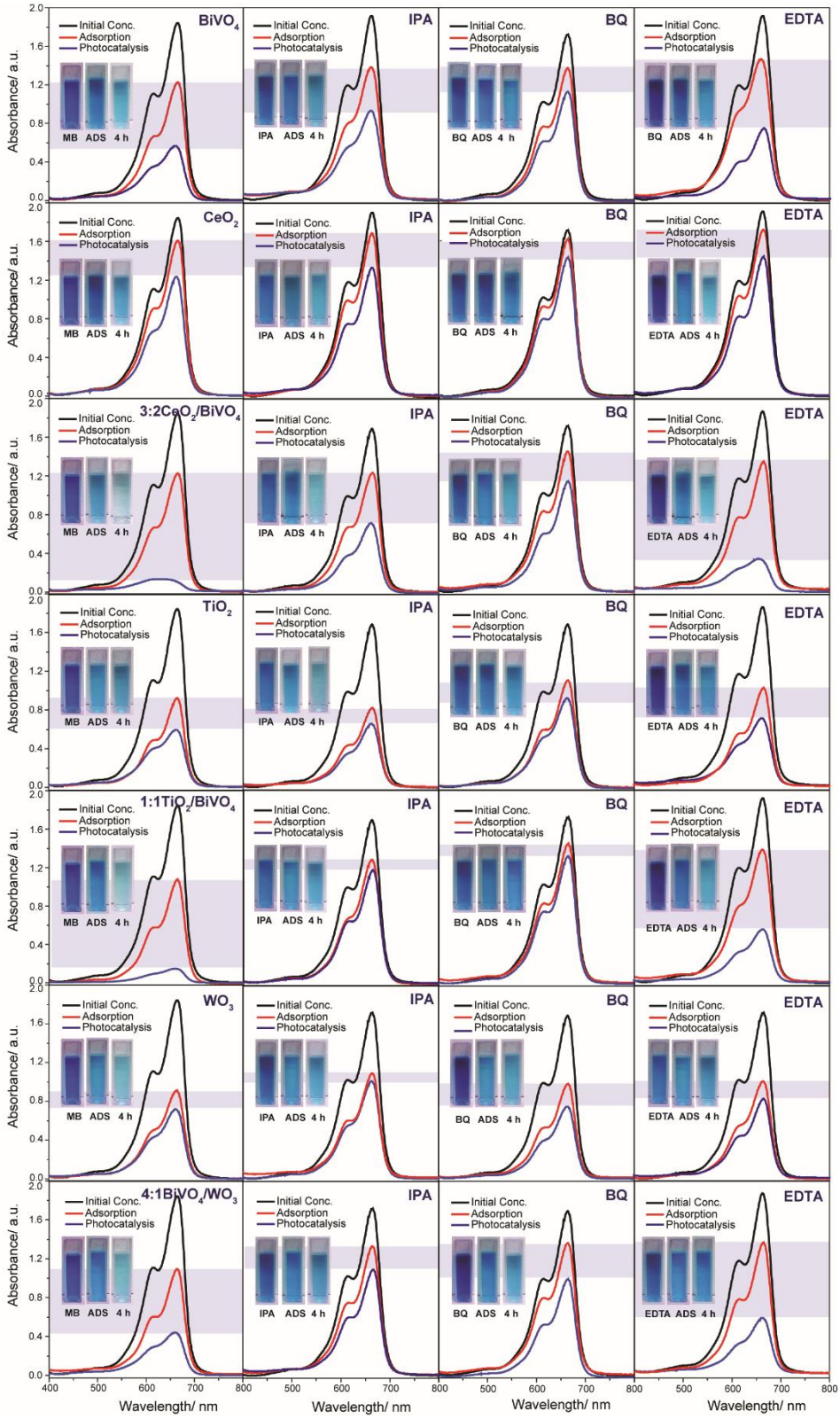

Figure 6.23 Photodegradation of MB (change of UV-vis spectra) with different composite films in the absence and presence of IPA, BQ and EDTA scavengers under solar light irradiation for 2 h.

Additionally, photocatalysis experiments for scavenging of the pure $BiVO_4$, CeO_2, TiO_2 and WO_3 films were also carried out in similar conditions as carried out for scavenging experiments. The BQ almost completely quenched the RhB and MB degradation of both the pure $BiVO_4$ and CeO_2 indicating that $^{\cdot}O_2^-$ is the main active specie in these systems. For the photodegradation of RhB and MB with the TiO_2 and WO_3 films, a large suppression on addition of IPA and BQ were observed. Therefore, the major oxidation species in the photocatalysis of the TiO_2 and WO_3 were also $^{\cdot}O_2^-$ and $^{\cdot}OH$.

In comparison to the condition without scavenger, the 3:2 $TiO_2/BiVO_4$ composite films with IPA scavenger showed a slight decrease in its absorption spectra of RhB followed by with BQ scavenger. Similarly, the order of active species for scavenging in the 1:1 $TiO_2/BiVO_4$ system was IPA > BQ >> EDTA inhibiting the photodegradation of MB. This indicates that the $^{\cdot}OH$ was probably a major active specie for degradation of both RhB and MB followed by $^{\cdot}O_2^-$. Similarly, a large suppression on addition of IPA and BQ were observed for the degradation of RhB and MB.

In the $BiVO_4/WO_3$ composite system, the spectra of RhB and MB degradation were slightly decreased upon addition of IPA and BQ by comparing with a dye solution without scavenger, this suggested that the $^{\cdot}OH$ and $^{\cdot}O_2^-$ radical species played the predominant role in photocatalytic degradation of RhB and MB.

Comparatively, the main active species of the $CeO_2/BiVO_4$ composite film in the photodegradation process of RhB and MB dyes was $^{\cdot}O_2^-$. While, the main active species in the $TiO_2/BiVO_4$ and $BiVO_4/WO_3$ composite systems were $^{\cdot}OH$ followed by a small amount of $^{\cdot}O_2^-$.

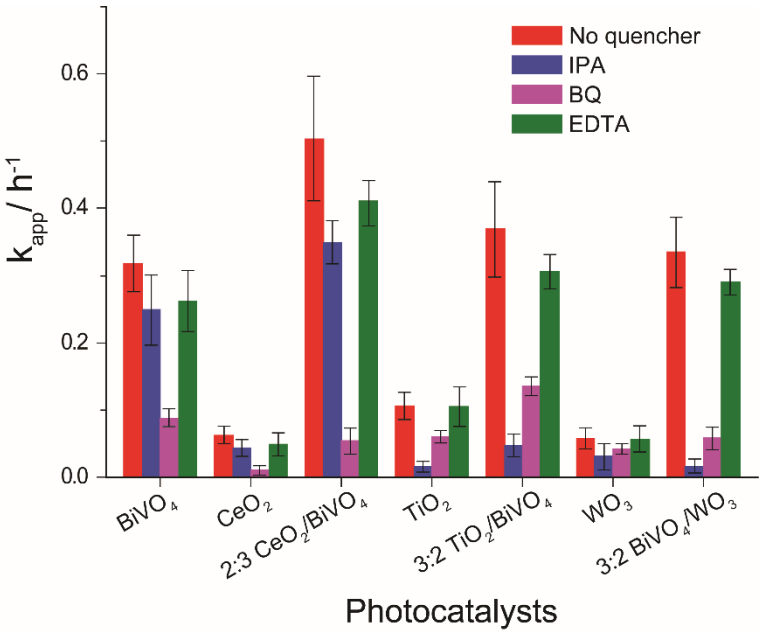

Figure 6.24 Pseudo first order rate constants of photodegradation of RhB by using different photocatalyst films with and without scavengers under solar light irradiation.

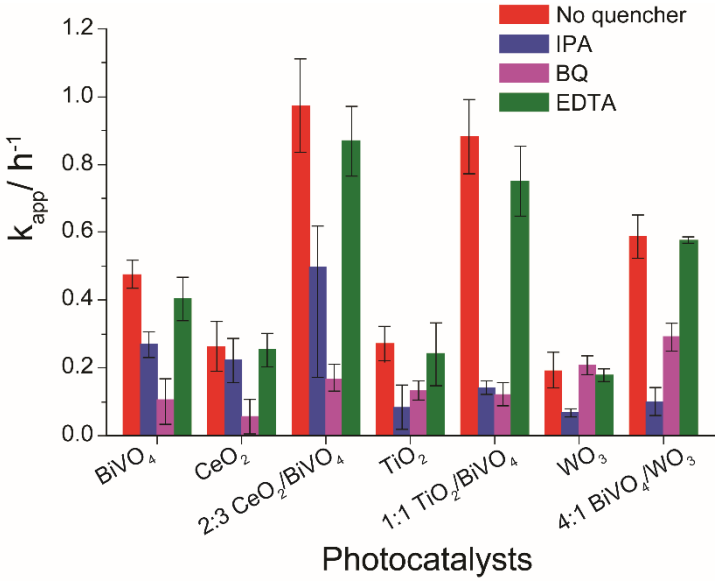

Figure 6.25 Pseudo first order rate constants of photodegradation of MB by using different photocatalyst films with and without scavengers under solar light irradiation.

Initial model for a photodegradation rate of each composite with different quenchers, Δk_{app} (IPA), Δk_{app} (BQ), and Δk_{app} (EDTA), was defined as quencher effects. Thus, the summation of those three quenchers in each composite system, $\Sigma\Delta k_{app}$ (quencher), should be equal to Δk_{app} (unquencher). In Figures 6.24 and 6.25, it could be observed that the $\Sigma\Delta k_{app}$ (quencher) of three composites were not equal to Δk_{app} (unquencher). This suggested that either multiple mechanisms at play in degradation of RhB and MB dyes or complex mechanism involving multiple photogenerated species, and more study is need to confirm the fact. However, these experiments also point out the possibility of a photocatalyst system being poisoned. Moreover, these quenching studies of three composites were in agreement with their Mott-Schottky results, which will be discussed in the next section.

6.5.3 Discussion of mechanisms

From photocatalytic testing with quenchers, it was found that there are three possible mechanisms for photocatalytic degradation of dyes as summarised in Figure 6.26, including (1) direct photolysis of dyes, (2) dye-photosensitization reaction, charge injection from photoexcited dye leaving unstable dye anion/cation, and (3) photocatalytic degradation of dyes, attack by radical generated by photoexcitation of semiconductor.[59, 60] However, it is believed that the reaction of direct dye degradation is much slower than of the mechanism by semiconductor photocatalysts.[59]

Since, RhB and MB dyes can absorb some of visible light, (1) mechanism, the photolysis of dye degradation, and (2) mechanism, will occur in this system as confirming by monochromatic results in Figure 6.21. For (1) mechanism, Figure 6.26(a), the dye is excited by visible light photon from ground state (Dye) to triplet excited state (Dye*). Then, one e^- inject from the excited dye to the CB of the SC, leaving unstable dye as a semi-oxidized radial cation ($Dye^{+\bullet}$), and this reactive dye can oxide and further degrade dye molecules by itself.

In the case of semiconductor photocatalysts have absorption edge lower than the used monochromatic filters, but it can catalyse the degradation of MB when a 650 nm filter is used. This can be explained by (2) mechanism in Figure 6.26(a), the dye-photosensitization reaction. The excited e^- from the ground state of the adsorbed dye molecules can be injected into the CB of the semiconductor particles. Subsequently, the trapped e^- can react with adsorbed O_2 to to produce $O_2^{-\bullet}$ and/or $HO_2^{\bullet}$. These species can further form $HO^{\bullet}$ radicals which are a highly active species for oxidation of dyes.

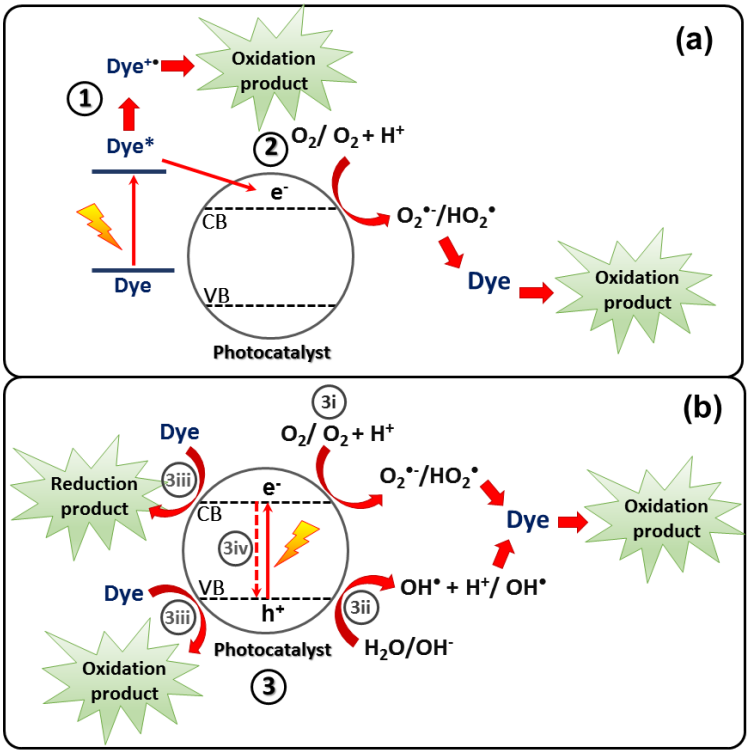

Figure 6.26 Possible main mechanisms: (a) direct degradation of dyes, (1) photolysis and (2) dye-photosensitization reactions, and (b) indirect degradation of dyes by (3) photocatalytic reaction.

Based on the results from above Mott-Schottky analysis, quenching study and monochromatic light experiment, possible mechanisms and position of band potentials of $BiVO_4/CeO_2$, $BiVO_4/TiO_2$ and $BiVO_4/WO_3$ composites, and their

individual materials are proposed in Figure 6.27. The results of photocatalytic activities for RhB and MB dyes degradation of all three composites had better than of their individual components. The $BiVO_4/CeO_2$ composite exhibited better photocatalytic performance than the $BiVO_4/TiO_2$ and $BiVO_4/WO_3$ composites.

Considering RhB and MB dyes can adsorb under visible light irradiation so that one e^- can be excited from ground state to excited state, RhB (0.95 V vs. NHE) and RhB* (−1.42 V vs. NHE),[54, 61] MB (0.046 V vs. NHE) and MB* (−1.66 V vs. NHE).[62] According to orbital energies of dye, an e^- from photoexcited dye can be trapped by O_2 to form $O_2^{\bullet-}$ injected into the CB of the photocatalyst for further reaction. Photolysis mechanism (1) may occur in all of photocatalyst systems reported here (Figure 6.27) relating to the results in degradation of both dyes without photocatalyst.

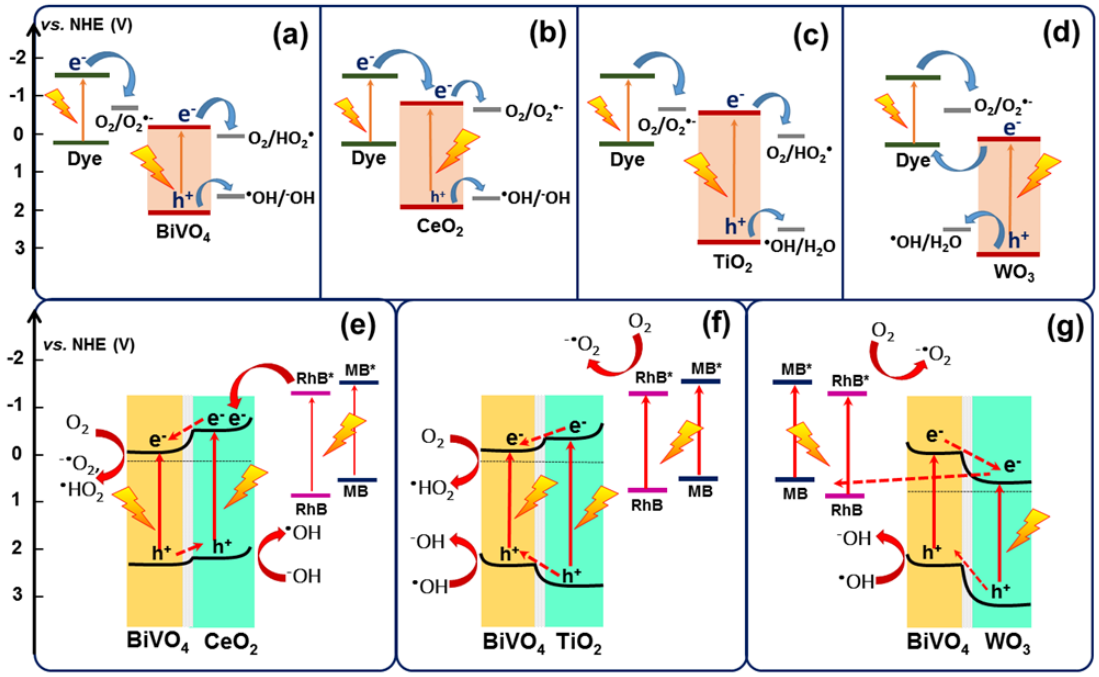

Figure 6.27 The proposed photocatalytic dye degradation mechanism over the (a) $BiVO_4$, (b) CeO_2, (c) TiO_2, (d) WO_3, (e) $CeO_2/BiVO_4$, (f) $TiO_2/BiVO_4$, and (g) $BiVO_4/WO_3$ composites under simulated solar light irradiation at pH ~5.0.

Alternatively, (3) mechanism in Figure 6.26, the semiconductor can be excited under light irradiation, then generated h^+ and e^- in the VB and CB of the semiconductor. The e^- can be trapped by adsorbed O_2 on the semiconductor surface to generate various reactive oxygen species such as (3i) reaction, $^{-\bullet}O_2$ ($O_2/O_2^{-\bullet}$ = −0.248 V *vs.* NHE),[63, 64] and $^{\bullet}HO_2$ ($O_2/^{\bullet}HO_2$ = −0.046 V *vs.* NHE), and (3ii) reaction, the generated h^+ can oxidize ^-OH or H_2O to $^{\bullet}OH$ ($^{\bullet}OH/OH^-$ = 1.99 V, $^{\bullet}OH/H_2O$ = 2.73 V *vs*. NHE), respectively, (3iii) and/or h^+ can directly oxidize the absorbed dye molecules.[63-65] Thus, the degradation efficiency greatly depends on the adsorption of dye, O_2 and H_2O on the surface of semiconductor. However, (3iv) the e^- can recombine with the h^+ of these. Importantly, the rate of the e^- and h^+ transfer are determined by the redox potentials of the adsorbed dye*, the semiconductor, O_2 and H_2O.

Table 6.12 Summary of dominant mechanisms for degradation of dyes over different materials and their photocatalytic rate constant.

Materials	**Dominant mechanisms**	**K_{app} (h^{-1})**	
		RhB	**MB**
$BiVO_4$	(2) and (3i)	0.354	0.495
CeO_2	(3i)	0.098	0.383
TiO_2	(3i) and (3ii)	0.126	0.363
WO_3	(3ii)	0.108	0.314
$CeO_2/BiVO_4$	(2) and (3i)	0.458	0.989
$TiO_2/BiVO_4$	(2) and (3ii)	0.470	1.12
$BiVO_4/WO_3$	(3ii)	0.423	0.693

The pure $BiVO_4$ had higher photocatalytic efficiency than the CeO_2, TiO_2 or WO_3. This is due to the different mechanisms of each materials involved in photocatalytic degradation of dye as shown Figures 6.27(a)-(d). Since the $BiVO_4$ has an absorption edge of ~526 nm, while the absorption edges of others materials are shorter than 500 nm, the $BiVO_4$ will able to be activated by a wider range of light, this corresponded to

the band position energy of $BiVO_4$ and its higher photocatalytic activities under a 350 nm monochromatic light.

As Figure 6.27(a), the main mechanism of the $BiVO_4$ system are photolysis and photocatalysis under visible light irradiation. The photocatalysis mechanism can produce $O_2^{-\bullet}$ from (2) mechanism and $HO_2^{-\bullet}$ from (3i) reaction at CB as major species, and small amount of $^{\bullet}OH$ at VB, (3ii) reaction, for dye oxidation.

The mechanism of CeO_2 is shown in Figure 6.27(b), is similar to $BiVO_4$ system that can generate $O_2^{-\bullet}$ and $HO_2^{-\bullet}$ under solar irradiation. However, the photocatalytic activity of this material was less than of $BiVO_4$ due to less adsorbed dye on its surface confirming by zeta potentials results (PZC = 7.34).

In the TiO_2 system, Figure 6.27(c), the main mechanism is photocatalysis under UV light irradiation, $^{\bullet}OH$ species can be generated by oxidation process of photo-generated h^+ and adsorbed water at VB of the TiO_2, (3ii) reaction, and $^{\bullet-}O_2$ also be produced at its CB, (2) and/or (3i) reaction. However, the absorption edge of TiO_2 is lower 350 nm which can be only activated by UV light irradiation, less than 5% of solar light, corresponding to its low photocatalytic performance under monochromate light between 350 to 700 nm.

For WO_3 system, $^{\bullet}OH$ from (3ii) reaction is only an active specie for dye photodegradation, confirming by quencher experiment, which can be produce by oxidation process at VB of the WO_3. Since the WO_3 provided the high dye adsorption property led to less adsorption in H_2O or ^{-}OH molecules on its surface. Moreover, the photoexcited e^- at CB of the WO_3 can easily transfer to the ground state of dye as shown in Figure 6.27(d). Thus, photocatalytic activity of this photocatalyst exhibited lower than other materials.

For $CeO_2/BiVO_4$ composite is shown in Figure 6.27(e), both the CeO_2 and the $BiVO_4$ can be excited under visible light irradiation. Thus, photogenerated h^+ and e^- occur in

the VB and CB of both materials. Since $BiVO_4$ has the CB and VB potential edges more positive than CeO_2, the interface band bending are formed when CeO_2 contacts with $BiVO_4$ resulting in the formation of a potential barrier between two materials.

Photoexcited e^- in the CB can be transferred from the CB of CeO_2 to $BiVO_4$ and trap the absorbed O_2 to create $^{-\bullet}O_2$ and/or $^{\bullet}HO_2$ radicals, (3i) reaction corresponding to above results for quenching studies of both dyes over this composite. From the quenching study, some $^{\bullet}OH$ were also observed in this system, this suggests that the photogenerated h^+ in the VB of $BiVO_4$ and/or CeO_2 could oxidize the adsorbed OH^- to $^{\bullet}OH$, (3ii) reaction. The charge transfers of either photoexcited materials together with the injection of one e^- from the photoexcited dye to the CB CeO_2 should lead to enhance photocatalytic activity for dye degradation.

The CB and VB of $BiVO_4$ are both located between the CB and VB of TiO_2. The band gap energy of $BiVO_4$ (2.4 eV) is significantly smaller than TiO_2 (3.2 eV), as shown in Figure 6.27(f) for $TiO_2/BiVO_4$ composite. The photoexcitation of TiO_2 can generate e^- and h^+ pair at CB and VB by UV light activation. The photogenerated e^- at CB of TiO_2 can transfer to the CB of $BiVO_4$, while the photogenerated h^+ at VB and transfer to the VB of $BiVO_4$ then the e^- and h^+ will recombine. However, these mechanisms can occur only under UV light.

Thus, the possible mechanisms of this system are photolysis and photocatalysis of $BiVO_4$ in $TiO_2/BiVO_4$ composite leading to less photocatalytic activity for degradation of both RhB and MB dyes than $CeO_2/BiVO_4$ composite. As shown in Figure 6.27(f), the adsorbed RhB and on the composite surface can adsorb the visible light to generate the RhB* or MB* and one e^-, then the e^- can trap the adsorbed O_2 to $^{-\bullet}O_2$ under visible light irradiation, (2) mechanism. The $^{\bullet}OH$ radicals can also be produced by (3ii) reaction from photocatalysis of the $BiVO_4$ in the $TiO_2/BiVO_4$ composite as the main mechanism related to its quenching study and monochromatic photocatalysis

the photocatalytic rates of pure $BiVO_4$ and $TiO_2/BiVO_4$ were similar and both showed higher than of pure TiO_2 under a 450 nm monochromatic light.

In the $BiVO_4/WO_3$ composite (Figure 6.27(g)), the CB and VB potential edges of $BiVO_4$ are more negative than those of WO_3, which is the opposite configuration to the $CeO_2/BiVO_4$ composite. The $BiVO_4$ and WO_3 in the $BiVO_4/WO_3$ composite can be activated by visible light irradiation and generated e^- and h^+ pairs. The e^- at CB of $BiVO_4$ can transfer to the CB of WO_3, then will recombine with dye, cannot reduce the absorbed O_2 to radical species, due to both CB potentials are more positive than redox potential of reduction of O_2 to $O_2^{-\bullet}$. However, the photogenerated h^+ at the VB of WO_3 can transfer to the VB of $BiVO_4$, which can oxidize H_2O and OH^- to $^\bullet OH$, (3ii) reaction. As dye molecules preferentially adsorb on the surface of WO_3 compared to $BiVO_4$, confirmed by the highest adsorptive properties in dark condition of both dyes and its high negative surface charge (Figure 6.18), it can be concluded that the main mechanism is production of $^\bullet OH$ at the VB of the $BiVO_4$ in the composite that leads to showing the lowest photocatalytic activity as compared to the $CeO_2/BiVO_4$ and $TiO_2/BiVO_4$composites.

6.6 Conclusions

Three composite photocatalysts, based $BiVO_4$, were successfully synthesised by wet chemical processes. This included $CeO_2/BiVO_4$, $TiO_2/BiVO_4$ and $BiVO_4/WO_3$.

The physical and photocatalytic properties of those three composites were investigated and compared. The closeness of absorption properties of all composite photocatalysts compared to pure $BiVO_4$ along with the XRD, XPS and TEM analyses confirm the formation of the composite without significant doping.

The superior photocatalytic performance of the three composite photocatalysts were demonstrated with the enhanced degradation of RhB and MB dyes solution under solar light and visible light irradiation compared to pure materials. The composition of

each system was varied and an optimum found for each of RhB and MB degradation, the order of photocatalytic performance for RhB and MB degradation was $CeO_2/BiVO_4$ > $TiO_2/BiVO_4$ > $BiVO_4/WO_3$, respectively.

As the degradation performance greatly depends on the band edge potentials of each material, adsorption of dye, O_2 and H_2O on the surface and redox potentials of the adsorbed dye, Mott-Schottky analysis, active species trapping studies and monochromatic light experiment were carried out to investigate the possible mechanisms of dye degradation.

The CB and VB positions of CeO_2 were more negative than those of $BiVO_4$ ($BiVO_4/CeO_2$ composite), while WO_3 had more positive CB and VB positions than $BiVO_4$ ($BiVO_4/WO_3$ composite), and $BiVO_4$ showed the CB and VB positions in between the CB and VB of TiO_2 ($BiVO_4/TiO_2$ composite).

It was demonstrated that the $CeO_2/BiVO_4$ composite can produce $^{\bullet-}O_2$ and/or $^{\bullet}HO_2$ by photogenerated electron transfer from the CB of CeO_2 to $BiVO_4$, and $^{\bullet}OH$ by photogenerated hole transfer from the VB of $BiVO_4$ to CeO_2. However, as the dyes favour to adsorb on the surface of a high negative surface charge of $BiVO_4$, production $^{\bullet-}O_2$ and/or $^{\bullet}HO_2$ as the main mechanism of this system.

Under solar light irradiation, the $TiO_2/BiVO_4$ composite system also can produce $^{\bullet-}O_2$ and $^{\bullet}HO_2$ by electron transfer from the CB of TiO_2 to $BiVO_4$. However, TiO_2 can be only activated by UV light irradiation, which provides less than 5% of solar light. Thus, the generation of reactive species of this $TiO_2/BiVO_4$ composite system is less than that of $CeO_2/BiVO_4$ composite system leading to providing lower photocatalytic activities for degradation of both RhB and MB dyes.

For the $BiVO_4/WO_3$ composite, there are two mechanism at VB of $BiVO_4$ produce the $^{\bullet-}O_2$ and $^{\bullet}OH$ for degrading dyes, but both cationic dyes preferably adsorb on the surface of WO_3 than $BiVO_4$.

As such, the $BiVO_4/WO_3$ composite exhibited much lower photocatalytic performance as compared to the $CeO_2/BiVO_4$ and $TiO_2/BiVO_4$ composites. Furthermore, in presence of visible light the adsorbed RhB and MB dyes can sensitise together with the adsorbed O_2 on surface of the photocatalysts for generation of oxidizing and highly reactive radical species ($^{\bullet-}O_2$ and/or $^{\bullet}HO_2$) related to the presence of photocatalytic reaction in all composite systems under visible light irradiation.

References

1. A. Kudo and Y. Miseki, *Chem. Soc. Rev.*, 2009, **38**, 253–278.
2. D. S. Bhatkhande, V. G. Pangarkar and A. A. C. M. Beenackers, *J. Chem. Technol. Biotechnol.*, 2002, **77**, 102–116.
3. D. Wang, R. Li, J. Zhu, J. Shi, J. Han, X. Zong and C. Li, *J. Phys. Chem. C*, 2012, **116**, 5082–5089.
4. M. Pelaez, N. T. Nolan, S. C. Pillai, M. K. Seery, P. Falaras, A. G. Kontos, P. S. M. Dunlop, J. W. J. Hamilton, J. A. Byrne, K. O'Shea, M. H. Entezari and D. D. Dionysiou, *Appl. Catal., B*, 2012, **125**, 331–349.
5. F. F. Abdi, T. J. Savenije, M. M. May, B. Dam and R. van de Krol, *J. Phys. Chem. Lett.*, 2013, **4**, 2752–2757.
6. S. Gupta and M. Tripathi, *Chin. Sci. Bull.*, 2011, **56**, 1639–1657.
7. S. Ahmed, M. G. Rasul, W. N. Martens, R. Brown and M. A. Hashib, *Desalination*, 2010, **261**, 3–18.
8. L. Li and B. Yan, *J. Alloys Compd.*, 2009, **476**, 624–628.
9. L. Chen, Q. Zhang, R. Huang, S. F. Yin, S. L. Luo and C. T. Au, *Dalton Trans.*, 2012, **41**, 9513–9518.
10. H. Jiang, M. Nagai and K. Kobayashi, *J. Alloys Compd.*, 2009, **479**, 821–827.
11. J. Su, X. X. Zou, G. D. Li, X. Wei, C. Yan, Y. N. Wang, J. Zhao, L. J. Zhou and J. S. Chen, *J. Phys. Chem. C*, 2011, **115**, 8064–8071.
12. Y. Hu, D. Li, Y. Zheng, W. Chen, Y. He, Y. Shao, X. Fu and G. Xiao, *Appl. Catal., B*, 2011, **104**, 30–36.

13. L. Zhang, G. Tan, S. Wei, H. Ren, A. Xia and Y. Luo, *Ceram. Int.*, 2013, **39**, 8597–8604.

14. P. Chatchai, Y. Murakami, S. Y. Kishioka, A. Y. Nosaka and Y. Nosaka, *Electrochim. Acta*, 2009, **54**, 1147–1152.

15. P. Chatchai, A. Y. Nosaka and Y. Nosaka, *Electrochim. Acta*, 2013, **94**, 314–319.

16. J. Su, L. Guo, N. Bao and C. A. Grimes, *Nano Lett.*, 2011, **11**, 1928–1933.

17. J. Jiang, M. Wang, R. Li, L. Ma and L. Guo, *Int. J. Hydrogen Energy*, 2013, **38**, 13069–13076.

18. R. Bajaj, M. Sharma and D. Bahadur, *Dalton Trans.*, 2013, **42**, 6736–6744.

19. S. K. Pilli, T. G. Deutsch, T. E. Furtak, L. D. Brown, J. A. Turner and A. M. Herring, *Phys. Chem. Chem. Phys.*, 2013, **15**, 3273–3278.

20. S. Obregon and G. Colon, *RSC Adv.*, 2014, **4**, 6920–6926.

21. J. Liqiang, S. Xiaojun, S. Jing, C. Weimin, X. Zili, D. Yaoguo and F. Honggang, *Sol. Energy Mater. Sol. Cells*, 2003, **79**, 133–151.

22. G. Magesh, *Indian J. Chem., Sect. B*, 2009, **48**, 480.

23. N. Wetchakun, B. Incessungvorn, K. Wetchakun and S. Phanichphant, *Mater. Lett.*, 2012, **82**, 195–198.

24. M. Gotić, S. Musić, M. Ivanda, M. Šoufek and S. Popović, *J. Mol. Struct.*, 2005, **744–747**, 535-540.

25. A. Zhang, J. Zhang, N. Cui, X. Tie, Y. An and L. Li, *J. Mol. Catal. A: Chem.*, 2009, **304**, 28–32.

26. Y. Xiaodan, W. Qingyin, J. Shicheng and G. Yihang, *Mater. Charact.*, 2006, **57**, 333–341.

27. L. Miao, S. Tanemura, S. Toh, K. Kaneko and M. Tanemura, *J. Cryst. Growth*, 2004, **264**, 246–252.

28. X. Xue, W. Ji, Z. Mao, H. Mao, Y. Wang, X. Wang, W. Ruan, B. Zhao and J. R. Lombardi, *J. Phys. Chem. C*, 2012, **116**, 8792–8797.

29. S. Humaira, K. C. Kemp, C. Vimlesh and S. K. Kwang, *Nanotechnology*, 2012, **23**, 355705.

30. Y. Djaoued, S. Balaji and N. Beaudoin, *J. Sol-Gel Sci. Technol.*, 2013, **65**, 374–383.

31. B. Naik, S. Martha and K. M. Parida, *Int. J. Hydrogen Energy*, 2011, **36**, 2794–2802.

32. P. Burroughs, A. Hamnett, A. F. Orchard and G. Thornton, *Journal of the Chemical Society, Dalton Trans.*, 1976, 1686–1698.

33. S. Yang, W. Zhu, Z. Jiang, Z. Chen and J. Wang, *Appl. Surf. Sci.*, 2006, **252**, 8499–8505.

34. H. Li, C.-Y. Wu, Y. Li and J. Zhang, *Appl. Catal., B*, 2012, **111–112**, 381–388.

35. L. Chen, J. Li and M. Ge, *J. Phys. Chem. C*, 2009, **113**, 21177–21184.

36. S. Watanabe, X. Ma and C. Song, *J. Phys. Chem. C*, 2009, **113**, 14249–14257.

37. M. Gurulakshmi, M. Selvaraj, A. Selvamani, P. Vijayan, N. R. Sasi Rekha and K. Shanthi, *Appl. Catal., A*, 2012, **449**, 31–46.

38. M. T. Uddin, Y. Nicolas, C. Olivier, T. Toupance, M. M. Müller, H. J. Kleebe, K. Rachut, J. Ziegler, A. Klein and W. Jaegermann, *J. Phys. Chem. C*, 2013, **117**, 22098–22110.

39. S. A. K. Leghari, S. Sajjad, F. Chen and J. Zhang, *Chem. Eng. J.*, 2011, **166**, 906–915.

40. S. Zhang, H. Li and Q. Zhong, *Appl. Catal., A,* 2012, **435–436**, 156–162.

41. W. Luo, Z. Yang, Z. Li, J. Zhang, J. Liu, Z. Zhao, Z. Wang, S. Yan, T. Yu and Z. Zou, *Energy Environ. Sci.*, 2011, **4**, 4046–4051.

42. S. J. A. Moniz, J. Zhu and J. Tang, *Adv. Energy Mater.*, 2014, **4**, n/a-n/a.

43. C. Zhen, L. Wang, L. Liu, G. Liu, G. Q. Lu and H.-M. Cheng, *Chem. Commun.* 2013, **49**, 6191–6193

44. G. Wang, Y. Ling, H. Wang, X. Yang, C. Wang, J. Z. Zhang and Y. Li, *Energy Environ. Sci.*, 2012, **5**, 6180–6187.

45. C. Ponchio, Y. Murakami, S. Y. Kishioka, A. Y. Nosaka and Y. Nosaka, *Meeting Abstracts*, 2008, **MA2008–02**, 2752.

46. L. Tong, A. Iwase, A. Nattestad, U. Bach, M. Weidelener, G. Gotz, A. Mishra, P. Bauerle, R. Amal, G. G. Wallace and A. J. Mozer, *Energy Environ. Sci.*, 2012, **5**, 9472–9475.

47. M. L. Guan, D. K. Ma, S. W. Hu, Y. J. Chen and S. M. Huang, *Inorg. Chem.*, 2010, **50**, 800–805.

48. . Zhuang, W. Dai, Q. Tian, Z. Li, L. Xie, J. Wang, P. Liu, X. Shi and D. Wang, *Langmuir*, 2010, **26**, 9686–9694.

49. R. Holyst, A. Bielejewska, J. Szymanski, A. Wilk, A. Patkowski, J. Gapinski, A. Zywocinski, T. Kalwarczyk, E. Kalwarczyk, M. Tabaka, N. Ziebacz and S. A. Wieczorek, *Phys. Chem. Chem. Phys.*, 2009, **11**, 9025–9032.

50. J. d. S. Macedo, N. B. da Costa Júnior, L. E. Almeida, E. F. d. S. Vieira, A. R. Cestari, I. d. F. Gimenez, N. L. Villarreal Carreño and L. S. Barreto, *J. Colloid Interface Sci.*, 2006, **298**, 515–522.

51. A. T. Bell, *Science*, 2003, **299**, 1688–1691.

52. A. L. Linsebigler, G. Lu and J. T. Yates, *Chem. Rev.*, 1995, **95**, 735–758.

53. P. V. Kamat, *Journal of the Chemical Society, Faraday Transactions 1: Physical Chemistry in Condensed Phases*, 1985, **81**, 509–518.

54. T. Takizawa, T. Watanabe and K. Honda, *J. of Phys. Chem.*, 1978, **82**, 1391–1396.

55. J. Xu, L. Li, C. Guo, Y. Zhang and W. Meng, *Appl. Catal., B*, 2013, **130–131**, 285–292.

56. J. Xu, W. Meng, Y. Zhang, L. Li and C. Guo, *Appl. Catal., B*, 2011, **107**, 355–362.

57. Y. Park, Y. Na, D. Pradhan, B. K. Min and Y. Sohn, *Cryst. Eng. Comm.*, 2014, **16**, 3155–3167.

58. S. Xiao, Y. Li, J. Hu, H. Li, X. Zhang, L. Liu and J. Lian, *Cryst. Eng. Comm.*, 2015, **17**, 3809–3819.

59. A. Ajmal, I. Majeed, R. N. Malik, H. Idriss and M. A. Nadeem, *RSC Adv.*, 2014, **4**, 37003–37026.

60. .Hennig, *Angew. Chem. Int. Ed. Engl.*, 2015, **54**, 4429–4429.

61. D. Du, W. Li, S. Chen, T. Yan, J. You and D. Kong, *New J. Chem.*, 2015, **39**, 3129–3136.

62. J. S. Shen, T. Yu, J.-W. Xie and Y.-B. Jiang, *Phys. Chem. Chem. Phys.*, 2009, **11**, 5062–5069.

63. S. Nishimoto, T. Mano, Y. Kameshima and M. Miyake, *Chem. Phys. Lett.*, 2010, **500**, 86–89.

64. W. Liu, M. Wang, C. Xu, S. Chen and X. Fu, *Mater. Res. Bull.*, 2013, **48**, 106–113.

65. M. Sun, Y. Su, C. Du, Q. Zhao and Z. Liu, *RSC Adv.*, 2014, **4**, 30820–30827

CHAPTER 7

CONCLUSIONS AND PERSPECTIVES

7.1 Conclusions

Semiconductor heterogeneous photocatalysis has attracted increasing attention as a potential method to solve environmental problems, especially for degradation of organic pollutants in wastewater. As the visible light is an abundant natural resource of our world, the primary motivation in this thesis has been developed Bismuth vanadate ($BiVO_4$) as a visible light driven photocatalyst for degradation of organic dye pollutants. This research work also focused on the study of operating parameters for photocatalytic degradation of dyes, the preparation of $BiVO_4$ nanoparticles by a single-step microwave synthesis as a simple and energy saving method, and the modification of $BiVO_4$ by coupling with other metal that provided appropriate different electronic band structure in order to improve its photocatalytic activity. The photocatalytic properties of all synthesised materials were monitoring on degradation of Rhodamine B (RhB) and Methylene Blue (MB) as model organic pollutants under a simulated solar irradiation. All results obtained in the present work is summarised as below.

In chapter 4 a series of experiments were performed to develop a better understanding of photocatalytic reaction especially in the context of what was seen in Chapter 2, where the variation in experimental method made comparison difficult. An experimental setup for investigation of photocatalytic reaction as intrinsic kinetics was designed so that the photocatalytic reaction influencing parameters through degradation of Rhodamine B (RhB) and Methylene blue (MB) as models of organic dye pollutants including thickness of catalyst film, dye concentration, light intensity and reactor volume were investigated. The performance increased with thickness up

to ~ 2–3 μm and light intensity up to 100 mW cm^{-2}. The area to volume had no effect within the examine region and low initial concentration of dye appear leading to over estimation.

A comparison between a catalyst in powder and film forms were investigated with, cyclability photocatalytic dye degradation. The films were shown to be more stable than of the free powders. As such the film based catalysts are employed thought the rest of this thesis.

Following on this, Chapter 5 investigated a single-step microwave method developed to synthesise high-purity $BiVO_4$ nanoparticles. The operational parameters for the microwave synthesis of $BiVO_4$, namely pH of precursor solution, treatment temperature and time were investigated and optimised. The results shown that the crystalline structure and morphology of the obtained $BiVO_4$ powder could be controlled by the pH of reaction mixture and microwave treatment time.

Monoclinic $BiVO_4$ with spherical particles (~40 nm) were obtained using a pH 7 precursor solution, under microwave operating at 90°C (power < 300 W) and 1 hour processing time. The products of above condition exhibited high photocatalytic performance for degradation of RhB and MB under simulated sunlight irradiation.

The crystallinities, morphologies and photocatalytic properties of the synthesised $BiVO_4$ by the microwave method were further compared to of synthesised $BiVO_4$ by the precipitation and hydrothermal methods under the same starting precursors, solvents, and pH of final solution. Pure monoclinic $BiVO_4$ materials were investigated, produced by each of their differently synthetic methods. The monoclinic structure and high surface area of the microwave synthesised material provided similar photocatalytic activity to the precipitated sample, however the use of microwave irradiation has the additional benefit of a shorter reaction time and being able to avoid the need for a secondary heat treatment. Since electron under

this bias can prevent the rapid recombination of the photogenerated charge carriers under sunlight irradiation, the photocatalytic performance was improved. Mott-Schottky analysis was performed to investigate the electronic property of the $BiVO_4$. This shows that $BiVO_4$ can generate $^{\bullet-}O_2$ and/or $^{\bullet}HO_2$ active species for degradation of RhB and MB dyes under solar light irradiation.

In the following Chapter, Chapter 6 anther method for enhancing charge separation was investigated. In order to improve the photocatalytic performance of $BiVO_4$, heterostructures between $BiVO_4$ and selected metal oxides, CeO_2, TiO_2 and WO_3, were produced. These aims to reduce recombination and improve transportation of charge carriers to reaction sites. Composite materials including $CeO_2/BiVO_4$, $TiO_2/BiVO_4$ and $BiVO_4/WO_3$, were successfully synthesised by wet chemical processes. In each of these $BiVO_4$ had the lowest band gap, meaning light harvesting efficiency for all composites was comparable. XRD, XPS and TEM analyses confirm the formation of the composite without significant doping. Superior photocatalytic performance for degradation of RhB and MB dyes under solar light and visible light irradiation was observed of all photocatalysts relative to their component materials were demonstrated.

The highest photocatalytic performance for photodegradation of RhB under solar light irradiation was found to be from 2:3 $CeO_2/BiVO_4$, 3:2 $TiO_2/BiVO_4$ and 3:2 $BiVO_4/WO_3$ composites, respectively while for photodegradation MB under visible light irradiation 2:3 $CeO_2/BiVO_4$, 1:1 $TiO_2/BiVO_4$ and 4:1 $BiVO_4/WO_3$ composites were seen to be the optimal ratios for each pair.

Each of the above pair provides different conduction band and valence band off sets. As such, the possible mechanisms of those three composites in photocatalytic reaction have investigated by monochromatic light experiments, Mott-Schottky analysis and reactive species quenching studies. The results of monochromatic light

experiments confirm the adsorbed RhB and MB dyes can sensitise the photocatalyst surface under visible light irradiation leading to their degradation. The Mott-Schottky results can prove that conduction band and valence band positions of $BiVO_4$ are more positive than of CeO_2, in between those of TiO_2 and more negative than WO_3. The reactive species quenching study, in conjunction with the above Mott-Schottky results, indicated that production of $O_2^{\bullet-}$ and $^{\bullet}HO$ are the main mechanism of $CeO_2/BiVO_4$ system, the main active species of $TiO_2/BiVO_4$ composite are $^{\bullet}OH$ and $^{\bullet}HO_2$, while of $BiVO_4/WO_3$ system is only $^{\bullet}OH$.

7.2 Perspectives

In this thesis, $BiVO_4$ provided an excellent photocatalytic activity for degradation of organic dyes which can be activated under visible light (λ = 526 nm). All of the developments showed that $BiVO_4$ and/or its composites, coupled with other metal oxide, have the potential as excellent visible-light-driven photocatalyst with high photocatalytic activity. Furthermore, to comply with the challenging requirements of economically viable industrial production, long-term stability of the mechanical stable $BiVO_4$ films in photocatalytic processes and new method such single step microwave synthesis for fabrication $BiVO_4$ nanoparticles, a simple, fast synthesis procedures, industrially viable low temperature synthesis method and environmentally benign alternate to other approaches, were studied and reported here.

Although this thesis has demonstrated a number of developments in the use of $BiVO_4$ as a visible light photocatalyst for wastewater purification there remains a great deal of work to be done. The following are some areas which are believed to be of specific intents for future investigation.

- To date, there have been few studies in the charge carrier dynamics including such recombination dynamics, in $BiVO_4$ co-catalysts systems. This

requires a deep understanding in the surface/interface processes at the atomic scale which need to be studied by a transient optical spectroscopy techniques. The transient absorption studies of induced absorption from hole and electron doping in the semiconductor could also help further prove the hypothesised enhancement in change carrier lifetime.

- As microwave synthesis is a facile method, time and energy saving and more environmental friendly than other wet chemical methods, it should be advantages, if the composites, $CeO_2/BiVO_4$, $TiO_2/BiVO_4$, and $BiVO_4/WO_3$, can be prepared by this method.
- Technique such as an ultraviolet photoelectron spectroscopy (UPS) would give added confidence to the measured values of the electronic structures of the $CeO_2/BiVO_4$, $TiO_2/BiVO_4$, and $BiVO_4/WO_3$ composites.
- Further studies on the produced reactive species from this system, intermediates and products from degradation of RhB and MB dyes should be attempted, using High Performance Liquid Chromatography (HPLC), Mass Spectrometry (MS), total organic carbon analysis (TOC) and other techniques.
- Other organic dyes such as anionic dye and neutral dye can also be used as model pollutants for the photocatalysis test.
- A further challenge is translating academic research from laboratory-scale experiment into device scale up for industrial manufacturing to meet demands of the potentials for solar energy utilization in environmental purification areas.

APPENDIX A

ABBREVIATION AND SYMBOLS

AOPs	Advanced oxidation processes
Å	Angstrom
A	Area
A	Proportionality constant
A_{CO}	The illuminated collector area per order
A_m	The cross-sectional area of absorbed gas
A_r	tThe illuminated collector area
Ag/AgCl	Silver/ silver chloride reference electrode
B	The peak width measured at half height measured in radius
BE	Electron binding energy
BET	Brunauer-Emmett-Teller
BiO_8	Bismuth dodecahedra
BQ	Benzoquinone
$BiVO_4$	Bismuth vanadate
C	Capacitance
C	Constant related to the free energy of adsorption
CB	Conduction Band
CBD	Chemical bath deposition method
CeO_2	Cerium dioxie
CO_2	Carbondioxide
CSD	Chemical solvent decomposition
CV	Cyclic voltammetry

CVD	Chemical vapor decomposition
C_e	Equilibrium concentration of dye solution
C_t	Concentration at time
C_0	Initial concentration
°C	Degrees Celsius
cm	Centimeter
cm^{-3}	Cubic centimeter
cm/mol	Centimeter per mole
cm^3/min	Cubic centimeter per minute
DER	*N,N*-diehyl-*N'*-ethylrhodamine
DR	*N,N*-diethylrhodamine
DMPO	5,5-dimethyl-1-pyrroline N-oxide
D_{hkl}	Interplanar distance between (hkl) planes
d	The lattice planar spacing or thickness
dm^3	Cubic decimeter
d_{BET}	BET-particle diameter
E	Binding energy
E	Energy released in the heat form
E	Potential
EDTA	Ethylenediaminetetraacetic acid
EER	*N*-ethyl-*N'*-ethylrhodamine
EPR	Electron paramagnetic resonance
ER	*N*-ethylrhodamine
E_{EO}	The electrical energy
E_F	Fermi level
E_{FB}	Flat band potential
E_g	Optical band gap of the semiconductor

EM	Electron microscopy
E_{CB}	Conduction band energy
E_{vac}	Energy of vacuum level
E_{VB}	Valence band energy
E^0	The standard electrode potential
e	The elementary charge
e^-	Electron
e^-_{CB}	Electron in the conduction band
eV	Electron volt
FTO	Fluorine-doped tin oxide
g/L	grams per liter
g/mol	grams per mole
H_2O	Disambiguation (water)
H_2O_2	Hydrogen peroxide
H^+	Hydron
$^{\bullet}HO_2$	Hydroperoxyl radical
h	Hour
h	Plank's constant (6.63×10^{-34} J.s), hour
$h\nu$	Photon energy
h^+_{VB}	Hole in the valence band
I_0	Intensity of the incident beam
I	Intensity of the transmittance
ITO	Deposited onto indium tin oxide
IPA	Isopropanol
IUPAC	International Union of Pure and Applied Chemistry
JCPDS	Joint Committee Powder Diffraction Standards
K	Adsorption coefficient of the reactant

K	Conductivity value
KE	Kinetic energy
K_{α}	K-alpha emission
k	Boltzmann constant
k	Oxidation rate constant
k_{app}	The apparent rate constant (Langmuir Hinshelwood kinetics)
k_L	Langmuir adsorption constant
keV	Kilo electron volt
kV	Kilo volt
kW h	Kilo watt hour
LC-MS	Liquid chromatography-mass spectrometry
LH	Langmuir Hinshelwood
L	Liter
L/min	Liter per minute
$Lmol^{-1}s^{-1}$	Liter per mole per second
LMB	leuco-methylene blue
LVS	Linear sweep voltammetry
h	hour
M	Mole per liter
MO	Methyl orange
MOD	Metalorganic decomposition
MB	Methylene blue
MB_{ads}	Adsorbed methylene blue
$MB^{\bullet -}$	Semi-methylene blue
$MB^{\bullet +}$	Oxidized methylene blue
MB^{*}	Excited state of methylene blue

mg	Milligram
min	Minute
mA	Milliampere
mL	Milliliter
mW	Milliwatt
m^2	Square meter
N	Neutral center
N_a	Avogadro's number (6.02×10^{23})
NHE	Normal hydrogen electrode
NH_4^+	Ammonium ion
NO_3^-	Nitrate
nm	Nanometer
nm^2	Square nanometer
ns	Nanosecond
$^{-\bullet}O_2$	Superoxide anion radical
Organic−$OO^\bullet$	Organic peroxide radical
$^\bullet OH$	Hydroxyl radical
^-OH	Hydroxyl ion
P	Power
P	Pressure
P_0	Saturation pressure at the measurement temperature
PEG	Polyethylene glycol
PEI	polyethyleneimine
PS	Polystyrene
Pt	Platinum
PZC	Point of zero charge

R	Rhodamine 110
RhB	Rhodamin B
SAED	Selected area electron diffraction
SC	Semiconductor
SCS	Solution combustion synthesis
SEM	Scanning Electron Microscopy
SIR	Selected ion recording
STP	Standard temperature and pressure
S_{BET}	Specific surface area from BET
T	Temperature
T	Transmittance
TEA	Triethylamine
TEM	Transmission Electron Microscopy
TEOS	Tetraethylorthosilicate
TiO_2	Titanium dioxide
t	Time
USP	Ultrasonic spray pyrolysis
UV-Vis	Ultraviolet-Visible
V	Volume
V	Volt
V_m	Volume of gas adsorbed
VB	Valence band
VO_4	Vanadium tetrahedra
XPS	X-ray photo-electron spectroscopy
XRD	X-ray diffraction
X_e	Amount of adsorbed dye per gram weight of absorbent
X_m	Amount of adsorbed dye at saturation

W	Watt
WO_3	Tungsten trioxide
Z	Atomic number
α	Adsorption
λ	Wavelength
λ_{max}	Maximum adsorption wavelength
μA	Microampere (10^{-6} ampere)
μL	Microliter (10^{-6} liter)
μM	Micromolar (10^{-6} molar)
μm	Micron (10^{-6} meter)
Φ_{SC}	Work function of semiconductor
ε	Molar absorptivity
ε_0	The permittivity of the vacuum
θ	The Bragg angle for the reflection
ν	Frequency of vibration
ν_{as}	Frequency asymmetric
ν_s	Frequency symmetric

APPENDIX B

PUBLICATIONS

Pingmuang, K., Nattestad, A., Kangwansupamomkon, W., Wallace, G. G., Phanichphant, S., and Chen, J., Photocatalytic mechanisms for dye degradation of composites based $BiVO_4$ nanoparticles. (Manuscript in preparation, December 2015).

Pingmuang, K., Nattestad, A., Kangwansupamomkon, W., Wallace, G. G., Phanichphant, S., and Chen, J., Microwave Synthesis of Pure Monoclinic $BiVO_4$ Nanoparticles for Photocatalytic Dye Degradation. *Appil. Mater. Today*, 1(2), **2015**, 67**–**73.

Worajittiphon P., Pingmuang K., Wetchakun N., Inceesungvorn B., Phanichphant S., Enhancing the photocatalytic activity of ZnO nanoparticles for efficient Rhodamine B degradation by functionalised graphene nanoplatelets *Ceram. Int.*, 40(1), **2014**, 1885**–**1889.

Antiohos D., Pingmuang K., Romano M., Beirne S., Romeo T., Aitchison P., Minett A., Wallace G., Phanichphant S., Chen J., Manganese oxide - microwave exfoliated graphene oxide composites for asymmetric supercapacitor device applications. *Electrochim. Acta*, 101, **2013**, 99**–**105.

Pingmuang K., Wetchakun N., Kangwansupamonkon W., Ounnunkad K., Inceesungvorn B., Phanichphant S. Photocatalytic mineralization of organic acids over visible-light-driven Au/$BiVO_4$ photocatalyst. *Int. J. Photoenergy*, **2013**, 943256.

Wetchakun N., Chaiwichain S., Inceesungvorn B., Pingmuang K., Phanichphant S., Minett A. I., Chen J., $BiVO_4/CeO_2$ nanocomposites with high visible-light-induced photocatalytic activity, *ACS Appl. Mater.*, 4, **2012**, 3718**–**3723.